Università di Parma

DOTTORATO DI RICERCA IN SCIENZE DELLA TERRA

Calibration and validation (CAL/VAL) of Remote Sensing data and spectral characterization of volcanic rocks

by Stefania Amici

Tutor: Chiar.ma Prof.ssa Maria Sgavetti

Co-Tutore : Dr. Maria Fabrizia Buongiorno

PhD Coordinator: Prof.

XXI Ciclo – 2006/2008

Dipartimento di Scienze della Terra

Abstract

A calibration method has been applied on satellite data in the visible infrared spectral range from which spectral reflectance and emissivity may be retrieved. This dissertation describes the steps needed for multispectral/hyperspectral data calibration and a number of algorithms for reflectance and emissivity retrieval. The methodology is applied to retrieve reflectance and emissivity of volcanoo Teide and is validated through a comparison with “ground truth”. The “ground truth” spectra have been acquired during a field campaign carried on September 2007. As application of calibrated-validated data, the classification of the volcano Teide and the temperature map are discussed.

Contents

Acknowledgments 9

1.INTRODUCTION 10

2 BACKGROUND 12

2.1 PRINCIPLE OF SPECTROSCOPY 12

2.1.1Elettromagnetic radiation 12

2.1.2 Quantum theory 13

2.1.2Absorbing process 15

2.1.3Electronic process 15

2.1.5 Vibrational process 16

2.1.6 Scattering process 17

2.2INFRARED RADIATION 19

2.2.1Emissivity 19

2.2.2 Methods for measuring surface emissivity 22

2.2.3 Fourier Transform Spectrometer (FTS) 22

2.2.4 μFTIR Model 102F for in situ emissivity measurement 23

2.2.5. Emissivity from radiance 25

2.2.6 μFTIR measurement procedure 25

2.2.7 Relevance of in situ emissivity measurements 30

2.3 VISIBLE/NEAR VISIBLE RADIATION 30

2.3.1 Reflectance **30**

2.3.2 Methods for measuring surface reflectance **32**

2.3.3 ADS FieldSpec PRO spectrometer for in situ reflectance measurement **33**

2.3.4 Reflectance from radiance **35**

2.3.5 ADS FieldSpec PRO measurement procedure **38**

2.3.6 Relevance of reflectance in situ measurements **41**

3. REMOTE SENSING **42**

3.1 INTRODUCTION **42**

3.2 IMAGING SPECTROMETERS **42**

3.1.1 Spatial resolution **43**

3.1.2 Temporal resolution **45**

3.1.3 Spectral resolution **46**

3.1.4 Radiometric resolution **47**

3.3 SATELLITE SENSORS **48**

3.3.1 ASTER **48**

3.3.2 EO-1 Hyperion **51**

3.4 ATMOSPHERIC CONTRIBUTION **53**

3.4.1 Atmospheric effect in the Infrared range **53**

3.4.2 Atmospheric effect in the Visible-Near Infrared range **54**

3.5 CALIBRATION AND VALIDATION (CAL/VAL) OF REMOTE SENSED DATA **55**

3.5.1 Data calibration: VNIR-Atmospheric correction processor **58**

3.5.2 CIRILLO code **58**

3.5.2.1Sub-procedure A: estimation of atmospheric and topographic corrections for spectral region of VNIR (Visible Near Infrared, 0.4-2.5 μm) 59
3.5.2.2 Sub-procedure B: estimation of atmospheric corrections for spectral region of TIR (Thermal Infrared, 2.5-15.0 μm) 64

3.5.3 IR data calibration: TES code, for emissivity 65

3.6 SENSITIVITY ANALYSIS 66

3.6.1 Signal to noise ratio 66

3.6.2 Method description 66

4.VOLCANO TEIDE VALIDATION CAMPAIGN 68

4.1 INTRODUCTION 68

4.2 VOLCANO TEIDE GEOLOGICAL BACKGROUND 69

4.3 VOLCANO TEIDE CAMPAIGN 74

4.3.1 Pre-campaign studies 74

4.3.2 Seasonal weather condition study 74

4.3.3 Campaign description 78

4.3.4Satellite Data acquisition TERRA-ASTER and EO1-Hyperion 79

4.4 TERRA-ASTER AND EO1- HYPERION DATA REDUCTION 82

4.4.1 ASTER calibration 82

4.4.2 ASTER SNR 83

4.4.3 ASTER product: emissivity 84

4.4.4. ASTER product: reflectance 85

4.4.5 EO-1 Hyperion calibration 85

4.4.6 EO-1 Hyperion SNR 86

4.4.7 EO-1 Hyperion product: reflectance 87

4.5 IN FIELD MEASUREMENT 89

4.5.1 In field test sites 89

4.5.2 In situ Reflectance and Emissivity measurements on Volcano Teide 91

4.5.2 Temperature measurement 104

5. LABORATORY SPECTROSCOPY 107

5.1 SAMPLES TREATMENT 107

5.2 CHEMICAL ANALYSIS 108

5.3 LABORATORY REFLECTANCE MEASUREMENT OF SAMPLES 109

6. RESUKLTS AND DISCUSSION 113

6.1 SATELLITE DATA VALIDATION 113

6.2.1 Liano de Ucanca (Point O): a validation test site 113

6.2 . VNIR RANGE DATA DISCUSSION 117

6.2.1 Comparison of in situ reflectance with Hyperion and ASTER 118

6.2.2 Volcano Teide summit crater Point Z 119

6.2.3 Mna Majua test site Point F 120

6.2.4 El Piton test site Point P 122

6.3 IR RANGE DATA DISCUSSION 124

6.3.1 Comparison of in-field emissivity with ASTER 124

6.3.2 Mna Majua:point F 125

6.3.3 Lava negra 1798: Point L 126

6.3.4 Montana Mostaza: Point U 128

6.3.5 El Piton: Point P 129

6.3.6 M. Chaorra: Point M 130

6.3.7 Point N 132

6.3.8 Boca Tauce : Point S 133

6.4 TEMPERATURE VALIDATION 135

6.5 MAP OF TEMPERATURE 137

6.6 APPLICATIONS 139

6.6.1 Volcano Teide classification 139

6.6.2 Hyperion classification map 141

6.6.3 ASTER classification map 144

CONCLUSIONS 146

REFERENCES 150

APPENDIX 1: FIELDSPEC AND MICRO FTIR IN SITU MEASUREMENT DETAILS 157

APPENDIX 2: ERROR EVALUATION FOR IN SITU REFLECTANCE AND EMISSIVITY MEASUREMENTS 171

APPENDIX 3 STANDARD DEVIATION VALUES FOR IN SITU EMISSIVITY MEASUREMENTS AS ERROR BARS 185

APPENDIX 4 EVEREST 130,2L OPERATING INSTRUCTIONS 193

APPENDIX 5 DATA DISSEMINATION STRATEGY: FRIENDSPECLIB 195

A 5.1 SPECTRAL LIBRARY ARCHITECTURE 195

A5.2 FLOW DIAGRAM OF RDBMS 197

Abbreviations

ASTER Advanced Spaceborne Thermal Emission and Reflection Radiometer
BB Blackbody
BRDF bidirectional reflectance distribution function
DEM Digital Elevation model
DWR Downwelling Radiance
EMR Electromagnetic radiation
FSC FieldSpec
FTIR Fourier Transform Infrared spectroscopy
FTS Fourier Transform Spectrometer
IFOV Istantaneous field of view
EO1-Hyperion
LWIR Long-wave infrared (7 – 15 μm)
MCT Mercury cadmium telluride
MWIR Mid-wave infrared (3 – 5 μm)
RADAR radio detection and ranging
SEBASS Spatially Enhanced Broadband Array Spectrograph System
SVM Support Vector machine
SWIR Short-wave infrared(1.5-3μm)
SWATH the width of the track covered by a sensing system
TES(A) Temperature-emissivity separation (algorithm)
TIR Thermal infrared
VNIR Visible and near-infrared (0.3 – 3 μm)

Acknowledgments

First I'd like to thank Professor Maria Sgavetti for her supervision and support over the past three years. I'd also like to thank Dr Maria Fabrizia Buongiorno at INGV field spectroscopy facility and opportunity to participate to field campaign on volcano Teide.

I extend thank to the colleagues of INGV Dr. Massimo Musacchio, Dr. Luca Merucci, Dr. Stefano Corradini , for supplying me with atmospheric correction tools. I'd like also to thank Dr Alessandro Piscini and Dr. Marco Chini for precious tips and support on image classification procedures.

A special thank to Dr Dave Pieri , ASTER science Team Member, for the data acquisition planning support and for his kind advice by email.

I extend thanks to Dr. Angioletta Coradini and Eleonora Ammanito for supplying me with laboratory facility at INAF-CNR.

A special thank to Dr Loredana Pompilio for the support in the last phase of the scripture.

A thank to European Community that funded Preview project allowing to realize the validation field campaign.

1 Introduction

Over the last 30 years remote sensing spectroscopy has found frequent application in many research fields, from Earth observation (i.e. weather forecasting, agriculture, risk management, geology, etc.) to planetary surface ~~s~~ investigations (i.e. lunar and Martian exploration missions). In particular, multispectral and hyperspectral images acquired by satellites are now routinely applied to geomorphological, geological, and geophysical investigations. The data acquired by the sensors ("raw data") have to be calibrated and validated before being used for interpretation. The calibration is a pre-processing phase that allows raw data to be expressed in physical units. The next processing phase takes into account atmospheric and topographic effects: atmospheric correction compensates for errors introduced by the interaction of radiation and atmosphere; the topographic correction takes into account differences in surface illumination due to inclination and slope. This processing phase is accomplished by applying specific models. A processing sequence is considered "validated" if good correspondence is obtained between the spectral features measured in the field on the land surface and satellite retrieved features. Validation is important and usually consists of comparisons between ground measurements (e.g. reflectance, emissivity, etc.—the so-called "in situ truth") and satellite spectral data (possibly acquired simultaneously acquisition). The validation process confirms data quality, as well as the quality of the retrieved geophysical parameters. This thesis was carried out as part of a European project called PREVIEW (http://preview-risk.web.cern.ch/preview-risk/preview.aspx). One task within the project was the CAL/VAL (calibration and validation) of satellite data acquired over volcanoic terrains.

The principal calibration and validation activity involves data acquired by Hyperion and ASTER satellite-borne sensors over Volcano Teide on Tenerife Island, part of the Canary Islands archipelago. Teide has been chosen for several different reasons: its current activity is related to persistent fumarolic activity at the summit crater and, though active, does not change much with time, a key point in the choice of a calibration test site. For the validation phase, in situ measurements are thus very important because they represent the "in situ truth" (end-members). In this work, protocols of measurements have been defined in order to guarantee the repeatability of measurements and to create a consistent systematic spectral library. This is important since Volcano Teide has not yet been spectrally investigated from combined and coordinated in situ and satellite points of view.

A explanation of models and CAL/VAL procedure applied are described in section 3.

The Volcano Teide field campaign, conducted in September 2007, is described in section 4. Spectroscopic measurements were carried out on a series of target sites, representative of both recent and old volcanic surfaces. Measurements were made using a μFTIR (manufactured by Designs and Prototypes Corp.) measurements in the mid-infrared (8-14micron) and an ASD FieldSpec Pro portable spectrometer operating in the 300-2500nm wavelength range, and have been used for emissivity and reflectance investigations respectively. Laboratory sample spectra were acquired to complete the description and characterization of the in situ data suite. On demand satellite data acquisitions (EO1-Hyperion and ASTER) were required over the area of interest.

Results of validation and comparison of in situ and satellite retrieved spectra are show in section 6.

Temperature validation was achieved by comparing in situ temperatures measurements with data acquired during a night ASTER passage, and are shown in section 6.4.

The map of temperature results and classification are shown in section 6.4. and 6.5 respectively.

2. Background

2.1 Principle of spectroscopy

Spectroscopy is the study of the interaction between radiation and matter (solid, liquid and gas) as a function of wavelength (λ). A photon that interacts with matter is subject to absorption, reflection or transmission effects. Those photons, that are reflected from grain surfaces or refracted through a particle, are said to be scattered. Scattered photons may encounter another grain or be scattered away from the surface so they may be detected and measured. Photons may also originate from a surface, a process called emission. All natural surfaces above absolute zero emit photons. Emitted photons are subject to the same physical laws of reflection, refraction, and absorption to which incident photons are bound.

In this context we will concentrate on spectroscopy based on the analysis of the information contained in the radiation reflected or emitted by the object. Reflectance and emittance spectroscopy of natural surfaces are consolidated methods used in Earth and solar planets Remote Sensing. Since most of diagnostic absorption bands that characterize the main minerals present in the rocks occur in the in VNIR (visible-near-infrared ,0.4 to 3.0-µm wavelength range) reflectance spectroscopy is used to characterize mineralogical species. Emissivity spectra of LWIR **(**Long-wave infrared, (7 – 15 µm) give information about of the rocks.

2.1.1 Elettromagnetic radiation

Electromagnetic radiation (EMR) consists of electric and magnetic field components which oscillate in phase perpendicular to each other and perpendicular to the direction of energy propagation. (fig.2.0)

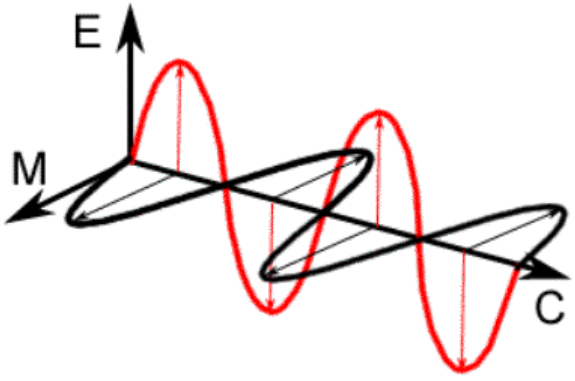

Figure 2.0 Electro-magnetic field propagation.

Electromagnetic radiation is classified into several types according to the frequency (or wavelength) of the light wave; these types include (in order of increasing frequency and decreasing wavelength as shown in figure 2.1.

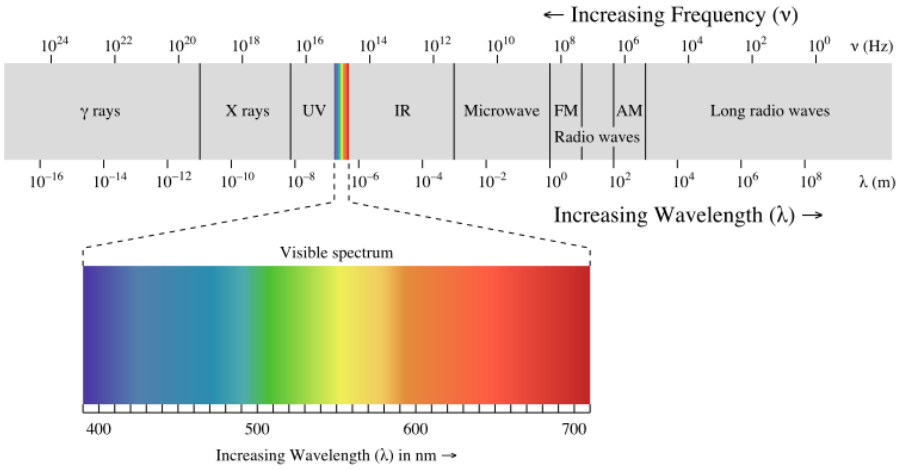

Figure 2.1 Electromagnetic spectrum versus wavelength and frequency.

The amount of scattering versus absorption controls the amount of photons we receive from a surface.

2.1.2 Quantum theory

The quantum theory is based on the idea that radiant energy is transmitted in indivisible packets whose energy is given integral parts, of size hν, (where h is the Planck constant=6.6252x10-34Js, and ν is the frequency of radiation), and these are called quanta or photons.

The particular importance of the quantum approach for remote sensing is that it provides the concept of discrete energy levels in materials, and the values and arrangement of these levels is different for each material. Information about a given material is thus available in electromagnetic radiation as a consequence of transition to a higher energy level being caused

by the absorption of energy, or from higher to lower energy level being caused by emission of energy. The amount of energy either absorbed or emitted corresponds precisely to the energy difference between the two levels involved in the transition. Because the energy levels are different for each material, the amounts of energy that a particular substance can absorb or emit are different from those of any other material. Consequently, the positions and intensities of the bands in the spectrum of a given material are characteristic of that material.

The energy distribution in any material is basically a question of the relative position of all particles at a given time. The total energy of a system may be expressed as the sum of four different kinds of energy: translational, rotational, vibrational, and electronic. Because different amounts of energy are required to cause transitions within each of these different energy types, evidence for a transition will occur in a specific part of the spectrum. Translational energy will be neglected due to its no quantization. The other three types of energy are limited in space to the size of molecule and are truly quantized.

Rotational energy is kinetic energy of rotation of a molecule as a whole in space and transition between the rotational energy levels which produce rotational spectra require only small amounts of energy. As consequence, pure rotational transitions may be observed in the mid- and far-infrared and microwave regions, where the energy is very low and insufficient to cause or result from vibrations or electronic transition.

Vibrational energy is involved with the movement of atoms relative to each other about a fixed position. Transitions here require greater amounts of energy than for rotations, and consequently evidence for such vibrational transitions occur in the mid near infrared regions. Because the energy necessary to cause the energy necessary to cause vibrations is greater than that necessary to cause rotations, vibrational transitions in the situation where the material is free to rotate (as gases).

Electronic energy is the energy required to cause the electrons about individual atoms or located in bonds, to adopt a different configuration, and this requires even larger amounts of energy. This type of transition is observed mainly in the visible, ultraviolet, and x-ray spectral range.

2.1.2 Absorbing process

When photons enter an absorbing medium, they are absorbed according to Beers Law:

$$I = I_0 e^{-kx} \quad (1)$$

Where I is the observed intensity, I_0 is the original light intensity, intensity, k is an absorption coefficient and x is the distance travelled through the medium. The absorption coefficient is traditionally expressed in units of cm^{-1} and x in cm.

Equation 1 holds for a single wavelength. At other wavelengths, the absorption coefficient is different, and the observed intensity varies. The absorption coefficient as a function of wavelength is a fundamental parameter describing the interaction of photons with a material. (Clark R.N., 1995)

2.1.3 Electronic process

Isolated atoms and ions have discrete energy states. Absorption of photons of a specific wavelength causes a change from one energy state to higher one. Emission of photo occurs as a result of a change in an energy state to a lower one. When a photon is absorbed it is usually not emitted at the same wavelength. In a solid, electrons may be shared between individual atoms. The energy level of the shared electrons may become smeared over a range of values called *energy bands*. However, bound electrons will still have quantized energy states. The most common electronic process revealed in the spectra of minerals is due to unfilled electron shells of transition elements and iron is the most common transition element in minerals. For all transition elements, unfilled d orbitals have identical energies in an isolated ion, but the energy levels slit when the atom is located in a crystal field. This splitting of orbital energy states allows an electron to be moved from a lower level into a higher one by absorption of a photon having an energy matching the energy difference between the states. The crystal field varies with crystal structure from mineral to mineral thus the amount of splitting varies and the same ion produces different absorption, making specific mineral identification possible from spectroscopy.

Absorption bands can also be caused by charge transfer or inter element transition where absorption of a photon causes an electron to move between ions or between ions and ligands. In general absorption band caused by charge transfer are diagnostic of mineralogy. In some minerals, there are two energy levels in which electrons may reside: a higher level called the *conduction band*, where electrons move freely throughout the lattice, a lower energy region called *valence band* where electrons are attached to individual atoms. The difference between the energy levels is called the band gap.

A few minerals show a color by *color centers*. A *color center* is caused by irradiation of an imperfect crystal. Energy levels are produced because of the defects and electrons can become bound to them. The movement of an electron into the defect requires photon energy.

2.1.5 Vibrational process

Vibrational spectroscopy is based on the principle that vibrational motions occur within a crystal lattice at frequencies that are directly related to the crystal structure and elemental composition. The bonds in a molecule or crystal lattice are like springs with attached weights: the whole system can vibrate. The frequency of vibration depends on the strength of each spring and their masses Clark, R.N., 1995) For a molecule with N atoms, there are 3N-6 normal modes of vibrations called fundamentals. Each vibration can occur at roughly multiples of the original fundamental frequency. The additional vibrations are called overtones when involving different t multiples of a single fundamental and combinations when involving different types of vibrations. A vibrational

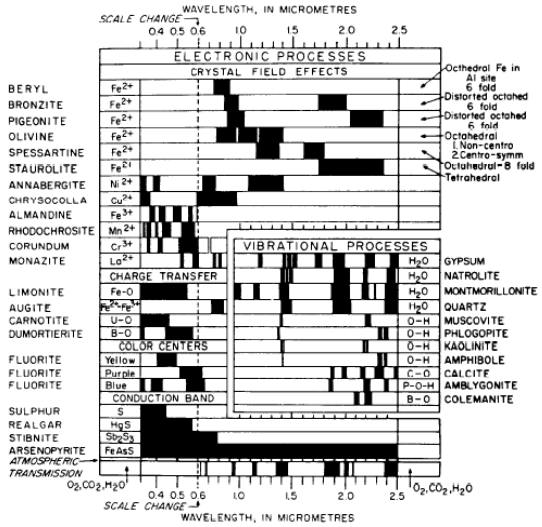

Figure 2.2 Spectral signature diagram from Hunt (1977). The widths of the black bars indicate the relative widths of absorption bands.

An extensive suite of studies in the past 35 years has demonstrated the utility of vibration spectroscopy for quantitative determination of mineralogy and petrology.

2.1.6 Scattering process

Scattering is the process that makes reflectance spectroscopy possible: photons enter a surface, are scattered one or more times, and while some are absorbed, others are scattered from the surface so we may see and detect them.

Scattering can also be thought of as scrambling information. The information is made more complex, and because scattering is a non-linear process, recovery of quantitative information is difficult.

Consider the simple Beers Law in equation 1. In transmission, light passes through a slab of material. There is little or no scattering (none in the ideal case; but there are always internal reflections from the surfaces of the medium). Analysis is relatively simple. In reflectance, however, the optical path of photons is a random walk. At each grain the photons encounter, a certain percentage are absorbed. If the grain is bright, like a quartz grain at visible wavelengths, most photons are scattered and the random walk process can go on for hundreds of encounters (Clark, R.N., 1995).

If the grains are dark, like magnetite, the majority of photons will be absorbed at each encounter and essentially all photons will be absorbed in only a few encounters. This process also enhances weak features not normally seen in transmittance, further increasing reflectance spectroscopy as a diagnostic tool.

In a mixture of light and dark grains (e.g. quartz and magnetite) the photons have such a high probably of encountering a dark grain that a few percent of dark grains can drastically reduce the reflectance, much more than their weight fraction. A general rule with mixtures is that at any given wavelength, the darker component will tend to dominate the reflectance. The effect is illustrated in Figure 7 with spectra of samples having various proportions of charcoal grains mixed with montmorillonite Clark, R.N., 1995).

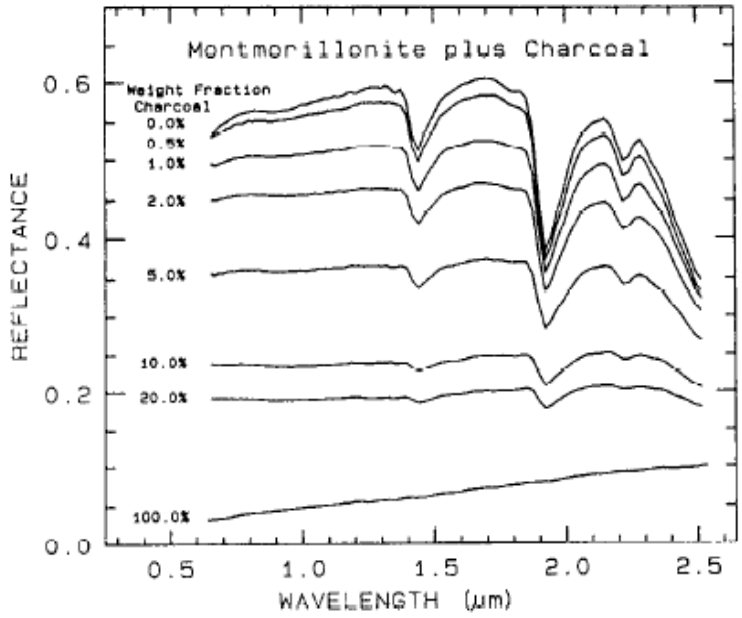

Figure 2.3 Reflectance spectra of intimate mixture of montmorillonite and charcoal shows the non-linear aspect of reflectance spectra of mixtures. Clark, R.N., 1983.

The amount of light scattered and absorbed by a grain is dependent on grain size. A larger grain has a larger internal path where photons may be absorbed according to Beers Law. It is the reflection from the surfaces and internal imperfections that control scattering. In a smaller grain there are proportionally more surface reflections compared to internal photon path length, or in other words, the surface-to-volume ratio is a function of grain size. As the grain size increases, the reflectance decreases. Absorptions in a spectrum have two components: continuum and individual features. The continuum is the "background absorption" onto which other absorption features are superimposed. It may be due to the wing of a larger absorption feature (Clark, R.N., 1998). The depth of an absorption band, D, is usually defined relative to the continuum, R_C:

$$D = 1 - Rb,/Rc \quad (2)$$

where Rb, is the reflectance at the band bottom, and Rc, is the reflectance of the continuum at the same wavelength as R_b. The depth of absorption is related to the abundance of the absorber and the grain size of the mineral. Consider a particulate surface with two minerals, one whose spectrum has an absorption band. As the abundance of the second mineral is increased, the band depth, D, of the absorption will decrease. Next consider the reflectance

spectrum of a pure powdered mineral. As the grain size is increased from a small value, the absorption band depth, D, will first increase, reach a maximum, and then decrease. This can be seen with the pyroxene spectra. If the particle size were made larger and larger, the reflectance spectrum would eventually consist only of first surface reflection. The reflectance can never go to zero because of this reflection, unless the index of refraction of the material is 1.0.

2.2 Infrared radiation

In the frame of this study, infrared energy may be considered as energy emitted between 3 µm and 14 µm in the electromagnetic spectrum. A strong H_2O absorption features at 5-8 µm split the spectrum into two spectral regions within which surface observation can be made(Salisbury, 1998). For the purpose of this study on the interval 8-14 µm will be considered.

2.2.1 Emissivity

The Earth's surface and atmosphere radiate thermal energy outward owing to heating by solar irradiation and by internal heat flow (generally a very minor contribution). Sensors that measure this emitted radiation in parts of the thermal region of the spectrum (whether in laboratory or from space) can produce very informative data (especially as images) that provide both distinctive signatures and, indirectly, indications to determine the physical and chemical characteristics of the object under study. Depending on the wavelength region examined properties of geologic interest can include surface roughness, mineralogy, temperature, particle size, and-or elemental abundances.

Remote sensing of direct temperature effects is carried out by sensing radiation emitted from matter in the thermal infrared region of the spectrum.

Energy emitted by a surface in the thermal infrared region, ca be described by the Planck equation. Depending on what terms (parameters) and unit systems are used, the Planck equation can be written in various ways. As often used in remote sensing calculations, this differential form is given as:

$$L(\lambda) = \frac{\varepsilon(\lambda)\, C_1}{\quad} \qquad (3)$$

$$\lambda^5 P (\exp(C_2/\lambda T) - 1)$$

where L is the radiance detected at the sensor, T is the temperature, ε is the emissivity, C_1 is the first radiation constant ($3.7411x10^8 W\mu m^{-4}/m^2$) and C_2 is the second radiation constant ($1.4388x10^4\ \mu mK^{-1}$) and λ is the wavelength expressed in micrometers (Holst G., 2000).

The "pixel integrated' temperature (also known as colour temperature) derived by the total radiance $L(\lambda)$ in equation (3) as calculated by the inverse Plank equation :

$$T = \frac{C_2}{\lambda \ln ((\varepsilon(\lambda) C_1 \lambda\text{^}5/ P L(\lambda)) + 1)} \quad (4)$$

Figure 2.4 illustrates Plank's emitted radiance (as intensity) in logarithmic coordinates. Each curve has a maximum at λ_{peak} Wien's displacement law provides λ_{peak}= 2898/T μm as the temperature increases, the rate of emission increases very rapidly.

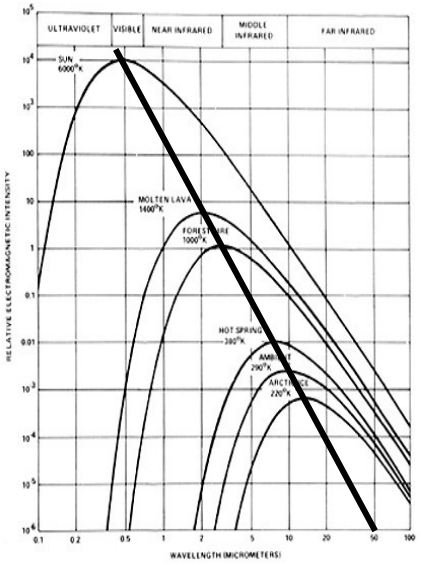

Figure 2.4 Planck spectral emission plotted in logarithmic coordinates for various absolute temperatures ranging from the Sun to the Earth's surface (average ambient temperature and sea ice).The light line is Wien's law.

Body's temperature represents one thermal state but may be expressed by two temperatures: the first is its internal temperature (from the kinetic motion of its atoms) as measured by a thermometer; the second is the external temperature measured by its emitted radiation. The

radiant flux, F_B (total power density, W/cm^2) emitted by a blackbody in an interval $\Delta\lambda=\lambda_2-\lambda_1$ is related to its internal (kinetic) temperature T_k by the Stefan-Boltzmann Law.

$$L_B = \int_{\lambda_1}^{\lambda_2} L(\lambda, T) d\lambda = \sigma T_k^4, \quad (5)$$

where σ is a constant equal to 5.67 x 10^{-8} W/m^2 K^{-4}.

The Stefan Boltzmann law describes the total maximum radiation (continuum emission of energy) that can be released from a surface. An object with an emissivity value equal to unity radiates a featureless spectrum described by the Plank function and is defined as blackbody emitter. Most objects do not emit all the radiation described by Plank's law. Rather, they have spectra with emissivity values less than one at discrete wavelengths. Commonly called absorption bands, these features are signatures of the object or mineral being analyzed (Ramsey M. S. and Cristensen P. R.. 1998). The wavelengths corresponding to the largest absorption band (reststrahlen bands) are present in carbonate and silicate minerals.

The emissivity of a real body (so-called real or "graybodies") is defined as the fraction:

$$\varepsilon(\lambda)/=L_{actual}(\lambda,T)/L_{BB}(\lambda,T) \quad (6)$$

where L_{actual} is the energy radiated by a surface, at any given wavelength (λ), T is the kinetic temperature and L_{BB} is the radiated energy of a blackbody at the same kinetic temperature.

The emissivity may vary with wavelength, the object shape, surface quality and viewing angle. While it is instructive to study the emissivity of specific targets, the radiation measured depends upon the target and its environment. For no perfect the radiant flux will always be less than the blackbody flux and is calculated by

$$L_R = \varepsilon\sigma T_k^4 \quad (7)$$

2.2.2 Methods for measuring surface emissivity

Instruments dedicated to the measurement of spectral features are named spectral radiometers. Traditionally, spectral radiometers have been divided into two type: radiometers which sense in a limited number of pre-set spectral bands and spectrometers (or spectro-radiometes) which permits the measurement of the spectral distribution of radiant energy by collecting radiant energy at all wavelengths simultaneously. Two distinct methods have been developed for retrieving emissivity: one derives emissivity from surface reflectance spectra and are largely confined to laboratory, a second one measures surface radiance to calculate emissivity and has been developed as in field technique. We will focus on this second method.

2.2.3 Fourier Transform Spectrometer (FTS)

The Fourier Spectrometer derives its name from the mathematical Fourier transformation which is applied to the measurement data to determine the spectrum. The principal application of the Fourier spectrometer has been in the infrared for situations in which detector noise limits to signal-to-noise ratio, although interest in applications in the visible region has recently increased (Becherer G., 1979).

Operating principle of the Fourier spectrometer is shown in figure 2.5. A beam radiant energy of unknown spectral distribution is incident on a beamsplitter where it is divided into transmitted and reflected components.

The light is reflected on the mirrors and the light from the two optical paths are reunited at the beam-splitter. The light from the vertical and the horizontal optical paths interfere with each other and hit the infrared detector (or a two-dimensional array of IR-detectors). By moving the right mirror and simultaneously studying the interference pattern of the light at the detector an interferogram can be acquired.

There is a one-to-one correspondence between this interferogram and the spectrum of the light. This relationship will not be derived here, but it involves a Fourier-transform, hence the name of this method. There are several different optical designs for imaging spectrometers based on spatial FTS.

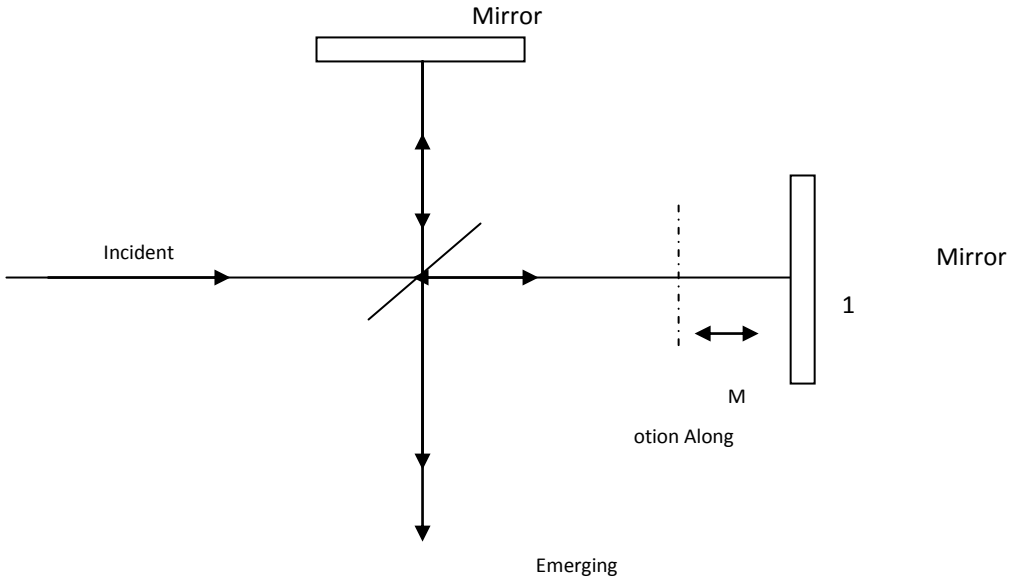

Figure 2.5 Basic configuration of Michelson–Fourier spectrometer (Becherer, G. 1979).

2.2.4 µFTIR Model 102F for in situ emissivity measurement

The µFTIR, Model 102F spectrometer is developed by Design and Prototypes (www.dpinstruments.com) for field measurements of Earth's surface and atmosphere spectral radiance. The spectrometer, operates at wavelengths ranging from 2 to 16 µm with a spectral resolution of 2 cm^{-1}. It has two liquid nitrogen cooled detectors, HgCdTe (or MCT) and InSb, for measurements collection in the 8-14 µm and 3-5 µm atmospheric windows respectively. The main features of the µFTIR are resumed in table 3.4 while figure 2.6 shows the instrument schematic diagram.

FTIR	
Spectral range	2-16 µm
Spectral resolution	2, 4, 8, 16 cm^{-1}
Operating temperature range	15-35 °C (instrument temperature)
FOV	4.8° (additional input optic 2.4°)
Computer OS and type	DOS 6.22, 8GB HD, Pentium 166MHz/32MB
Input voltage range	12V DC (±10%)
Weight	7 Kg
Size	36cm x 20cm x 23cm

Table 3.4 Model 102 F portable µFTIR main spectro-optical characteristics.

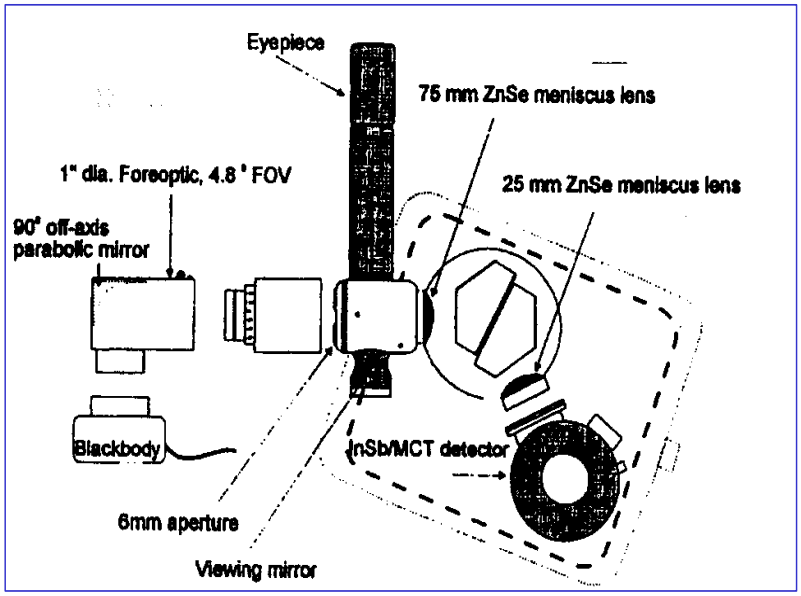

Figure 2.6 Schematic diagram of the model 102F portable FTIR by Design & Prototypes, LTD.

2.2.5. Emissivity from radiance

To compute spectral emissivity by radiance measurements, the radiation emitted by the surface is compared with the radiation emitted by a blackbody at the same kinetic temperature. The upwelling target radiance is composed of both target emission and reflected downwelling radiance ($L_{DWR}(\lambda)$). We remind that downwelling radiance is the energy absorbed by the atmosphere and re-emitted at wavelength being detected by the remote sensing instrument.

The μFTIR compute an advanced algorithm derived from the radiative transfer equation in TIR spectral range:

$$\varepsilon(\lambda) = \frac{L(\lambda) - L_{DWR}(\lambda)}{L_{BB}(T_S, \lambda) - L_{DWR}(\lambda)} \tag{8}$$

where $L(\lambda)$ is the spectral radiance field measured by the spectrometer, $L_{BB}(T_S,\lambda)$ is the spectral radiance field of a blackbody (BB) at temperature T_S , $\varepsilon(\lambda)$ is the target spectral emissivity (Salvaggio and Miller 2001, Korb et al 1996). Measurements of downwelling radiance of the hemisphere above the target are taken using a diffuse reflective surface, usually InfraGold or crinkled alluminium. The μFTIR is provided of a InfraGold plate (Figure 3.6) with emissivity ε = 0.040. Moreover the sample temperature T_S must be found by direct independent measurement. The instrument calibration is carried out by means two blackbody measurements at two different temperatures.

2.2.6 μFTIR measurement procedure

A protocol for the FTIR measurement has been implemented in order to assure repeatability and good accuracy of measurements.

We can distinguish three phases: *Pre Campaign*, *In field campaign protocol* consisting of instrument preparation, instrument calibration and emissivity computation and a *Post Campaign* phase. Figure 2.6 summarize the flow diagram of a spectral surface emissivity measurements obtained by μFTIR.

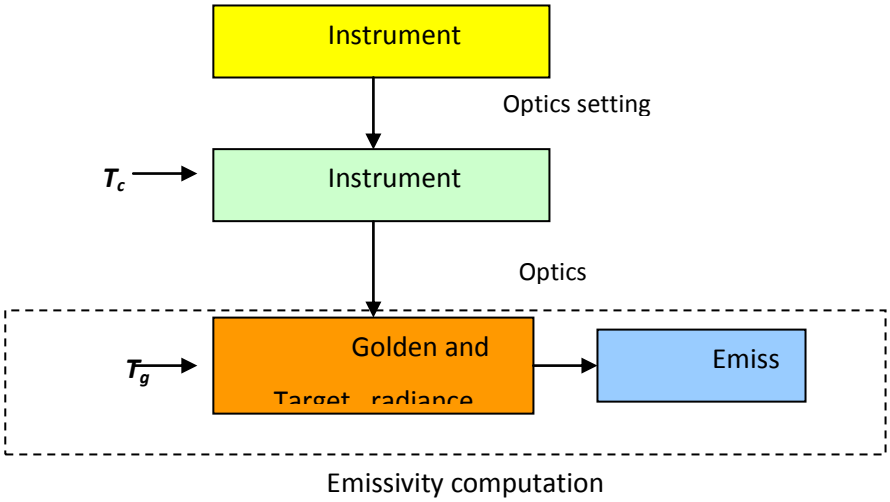

Figure 2.6 Surface spectral emissivity measurements flow diagram.

1. Pre campaign activity

Pre-campaingn activities may be summarized as follows:

- Check list the whole components of the instruments(Black Bodies, optics, Nitrogen availability, golden reference plate, batteries)
- Recharge the batteries for a minimum of 9 hours.
- Check the batteries of the GPSs and set the modality N for the automatic acquisition if connected with the
- A camera for the pictures of the target
- Maps with the selected test sites that will be measured.
- Sheets for the notes . It can be used the same template developed for the FieldSpec (see Table 3.2)

2. In field Campaign Protocol

The different phases are showed in the diagram of figure 3.6 are described in the following.

Instrument preparation*:* The first step consists in cooling the instrument. Nitrogen dewar must be filled about 30-60 minutes in advance in other to allow the thermalization of the system.

Secondly the optics for calibration and that one for acquisition are mounted for the two kinds of measurement.

At least the distance from optics to the target (less then 1m) is set and the instrument may be switched on.

- An important rule is plaid by the instrument parameter setting: from the main menu of graphic interfacethe selection of the following instrument setting are suggested.
- the number of spectra to be averaged (*Coadds = 16*),
- the measurements spectral resolution (*2 cm^{-1}*)
- and the wheighting function to be used to window the interferogram data (*FFT Apodization = Hamming*).

The optical head is temperature controlled to increase the calibration accuracy of the instrument, because instrument self-emission varies strongly with instrument temperature. Maintaining instrument temperature constant within 0.1 °C between calibration measurements limits the fractional calibration error from this variability to less than 0.002 (Korb, A.R.et al. 1996)

Instrument calibration: The instrument calibration is the most important phase in order to obtain good measurements from quality and accuracy point of view. Ambient temperature variation, due to weather condition changing, can affect the calibration. These imply to repeat a calibration sequence at the beginning of every measurement cycle. The blackbodies radiance are measured by pressing the blackbody onto the instrument foreoptic (Korb, A.R.et al. 1996). The blackbody provided is powered and temperature controlled by the instrument itself and the cold and warm calibration temperatures can be set from the acquisition software.

After having mounted the BB system assembling, we measure the surface (target) temperature Ts is measured by using a thermocouple and the ambient temperature, Ta, by a thermometer. These temperatures are very important to select the blackbodies set point for the calibration (Salvaggio, C., Miller, C., 2001).

The blackbodies temperature has to be set as follows:

$$T_c = T_a - 2\ °C \quad (9)$$

$$T_h = T_s + 2\ °C$$

Where T_c is the temperature of cold Blackbody (BB_c) and T_h is the temperature of the hot Blackbody (BBh) . These two temperatures will be set by main menu [Instrument --> temperature]

The last step is the acquisition of the blackbodies radiances.

From main menu we go on [Process --> Calibrate Instrument --> Acquire data and Calibrate --> Acquire];

First the BB_c, and then the BB_h. After the measurement we have to remember to set BB_{off} and exit.

A label "instrument calibrated" will appear vertically on the left side of the screen.

Emissivity computation measurement: The first step, after BBs measurements, consists in dismounting the blackbody and in mounting the measurements optics.

Secondly the golden plate reference is placed on ground, over the target, in the field of view of the instrument and a measure of its surface temperature by thermocouple (T_{gold}) is realized (figure 2.7). At this time the downwelling radiance ($L_{DWR}(\lambda)$) acquisition is carried on and the golden plate is removed and the target radiance ($Ls(\lambda)$) is measured.

At this point the sample the temperature is measured as request by the software interface and the emissivity is visualized on the screen. Alternatively an auto-fitting by Plankian may be implemented (Figure 2.7).

The data are saved in ASCII format by Export function on main menu according to the filename coding.

The GPS localization, the snapshot and a sample (if possible) of the test site are realized to complete the characterization of the site.

In the following table are summarized the characteristics of the thermocouple. Temperature measurement is very important and tricky in fact it may change during the measurement sequence affecting the results due to the not affordability of the calibration that have to been performed again.

Temperature Scale:	Celsius or Fahrenheit user-selectable
Thermocouple Range	K-TYPE -200°C to 1372°C
Resolution:	K-TYPE 0.1°C
Accuracy:	Accuracy is specified for operating temperatures over the range of 18°C to 28°C for 1 year, not including thermocouple error. K -TYPE ±(0.05% rdg + 0.3°C) -50°C to 1370°C
Temperature Coefficient:	0.1 times the applicable accuracy specification per °C from 0°C to 18°C and 28°C to 50°C.

Table 3.5 ΩOMEGA-HH506R thermocouple characteristics

3. Post Campaign activity

Activities post campaign may be summarized as follows:

- After campaign a check of data quality is required.
- Instrument check is due to verify the state of the instrument after campaign and after expedition back to laboratory;
- Notes and comments relative to the campaign are registered on the LogBook (Date, duration of the campaign, operator, comments and possible failure or damaged have to be pointed out)
- Every component is lodged in the laboratory in the proper place in order to be ready for the next measurements activities.

Figure 2.7 A) FTIR in situ target acquisition setting; B) GPS acquisition point; C) software interface showing an emissivity plot preview; D) Gold plate temperature measurement.

2.2.7 Relevance of in situ emissivity measurements

Thermal infrared emission spectra(emissivity) are critical for most geoscientists working on surface processes and lithological mapping because the energy emitted from the surface is dependent on specific properties of the major rock forming and alteration minerals (Clark, 2004). Surface composition may be retrieved by spectra features.

In particular:

- Emissivity is related to vibrational processes of SI-O group and O-H cation groups. This implies that it trace the silicates that constitute the effusive rocks and their alteration products.
- Emissivity is important to discriminate the rock bodies and by means their emissivity values it is possible to retrieve their temperature values.
- Since surface temperatures may be retrieved by emissivity, relevant applications are in volcanic and ecologic field.
- Another application consists in characterizing test sites by is situ emissivity measurements, for the validation of models used to calibrate the remote sensed data.

In this work, in field measurement of emissivity on volcanic surfaces, have been done and will be applied to for validation of models used to calibrate satellite data (i.g. ASTER and EO1-Hyperion).

2.3 Visible/Near visible radiation

In the frame of this study we will consider the radiation in the spectral range of 350nm to 2.5nm (0.35um-2.5nm). HO_2 absorption bands in correspondence 0f 1.4 μm and 1.9μm may affect the spectra. The noisy bands will be removed so a gap will be visualized on the spectra.

2.3.1 Reflectance

The spectral reflectance of Earth materials is often the most diagnostic criterion for lithologic discrimination (Siegal, B.S. and Gillespie, A.R., 1980). Spectral reflectance is a measure of the

amount of light reflected by a material. Reflectance is a consequence of the chemistry and structure of material modified by environmental factor and physical condition of the material.

In the following, theory of reflection is briefly described.

The bidirectional reflectance distribution function (BRDF) is a function characterizing the amount of electromagnetic radiation reflected (scattered), as a function of the directions of the incident and reflected radiation (Rees, G., 1999). Consequently, BRDF is defined as the ratio of the reflected radiance (from a surface) to the incident irradiance (see appendix 0) It is a normally function of the directions of both the incident radiation (E) and the reflected radiation (L), and is denoted by

$$R(\theta_0,\phi_0,\theta_1\phi_1) \tag{10}$$

where θ_0, and ,θ_1 are the angles between the incident and reflected radiation , respectively, and the normal surface, and ,ϕ_0 and ,ϕ_1 are the corresponding azimuth angle (see figure 2.8). The BDRF is symmetric with respect to the incident and reflected directions, i.e.

$$R(\theta_0,\phi_0,\theta_1\phi_1)= R(\theta_1,\phi_1,\theta_0,\phi_0) \tag{11}$$

The reflectivity of a surface is a function only of the incident direction, and is defined as the ratio of the radiance exitance to the irradiance. It is given in terms of BDRF by

$$\mathrm{r}(\theta_0,\phi_0) = \int_{\theta_1}^{\pi/2}\int_{\phi_1}^{2\pi} R(\theta_0,\phi_0,\theta_1,\phi_1)\cos\theta_1 \sin\theta_1 d\theta_1 d\phi_1 \tag{12}$$

In Lambertian assumption, the radiance of an ideally rough surface is isotropic for any illumination. Such a surface has a constant value of BDRF function.

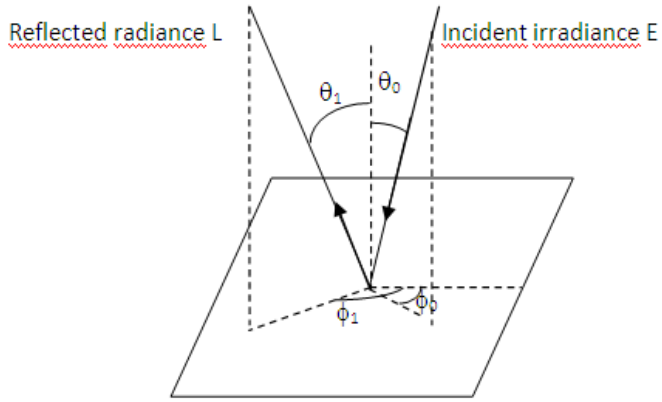

Figure 2.8 Reflectance ray trays.

2.3.2 Methods for measuring surface reflectance

Instruments dedicated to the measurement of spectral features are named spectral radiometers. Traditionally, spectral radiometers have been divided into two type: radiometers which sense in a limited number of pre-set spectral bands and spectrometers (or spectro-radiometes) which permits the measurement of the spectral distribution of radiant energy by collecting radiant energy at all wavelengths simultaneously. These kind of instrument are named multichannel spectrometer and use a spatial array of detectors to collect the dispersed energy from spectral dispersing element such as a grating.

A multichannel spectrometer is similar to a monocromator in the sense that it employs a grating or prism as a dispersing element but, unlike the monocromator, collects the dispersed energy in a number of wavelength channels simultaneously. The energy in each channel may be collected by a discrete detector element of a detector array. In figure 2.9 is showed the scheme of the essential

optical components in a multichannel spectrometer. The dispersed spectrum which is produced by the dispersing element is focused by optical elements located in or near the exit aperture. The focused beam is incident on a detection plane in which the various wavelengths are spread vertically. A scanning optical element may also be used so that the spectrum at various times appears at various horizontal locations.

Optical elements may, however, require further aberration correction since they now work over a larger field of view. A principal reason for employing multichannel techniques is to obtain improved signal-to-noise by collecting energy at all wavelengths of interest simultaneously.

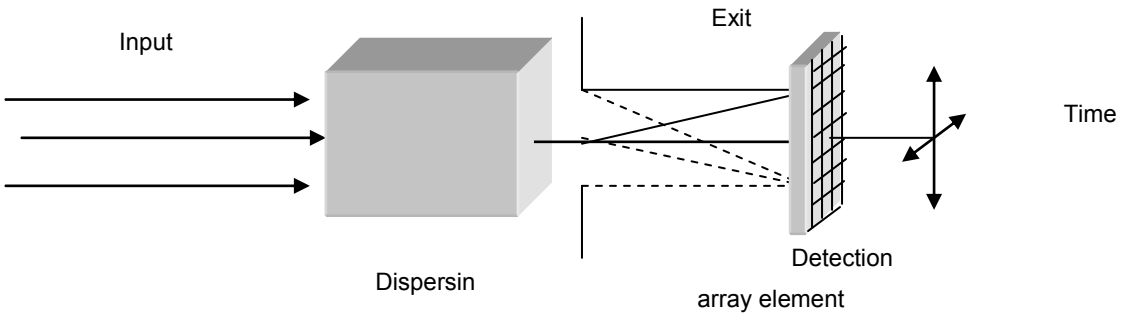

Figure 2.9 Basic component of a multichannel spectrometer, Focusing optical elements are used to exit aperture so that the spectral power at each wavelength appears along the vertical direction (Becherer G., 1979).

Evolution of multichannel spectrometer is the imaging spectrometer (see section 3.2) and is used mainly on board of airborne and satellite. New generation of imaging spectrometer lighter and more compact are suitable also for in situ measurements.

2.3.3 ADS FieldSpec PRO spectrometer for in situ reflectance measurement

ASD FieldSpec Pro FR (or briefly FieldSpec) portable, battery powered, spectroradiometer permits to detect individual absorption features due to specific chemical bonds in a solid, liquid or gas. Detection is dependent on the spectral range, spectral resolution, and signal-to-noise of the spectrometer (parameters that describe the instruments capability), the abundance of the

material and the strength of absorption features for that material in the wavelength region measured.

The spectrometer (Hatchel D., 1999) permits to operate in three detector ranges, 350-1050 nm, 1000-1800 nm, 1800-2500 nm, with just one instrument by using three spectrometes arrays: VNIR is a Silicon photodiode detector array (Figure 2.10 A)and SWIRs are InGaAs arrays (Figure 2.10 B).

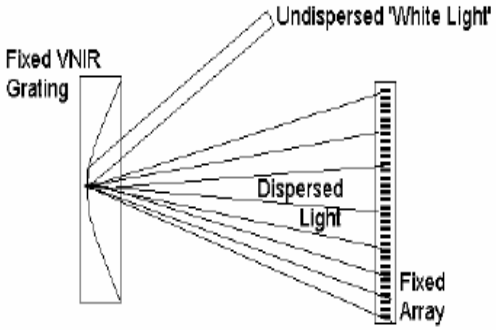

A) Diagram of VNIR spectrometer spectrometers

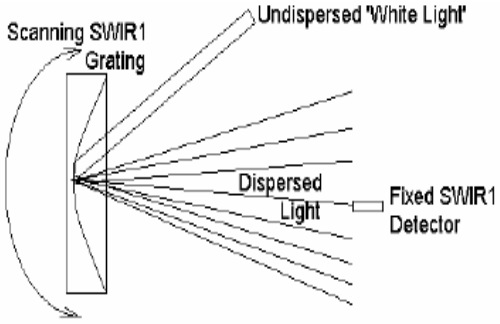

B) Diagram of SWIR 1 and SWIR 2

Figure 2.10 A) The VNIR spectrometer uses a fixed concave holographic reflective grating that disperses the light onto a fixed photodiode array that has 512 individual detection points or 'elements', in a line. Associated with each of these elements is a distinct signal whose magnitude is determined by the total integrated amount of light energy falling on that element. B)The SWIR1 spectrometer uses a concave holographic reflective grating that rotates up and then down on its axis thereby scanning the dispersed light across a fixed single InGaAs graded index TE cooled detector. As the dispersed light is scanned across the detector in the up scan direction, a distinct signal is recorded for each of 530 positions of an encoder in-line with the rotation axis of the grating The SWIR2 is constructed and operates exactly the same way as the SWIR1 spectrometer except; the grating and detector are manufactured for the longer SWIR2 wavelength region (Hatchell D. C, 1999).

Then the radiation is led by an optic fiber into the detector system with 10 nm spectral resolution where wavelength components are separated and reflected for independent collection by the detectors. The original field of view is 25°. With a foreoptic it can be reduced up to 1°.

The optimization of the spectroradiometer is performed immediately prior to the start of data collection. This process may need to be repeated periodically.

Each spectrometer detector converts the incident photons in electrons and accumulates a signal over a period defined by the integration time (typically set at 17 milliseconds). The integrated signal is converted to a voltage and then digitized by a 16-bit analogue to digital (A/D) converter.

The main characteristics of the FieldSpec Pro are shown in the following table.

Name	FieldSpec® Pro FR
Spectral	350-2500 nm
Spectral Resolution	3 nm @ 700 nm 10 nm @ 1400 & 2100nm
Sampling Interval	1.4 nm @ 350-1050 nm 2 nm @ 1000-2500 nm
Scanning	100 milliseconds
Detectors	One 512 element Si photodiode array 350-1000 nm Two separate, TE cooled, graded index InGaAs photodiodes 1000-2500 nm
Input	1.4 m fiber optic (25° field of view) Optional foreoptics
Calibration	Wavelength, reflectance, radiance*, irradiance*. All calibrations are NIST traceable (*radiometric calibrations provided)
Noise Equivalent Radiance (NeDL)	UV/VNIR 1.4 x 10^{-9} W/cm^2/nm/sr @ 700nm NIR 2.4 x 10^{-9} W/cm^2/nm/sr @ 1400nm NIR 8.8 x 10^{-9} W/cm^2/nm/sr @ 2100nm
Notebook Computer	Pentium processor, 800 MB hard disk, 16 MB Ram, 3.5" floppy disk drive, battery, AC power supply
Weight	7.2 kg or 15.8 lbs

Table 3.1 FieldSpec® Pro FR instrument characteristics.

2.3.4 Reflectance from radiance

The ASD FieldSpec Pro FR has been used to measure reflectance spectra. The spectral reflectance, R (λ), is a calculated by definition as:

R(λ) = Energy reflected from target(λ)/ Energy incident on target (λ) (13)

Because of the radiance is defined as radiant flux per unit projected area per unit solid angle (where the projected area may be that of a detector surface, a source surface, or an imaginary surface in space) and the flux is the amount of light energy that crosses a defined surface in a unit time (radiant power), in the case of optical radiant energy, the construction known as radiance, $L(\lambda)$, is used to quantify the optical radiant energy. Radiance has the units, Watts per square meter per steradian per nanometer ($W/m^2str^{-1}nm^{-1}$). So, in this case, if $L_t(\lambda)$ is the radiance reflected from the target, and $Li(\lambda)$ is the radiance incident on the target. The spectral reflectance may be expressed as:

$$R(\lambda) = L_t(\lambda) / L_i(\lambda) \quad (14)$$

if the instrument is configured to properly view $L_t(\lambda)$ and $L_i(\lambda)$, it really doesn't matter that it be calibrated to absolute units. All we really need is the response of the instrument for $L_t(\lambda)$ in some unit of measure and the response of the instrument for $L_i(\lambda)$ in the same unit of measure. In the case of an analog photo detector, PD, the current produced by the PD is linear in response to radiance (voltage is approximately logarithmic). This analog current signal can be converted to digital numbers, DN, as in the FieldSpec®, giving the following for a given wavelength channel:

$$R(\lambda) = DN_t(\lambda) / DN_i(\lambda) \quad (15)$$

While $L_t(\lambda)$ is measured by pointing the fiberoptic input of the FieldSpec® at the target, $L_i(\lambda)$, may be measured aiming the fiberoptic input at a diffuse white reflectance panel (sometimes called a calibration panel) that provides a diffuse homogeneous mix of all the full sky and sun radiance reflected at nearly 100 percent up to the fiberoptic input. The used calibration panel is a White Spectralon (Figure 2.12). It is a near 100% diffuse (Lambertian) reference reflectance panel made from a sintered poly - tetra - fluorethylene based material.

The instrument is controlled and data displayed and stored using a notebook computer providing foreoptic information, recording dark current and registered spectra. Since the dark current varies with time and temperature it is gathered for each integration time. Spectral data from ASD FieldSpec Pro FR spectroradiometer has been obtained for several test-sites locations spread across the study area (Mount Volcano Teide.). The spectrometer unit and computer are carried on a special tripod, while power is supplied from a battery pack carried around the waist.

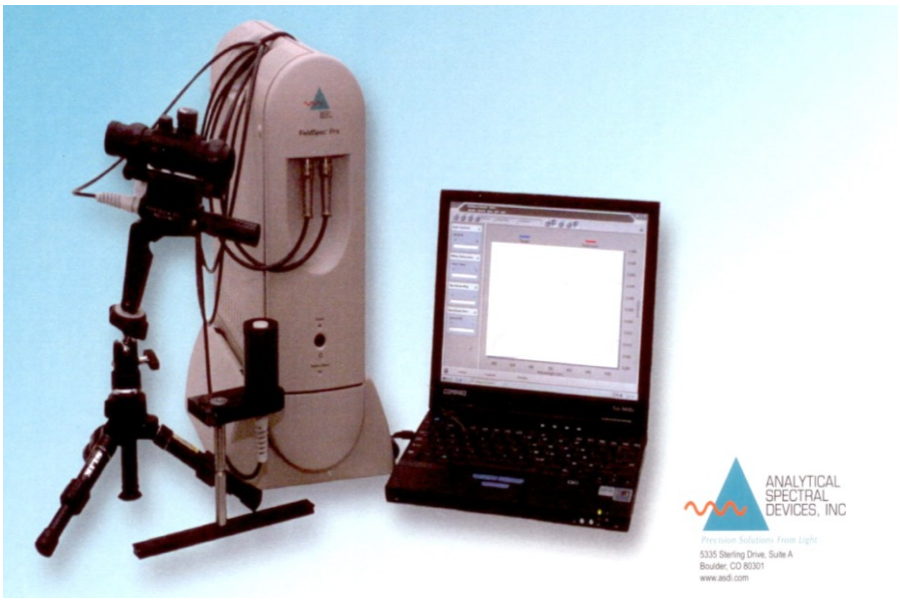

Figure 2.11 FieldSpec®Pro , pistol girp mounted on a tripod , acquisition system for calibration and reflectance measurement.

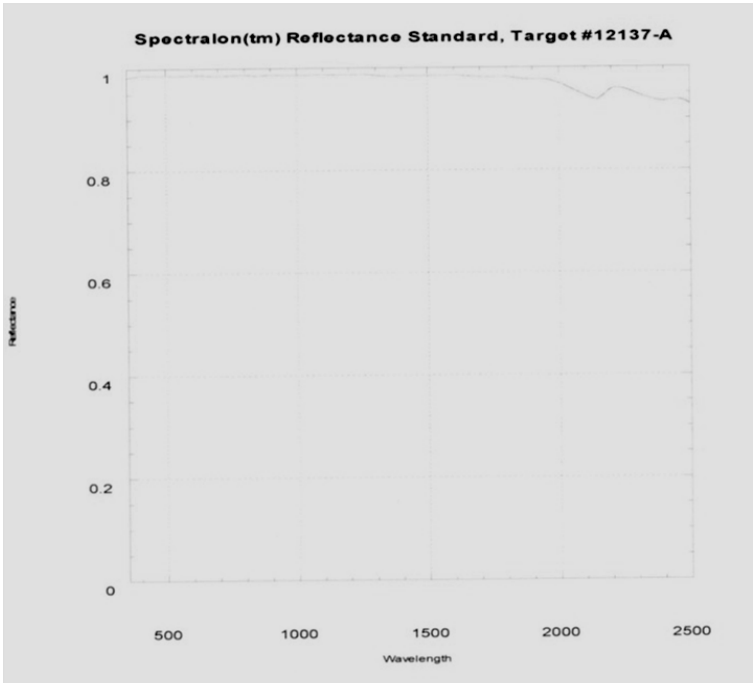

Figure 2.12 Spectralon reflectance standard shows a constant behavior overall most part spectral range.

2.3.5 ADS FieldSpec PRO measurement procedure

The first important requirement for the precision of the measurements is the repeatability. In attempting to measure reflectance spectra in field, measurements of radiant flux are being made after its transmission through a dynamic, turbulent, absorbing and scattering medium: the atmosphere (Milton E, J, 1987). Although the path length of the reflected beam through the atmosphere is usually very short, the path length of the incident beam is much longer and this jointly to the contribution of the sky light to the incident flux and the changes in atmospheric properties over time, means that the effect of the atmosphere upon field measurements of reflectance can be very significant. Changes in irradiation due to the atmosphere occur on several different times scales. Firstly, streams of atmospheric particulates cause very short period fluctuation, of the order of a few milliseconds, which have been reported as producing a coefficient of variation in irradiation of approximately 1% (Slater P.N., 1980).Secondly, there are longer period (seconds to minutes)changes in irradiation of the order of 5% of the mean which occur in clear in clear blue skies and are thought to be the result of high altitude cirrus clouds invisible to human eye (Duggin M.J,1974).Thirdly, there are the major changes in irradiation which occur when clouds pass in front of the Sun creating often a period of unpredictable fluctuation in irradiation as the cloud enters and leaves the solar beam. (Monteith 1973). It is possible to remove the effect of these temporal changes in irradiation from the calculation of reflectance factors by arranging for the target radiance and the standard panel radiance to be sampled at exactly the same instant . However, this requires the use of two radiometers, matched over a wide dynamic range, sensing identical wavelengths and affected in the same way by changes in temperature and other environmental variables. When measurements of radiance from the target and standard panel are made sequentially, it is important that the time delay between the two measurements should be as short as possible.

A **protocol of measurement** has been developed also for the ADS FieldSpec PRO.
We can distinguish three different phases: *1 pre-Campaign activity, 2 implementation of the protocol, 3 post-campaign instrumental controls*.

1. Pre-Campaign activity

In order to reduce possible failures occurrence a series of test and activities are carried on in the day before measurement and are summarized in the following points:

- Check list the whole components of the instruments (instrument body, pistol grip, acquisition laptop, inverter, batteries, connection cables Spectralon reference).
- Recharge the batteries for a minimum of 9 hours.
- Check the batteries of the GPSs ed end set the modality N for the automatic acquisition if connected with the
- A camera for the pictures of the the target
- Maps with the selected test sites that will be measured.
- Sheets for the notes (table 3.2)
- File names and folder code should be chosen taking into account that information about target, date and time are recommended.

2. In field campaign protocol

In order to maintain the repeatability and comparison criteria of the measurements some criteria have to been followed for each series of data acquisition.

- The instrument has to be turned on half an hour in advance the measurements for the stability of data due too electronic noise.
- Automatic acquisition (high contrast RS) program is initialized and work directories , files code, number of spectra to be averaged are set..
- After the selection of the target, a snapshot with a centimetre reference has to be taken in correspondence of the target.
- Metadata are registered on the sheet e.g. day, time, atmospheric temperature, weather condition, altitude, etc...)
- GPS geolocation is recorded (automatically or taking notes)
- Use a tripod to ensure a fixed geometry between sensor , the standard panel and the target. Hand –held measurements are less precise because of the variable geometry is involved and because of the (necessarily) close proximity of the operator to the target and of the target to the spectrometer.

- Spectra collection for reflectance measurement:

  Select the reflectance mode then follow these steps:

  The fiber optic point the white reference spectralon (**WRS**) panel and optimise botton (**OP**) is pressed. After optimization a measurement of the WRS is taken by pressing space bar.

  Point the target and take a measurement in the same mode.

  If sky condition change a new measurement of spectralon is required.

  A measurement of dark current (**DC**) should be taken after 5-10min.by pressing the DC button.

- Ensure that the sensor is at least 1m-2m above the upper surface of the target

  It is important to check that the reference panel fills the field-of –view (FOV) of the instrument and that it is not shaded by anything.

- The procedure can be summarised as:

  OP->**WRP**->surface target$_{\mathbf{1}}$-> ....surface target$_{\mathbf{n}}$-> **WRP**->**DC**-> surface target$_{\mathbf{n+1}}$....etc.

Operators should wear dark clothes and sit same distance from the target during the measurements. A person wearing white clothes and at 0-5m from the instrument may affect the radiance measurements of 10% in the red and 12% in the near infrared as demonstrated by Kimes et al 1983 that proved a decreasing error until 2% (both bands) in same measurement condition but with the operator wearing dark clothes.

Vehicles should be kept at least 3m from the target.

A field campaign sheet (see table 3.2) should be compiled during the measurements.

Instrument	**Date**	**Rif. Point**	**Lat Lon**	**ime**	**Weather**	**Comments**
FieldSpec Pro ASD Unit 6349	19-09-07	10	N 28°12’ 46.9’’ E -16°38’0.9’’	2:00	Sunny no wind	Lava flow 1798 Altitude…..
…	…	…	…		…	…
…	…	…	…		…	…
…	…	…	…		…	…

Table 3.2 : template of a the field measurement sheet.

3. Post Campaign activity

Post campaign activities as summarized as follows:

- After campaign a check of data quality is required.
- Instrument check is due to verify the state of the instrument after campaign and after expedition back to laboratory;
- Notes and comments relative to the campaign are registered on the LogBook (Date, duration of the campaign, operator, comments and possible failure or damaged have to be pointed out)
- Every component is lodged in the laboratory in the proper place in order to be ready for the next measurements activities.

2.3.6 Relevance of reflectance in situ measurements

The spectral reflectance of earth materials is often the most useful and diagnostic criterion for lithologic discrimination. Reflectance is a consequence of chemistry and structure of the material modified by environmental factors and physical condition of the material. Surface composition may retrieved by spectra features. The reflectance measurements provide information on electronic processes. Discernable features in igneous rock occur as result of presence of iron (Fe), its oxidation state and water. Further, the reflectance provides information on vibrational modes and idrates minerals.

These kind of measurements (“in situ truth”) are collected in spectral library and may be used for the following purposes:

- as reference for calibration of remote sensed data;
- for interpretation of spectral units in unsupervised classification;
- as end-members for supervised classification;
- as link between remote sensing and laboratory measurements.

3. Remote sensing

3.1 Introduction

With the term remote sensing we usually intend the process of acquiring information about a target without physically contact. Such information may be acquired by measuring (a) electromagnetic energy emitted, scattered, reflected or polarized by the element of the target; (b) force field that have been modified the scene and (c) mechanical vibrations or waves emanating from the scene.

There are two kinds of remote sensing. Passive sensors detect natural radiation that is emitted or reflected by the object or surrounding area being observed. Reflected sunlight is the most common source of radiation measured by passive sensors. Active device, on the other hand, emits energy in order to scan objects and areas whereupon a sensor then detects and measures the radiation that is reflected or backscattered from the target. RADAR (radio detection and ranging) is an example of active remote sensing where the time delay between emission and return is measured, establishing the location, height, speed and direction of an object. In this context we will concentrate on passive remote sensing based on the analysis of the information contained in the radiation reflected or emitted by the object. The sensors that will be considered are multispectral/hyperspectral *imaging spectrometers* (see section 3.2). In this section will be analysed the main characteristics of sensors for Remote Sensing (spatial, temporal, spectral, and radiometric resolutions) that affects their performances of sensor and data quality. A description of two sensors, (ASTER an Hyperion) which data will be analysed, is given.

3.2 Imaging spectrometers

An imaging spectrometer is an instrument which can simultaneously register both the spectrum and the two spatial dimensions of the radiation. The data recorded by an imaging spectrometer can be viewed as a data cube of numbers of the spectral radiance in three dimensions: two spatial dimensions, x and y, and one spectral dimension λ.

The array of light detectors (CCD) can simultaneously record the spectra in one direction and one spatial dimension in the other direction of the array. The second spatial dimension has to be temporally scanned. This can be achieved by turning a mirror in front of the spectrometer, by turning the whole spectrometer, or by moving it in one direction, for example by using it from an airplane or satellite (push broom).

The figure 3.1 shows how a spectral image is recorded by an imaging spectrometer mounted on satellite or airborne.

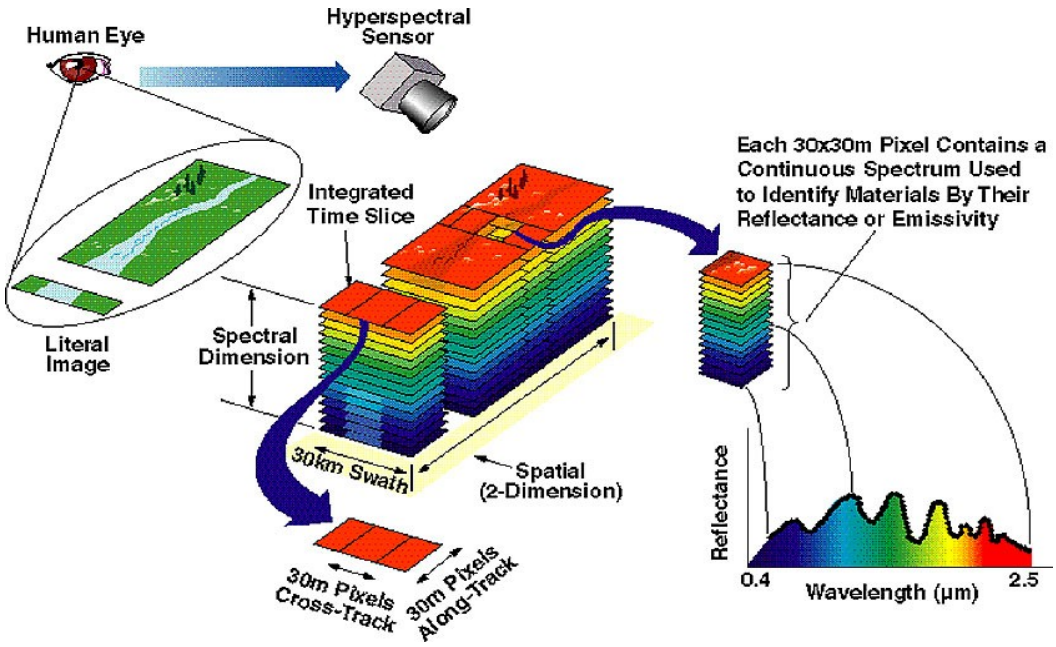

Figure 3.1 The data cube contains at the same time for each pixel spectral and spatial information. According to the type of sensor we can have discrete (multispectral sensor) or continuum (hyperspectral sensor) spectra.

3.1.1 Spatial resolution

The spatial resolution specifies the pixel size of satellite images covering the Earth surface. The detail discernible in an image is dependent on the spatial resolution of the sensor and refers to the size of the smallest possible feature that can be detected. For an electro-optical sensor the

simplest definition of spatial resolution is the Instantaneous Field of View (IFOV). Which is the area of the imaged surface that is projected through the sensor's optical system, onto a single detector element (pixel). .

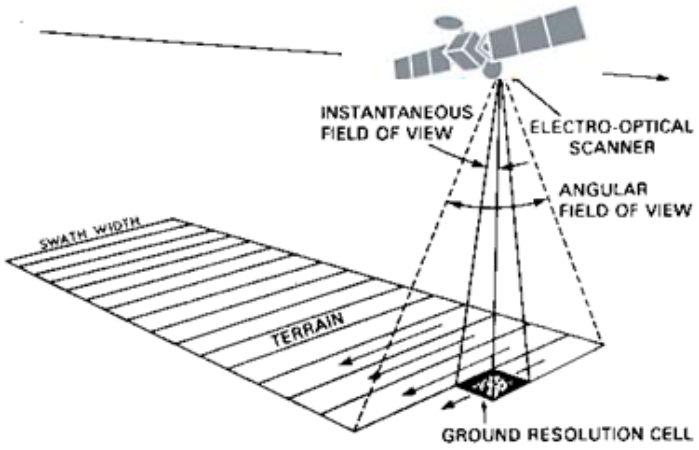

Figure 3.2 Spatial resolution and IFOV.

If we define: H the distance between sensor and the terrain (altitude) , f the focal length, of the optical system, l the pixel size and D the pupil of the devise, the IFOV may be described as an angular feature ($IFOV_{\alpha}$) or as length ($IFOV_l$)

$$IFOV_{\alpha}=D/f[rad] \quad (15)$$

$$IFOV_l=HD/f\ [m]$$

The size of the area viewed is determined by multiplying the IFOV by the distance from the ground to the sensor. This area on the ground is called the resolution cell and determines a sensor's maximum spatial resolution (Figure 3.3). For a homogeneous feature to be detected, its size generally has to be equal to or larger than the resolution cell. If the feature is smaller than this, it may not be detectable as the average brightness of all features in that resolution cell will be recorded. However, smaller features may sometimes be detectable if their reflectance dominates within a particular resolution cell allowing sub-pixel or resolution cell detection.

According to the spatial resolution range we can speak of:

high spatial resolution (between 0.6 - 4 m),

medium spatial resolution (between 4 - 30 m) and

low spatial resolution (30 - > 1000 m).

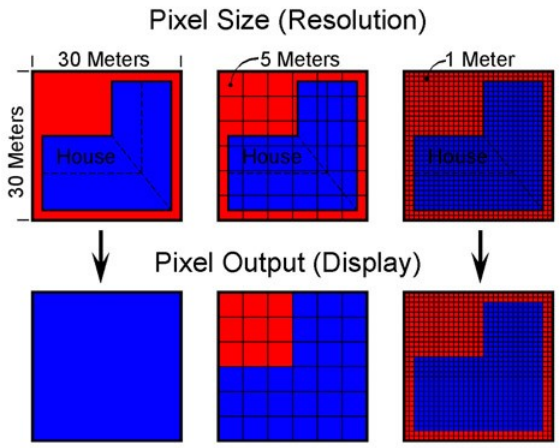

Figure 3.3 Target appearance by different spatial resolution: at 30m, the target is not indiscernible; at 5m resolution, mean features are discernable; at 1m, details are revealed http://www.satimagingcorp.com/characterization-of-satellite-remote-sensing-systems.html.

A good spatial resolution is linked to a small IFOV despite there is a limit due to the intensity signal coming from the target and detected by the sensor.

3.1.2 Temporal resolution

The temporal resolution specifies the time interval between successive opportunities to observe a given location. The revisit period of a satellite sensor is usually several days. Therefore the absolute temporal resolution of a remote sensing system to image the exact same area at the same viewing angle a second time is equal to this period (Figure 2.2). However, because of some degree of overlap in the imaging swaths (see appendix 0) of adjacent orbits for most satellites and the increase in this overlap with increasing latitude, some areas of the Earth tend to be re-imaged more frequently. Also, some satellite systems are able to point their sensors to image the same area between different satellite passes separated by periods from one to five days. Thus, the actual temporal resolution of a sensor depends on a variety of factors, including the satellite/sensor capabilities, the swath overlap, and latitude.

According to the temporal resolution range we can speak of:

-*High temporal resolution* (< 24 hours - 3 day)

-*Medium temporal resolution* (4 - 16 days)

-Low temporal resolution (> 16 days)

3.1.3 Spectral resolution

Spectral resolution describes the ability of a sensor to define fine wavelength intervals. The finer the spectral resolution, the narrower the wavelength ranges for a particular channel or band. In the first instance, a sensor's spectral resolution specifies the number of spectral bands in which the sensor can collect reflected radiance. But the number of bands is not the only important aspect of spectral resolution. The position of bands in the electromagnetic spectrum is important, too (Fig. 3.4). Advanced multi-spectral sensors called hyperspectral sensors, detect hundreds of very narrow spectral bands throughout the visible, near-infrared, and mid-infrared portions of the electromagnetic spectrum. Their very high spectral resolution facilitates fine discrimination between different targets based on their spectral response in each of the narrow bands.

-*High spectral resolution: - 220 bands*

-*Medium spectral resolution: 3 - 15 bands*

-*Low spectral resolution: - 3 bands*

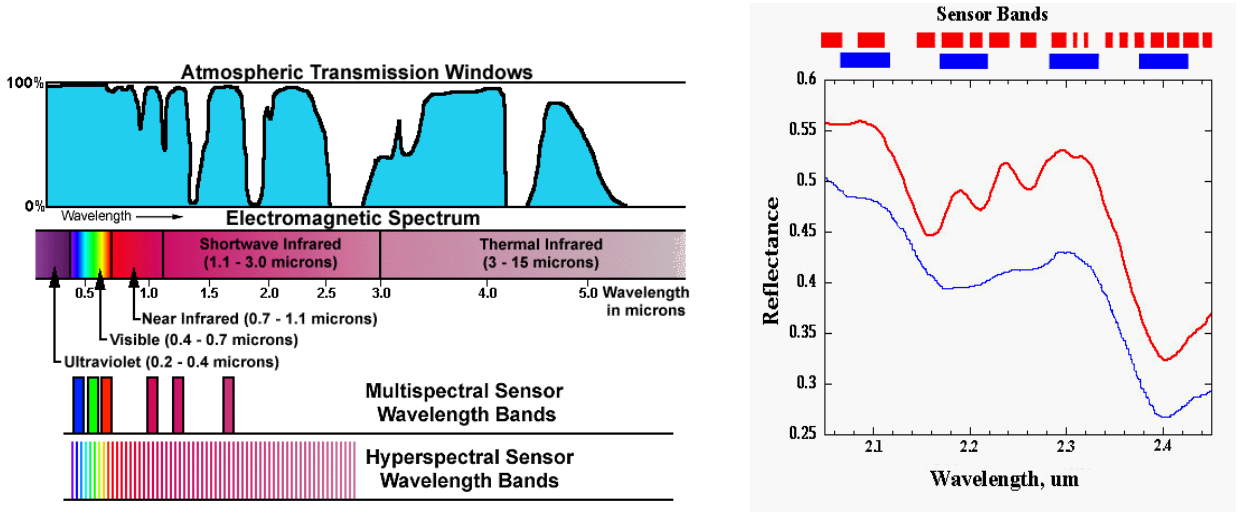

Figure 3.4. a) Spectral resolution determines the kind of sensor: multispectral or hyperspectral; b) Reflectance curves produced when a target is sensed using a sensor with a higher spectral resolution (Red) vs. a lower spectral resolution (Blue) ,(http://www.cas.sc.edu/geog/rslab/rscc/fmod1.html).

3.1.4 Radiometric resolution

While the arrangement of pixels describes the spatial structure of an image, the radiometric characteristics describe the actual information content in an image. Every time an image is acquired on film or by a sensor, its sensitivity to the magnitude of the electromagnetic energy determines the radiometric resolution. The radiometric resolution of an imaging system describes its ability to discriminate very slight differences in energy. The finer the radiometric resolution of a sensor, the more sensitive it is to detecting small differences in reflected or emitted energy. Imagery data are represented by positive digital numbers which vary from 0 to (one less than) a selected power of 2. This range corresponds to the number of bits used for coding numbers in binary format. Each bit records an exponent of power 2 (e.g. 1 bit=2 1=2). The maximum number of brightness levels available depends on the number of bits used in representing the energy recorded. Thus, if a sensor used 8 bits to record the data, there would be 28=256 digital values available, ranging from 0 to 255. However, if only 4 bits were used, then only 24=16 values ranging from 0 to 15 would be available. Thus, the radiometric resolution would be much less. Image data are generally displayed in a range of grey tones, with black representing a digital number of 0 and white representing the maximum value (for example, 255 in 8-bit data). By comparing a 2-bit image with an 8-bit image, (Figure 3.5) we can see that there is a large difference in the level of detail discernible depending on their radiometric resolutions.

Figure 3.5 radiometric resolution affects image 2-bit image (left image) with an 8-bit image (right image).

3.3 Satellite sensors

3.3.1 ASTER

ASTER (Advanced Spaceborne Thermal Emission and Reflection Radiometer) currently represents the only commercially instrument now providing moderate spectral and moderately high spatial resolution in TIR. It was launched on the TERRA satellite in December 1999 as part of NASA's Earth Observing System (EOS). ASTER is a cooperative effort between NASA, Japan's Ministry of Economy, Trade and Industry (METI) and Japan's Earth Remote Sensing Data Analysis Centre (ERSDAC).It is one of five sensors on Terra and designed to acquire repetitive , high spatial resolution multispectral data in VNIR-TIR spectral range. (Yamaguci et al 1998, Abrams, 2000).

As regards the spectral features ASTER has three separate optical subsystems: the visible and near-infrared (**VNIR**) radiometer, the shortwave-infrared (**SWIR**) radiometer, and the thermal infrared (TIR) radiometer (Pieri, D.C. and Abrams, M.J., 2004). The respectively three radiometer payloads are described in figure 3.6a, figure 3.6b and figure 3.6c.

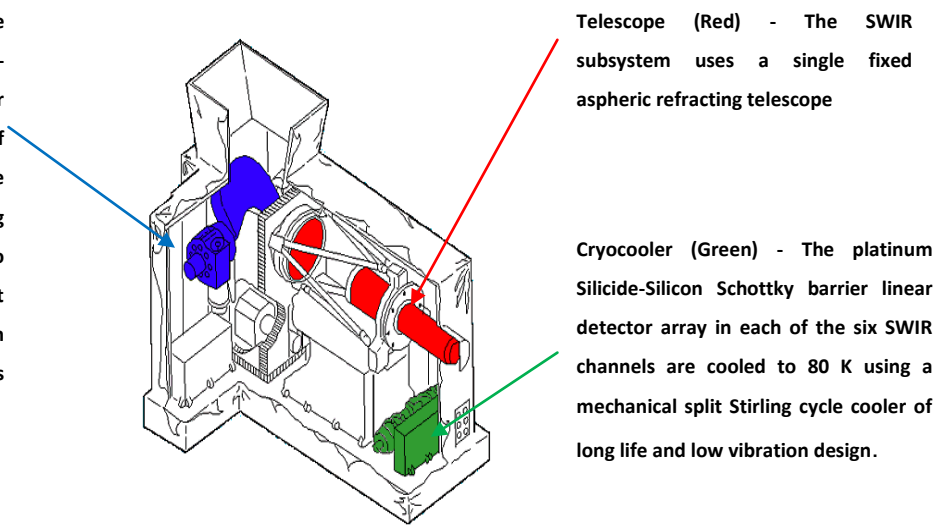

Figure 3.6 a) ASTER instrument : **VNIR subsistem Design**. The VNIR subsystem consists of two independent telescope assemblies to minimize image distortion in the backward and nadir looking telescopes. The detectors for each of the bands listed in Table II consist of 5000 element silicon charge coupled detectors (CCD's) (http://asterweb.jpl.nasa.gov).

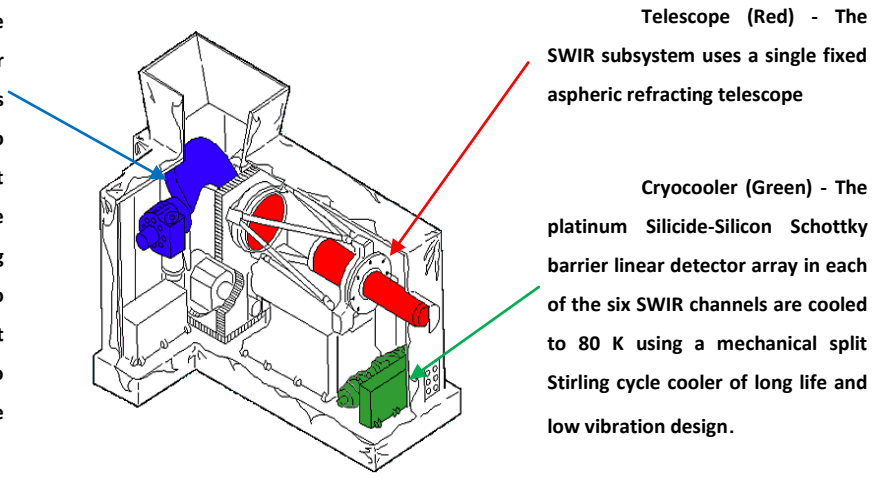

Figure 3.6 b) ASTER instrument : SWIR subsistem Design; The SWIR subsystem uses a single aspheric refracting telescope. The detector in each of the six bands (Table II) is a Platinum Silicide-Silicon (PtSi-Si) Schottky barrier linear array cooled to 80K. Six optical bandpass filters are used to provide spectral separation (http://asterweb.jpl.nasa.gov).

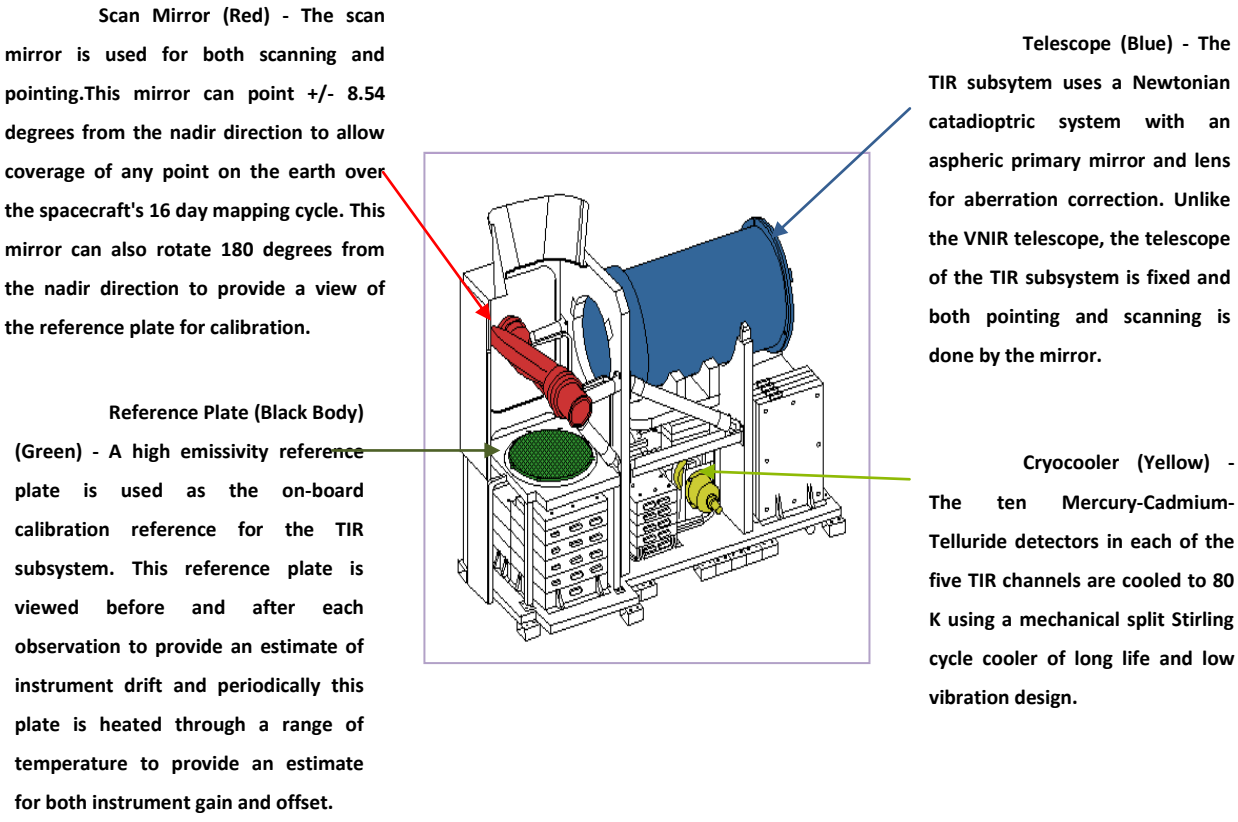

Figure 3.6 c) ASTER instrument : TIR subsistem Design; The TIR subsystem uses a Newtonian catadioptric system with an aspheric primary mirror and lenses for aberration correction.The telescope of the TIR subsystem is fixed with pointing and scanning done by a mirror. Each band uses 10 Mercury-Cadmium-Telluride (HgCdTe) detectors in a staggered array with optical band-pass filters over each detector element (http://asterweb.jpl.nasa.gov).

The main features of the three radiometers are summarised in the following table.

Characteristic	VNIR	SWIR	TIR
Spectral Range	Band 1: 0.52 - 0.60 µm Nadir looking	Band 4: 1.600 - 1.700 µm	Band 10: 8.125 - 8.475 µm
	Band 2: 0.63 - 0.69 µm Nadir looking	Band 5: 2.145 - 2.185 µm	Band 11: 8.475 - 8.825 µm
	Band 3: 0.76 - 0.86 µm Nadir looking	Band 6: 2.185 - 2.225 µm	Band 12: 8.925 - 9.275 µm
	Band 3: 0.76 - 0.86 µm Backward looking	Band 7: 2.235 - 2.285 µm	Band 13: 10.25 - 10.95 µm
		Band 8: 2.295 - 2.365 µm	Band 14: 10.95 - 11.65 µm
		Band 9: 2.360 - 2.430 µm	
Ground Resolution	15 m	30m	90m
Data Rate (Mbits/sec)	62	23	4.2
Cross-track Pointing (deg.)	±24	±8.55	±8.55
Cross-track Pointing (km)	±318	±116	±116
Swath Width (km)	60	60	60
Detector Type	Si	PtSi-Si	HgCdTe
Quantization (bits)	8	8	12

Table 2.1 Spectral and spatial characteristics of ASTER

The Terra platform follows a sun-synchronous , polar orbit with a repetition time of 16 days. However at higher latitudes this number drops to less than 7 days. In addition ASTER has a unique cross-track pointing capability of up to 24° off axis, allowing image collection up to ±85° latitude. This side looking ability can further decrease repeat acquisition time to several days at the high latitudes, however it lowers spatial resolution and increases the atmospheric path length. Using the one of the backward-looking telescope in the VNIR the instrument can generate along track digital elevation models (DEMs). The resulting DEMs have a posting of 30 metres and are optically generated using the parallax between the two images.

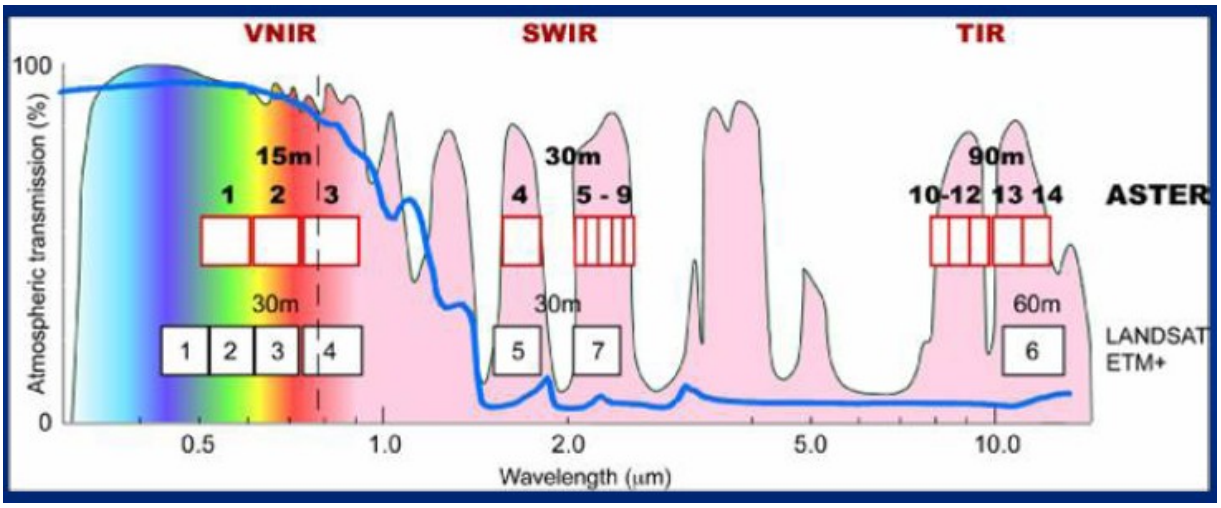

Figure 3.7 ASTER instrument spectral characteristics: spectral and spatial resolution for each channels are showen on the atmospheric transmission profile.

The data are released as Level 1B. This means that the reflected and emitted electromagnetic radiation from Earth's surface are detected and recorded by the three sensors as raw instrument data, calibrated and geometrically corrected. These data are used to produce higher–level data products and are distributed by ASTER GDS (Ground Data System). Two surface reflectance products are available, one each for VNIR and SWIR. These products are atmospherically and topographically corrected basing on available climate data and on global digital elevation data sets respectively (Gillespie, A. et al., 1998). The data set are expressed in unitless reflectance; the percent reflectance can be derived from the product by multiplying each value by 0.001(Bailey G.B., 2007). As regards TIR range , ASTER standard products AST05 and AST08 had the goal to give the emissivity and temperatures within a+- 0.015 and+- 1.5 K respectively (Gillespie, 1998).

The ASTER data used in this work are Level1B type a calibration procedure will be described in the section 4.3. and AST05 standard emissivity product that will be used as comparison.

3.3.2 EO-1 Hyperion

The EO-1 Hyperion (Hyperspectral Imager) provides a new class of Earth observation data for improved Earth surface characterization. The Hyperion provides a science grade instrument quality calibration based on heritage from the LEWIS Hyperspectral Imaging Instrument (HSI). The Hyperion capabilities provide resolution of surface properties into hundreds of spectral bands, versus the ten multispectral bands flown on traditional Landsat imaging missions. Through this

large number of spectral bands, complex land eco-systems shall be imaged and accurately classified. The Hyperion provides a high resolution hyperspectral imager capable of resolving 220 spectral bands (from 3.5 to 2.5 µm) with a 30 meter resolution. The instrument can image a 7.7 km by 100 km land area per image and provide detailed spectral mapping across all 220 channels with high radiometric accuracy. The instrument (figure 3.8) originally conceived a drop in to the ALI instrument and is now base lined to be a standalone instrument on EO-1.

Compared with ASTER (VIS –NIR range) Hyperion offers a better possibility for mineralogical analysis.

Figure 3.8 Hyperion payload (http://eo1.gsfc.nasa.gov/Technology/Hyperion.html).

	BAND #	WAVELENGHTH (NM)
VNIR Channels	1 - 7	356 - 417nm
	8 - 55	426 - 895 nm
	56 - 57	913 - 926 nm
	58 - 70	936 - 1058 nm
SWIR Channels	71 - 76	852 - 902 nm
	77 - 78	912 - 923 nm
	79 - 224	933 - 2396 nm
	225 - 242	2406 - 2578 nm
Ground	30m	
Data		
swath	7.5x 18 km	

Table 2.2 Spectral and spatial characteristics of Hyperion.

Unfortunately Hyperion has not on board calibration system. This imply that due to the degradation of components also performances change with time; the nominal performances may differ from the real one.

As regards SNR (Signal to Noise ratio) for instance, it is declared to be equal to 190 to 40 (http://edcsns17.cr.usgs.gov/eo1/faq.php?id=20) as the wavelengths increase. In order to evaluate the SNR on the processed Hyperion image, a procedure , based on a statistical approach, has been implemented and will be described in the section 3.6.1.

3.4 Atmospheric contribution

The useful information about a target area of the land, sea or clouds is contained in the physical properties of the radiation that leaves that target area, whereas what is measured by a remote sensing instrument. It is therefore necessary to correct the satellite (or aircraft) received data to allow for the effects on the radiation as it passes through the atmosphere. In theory the passage of the radiation through the atmosphere is described by the *radiative transfer equation*; the values of the various parameters that appear in the radiative transfer equation are not known sufficiently accurately to make direct and explicit solution of the radiative transfer equation a feasible approach. Thus more empirical methods are used depending, among the other things, on the wavelength of radiation concerned. We will consider the effect of atmosphere on the detected signal in the VIS-NIR and TIR respectively spectral range.

3.4.1 Atmospheric effect in the Infrared range

In thermal infrared spectral range the radiance leaving the surface, L_{sur}, (which is a combination of both emission and reflection) is related to the radiance derived from the sensor, L_{sen}, the transmission of the atmosphere T_r, and the atmospheric path radiance L_{path}, (which arises from both atmospheric emission and scattering) by the following simplified equation:

$$L_{sat} = L_{sur} * T_r + L_{path} \quad (16)$$

The atmospheric contributions may be retrieved by three main methods: the use of MODTRAN, the use of split window; and the use of a two look method. In this frame we concentrate on first

method that was applied for the correction of satellite data. It is a common practice to use radiation transfer models to estimate T_r and L_{path} allowing the surface radiance to be determined. The surface leaving radiance is a combination of radiation emitted by the surface and sky irradiance reflected by the surface. If the spectral emissivity of the surface is known these two components can be separated. The MODTRAN (Moderate Resolution Atmospheric Radiance and Transmittance Model) is a worldwide known computer package used to retrieve the radiation transfer model. It is based on ten-yearly heritage of improvements and several versions of LOWTRAN (Neizys *et al*.,1988). The MODTRAN requires as input an atmospheric profile of pressure, temperature and humidity. In section 3.5.2.2., the method and the procedure applied to calibrate and the ASTER (TIR range) data will be described.

3.4.2 Atmospheric effect in the Visible-Near Infrared range

For visible and near infrared wavelength radiation, the atmospheric corrections are particularly important, in the sense that they are much larger, as a percentage of the surface –leaving radiation, than is the case for microwave or thermal infrared radiation. When an electromagnetic wave strikes a particle, no matter the size of the particle, a part of the incident energy is scattered in all directions (Figure 3.9). This scattered energy is called diffuse radiation. An expression for the energy scattered by spherical particles can be obtained theoretically by solution of Maxwell's equations of electromagnetism. By using the parameter $\alpha=\pi D/\lambda$ where D is the diameter of the scattering particle, and λ is the wavelength of the incident radiation, we can distinguish the following case:

1) α <0.1 Rayleigh scattering. This is applicable to the scattering of solar radiation by air molecules, of which the majority has size of the order of 0.1nm. The Rayleigh scattering is not very sensitive to changes in atmospheric conditions.
2) 2 $0.1<\alpha<50$ in this case we have Mie scattering. this kind of scattering is applied to the scattering of solar radiation by particles with size greater than 10 nm like aerosol.

Sophisticated algorithms use models of atmospheric absorption and scattering. These algorithms take into account five contributions to the radiance measured at the satellite: 1) radiation scattered directly from the surface into the sensor; 2) radiation scattered directly from the atmosphere into the sensor; 3) radiation scattered from the surface and then

diffusely by the atmosphere into the sensor; 4) radiation scattered diffusely by the atmosphere and then directly from the surface into the sensor;5) radiation multiply scattered from the surface and atmosphere.

The at-satellite radiance L can be expressed as an equivalent reflectance. The atmospheric correction for the Hyperion and ASTER data (in VIS-NIR range) data is a module of a more complex and complete procedure (named CIRILLO) that will be explained in the section 3.5.2.

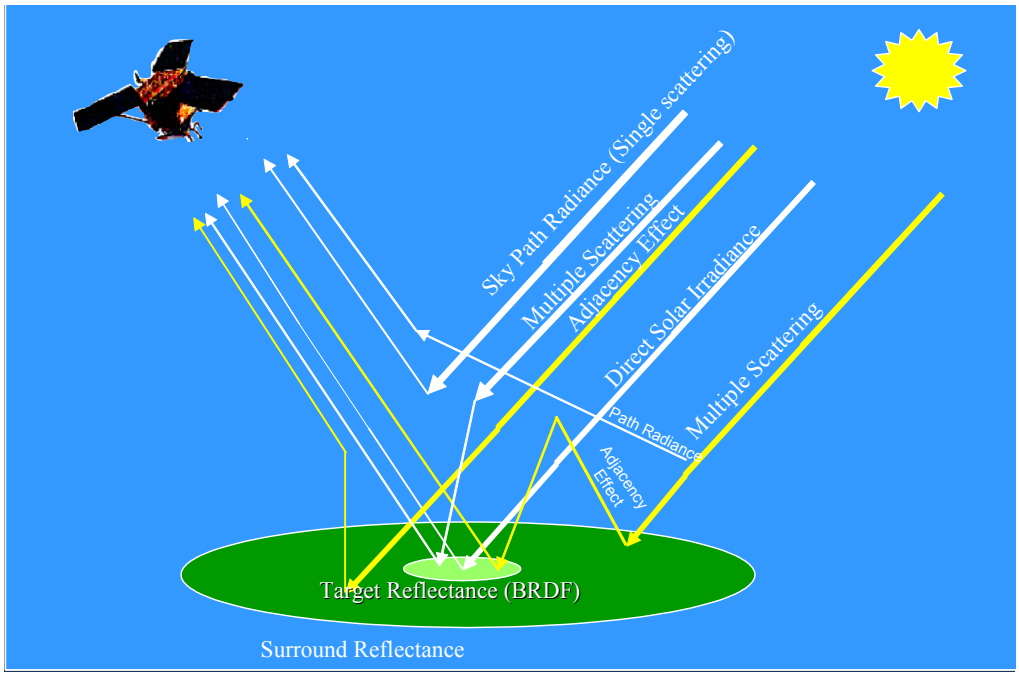

Figure 3.9 Different components involved in the reflectance process.

3.5 Calibration and validation (CAL/VAL) of remote sensed data

Researchers have long been concerned with the need to quantify the accuracy of remotely sensed land cover classifications at the local scale but with the increase in data sets from coarse resolution sensing systems, attention has turned to the challenge of global product 'validation' (Justice and Townshend 1994, Robinson 1996, Justice et al. 1998a). 'Validation' is the process of assessing by independent means the accuracy of the data products derived from the system outputs, 'validation' is distinguished from calibration which is the process of quantitatively defining the system response to known, controlled signal inputs. In general, 'validation' refers to

assessing the uncertainty of higher level, satellite sensor derived products (e.g. land cover, leaf area index) by analytical comparison to reference data, which is presumed to represent the target value(Justice et al. 2000). Intercomparison of data products or model outputs provides an initial indication of gross differences and possibly insights into the reasons for the differences, however independent 'validation' data are needed to determine product accuracy (Justice et al. 2000). Whereas there are accepted standards for instrument calibration, standards for 'validation' of higher order products have yet to be developed.

Scientific community dedicate a massive energy in this activity over all when the data are from sensor orbiting from long time. An example is the Hyperion sensor: as described previously it was launched on 2001 it has not an on board calibration system so observation of Moon and in situ validation campaigns are required to monitor the performances of the instrument in the time and to calibrate the data.

We can divide calibration in two phases: radiometric calibration of a sensor that imply the conversion of raw data from Digital Number (DN) in data expressed in physical units (e.g. radiance) and calibration of data from radiance in reflectance or emissivity (according the spectral range) . The radiometric calibration is generally provided by the builder of sensor and/or updated coefficients are periodically provided to allow the user to calibrate the raw data.

The second phase, the passage from radiance to reflectance (or from radiance to emissivity) required different steps and customised algorithms for (VIS-SWIR) or TIR range.

The correction for geometric effects, elevation of terrain, illumination and atmospheric contribute have to be taken into account.

These effects are correct by using models that need to be validated. The validation of models used to process the data is realised by "in situ truth" acquisitions. In the following diagram it is represented the process of Calibration validation (CAL/VAL) of a remote sensed data.

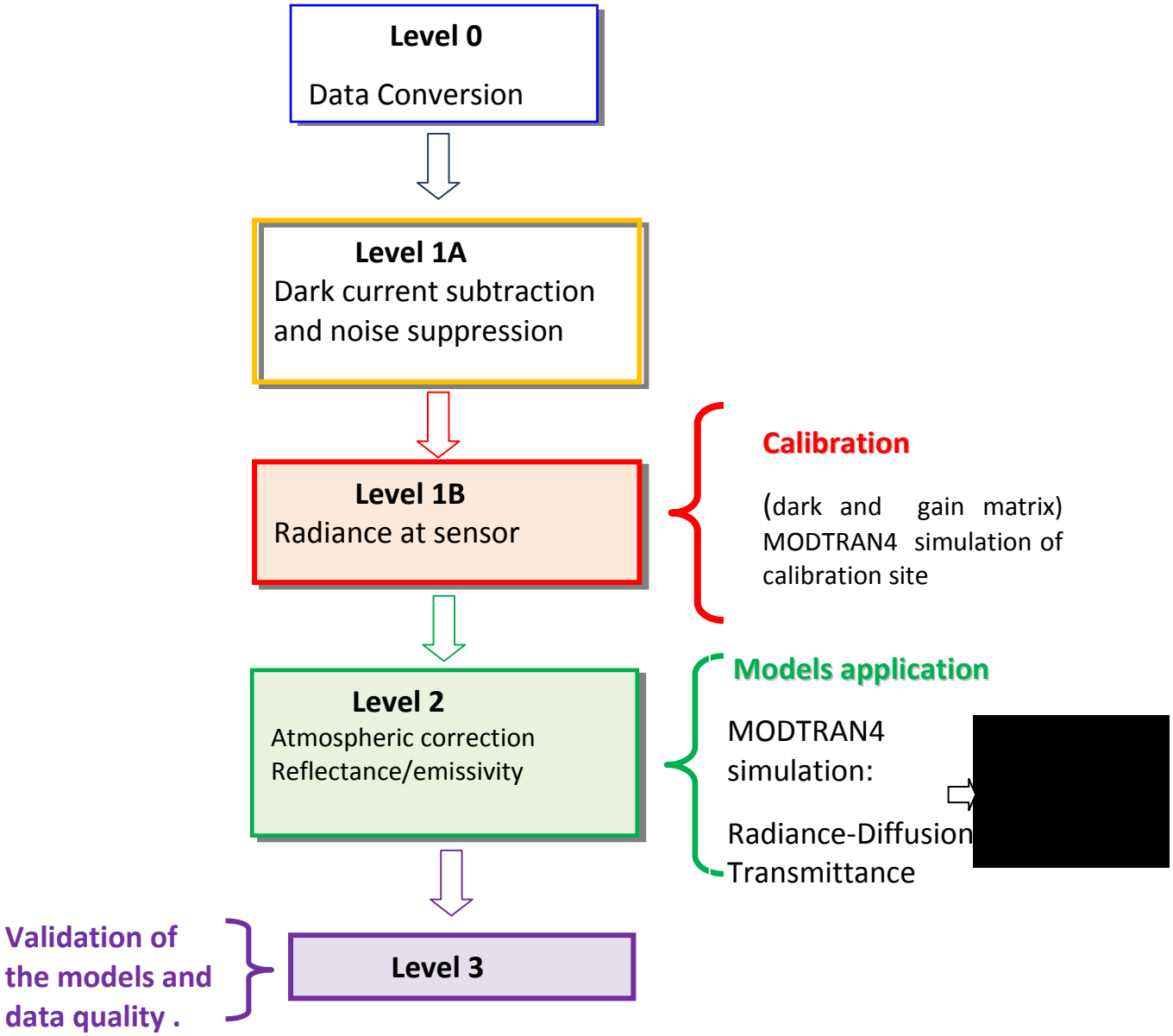

Figure 3.10 Flow diagram for CAL/VAL process of remote sensing data..

3.5.1 Data calibration: VNIR-Atmospheric correction processor

The Hyperion and ASTER data have been calibrated by using an atmospheric correction processor named CIRILLO (Musacchio , ASI-SRV).

CIRILLO has been developed for atmospheric correction of VNIR –TIR remote sensing data. It is composed by different modules: in VNIR range, it includes also a reflectance retrieval module; in the TIR range, it processes the data and pass the information to another processor based on the TES algorithm.

In the following paragraph the CIRILLO modules and the TES module (both used for data processing) will be described.

3.5.2 CIRILLO code

The algorithm CIRILLO (Musacchio et al. 2007, ASI-SRV) is developed to estimate atmospheric and topographic contribution on raw satellite images and correct them in order to produce higher level products. After a the *data pre-processing* consisting the conversion of DN to radiance at sensor and the geocoding, the core of atmospheric correction is implemented.

Cirillo is developed in IDL-ENVI language and it consists of two sub-procedures:

A. Estimation of atmospheric and topographic corrections for spectral region of VNIR (Visible Near Infrared, 0.4-2.5 μm).

   It is based on different sub-modules:

   - Atmospheric correction sub-module
   - Topographic terms sub-module
   - Ground reflectance sub-module

B. Estimation of atmospheric corrections for spectral region of TIR (*Thermal Infrared*, 2.5-15.0 μm)

   It is based on different sub-modules:

   - Atmospheric correction sub-module
   - Ground radiance sub-module
   - Apparent temperature sub-module

3.5.2.1Sub-procedure A: estimation of atmospheric and topographic corrections for spectral region of VNIR (Visible Near Infrared, 0.4-2.5 μm)

In the VNIR (0.4-2.5 μm) CIRILLO estimates atmospheric and topographic corrections neglecting atmospheric effects and assuming an horizontal and "lambertian surface". In VNIR range the data are mainly affected by diffusion and absorbing processes. We assumed to use the 6S radiative transfer model (Vermote et al., 1997a), that take into account the environmental reflection effects and the radiative transfer model MODTRAN (Berk et al., 1989) for diffusion. A phase correction, dues to the different illumination caused by the horography has been introduced.

The radiance measured by the sensor can be converted to "apparent" or "TOA" (Top Of the Atmosphere) ground reflectance ρ^* using the relation:

$$\rho^* = \frac{\pi \cdot L_m}{E_S \cdot d^2 \cdot \cos\theta_S} \tag{17}$$

where: L_m = is the radiance measured by the sensor ($W\,m^{-2}\mu m^{-1}sr^{-1}$)

E_S = is the solar irradiance at the top of the atmosphere ($W\,m^{-2}\mu m^{-1}$)

d = is the solar irradiance factor due to variability of the Sun-Earth distance

θ_S = is the solar zenith angle

Using TOA ground reflectance and considering the atmospheric effects and the illumination changes due to topography (tilted surfaces) the ground reflectance ρ can be computed by Equation (18):

$$\rho = \left[\frac{\rho^*}{t_g} - \rho_a - \frac{\langle \rho_e \rangle \cdot \left(t_S^{\downarrow} + t_m^{\downarrow} \right) \cdot t_m^{\uparrow}}{1 - \langle \rho_e \rangle \cdot s} \right] \frac{\left(1 - \langle \rho_e \rangle \cdot s\right)}{\left(\beta \cdot t_S^{\downarrow} + t_m^{\downarrow} \right) \cdot \left(t_S^{\uparrow} + t_m^{\uparrow} \right)} \tag{18}$$

where: t_g is the atmospheric transmittance of the path sun-ground sensor due to gas absorption

$t_S^{\uparrow}, t_m^{\uparrow}, t_S^{\downarrow}, t_m^{\downarrow}$ are the atmospheric transmittance of the path sun-ground $(\,)^{\downarrow}$, and of the path ground sensor $(\,)^{\uparrow}$ due to signal scattering $(\,)_S$, and to multiple path scattering $(\,)_m$

ρ_a is the reflectance contribution due to solar radiance scattered by the atmosphere

$\langle \rho_e \rangle$ is the environmental reflectance, that is the mean reflectance of the ground surrounding the pixel viewed by the sensor

S is the downward spherical albedo of the atmosphere

β is the illumination factor for a title surface estimated using the relations indicated below

$$\beta = \cos(\theta_n) \cdot \cos(\theta_s) + \sin(\theta_n) \cdot \sin(\theta_s) \cos(\varphi_n - \varphi_s) \quad (19)$$

Where:

θ_s, φ_s are the zenith and the azimuth angles of the Sun

θ_n, φ_n are the slope and aspect angles of the target

A part from geometric terms, all the other terms are depending on wavelength. In particular they are computed from 400nm to 2500nm with the spectral step of 1nm. For this reason, in order to consider Equation (17) and Equation (18) for a specific band of the sensor, these spectral quantities must be convoluted with the response functions of the sensor using the relation:

$$f_b = \frac{\int_{400\ nm}^{2500\ nm} f(\lambda)\Phi_b(\lambda)d\lambda}{\int_{400\ nm}^{2500\ nm} \Phi_b(\lambda)d\lambda} \quad (20)$$

where: $f(\lambda)$ indicates a generic spectral term

b is the band considered

$\Phi_b(\lambda)$ is the response function of the sensor for the band *b*

f_b is the in-band-value $f(\lambda)$.

We can summarise the different steps of CIRILLO procedure as follows:

1 Transformation of “at-the-sensor” radiance image to TOA surface reflectance.

2 Spectral values of atmospheric terms, (i.e. transmittances) are computed using the radiative transfer models MODTRAN4.0 and 6S.

3 After preparing the input data files for MODTRAN4.0 and 6S, CIRILLO runs the radiative transfer models several times, varying the surface elevation in the altitude range of the image considered (flat terrain require only one run) and storing the in-band values in a look-up table of atmospheric correction terms (LUT-AC) .

4 the next step is the evaluation of altitude and factor for each pixel of the image. For these calculations CIRILLO requires, as input, three images (files), geographically registered with the image to be corrected and with the same spatial resolution, containing elevation, slope and aspect.

5 From the obtained at-the-sensor radiance image, CIRILLO produces a ground reflectance image corrected from illumination changes due to tilted surfaces (topographic effect) and from atmospheric effects.

The figure 3.11 summarizes the algorithm flux diagram and the different steps performed by CIRILLO procedure to implement the Atmospheric and topographic corrections and to transform the “at-the-sensor radiance image” to TOA (Top Of Atmosphere) and then in surface reflectance . Input parameters may be summarised as follow:

- A run identifier (run name);
- A set of parameters relevant to the considered sensor and to the acquisition conditions of the image to be processed;
- A set of parameters that control the run options;
- A set of files of pre-computed, case specific, atmospheric correction terms;
- A set of parameters describing the characteristics of the atmosphere;
- The lower and the upper altitude considered for the radiative transfer modelling;
- A set of parameters relevant to topography;
- A set of parameters relevant to the adjacency effect correction.

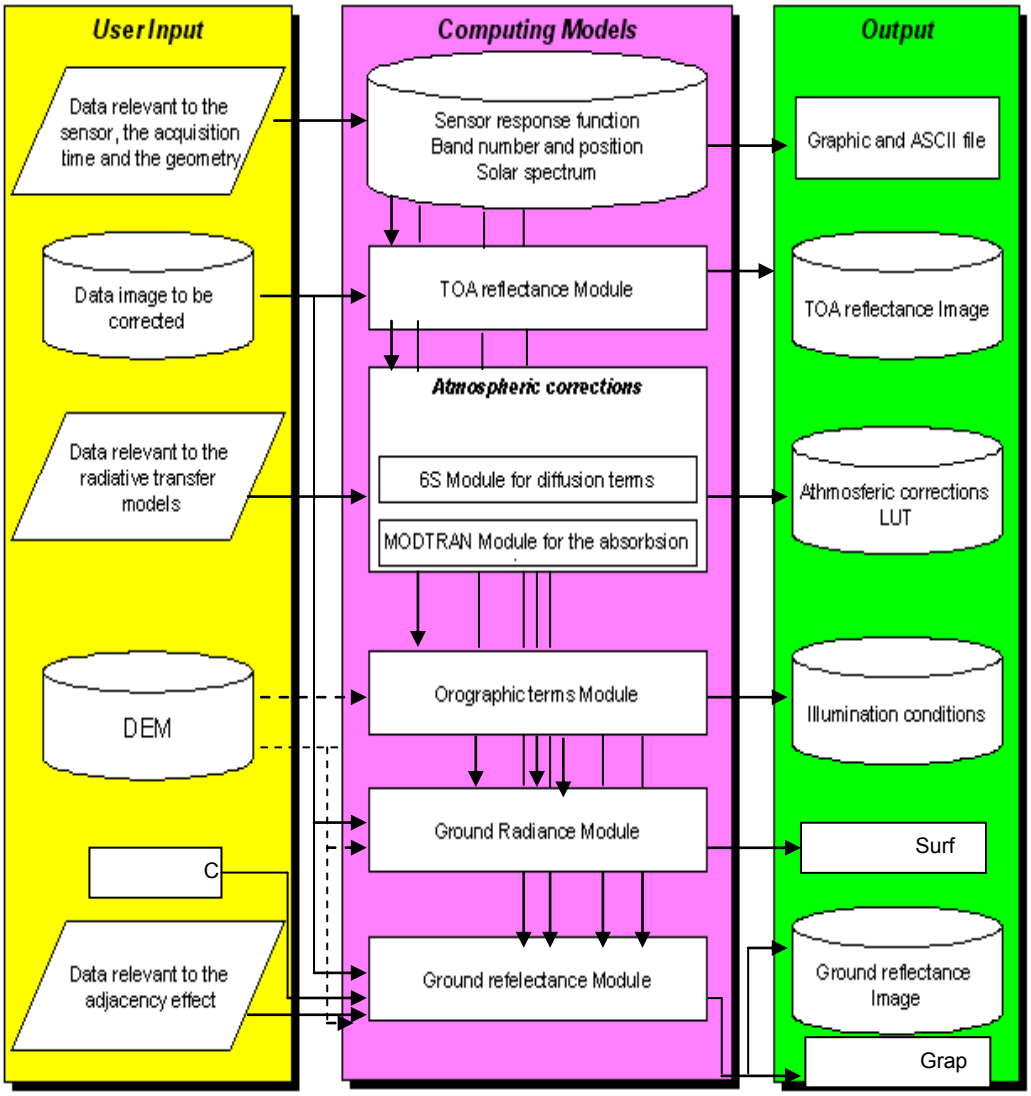

Figure 3.11 Diagram flow of CIRILLO code: input required to the user (yellow); correction modules for topographic and atmospheric correction (pink); produced products (green).

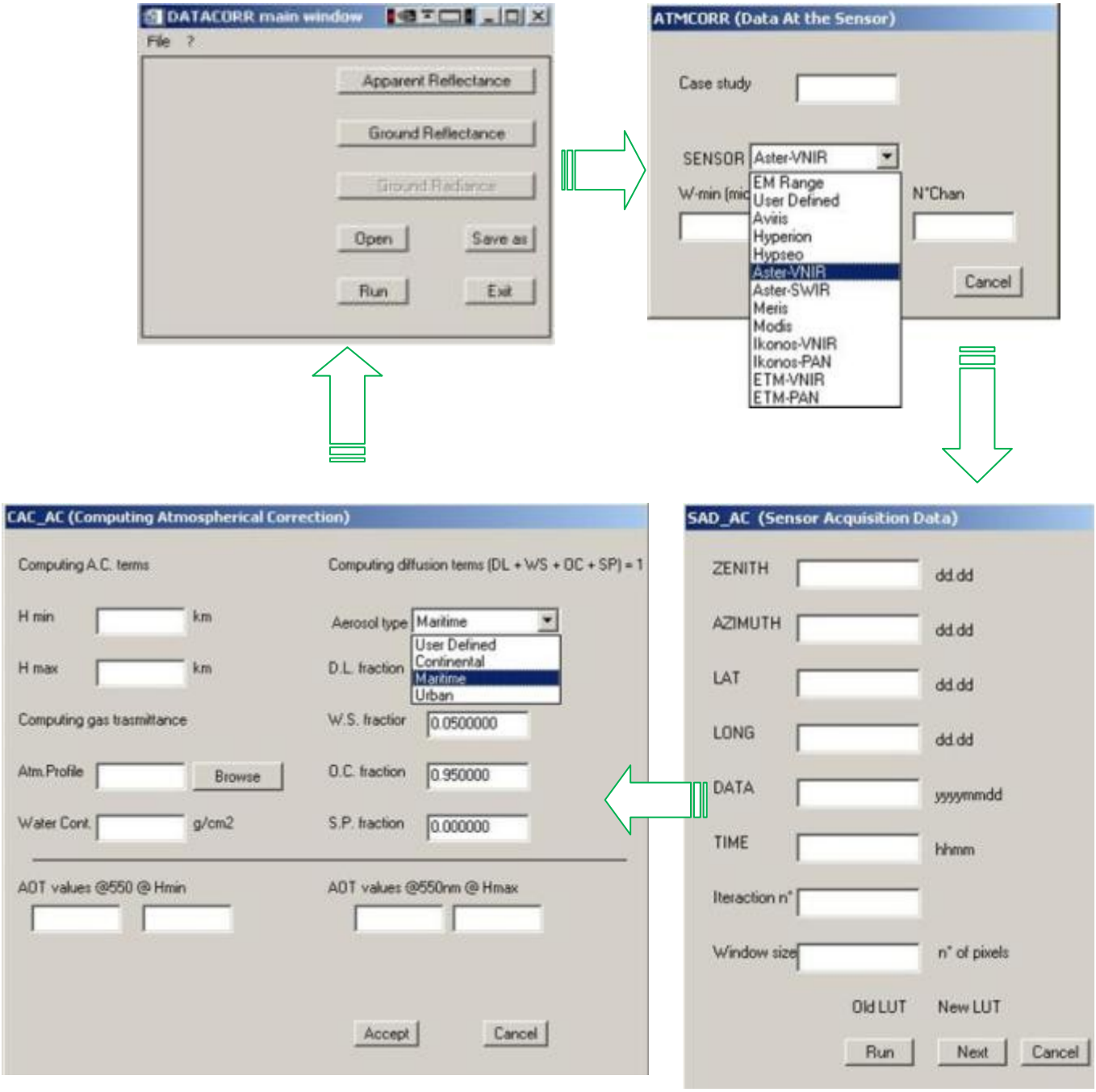

Figure 3.12 CIRILLO graphic interfaces : different steps for reflectance retrieval.

3.5.2.2 Sub-procedure B: estimation of atmospheric corrections for spectral region of TIR (Thermal Infrared, 2.5-15.0 µm)

In the TIR (3 µm – 15 µm) spectral region the radiance measured by the sensor is a function of the ground radiance (emitted by the surface) and can be expressed by relation (20):

$$L_m(\lambda) = L_u(\lambda) + \varepsilon(\lambda)\frac{B(\lambda,T_s)}{\pi}t_g^{\uparrow}(\lambda) + \frac{[1-\varepsilon(\lambda)]}{\pi}E_d(\lambda)t_g^{\uparrow}(\lambda) \quad (20)$$

where: L_m is the radiance measured by the sensor ($W\,m^{-2}\,\mu m^{-1}\,sr^{-1}$);

L_u is the path emitted radiance ($W\,m^{-2}\,\mu m^{-1}\,sr^{-1}$);

E_d is the irradiance emitted by the atmosphere towards the surface ($W\,m^{-2}\,\mu m^{-1}$);

B is the blackbody exitance (Planck's blackbody law, $W\,m^{-2}\,\mu m^{-1}$);

$t_g^{\uparrow}$ is the atmospheric transmittance due to absorption in the ground-sensor path (adim.);

ε e T_s are surface emissivity and temperature (adim., *K*);

In this region atmospheric effects are due to molecular absorption and this is the reason why atmospheric correction terms (transmittance and atmospheric radiances) are computed only with MODTRAN. They are calculated every 100 nm of wavelength of the sampling interval and then stored in LUT (Look Up Table). After, these spectral values are computed and calculated for specific sensor bands by relation (21) that is similar to equation (20):

$$f_b = \frac{\int_{\lambda} f(\lambda)\,\Phi_b(\lambda)d\lambda}{\int_{\lambda}\Phi_b(\lambda)d\lambda} \quad (21)$$

This procedure gives different outputs. It provides atmospheric correction terms for TES (Temperature and Emissivity Separation) algorithm

3.5.3 IR data calibration: TES code, for emissivity

The spectral radiance emitted by a body at a certain kinetic temperature T can be expressed as a function of the spectral emissivity of its surface ε and the Planck blackbody function B:

$$L(\lambda,T)=\varepsilon(\lambda)\cdot B(\lambda,T) \tag{22}$$

This equation represents a system of N equations in N+1 unknowns if the radiance L is measured at N different wavelengths λ. These unknowns are the N values of the spectral emissivity and the temperature. This represents an inverse underdetermined problem. In the literature, different "non-exact" solutions are given to this problem, called *Temperature and Emissivity Separation* (TES). Details of the different algorithms that have been proposed so far are discussed in the reported references (Gillespie et al., 1998; Li et al., 1999).and several approaches have been proposed to separate temperature and spectral emissivity from the radiance measurements.

The emissivity is normalized to a value ε_{max} which represents the maximum value that can be found in the area where the algorithm is applied. The inversion of the equation 23 gives five temperatures the highest of which is taken as the kinetic temperature estimate image Ts. A second step is then performed by calculating the spectral blackbody radiance image from the estimated temperature. Finally the spectral emissivity image is obtained by dividing the surface radiance by the blackbody radiance (Gillespie et al., 1998; Li et al., 1999). The spectral radiance measured at the ASTER sensor L_A in the TIR can be expressed as

$$L_A=\left[\varepsilon\cdot B(T_s)+(1-\varepsilon)\cdot L_d\right]\cdot\tau+L_u \tag{23}$$

where L_u is the upwelling radiance, Ld the downwelling radiance, Ts the surface temperature, ε the emissivity, τ the transmittance and $B(Ts)$ the Planck blackbody function. The ground radiance L in equation 22 can be estimated from the measured at sensor radiance, by introducing the atmospheric correction as in equation 23. The parameters Lu, Ld and τ have been calculated by means of the CIRILLO program preceding TES in the processing chain. The atmospheric correction terms that CIRILLO calculates with the MODTRAN transfer radiation code are associated with the corresponding regions in the satellite (ASTER) image by means of the registered DEM. In this way

the spectral images of the atmospheric correction terms are formed and given to the TES algorithm as an input. The procedure has been applied on a pixel-by-pixel basis over all the ASTER image. The output of the process is showed in section 4.4.3 .

3.6 Sensitivity analysis

3.6.1 Signal to noise ratio

Since the Hyperion and ASTER sensors have been orbiting from years, actual performances of sensors are different from the nominal. A method that can be applied on multispectral and hyperspectral data when information on instruments lack is the Gao method. The method is based on a concept using means and local standard deviation of small homogenous blocks in order to define respectively the average signal and the mean noise of the images. The signal to noise ratio (SNR) that provides a measure of precision of data at each wavelength, can be calculated.

The method has been automated by developing a routine in ENVI-IDL environment and "applicable" to multiband hyperspectral data independently from the type of sensor.

3.6.2 Method description

The image is divided in nxn blocks. (3x3 px is resulted the smallest size that assure homogeneity). For each block the Local Mean (LM) is computed:

$$LM(\lambda) = \frac{1}{N}\sum_{i=1}^{i=N} S_i(\lambda) \quad (24)$$

where S_i is the signal corresponding to the *i*th pixel for each band.

The Local Standard Deviation (LSD) for each block is computed by

$$LSD(\lambda) = \left[\frac{1}{(N-1)}\sum_{i=1}^{i=N}(S_i(\lambda) - LM)^2\right]^{1/2} \quad (25)$$

.

The computed LSDs provide information about the level of noise of the image. The following step consisted in calculate the LMs and LSDs of signal for each band on all blocks image.

A scatter plot of the LSDs versus LMs is calculated to estimate the noise characteristics of the signal. A straight line that passes through the maximum number of points in scatter plots determines the noise characteristics of the image and provides indication about the independence of noise from the signal. Within the minimum and the maximum of the LSDs, a number bins with equal width is set up (150 bins for a 500x500 px image is a good choice). Then the LSDs of all blocks are grouped in these bins and the bin with the largest number of blocks corresponds to the mean noise signal of the image. Taking into account the additively assumption, the spectral SNR estimation can be expressed by the following equation:

$$SNR(\lambda)=\text{average signal}(\lambda)/\text{mean noise}(\lambda) \quad (26)$$

where, average signal is the mean calculated over the image for each wavelength; mean noise is the quantity described previously.

An IDL procedure has been implemented to automate the process of SNR calculation according to the previously described method. The procedure has been used to process the Hyperion and ASTER data set. The results will be discussed on section 4.4.2

4.Volcano Teide validation campaign

4.1 Introduction

In the frame of the EC project PREVIEW a validation campaign has been planned in order to validate and integrate the satellite derived products services. PREVIEW (PREVention, Information and Early Warning pre-operational services to support the management of risks- http://www.preview-risk.com/) addresses the definition, the development and the validation in pre-operational conditions of information services; its goal is to support the management in all hazard phases (Prevention, Preparedness, Response and Recovery) of Windstorms, Forest fires, Plain floods and Flash floods, Earthquake & Volcanic risks, Landslides and Industrial accidents. Based on the review of the operational needs and of the existing research assets, a Portfolio of Services is defined in close cooperation with end-users. Research developments are performed to transfer the most promising available results and blocks to operational use. The information services are developed, tested and validated at European scale with operational users on pilot test sites. A long term deployment plan of these services is established, proposing the best scenarios and programmatic for their European operational deployment and organisation. PREVIEW is led by the EURORISK Consortium, a multi-disciplinary European Team of committing Actors of the domain: Civil Protections and Environmental Bodies; Scientific communities and Service operators, at national and regional level, for Meteorology, Hydrology, Seismology, Volcanology and GIS services based on Space data and Industry. The project is organised around a core team of partners coming from 6 countries and from European organisations, leading all the project activities according to a common methodology and performing the necessary transverse actions to ensure the harmonisation, the standardisation and the global and long term view of the resulting services. The Volcanic monitoring and damage evaluation represents one of the main project task; in particular the monitoring concern temperature trends, SO_2 concentrations and flux estimation. To improve the retrieval algorithms and techniques, a field campaign has been realized on volcano Teide (on Tenerife Island, part of the Canary Islands archipelago. The validation campaign has been performed between 16th -24th of September 2007 to acquire a suite of “in situ truth”. During the campaign both satellite and in field data were acquired.

Some samples have been collected for laboratory spectra acquisition and geophysical analysis.

4.2 Volcano Teide geological background

The Canarian Arcipelago is made up of seven islands that represent different stages of geologic evolution (Carracedo J. et al. 1998, Carracedo J., 1999). Tenerife is the central island of archipelago and has developed the complex formed by the rifts and Teide-Pico Veio (T-PV) stratovolcanooes that reach a height of 3718m, 7500 above the ocean floor. It is an active shield though quiescent volcanoo which last erupted in 1909. The United Nations Committee for Disaster Mitigation have designated Teide as one of 16 volcanooes identified by the International Association of Volcanoology and Chemistry of the Earth's Interior (IAVCEI) as being worthy of particular study in light of their history of large, destructive eruptions and proximity to populated areas http://www.volcanoo.si.edu/).

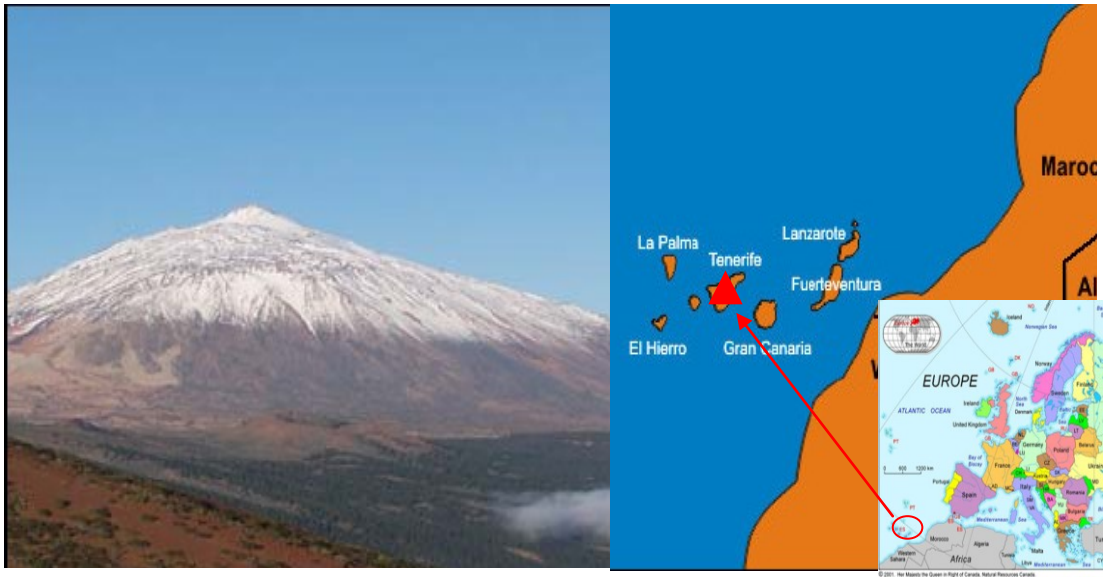

Figure 4.1: Teide volcanoo geographical location (picture courtesy GVM,http://www.volcanoo.si.edu/)

We can recognize four main "geological units" (figure 4.2) according to Carracedo , J.C.(2008) mainly related to the latest volcanoic phase of the island.

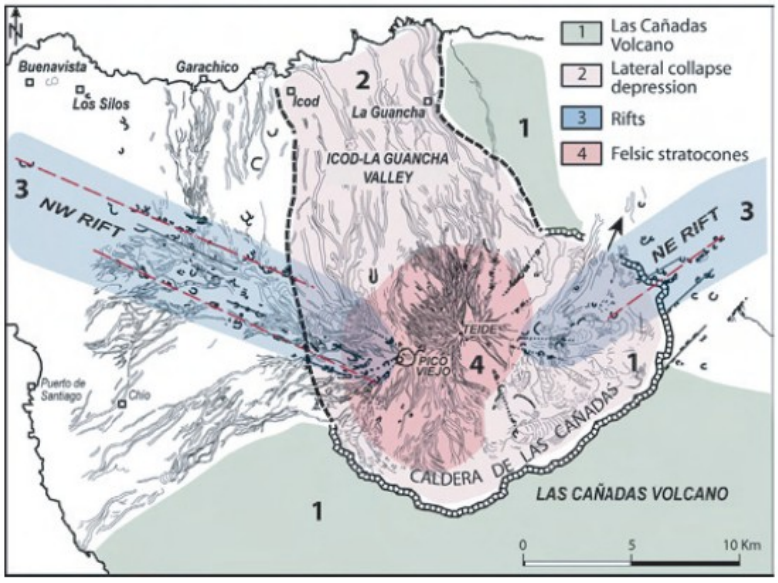

Figure 4.2 Main "geological units of the central part of Tenerife mainly related to the latest volcanoic phase (Carracedo , J.C., 2008)

1) **Las Cañadas Volcanoo** itself is an exceptional case in intraplate islands of the development of a volcanoo that evolved towards states of differentiation producing explosive phonolitic Plinian eruptions. The collapse of its north flank some 200 000 years ago formed a 16 × 20 km depression (the present Caldera of Las Cañadas) that, before being partially filled by subsequent volcanoism, had a breathtaking 3 km-high vertical headwall (Figure 4.2).
2) **Las Cañadas Caldera** is one of the most spectacular, best exposed, and most accessible volcanoic calderas on Earth. Its origin is still under debate and two hypothesis have been done: a first model describes the vertical collapse associated with the emptying of the superficial shallow magmatic chambers of the Las Cañadas volcanoo after large-volume explosive (caldera-forming) eruptions; the second one supposes a lateral gravitational collapses, similar to those described in Hawaii and observed in the eruption of Mount St Helens in 1980. A new third hypothesis is based on a combination of both.
3) **The Rifts**: The Northwest (NW) and Northeast Rifts (NE) are active rifts one running northwest and the other northeast, that converge in the area occupied by the two large stratovolcanooes. The volcanoic complex formed by these rifts and the stratovolcanooes, which constitute the final eruptive stage of Tenerife, have partially filled the caldera and almost covered the entire park with lavas and pyroclasts emitted in the last 30 ka. The rifts may have begun to form during the early stages of construction of the island, in association with deep crustal fractures. They are therefore extremely long-lasting

structures that may have controlled the growth of the island and determined its triangular pyramidal shape.

4) **Two large nested phonolitic stratovolcanooes: PicoViejo and Teide:** the Teide is the highest volcanoo after Mauna Loa and Mauna Kea. The construction of these felsic stratovolcanooes (PicoViejo and Teide) is closely related to the activity of the rifts and it is therefore difficult to mark a clear boundary between the two volcanoic systems. The figure 4.2 a, b, c, d shows the different phases of the evolution of the system as modeled by Carracedo J., (2007).

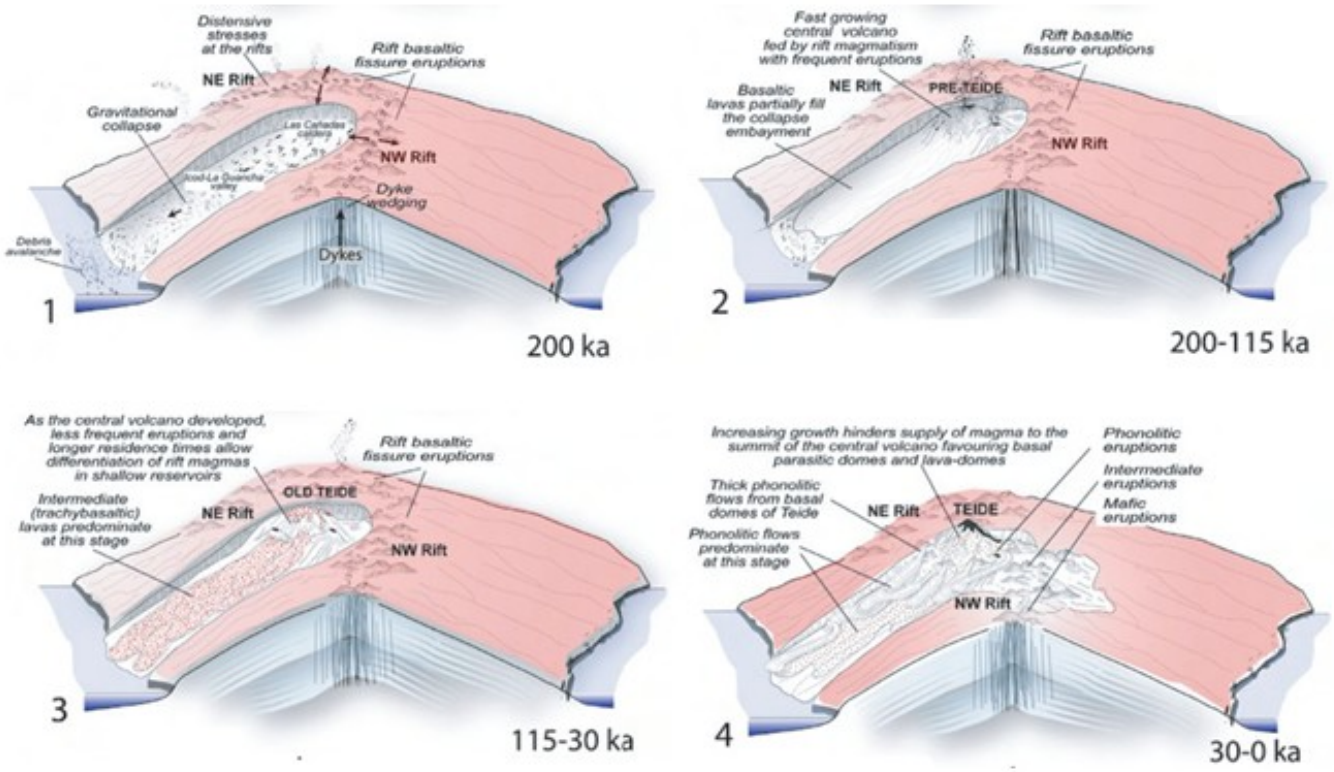

Figure 4.2 In this model (from Carracedo et al., 2007), the rifts play a relevant role in the creation of the different geological and volcanoological elements . the NW and NE rifts created a pre-caldera volcanoo until it became steep and unstable, subsequently triggering a landslide that formed a large depression (Las Cañadas Caldera and La uancha–Icod valley), later partially filled with two differentiated (felsic) stratovolcanooes (Teide and Pico Viejo) nested within the depression.

Despite it is an active volcano, the eruptive hazards related is moderate. Fissural basaltic and intermediate eruptions that largely predominate at the rifts, and are therefore the most probable (60–80 per cent probability), present low eruptive hazards, as shown by the absence of victims during the historic eruptions of the island (Boca Cangrejo 1492, Garachico 1705, Siete Fuentes 1706, Chahorra 1798, Chinyero 1909) (Figure 4.2).

In situ measurements (test sites) have been acquired during the PREVIEW campaign, in the south /south east area, delimited by Las Canadas Calderawhere no volcanic activity is present. This imply that no temporal variation of surface features (e.g texture, composition) can occur.; further, while north west/north parts of volcano have been studied quite in details, (Carracedo et al. 2006) south/south east regions have been less investigated (Carracedo et al.2006) and this study add new information. The following geological map shows the different Teide lava units.

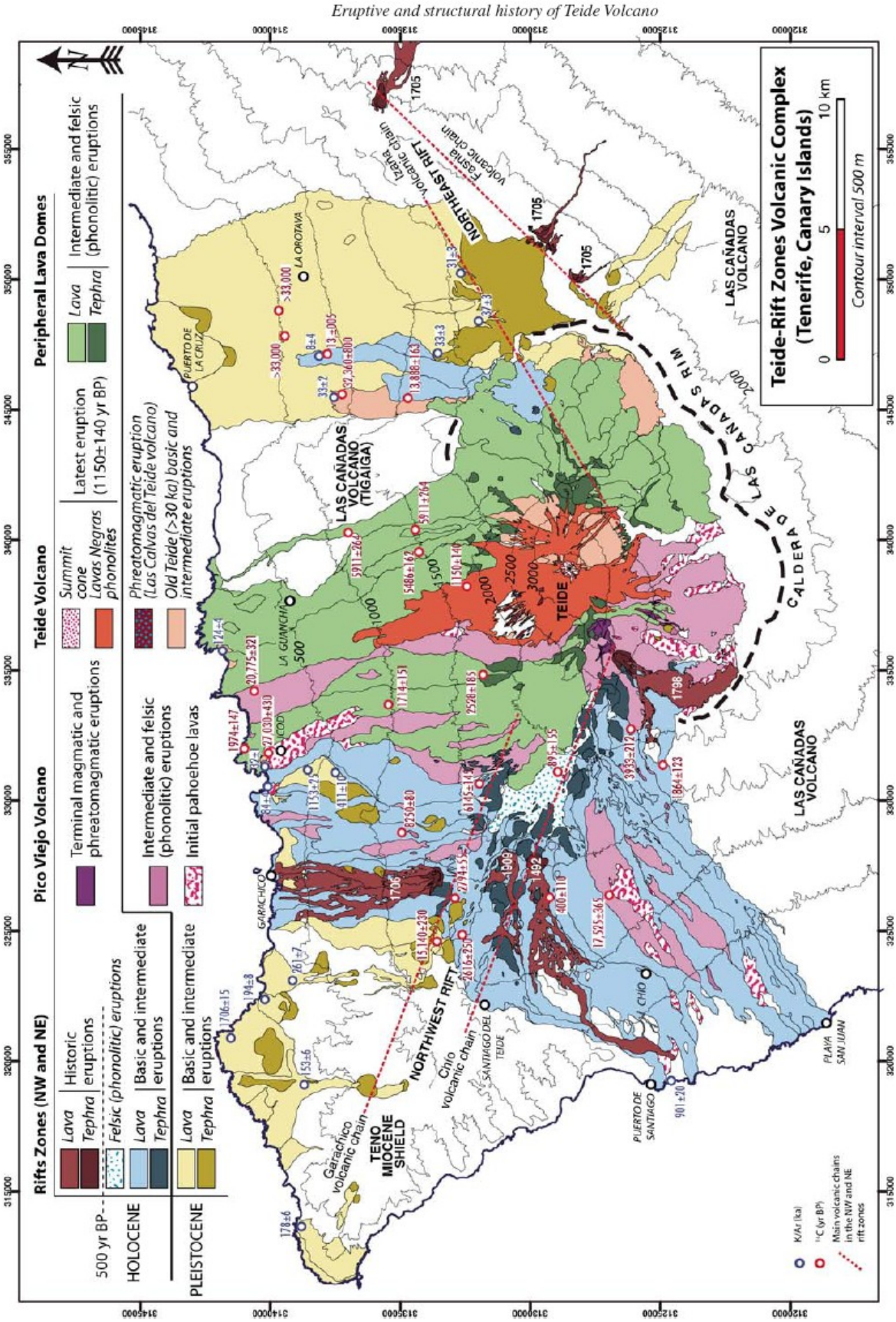

Figure 3. Geological map of the main units of the latest volcanic phase of Tenerife.

Figure 4.3 geological map of volcanoo Teide (Carracedo J. October 2007).

4.3 Volcano Teide campaign

4.3.1 Pre-campaign studies

A preliminary step for the field activities planning was the analysis of the weather condition to define the best period for the campaign organization and the definition of the geological test-site of interest for the validation. *Test sites meteorological characterisation*: the volcanic sites meteorological characterisation realized in this work is a procedure that permits to define, in a particular geographic area, the best period in which a field campaign would have been realized. The most meaningful meteorological parameters to consider for the characterisation are: solar irradiance, precipitable water, cloudiness, wind direction and wind speed. Choose a period of high solar irradiance is crucial to obtain a meaningful thermal contrast between ground and atmosphere that represents one of the most important requirements for both surface and volcanic plume retrieval (Teggi S. et al., 1999; Pugnaghi S. et al., 2006). The precipitable water columnar content and cloudiness are very important parameters to consider because the electromagnetic range of work for the volcanic plume and surface characteristics retrieval (temperature and emissivity). The algorithms developed works in the 8-12 μm spectral range where the main atmospheric absorber is the water vapour. To reduce the influence on water vapour on retrievals, results essential find a period in which such quantity is not too high. The cloudiness is also very important because in the spectral range of work the clouds are blackbodies that obscure the area of interest making the retrievals impossible. The top of volcano wind direction knowledge facilitate the planning of ground measurements site definition.

4.3.2 Seasonal weather condition study

The precipitable water columnar content and wind direction has been extracted by the radiosoundings measured at Guimar-Tenerife WMO meteo station (number 60018). The station started to collect data from November 2002 for 00 and 12 GMT. Figure 4.4 shown the monthly mean precipitable water varying years and for the different hours of measurements (00 and 12GMT). Figure 4.5 shows the mean precipitable water computed over all years considered for the different GMT times of measurements. As before in both figures also the solar irradiance trend has been shown (http://www.preview-risk.com/).

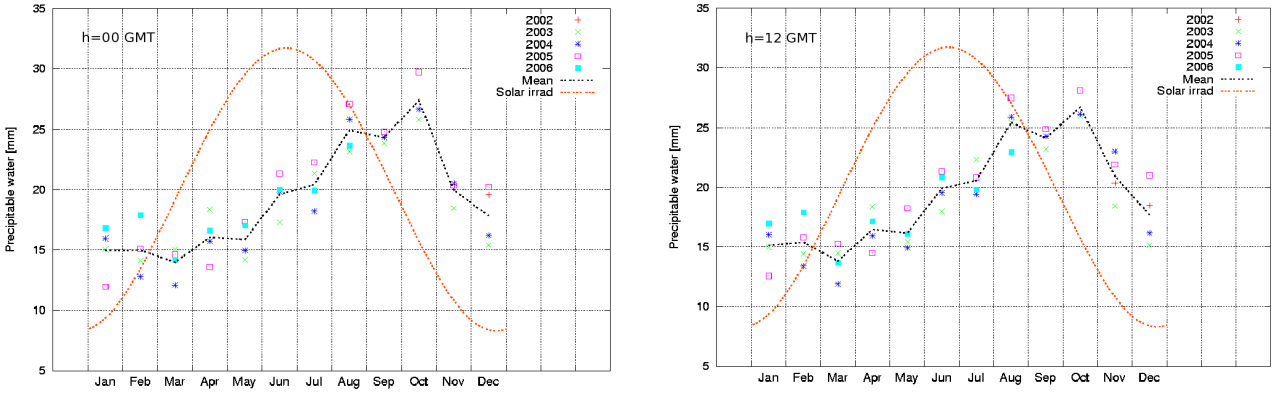

Figure 4.4: Monthly mean precipitable water from Tenerife WMO meteorological station dataset (2002-2006) for the different times of measurements. From top to bottom: 00 GMT, 12 GMT. The “mean” and “Solar irrad” lines shown in all graphs represents respectively the monthly mean precipitable water computed over years and the solar irradiance trend.

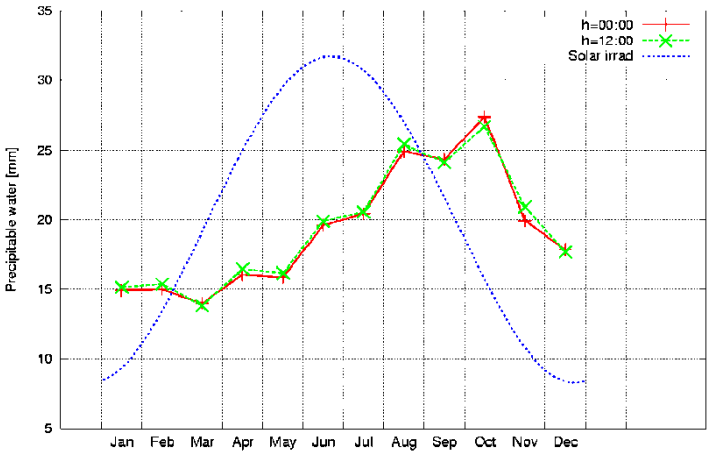

Figure 4.5 Monthly mean precipitable water over years from Tenerife WMO meteorological station dataset (2002-2006) for the different GMT times of measurements. The “Solar irrad” line represents the solar irradiance trend.

The solar irradiance reaches its maximum value in June (in particular during the summer solstice, 21/22 June). Looking at the monthly mean precipitable water trend and considering the summer season it can be seen that the minimal value is reached in June.

Figure 4.6 show the wind direction, in degrees from north, at 3700 m (Teide altitude) for 00 and 12 GMT.

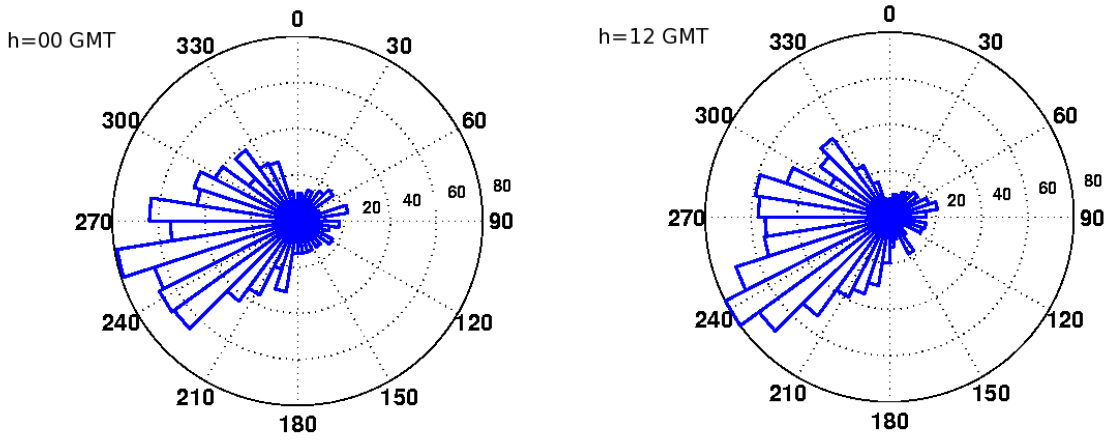

Figure 4.6 Wind direction rose at 3700 m from Tenerife WMO meteorological station dataset (2002-2006) for 00 and 12 GMT.

The wind rose in Figure 4.6 shown the prevalence of westerly to south-westerly winds at 3700 m for all the times of measurements. Figure 4.7 shows that the highest wind velocities are reached by wind coming from the southern-west sectors and that the mean wind velocity at 3700 m was approximately 18 knots for all times of measurements.

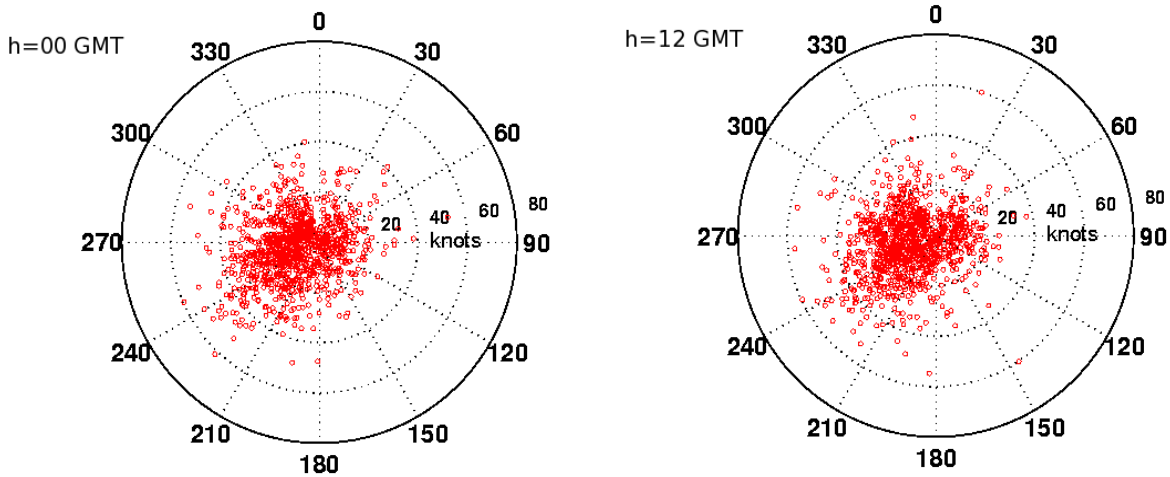

Figure 4.7 Wind speed in knots vs wind direction at 3700 m from Tenerife WMO meteorological station dataset (2002-2006) for 00 and 12 GMT.

The cloud cover and precipitation have been extracted by the Teide Observatory placed at Izana, 2400 m asl on south-west volcano flank. The dataset contain the monthly mean meteorological measurements collected from 1971 to 2000. Figure 4.8 shows the cloudiness data as the monthly mean numbers of days with no clouds and the monthly mean precipitation in mm. The plot shows the maximum precipitation in the autumn-winter season with minimum in June, July and August. The cloud cover results minimal in the same months. Considering the outcome of the meteorological analysis carried out, the best period for a field campaign on Teide volcano results June and July.

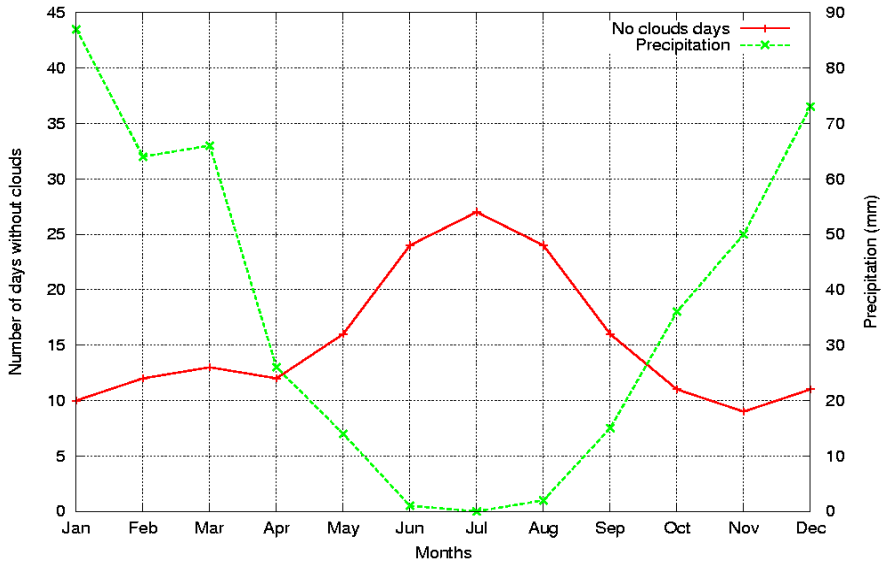

Figure 4. 8 Monthly mean cloud cover and precipitation from Izana station dataset (1971-2000).

A further preliminary work was done in order to identify test site which was based on the following criteria:

- To be as high as possible, wide, plane and open areas of homogenous surface material;
- To be easy reachable on the field and to recognizable and localizable on the image;
- they have to be located in a well know geological setting (Figure 4.25 and Figure 4.26).

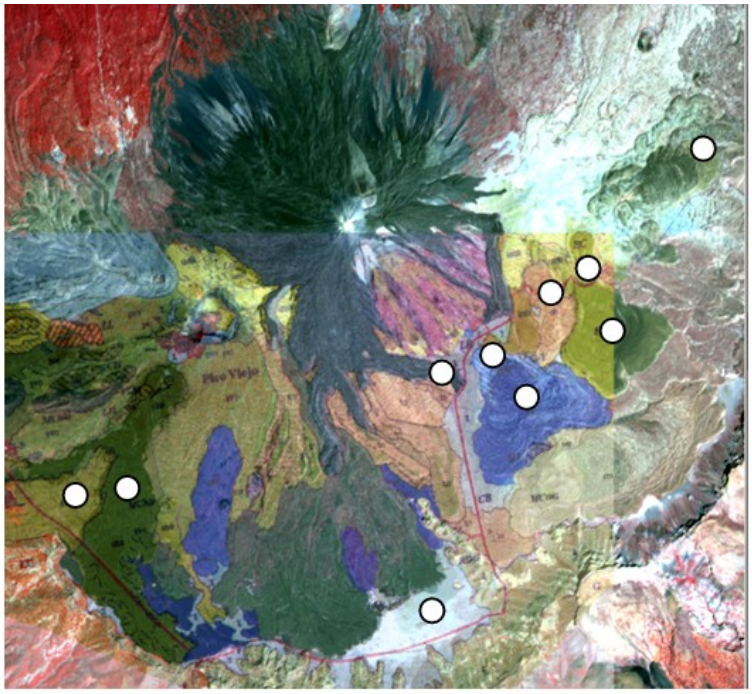

Figure 4.9 Geological Map (from Ablay G.J., Martì J. 2000) overlapping archived ASTER day data (04/08/07 11:52 GMT). It allows a pre selection of the test sites for in situ measurements.

This preliminary analysis allowed us to identify 10 sites as represented in Figure 4. 9Pico de Teide caldera: sites location overlapping archived ASTER data.

4.3.3 Campaign description

The campaign was carried on the 16th and 24th of September : the time window was chosen taking into account different factor as: meteorological characterization, satellites scheduled passage, availability of both on Tenerife and INGV team. The measurements were localized on the summit area of the Tenerife Island and in particular within the Teide Caldera: this area is less characterised and by the features that it exhibits, it can offer more possibility to identify a cal/val test site for of remote sensing data. In situ measurements of reflectance, emissivity and temperatures were realized very close- contemporaneous to the satellite passages. The ground atmospheric station and GPS acquired very close the satellite passage too. A characterization of reflectance at summit crater was realised in order to complete the spectral characterization of different surfaces (in situ spectral library).

4.3.4Satellite Data acquisition TERRA-ASTER and EO1-Hyperion

During the chosen time window on demand acquisition of optical satellite data were request. The following table shows ASTER and Hyperion acquisition calendar and archived available data.

Satellite /sensor	On demand	On demand	Data type	Data from Archive
TERRA-ASTER	*21/09/07 12:00 GMT	17/09/07 23:16 GMT	Level 1B + level 05	Day 04/08/07 Time: 11:52
EO1-HYPERION	*21/09/07	13/11/2003	Level 1B	Day 13/11/2003

Table 4.10 ASTER and Hyperion sensors' scheduling time and data from archive. (*acquired data but cloud cover equal to 100%).

The following figure shows the Hyperion and ASTER footprint, the shadowed is the Hyperion archived data.

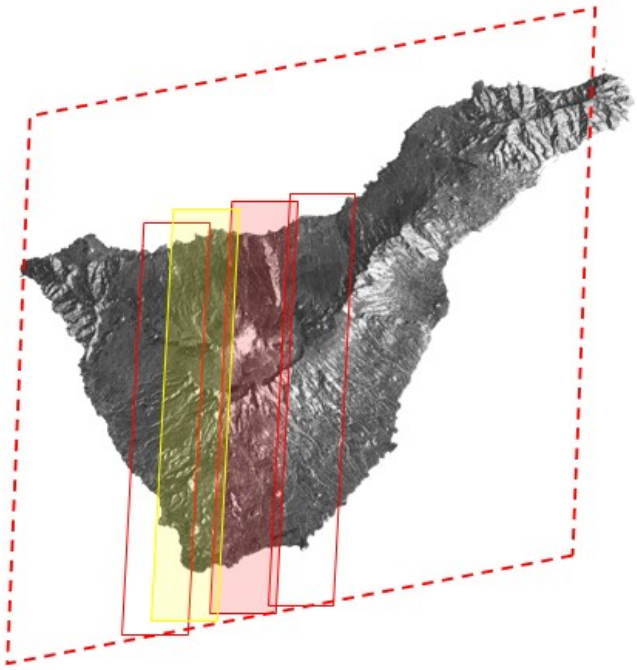

Figure 4. 10 ASTER (dashed line) and Hyperion (continuous line) footprint covering Pico de Teide caldera. Hyperion red shaded footprint, is the archived data that was ordered.

On demand **ASTER day and night acquisition was planned**. Night ASTER acquisition on 17/09/2007 (23:16 GMT) was no cloudy and very good quality data (Figure 4.11).

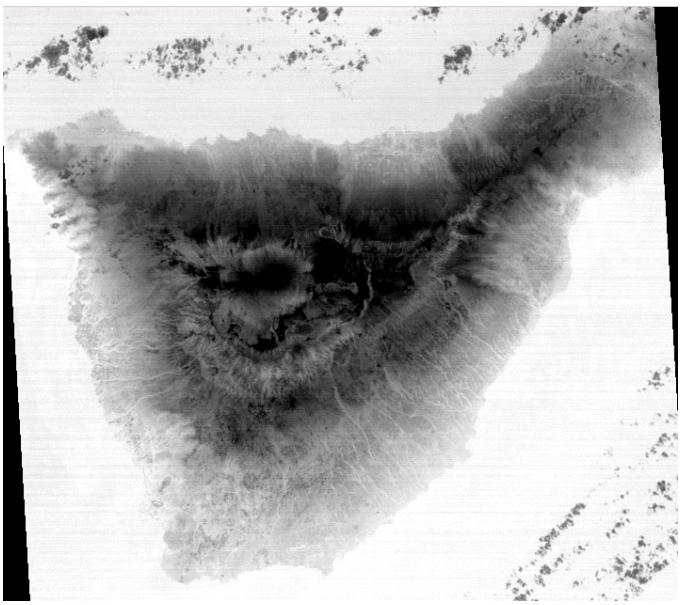

Figure 4.11 ASTER image(AST_L1B_00309172007231649_20071111054412_27970.hdf) acquired on 17/09/07 at 23:16 GMT, grey view , band 10= 8.29 micron.

Unfortunately the day acquisition, on 21/09/2007, was not so good being close to 100% cloud cover(Figure 4.12a). It is important to underline that Pico d Teide is often daily surrounded by an annular shaped clouds and to obtain clouds free image at the sensor time passage is not easy. We have been used the ASTER data acquired on 4/08/2007 (figure 4.12b).

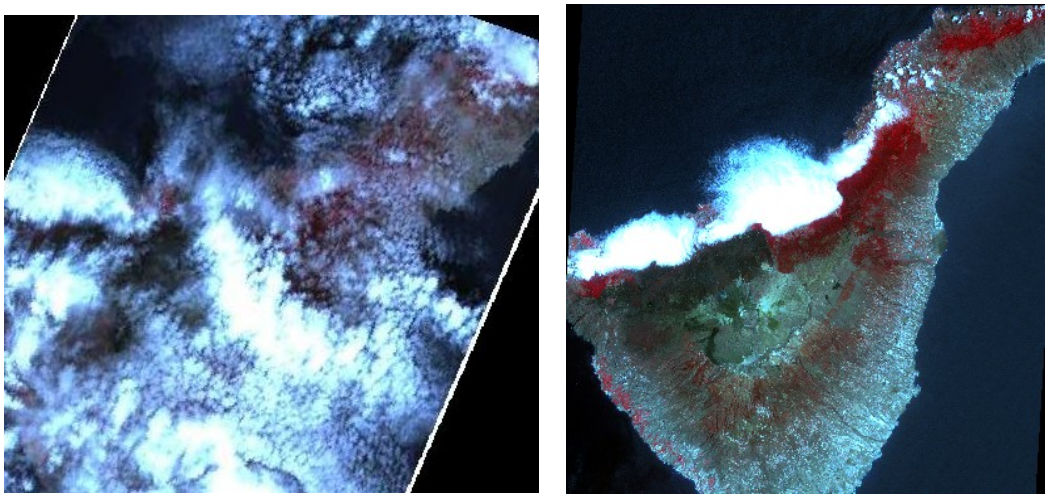

Figure 4.12 a)ASTER visible RGB image acquired on 21/09/07at 12:00 GMT(left); b)ASTER visible RGB image (AST_L1B_00308042007115343_20071109192744_18622_TIR.hdr)acquired on 04/08/07atm 11:53 GMT (right).

As regards **Hyperion data**, the same problem of cloudy coverage occurred a the acquired on demand data was so bad that was not de. A no cloudy, good quality image by Hyperion data archive acquired on November 13rd 2003 has been used.

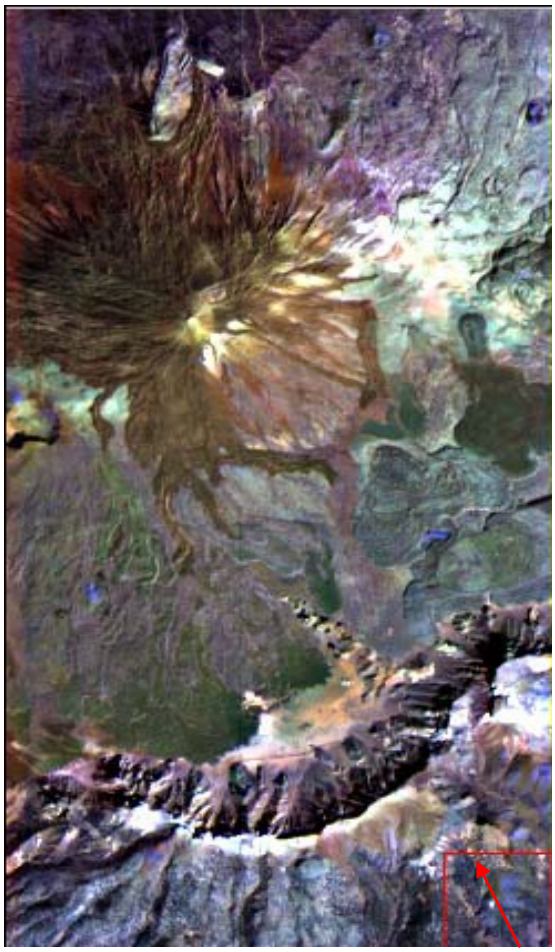

Figure 4.13 EO-1 Hyperion archived data (EO1H2070402003317110PV.1LB; Band=49= 844nm, G=41= 762.6 nm ,B= 630.3nm) acquired on13/11/ 2003.

We can note that Hyperion image cover only the central part of the volcanoo (Figure 4.13); a comparison of reflectance in situ measurements is possible only for a subset of the selected test sites that fall inside the image.

4.4 TERRA-ASTER and EO1- Hyperion data reduction

4.4.1 ASTER calibration

In order to calibrate ASTER data, (level 1 B) it is needed to evaluate the atmospheric correction terms. The path radiance, downwelling radiance and transmittance, have been carried out by means CIRILLO (see section 3.5.2) and using, as atmospheric profiles, the measurements collected by the Guimar WMO Meteo Station (lat 28.27, lon-16.42) on Tenerife Island.

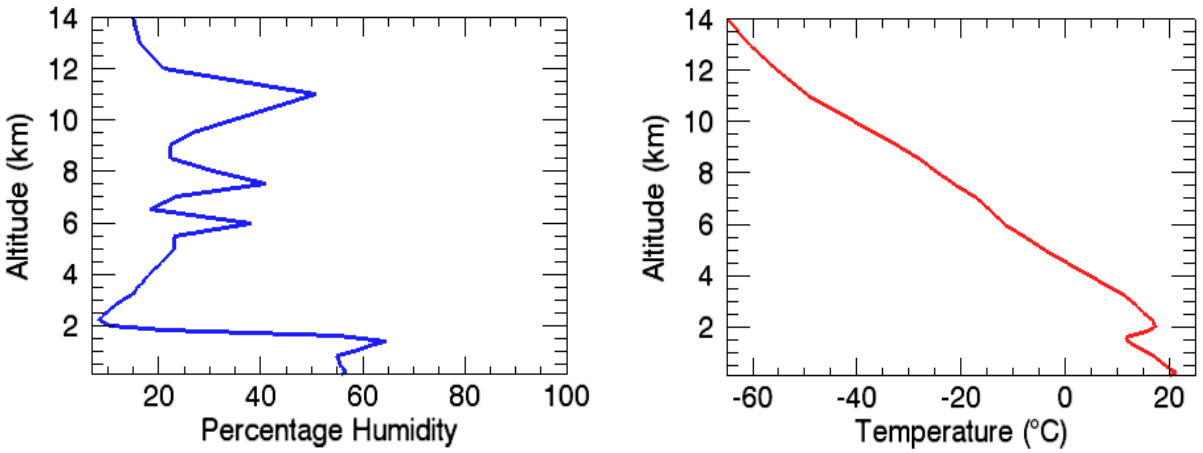

Figure 4.14 Temperature and humidity atmospheric profiles measured at Guimat WMO Meteo Station the 18 of September at 00 GMT. shows the 18 of September at 00 GMT temperature and humidity atmospheric profiles, used for the ASTER night time image

The Digital elevation Model is generated by Land Process Distributed Active Archive Center (LP DAAC) by using commercial software. The accuracy of this DEM is better than 25 meters (Bryan

ailey , 2007) Root Mean Square Error (RMSE) xyz owing to the inherent geometry accuracy of the ASTER data and the quality of production software.

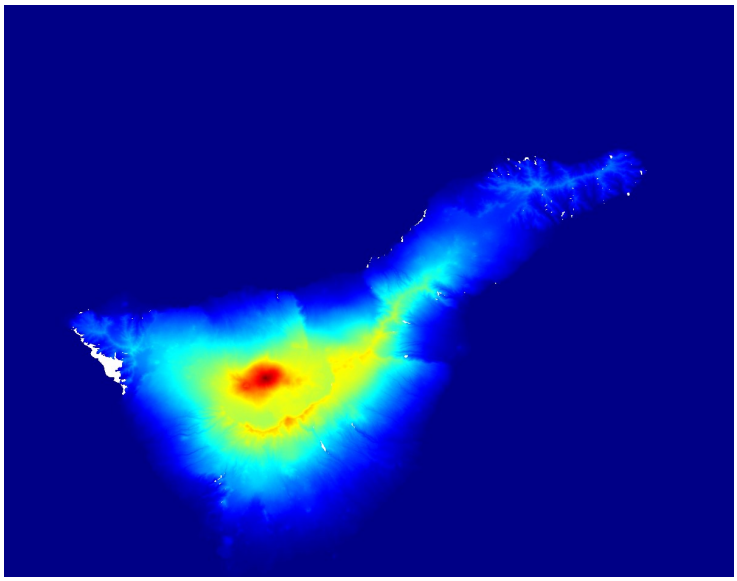

Figure 4.15 ASTER DEM of Teide volcanoo referenced to the Earth ellipsoid (WGS84) .

4.4.2 ASTER SNR

In order to evaluate the ASTER SNR on the night data acquired on Volcano Teide, an IDL procedure base on the method discussed in section 3.6.1.

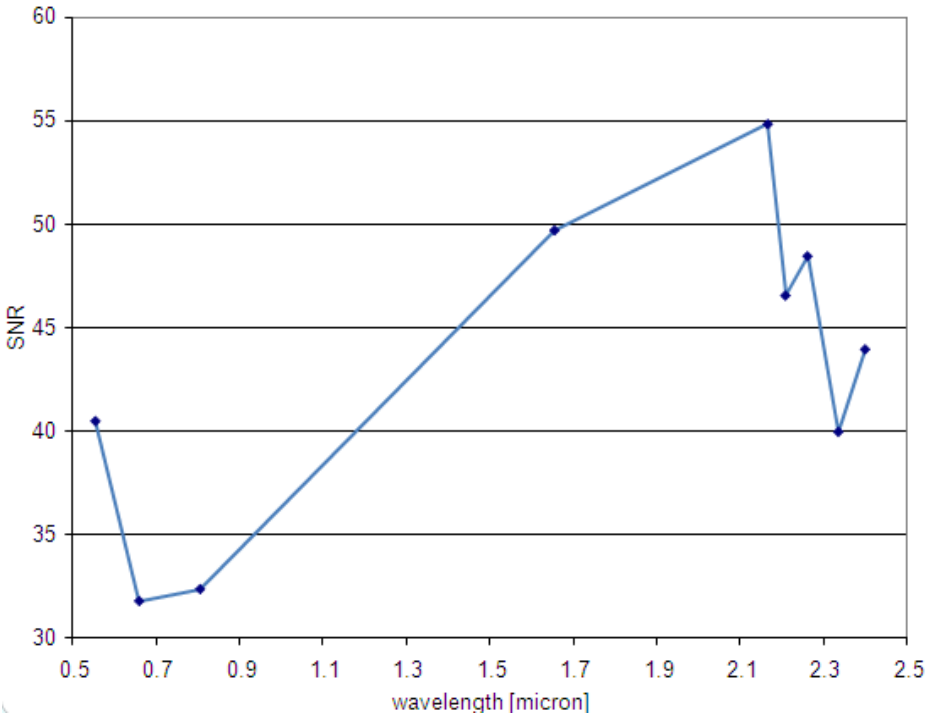

Figure 4.16 SNR retrieved for ASTER data (August 04 2007 day) .

We can note that the VNIR bands have SNR lower than the SNR for SWIR; as regards thermal range the error is evaluated taking into account the Noise Equivalent Temperature of ΔNET<0.3K.

4.4.3 ASTER product: emissivity

The pixel-by-pixel spectral surface emissivity was computed using the CIRILLO and TES algorithm as described in previous section.5.2.2. The result of emissivity retrieval of ASTER night data (17/09/2007) is showed in figure 4.17. A profile of radiance at sensor and of retrieved emissivity in the correspondence of same pixel, are plotted to point out the differences in features before and after the retrieval.

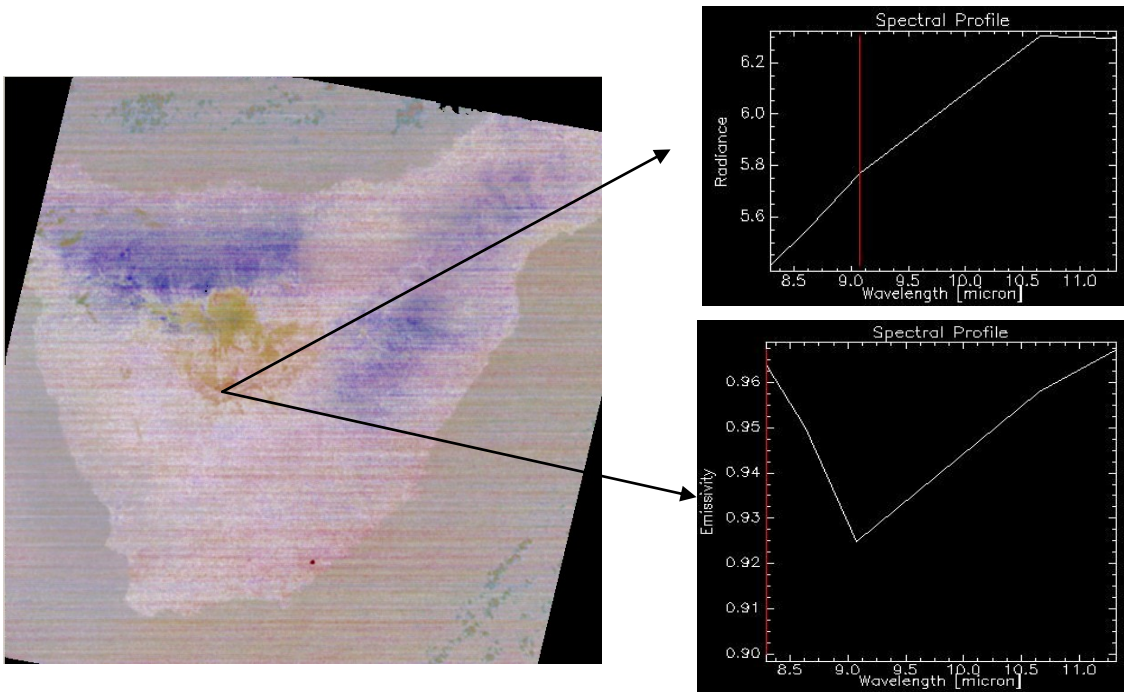

Figure 4.17 colour composite emissivity map (bands 11.31micron, 10.31micron and 9.075micron plotted as RGB) of ASTER (left); an example of spectrum before (right top) and after (right down) calibration and emissivity retrieval.

4.4.4. ASTER product: reflectance

Atmospheric and topographic corrections was performed by means CIRILLO procedure (see section 3..5.2.1) that transforms the "at-the-sensor radiance image" to TOA (Top Of Atmosphere) and then in surface reflectance (Figure 4.18).

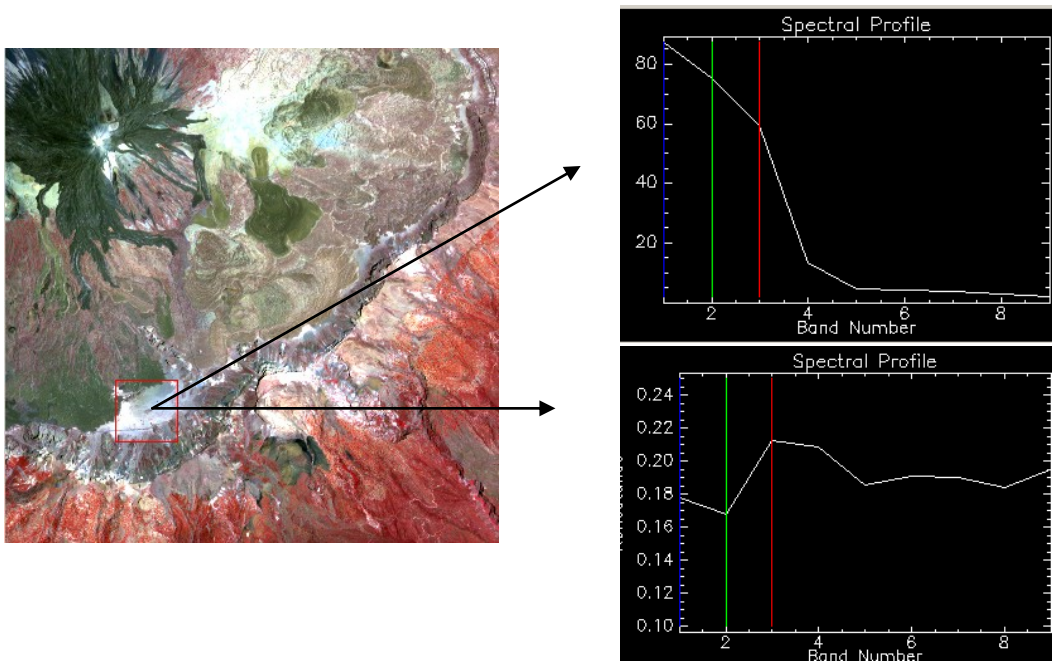

Figure 4.18 Reflectance image, and an example of spectrum an example of spectrum before (right top) and (right down).after calibration and reflectance retrieval.

4.4.5 EO-1 Hyperion calibration

The Hyperion image used in this study is EO1H2070402003317110PV.1Lb. EO stands for the satellite EO1 and H stands for Hyperion. The number 207 and 040 are the WRS path and row respectively. 2003 is the year of image acquisition while 317 is the Julian day. The first "1" indicates that Hyperion sensor is on. The second "1" indicates that the Ali sensor is on. The following "0" indicates that the AC sensor is off. P is the code for pointing mode and Vis the code for scene length.

There are 220 unique spectral channels collected with a complete spectrum covering from 357-2576nm. The Level 1 Radiometric product has a total of 242 bands but only 198 are calibrated. Calibrated bands are 8-57(426.8nm -925.4nm VIS) and 77-224(912.2- 395.5nm, SWIR)

(Figure 4.19). The reason for not calibrating all 242 channel is mainly due to the detectors low responsivity.

The digital values of level 1 product are 16 bit radiances and are stored as 16 –bit signed integer, the scaling factor is

$$VINIR(8\text{-}579)_{bands}=DN/40\ [W/m^2sr\mu m] \quad (27)$$

$$VNIR\ (77\text{-}224)_{bands}=DN/80\ [W/m^2sr\mu m] \quad (28)$$

The calibration factor is integrated in the CIRILLO code.

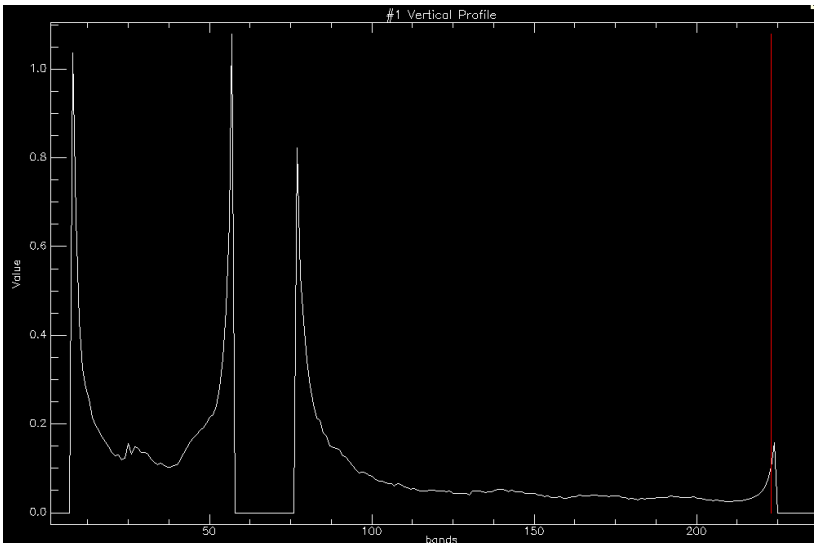

Figure 4.19 Hyperion gain exhibits zero values for un-calibrated bands.

4.4.6 EO-1 Hyperion SNR

We remind that Hyperion has not on board calibration facilities and vicarious calibration or moon calibration are periodically made by NASA .in order to trace the behaviour of the instrument. For our aims it is important to know the SNR and the same IDL procedure based on the method described in section 3.6.1 was applied to the Hyperion image .

The figure 4.20 shows the obtained result.

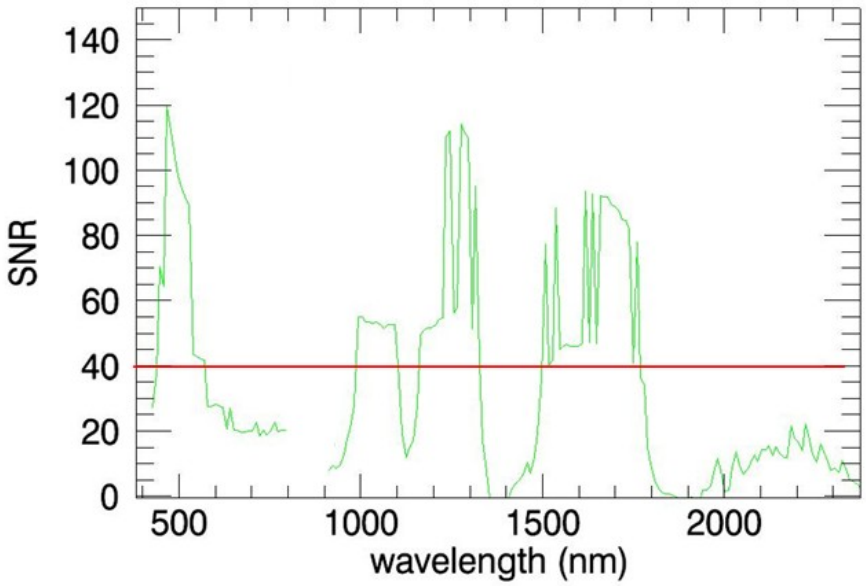

Figure 4.20 SNR retrieved by statistical analysis of image; The red line in figure represents the SNR minimum value declared by NASA. Only 4 wavelength intervals of spectrum are higher than the minimum value (SNR=40) while the maximum (SNR=135) is lower than the nominal maximum SNR value of 190.

We can note that SNR exhibits values between two range: one with values from 60 to 120 and a second one with values between 10 and 50. An hyperspectral sensor signal is considered to be good when its SNR is roughly greater than 100. We can expect that only bands with SNR between 60-120 will give significant spectral information; for the others bands noisy values are expected.

4.4.7 EO-1 Hyperion product: reflectance

The Hyperion data has been calibrated by the procedure described in section 3.5.2. At the end of the process we obtain a reflectance spectrum in correspondence of each pixel in the image.
In the following figure 4.21, the spectrum of un-calibrated pixel data and the reflectance spectrum after calibration, are showed.

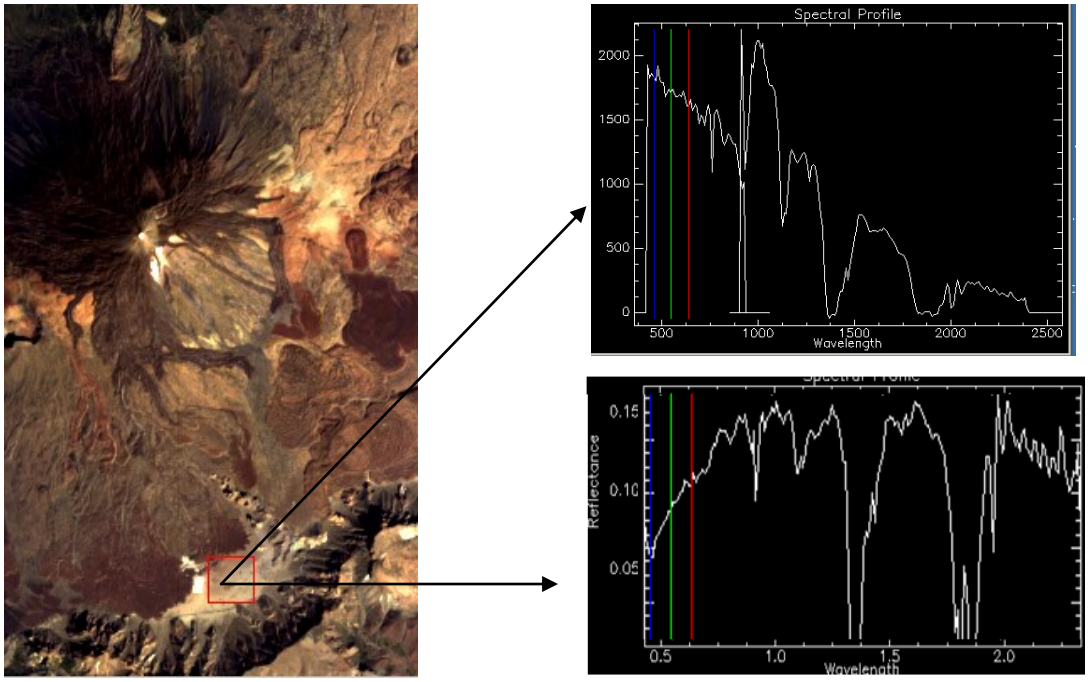

Figure 4.21 EO1-Hyperion data calibration result: raw spectrum(DN vs nanometer) is showed (top); the corresponding calibrated (reflectance vs micron) spectrum is showed down.

It is possible to note that some spikes are in correspondence of noisy regions where SNR is low (e.g greater than 2.0 micron).

4.5 In field measurement

4.5.1 In field test sites

In order to validate the calibration models used for satellite data reduction for both emissivity (by using µFTIR, see section2.2.5) and reflectance (by ADS FieldSpec, seen section 2.3.6) in situ measurements have been realised. A survey was realised to verify the pre-campaign selected sites based on ASTER image especially in term of accessibility with instrumentations.

Figure 4.22 A Simultaneous acquisition of FTIR and Field Spec measurements; B reaching test site for measurement

The weather conditions were good for the whole duration time of the campaign except for a ring cloud covering the top of volcano almost daily but for a restricted time.

The test sites are identified by capital letter and are characterized in reflectance and emissivity. One extra test site , on the top of PT crater, has been characterised in reflectance. In this case, emissivity has not been realised because it is very dangerous to carry µFTIR that require liquid Nitrogen cooling, above an altitude of 3718m; further the working temperature of µFTIR is 5-40°C degree.

Three test sites (El Piton/ Point P , M. Chaorra/Point M and Mna Majua/ Point F) were sampled, no more samples were collected due to the limit in expedition weight.

In figure 4.23 ASTER image has been loaded on Google and the geolocated positions of the in situ test sites (acronism FSC stands for FieldSpec and FTIR for the µFTIR) have been marked.

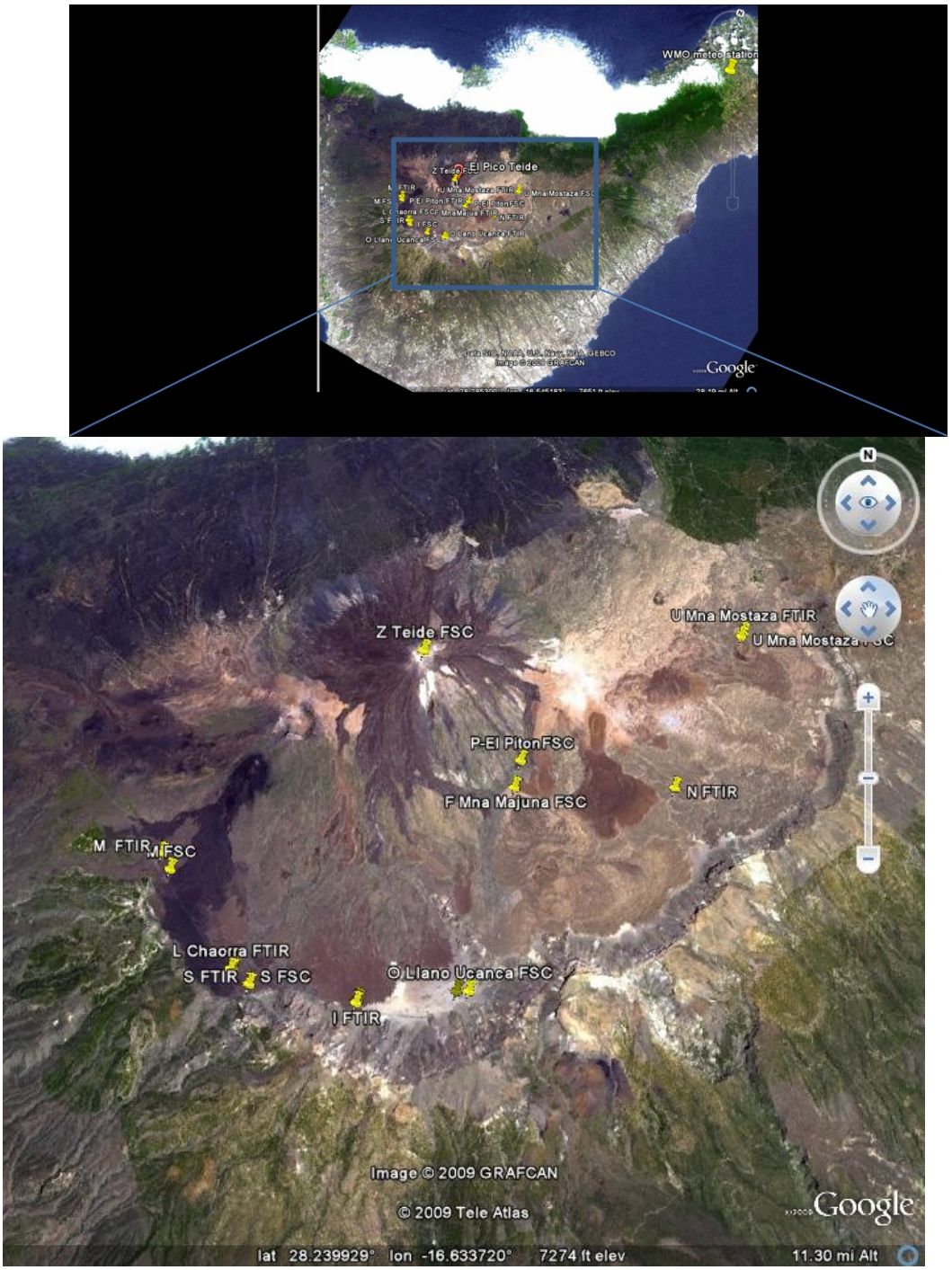

Figure 4.23 ASTER visible truth colour image is loaded on Google Earth: the test sites acquired by FSC and FTIR) are marked according their geolocation.

The following table is the list of the test sites where FieldSpec (FSC) and/or μFTIR (FTIR) measurements have been done. The name of the regions is derived from Carracedo J., 2006.

Site feature	Geology type	Altitude	FSC FTIR	Sample
Point P : El Piton	Tephra and oxidiane		X X	X
Point L: Lavas del Chaorra	Lava negra 1798	2085 asl	X X	
Point M: Lava de los Hornitos	Ph. Tephra-lava scoriae	2112 asl	X X	x
Point F: Mna Majua	Ph. lava/ pumice follow	2293 asl	X X	x
Point N Mna Rajada	Lava tephra intermediate felsic /phonolite pumice follow	2280 asl	X	
Point S Boca Tauce	Pl.bas. lava	2057 asl	X X	
Point O Llano Ucanca	colluvium	2017asl	X X	
Point U Mna Mostaza	Maphic phon lava	2142asl	X X	
Point I	Pl.bas. lava	2063 asl	X	
Point V	Pl.bas. lava		X	
Point Z (0,1,2): Teide summit	thepra phonolite	3718 asl	X	

Table 4.11: the test sites characterization is based on the Ablay, Martì (2002) lithotypes identification while name identification is based on Carracedo 2006.The FSC and FTIR stand for reflectance and emissivity measurements respectively.

4.5.2 In situ Reflectance and Emissivity measurements on Volcano Teide

The reflectance measurements were realised by the FieldSpec instrument, according to the protocol of measurements in a time range between 10:30 -15:30 time for the best illumination conditions.

The absolute reflectance spectra of the ground was obtained automatically by the instrument software as the ratio of the target radiance and of a standard white reference (Spectralon), multiplied by the Spectralon absolute spectral reflectance (details are in the protocol description, section 2.3.5).

We remind that the radiance measurement of the white reference need to be taken (at short intervals) every time before each reflectance measurement; in this way it is possible to avoid illumination variations between the measure of the target and that one of the reference (Milton, 1987). For each test site, the reflectance spectra are acquired within the satellite pixel size and a mean over 20 reflectance spectra is performed.

Emissivity measurements have been realised by μFTIR following an established protocol (see section 2.2.6). Due to features of instrument, (a measurement requires 20 minutes) 3-5 measurements within the pixel size are performed and a mean of 18 interferograms are performed.

On September 16th, test measurements according to the pre-campaign measurement protocol have been realized to check the instrument state, the autonomy of batteries and the cooling system state.

On September 17th the previously selected areas by satellite image, has been redefined taking into account the areas really accessible. **Point O (Liano de Ucanca)** was chosen for the sunset and night measurements being flat and well recognizable also by satellite.

On September 19th and 21st the acquisitions all over the test sites have been completed. The selected test sites are indentified by a capital letter and are shown in figure 4.23. The details of the measurements are shown in appendix 1.

Sept 16th 2007	*Instrument Test:* A check the instrument state and operation, the autonomy of batteries and cooling system and the measurement protocol, was performed.
Sept 17th 2007	*Planning:* Previously selected areas by satellite image, was refined taking into account the volcanooes accessibility. The test sites area were chosen for the sunset and night measurements .
Sept 19th and 21st 2007	*Measurements:* The acquisitions all over the test sites were performed

Table 4.12: in field μFTIR activities carried on volcanoo Teide 2007 campaign.

After the campaign a data quality check was done in order to select only good measurements. The acquired data set was organized and processed.

For the aims of the study a preliminary work consists in analysing emissivity and reflectance spectra for each test sites; by referring to Hunt G.R. (1980) an analysis of absorption features in the spectra is performed to identify electronic or vibrational effects. The description of the lithotype is done referring to Ablay Martì (2002) and Carracedo (2006). Each test site spectra are described in the following. The standard deviation plots for each spectrum are reported in appendix 2 for clarity of the representation and the range values are indicated in the figures captions.

El Piton (Point P)

El Piton or Pan de Azucar is characterised by Lavas Negras (1150 BP). The test site consists of tephra and some minor part of obsdiane (Ably, Martin 2002). Reflectance and emissivity have been measured in the south east side. The electronic absorption feature due to the Fe^{2+} charges between Fe and O is identified in the reflectance spectrum (Figure 4.24).

The vibrational absorption feature of Si-O tetraedic sites and the Al-O-Si in feldspar are recognizable in the emissivity spectrum (Figure 4.25).

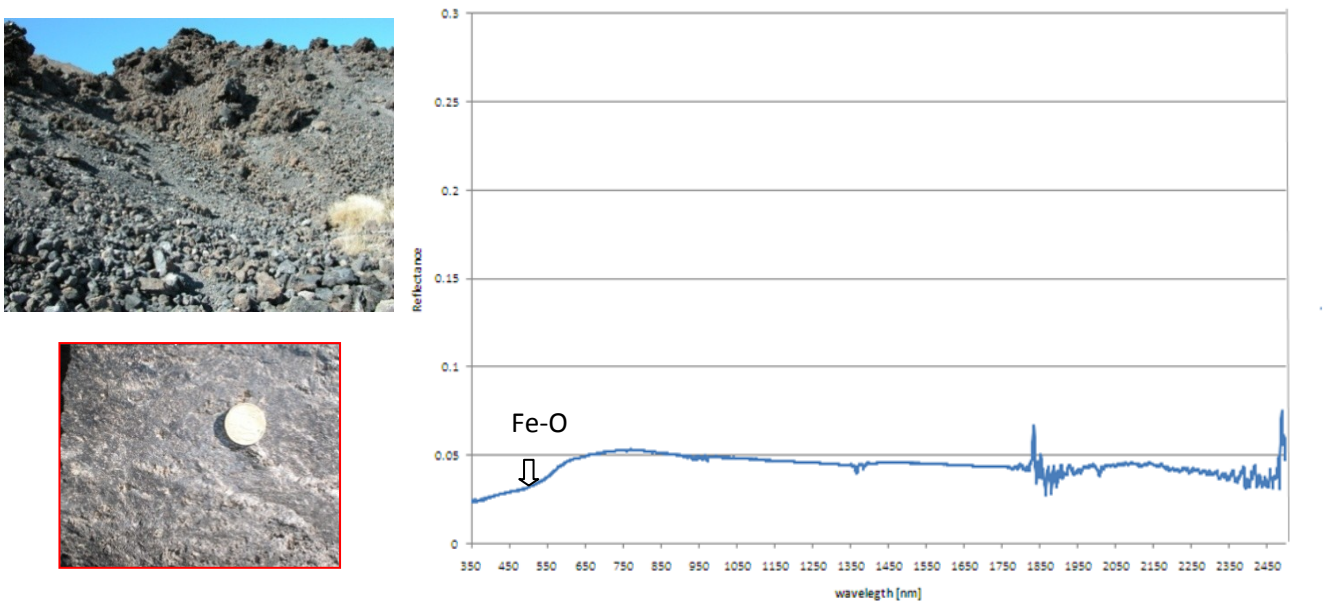

Figure 4.24 Mt Teide **reflectance spectrum** acquired on test site El Piton, named point P(28° 15' 19.7'', 16°37' 20.0''). Fe-O in oxides (opaque phase) is visible at 500-550nm. The standard deviation for this spectrum is in the range of 0.0002 to 0.03 in the noisy part of spectrum between 2400-2500nm)

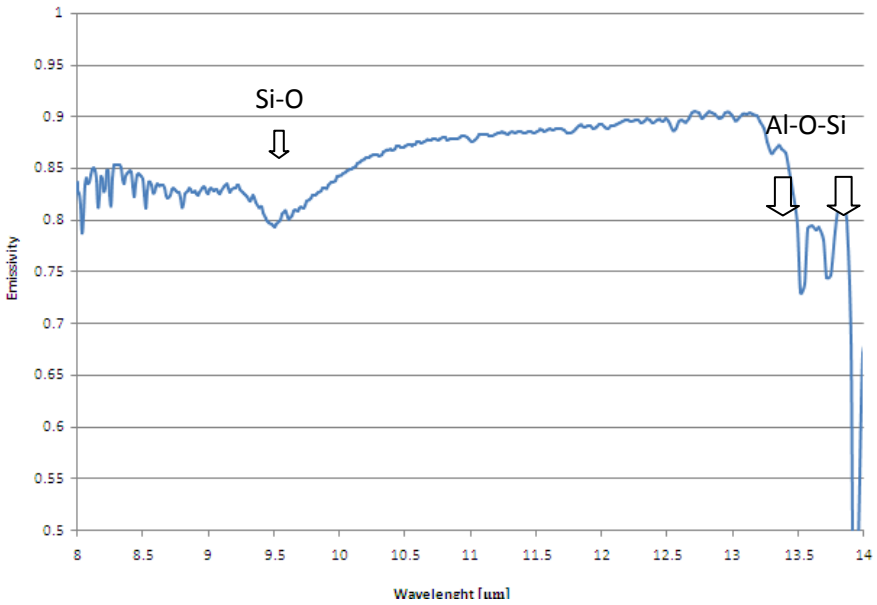

Figure 4.25 Mt Teide emissivity spectrum acquired on test site El Piton, named Point P (N 28° 15' 19''.9 E 16° 37 19''.7). It is possible to identify the Si-O stretch absorption band and the Al-O-Si in feldspar. The emissivity error is 2% of measurement (see appendix2) .

Mount Chahorra (Point L)

This test site represents an historical eruption (1798) associated with the Nord Rift (figure 4.3) and characterised by basaltic alkaline eruption. The lava is characterised by aphanitic microcrystalline texture (Carracedo J., 2006) . The rock is a basanite type . The reflectance and emissivity are showed in figure 4.26 and 4.27 respectively.

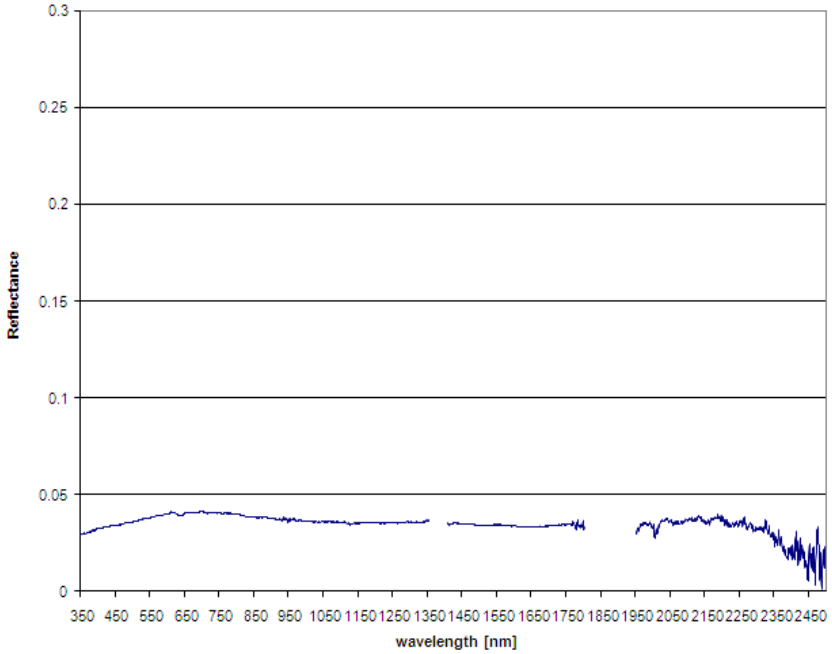

Figure 4.26 Mt Teide reflectance spectrum acquired on test site Chaorra , named point L (N28°13'2.3'' E16°40'53.8''). The standard deviation for this spectrum is in the range of 0.0002.to 0.03 in the noisy part of spectrum between 2400-2500nm(see appendix 2).

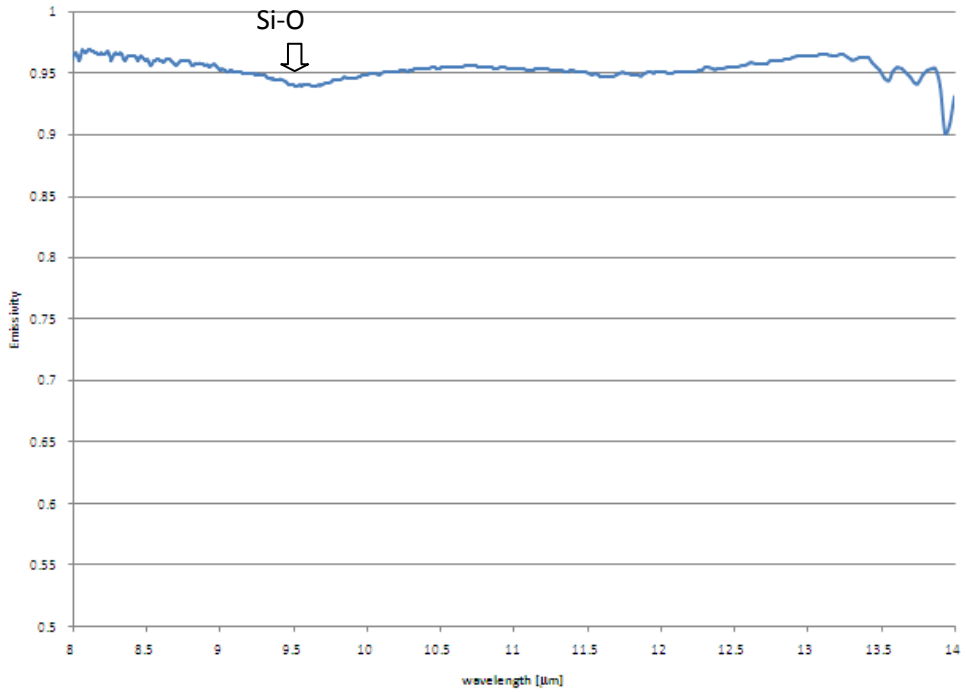

Figure 4.26 Mt Teide emissivity spectrum acquired on test site lava Negra , named point L (N 28° 13' 01.5'' E 16° 40' 55.7''). Also in this spectrum it is visible the Si-O stretch absorption band. The emissivity error is 2% of measurement.

Lava de los Hornitos (Point M)

The reflectance spectrum of Los Hornitos test site shows the Fe-O charge transfer in oxides (opaques) absorption band.

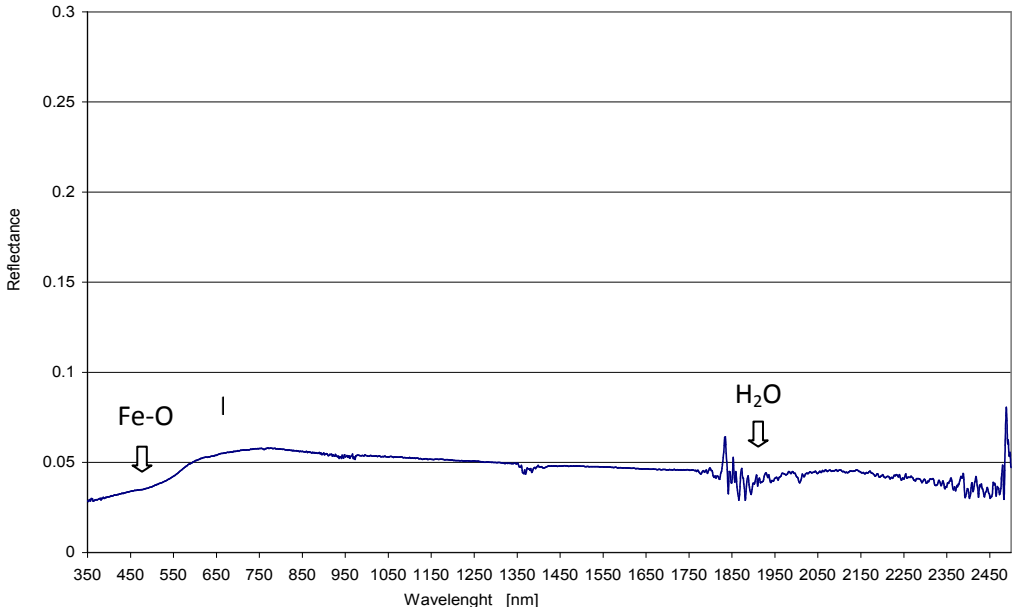

Figure 4.27 Mt Teide reflectance spectrum acquired on test site Lava de los Hornitos named point M (N 28°14'7.2'' E 16°41' 45.8''). It is possible to identify the Fe-O charge transfer in oxides (opaques). The standard deviation exibits values from 0.0004 to 0.005.with a maximum value 0.03 is the noisy part of spectrum between 2400-2500nm (see appendix 2).

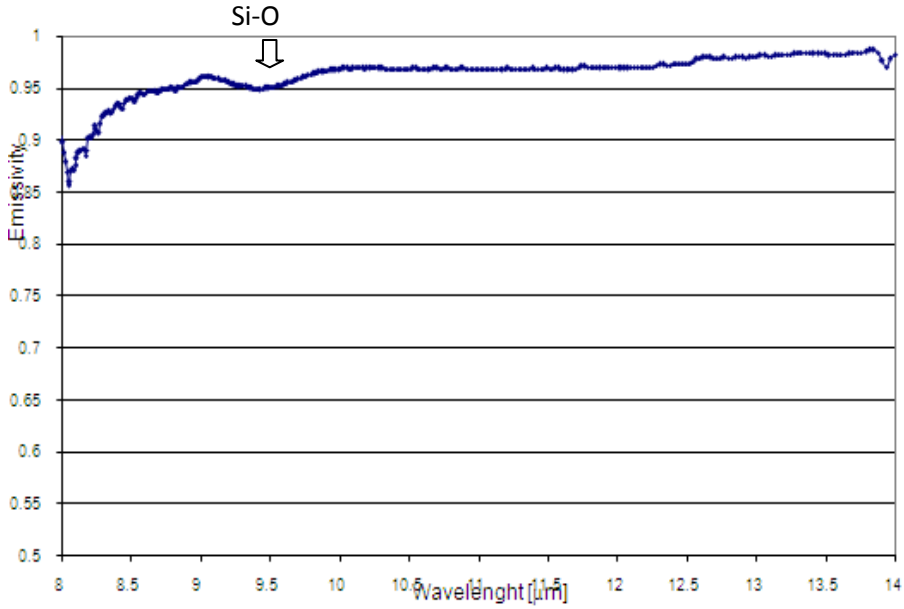

Figure 4.28 Mt Teide emissivity spectrum acquired on test site Lava de los Hornitos named point M(N 28° 14’ 18.2’’ E 16° 41’ 52.6’’). The Si-O stretch absorption band exhibits a minimum at 9.5um. The emissivity error is close to 2% of measurement.

Mna. Majua (Point F)

The eruption that originated Mna Mauja is supposed to be within 4000-5000 years. Mna Majua is a strombolian pumice cone, 700 m in diameter and 55 m high, breached on its South East side by a wide, lobate, blocky flow of weakly evolved phonolite lava at least 30 m thick. The absorption band due to Fe^{2+} in feldspate and the Al-OH vibrational overtone are remarkable.

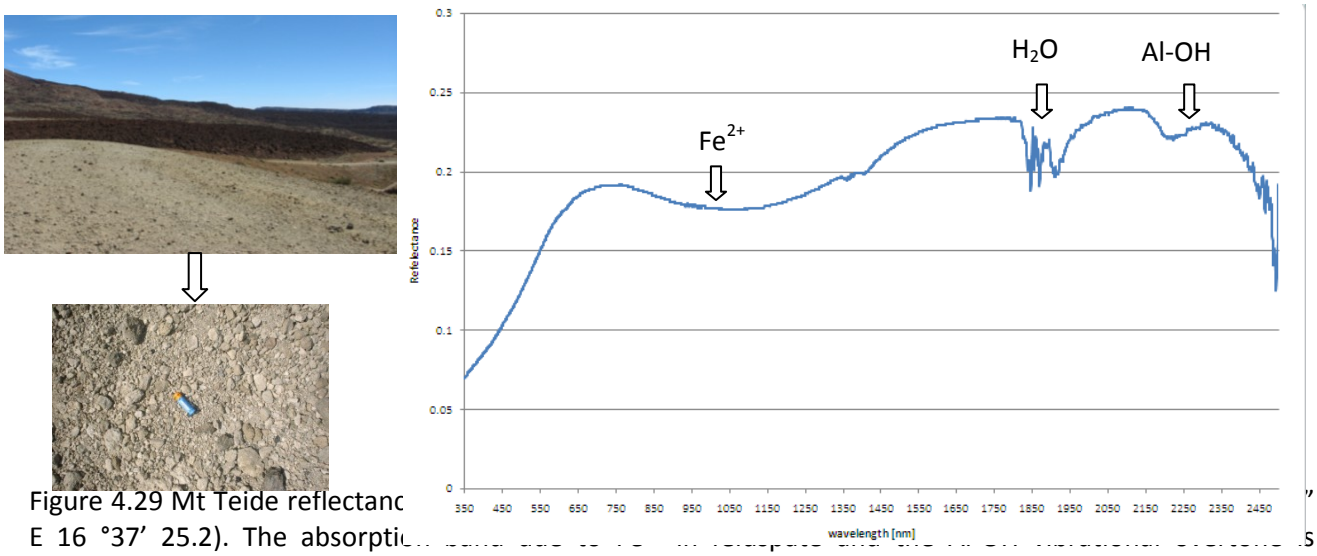

Figure 4.29 Mt Teide reflectanc [illegible] E 16 °37’ 25.2). The absorpti[illegible] recornizable. The standard deviation exibits values from 0.0005 to 0.005 with a maximum value 0.03 is the noisy part of spectrum between 2400-2500nm (see appendix 2).

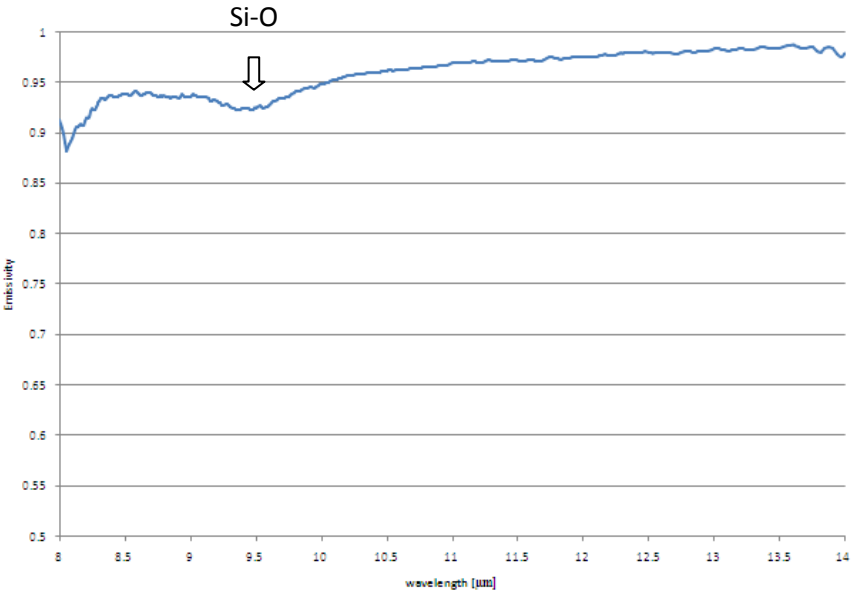

Figure 4.30 Mt Teide emissivity spectrum acquired on test site Mna Majua named point F (N 28° 15' 1.2'' E 16° 37' 25.3''). The Si-O stretch absorption band exhibits a minimum around 9.5um. The emissivity error is 2% of measurement.

Mna Rajada (Point N)

This site named **Mna Rajada** is part of the more extended M.na Blanca. characterised by lava tephra intermediate felsic /phonolite pumice follow. It is possible to identify the absorption bands due to Fe^{2+} in feldspate and the Al-OH vibrational overtone respectively.

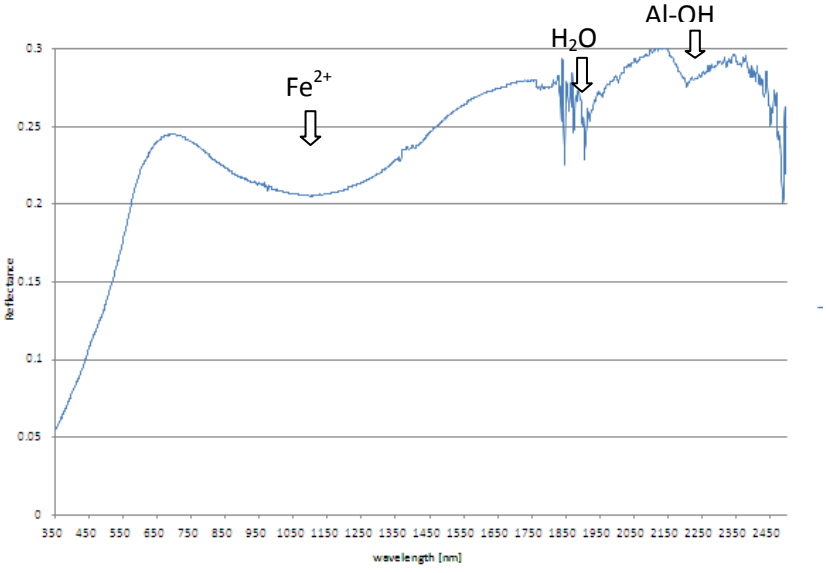

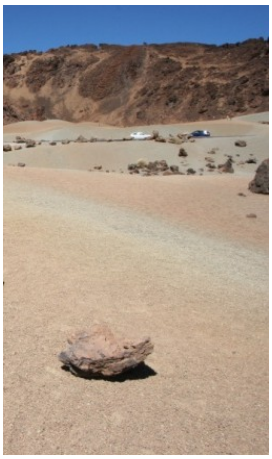

Figure 4.31 Mt Teide reflectance spectrum acquired on test site named Point N, N 28°15' 52.7'' E 16° 35' 19.6''). The absorption band due to Fe2+ in feldspate and the Al-OH vibrational overtone is recornizable. The standard deviation exibits values from 0.0003 to 0.005 with a maximum value 0.03 is the noisy part of spectrum between 2400-2500nm (see appendix 2).

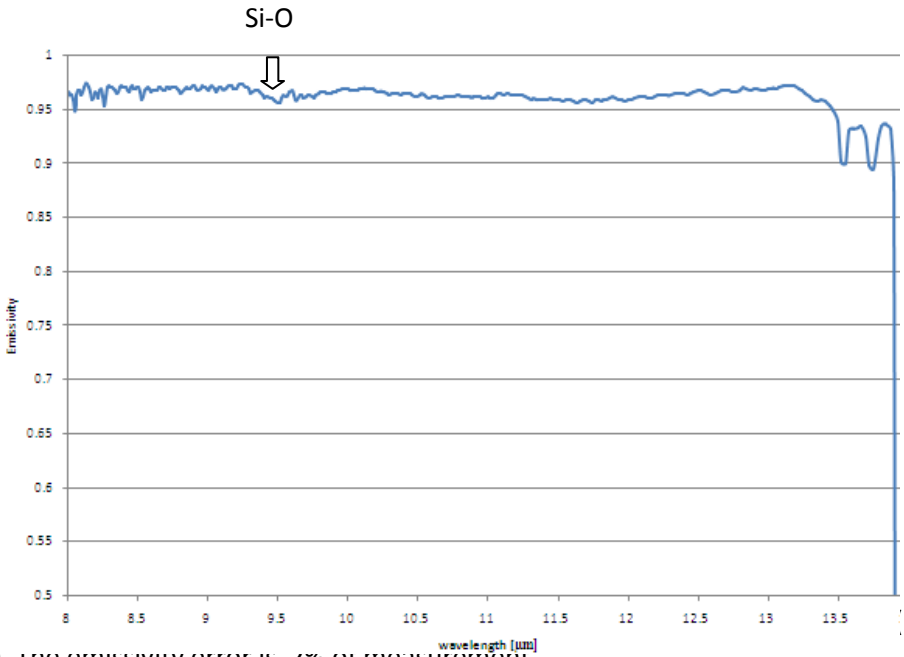

Figure 4.32 M N28° 15' 57.6'' E 16° 35' 21.9''). The emissivity error is 2% of measurement.

Boca Tauce (Point S)

This site is member of Pico Vejo; it is a wide, compound, pahoehoe low of porphyritic plagioclase basanite lava exposed with an undulating, fractured lava crust.

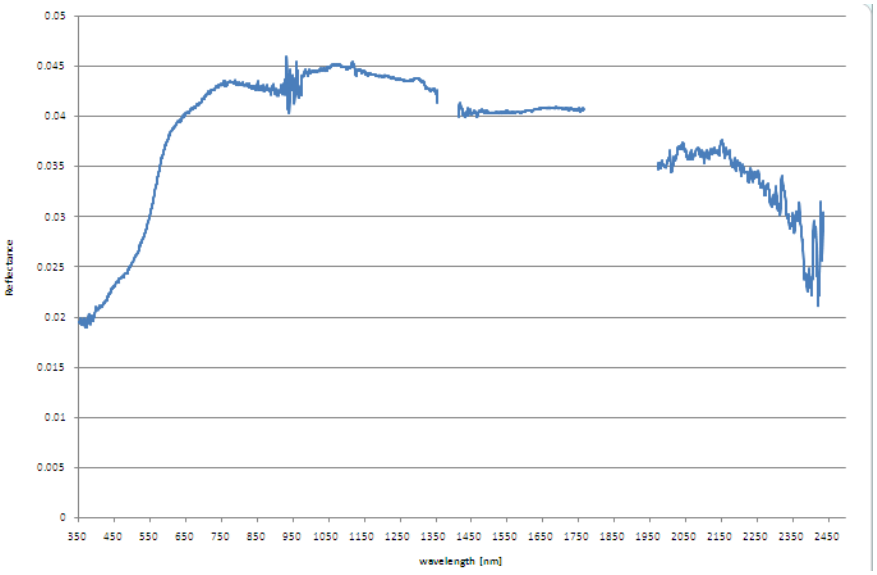

Figure 4.33 Mt Teide reflectance spectrum acquired on test site Boca Tauce named point S (N28°12'52.1'' E16°40'42.1''). The standard deviation exibits values from 0.0002 to 0.005.with a maximum value 0.035 is the noisy part of spectrum between 2400-2500nm (see appendix 2).

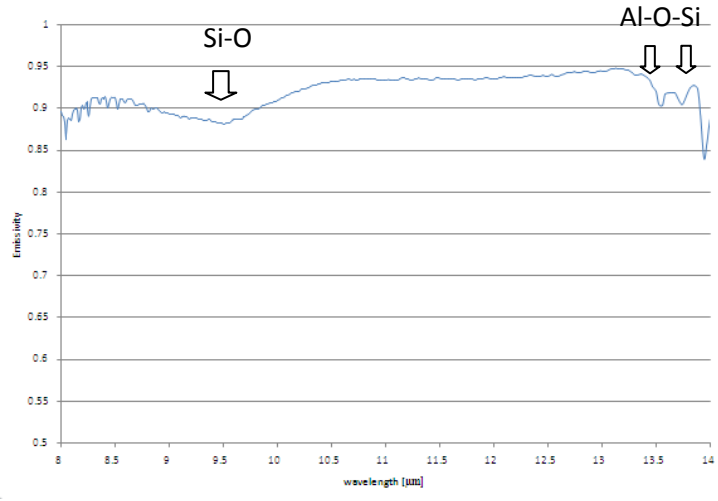

Figure 4.34 Mt Teide emissivity spectrum acquired on test site named point S (N 28° 12’ 51. 9’’E 16° 40’ 41.1’’). The emissivity error is 2%.

Llano Ucanca (Point O)

Llano de Ucanca is a very well recognizable area both from satellite data and geology map. It is a flat area of 1.8 km length and 0.75 km large located in the southeast part of LCC.

Because of these characteristics it was chosen as representative test site for satellite data validation. Llano de Ucanca is constituted by colluvium deposit recent in age. The lava surface presented some vegetation (brushes) so the spectra of the two different classes were acquired. In figure 4.36 are reported the spectra for of the brushes and of lava surface.

Figure 4. 35 Liano de Ucanca landscape view..

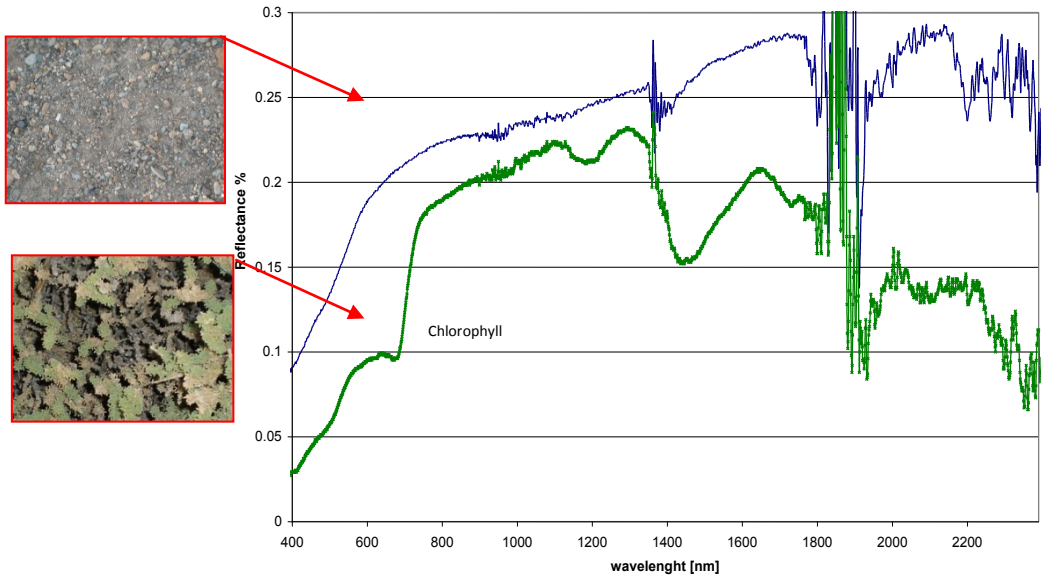

Figure 4.36 . Mt Teide reflectance spectrum acquired on test site Llano Ucanca named point O ; point O is characterised by two different kind of surface: brushes (green) and colluvium deposit(blue)(N 28°12' 46.9'' E 16° 38' 0.9'') . Standard deviation plots are showed in appendix 2.

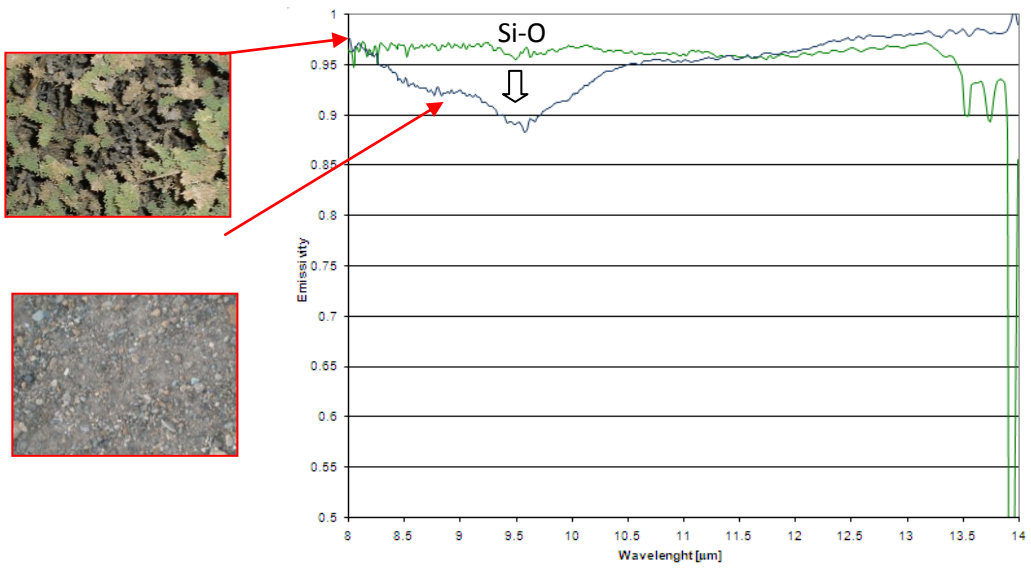

Figure 4.37 Mt Teide emissivity spectrum acquired on test site Llano Ucanca named Point O (N 28° 12' 46.9'', E 16° 38' 10.0''). The emissivity error is 2% of measurements.

Montana Mostaza (Point U)

Montana Mostaza is a large scoria cone in the eastern Las Canadas Caldera (LCC) associated with a pahoehoe low magnesian alkali basalt lava, extending for 1.2 km.

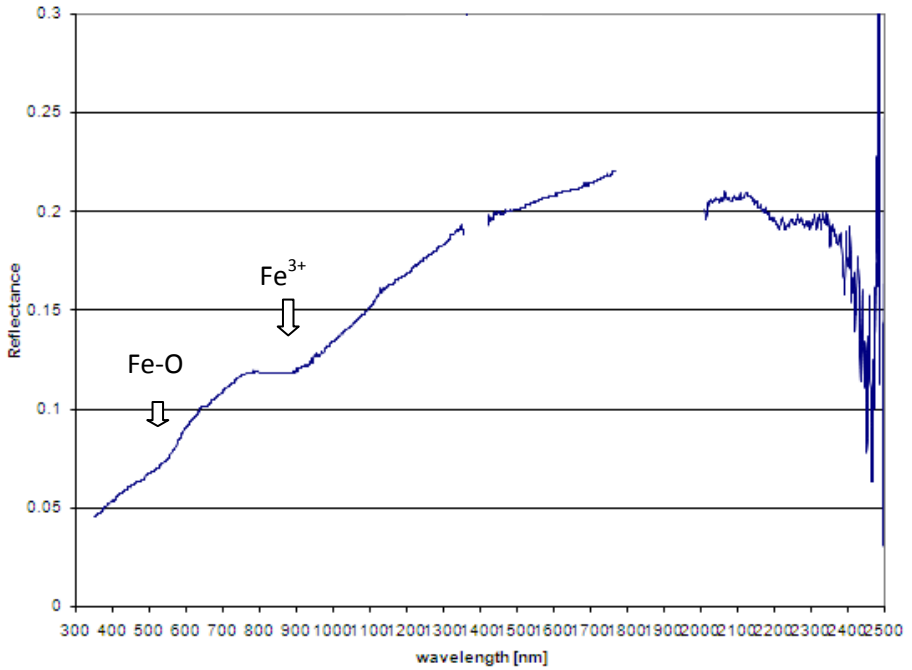

Figure 4.38 Mt Teide reflectance spectrum acquired on test site Point U (N 28 16' 54.2''E 16° 34' 19.1'') Standad deviation values range from0.0003 to 0.005 in the range 350-950nm. While is assumes values between 0.02 -0.03 in the range 1000-2500nm (appendix 2).

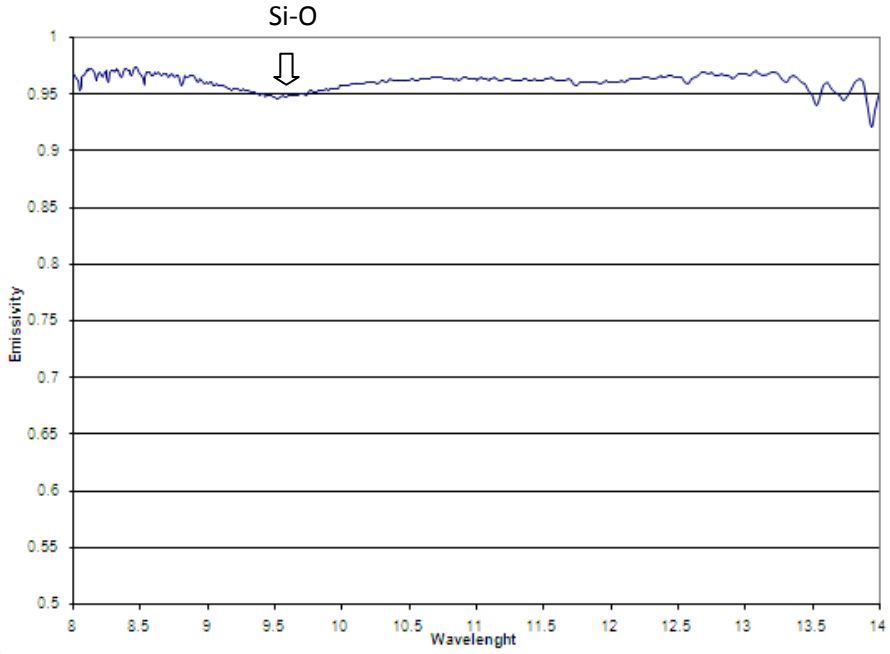

Figure 4.39 Mt Teide emissivity spectrum acquired on test site named Point U (N 28° 16° 57.4''E 16°.34' 17.2''). The emissivity error is 2% of measurements (see appendix2).

Point I and Point V

These two test sites have been measured by µFTIR and the emmissivities are plotted in the following figures.

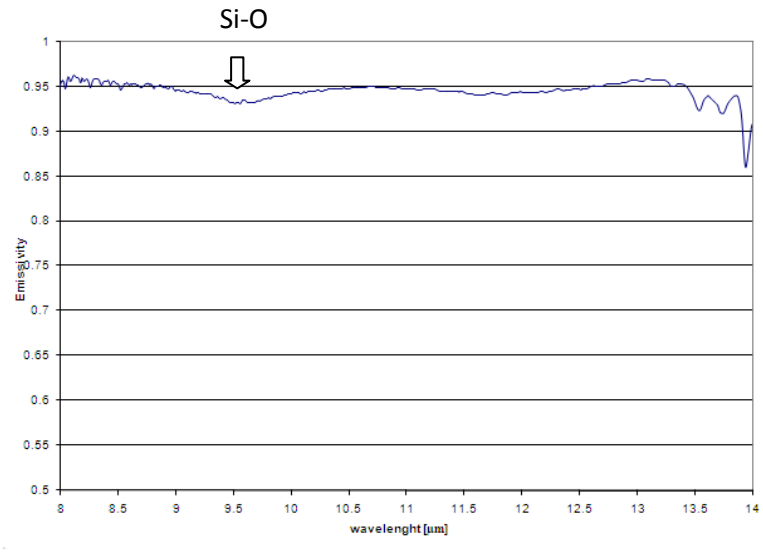

Figure 4.40 Mt Teide emissivity spectrum acquired on test site **named** Point I (N28° 12’ 39.9’’E16° 39’ 23.1’’). The emissivity error is 2% of measurements.

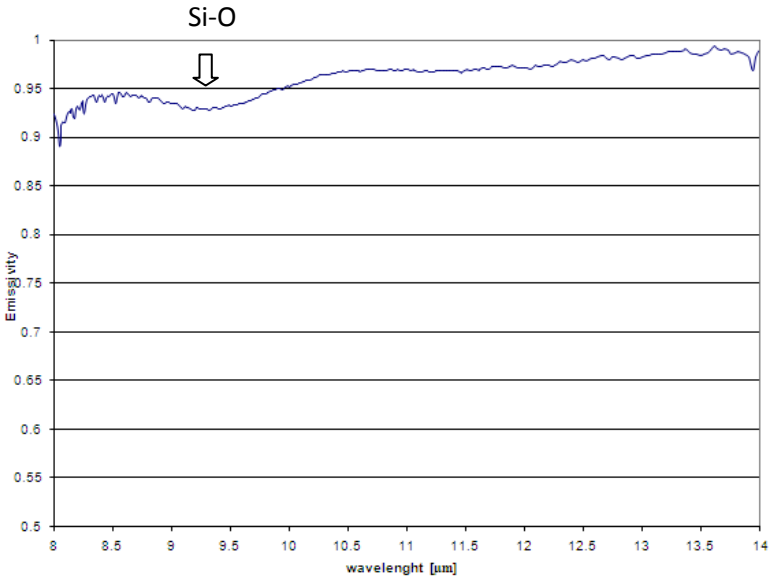

Figure 4.41 Mt Teide emissivity spectrum acquired on test site named Point V (N 28° 12’ 40.5’’E 16° 39’ 23.4’’). The emissivity error is 2% of measurements.

PicoTeide summit crater reflectance(Point Z)

On September 20th 2007, FieldSpec measurements were realized on the top of Teide crater where fumaroles activities are present. Since the µFTIR instrument needs liquid Nitrogen to be cooled, It was evaluated not safe bring it on the top of the volcano and only reflectance measurements were performed. Three different kinds of surfaces (idrate sulphate, alterated rock argil type and amorphic sulphate) where measured. It is easy to recognize the spectrum of Sulphur (Point Z0, blue lline in figure 4.42) very similar in behaviour (especially on 550 -950nm range) to the pure Sulfur sample acquired on laboratory (Figure 4.43).

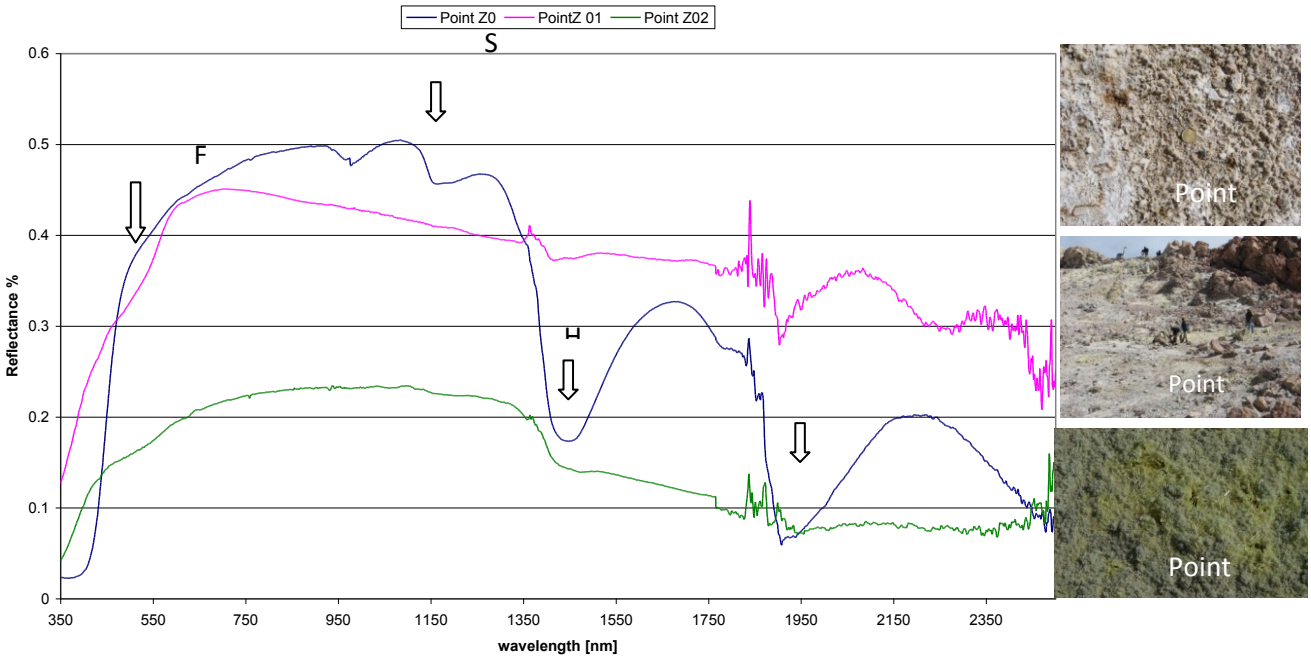

Figure 4.42 Mt Teide reflectance spectrum acquired on three different geologic units on the summit crater(N 28°16'20.17"E 16°38'32.81") Z0 fumaroles characterized by idrate sulphate(blue line); Z1 alterated rock argil type(pink line), Z2 amorphic sulphate (green line)

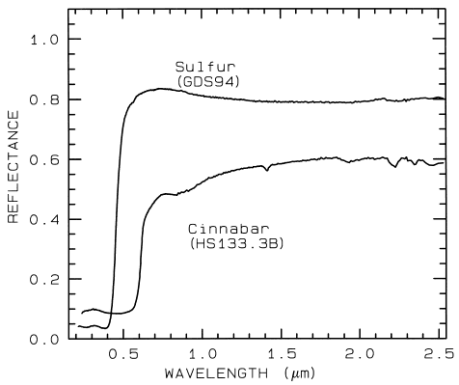

Figure 4.43 USGS, sulphur Laboratory reflectance: USGS http://specelab.cr.usgs.gov/PAPE RS.refl-mrs/refl4.html

4.5.2 Temperature measurement

In situ temperature measurement has been realised during the ASTER night passage on September 17th 2007. The selected test site is the LIano de Ucanca (Point O) since being flat, homogenous and constant in time not being subject to resurfacing due to recent eruptions. The used instrument is the EVEREST 130,2L; it is an infrared thermometer in the (8 -14)µm spectral range configured like a gun that the operator points directly to the target to make a temperature reading. Instantly he can read the readout temperature of the outdoor target on the liquid crystal display. (by Charles E. Everest).

The optical section, or front end of the infrared thermometer, collects a sample of the radiation given out by the turf. The instrument processes this sample through its circuitry and converts the information to a form that triggers the liquid crystal to display (Figure 4.51). Since no contact needs to be made between the thermometer and the surface to make a precise temperature measurement, the target is not altered (Buongiorno et al 2008). The Everest IR thermometer gives an instantaneous readout with 0.1°C resolution. Temperatures can be taken at a maximum distance of 300m without any accuracy loss. The response time of the thermometer can be slowed down by switching to "Data Averaging" in order to read a temperature average over an interval of time. This is especially helpful when wind gusts cause variations over the area being measured (Buongiorno et al 2008). The operating guide of the instrument is detailed on appendix 4.

Characteristic	value
Scale Range:	-30 °C to 100
Resolution:	0.1 °C
Accuracy:	±0.5 °C
Noise	±0.2 °C
Spectral Pass	8<λ<14 (µm)
Field of View:	4 degrees
Response	0.1 s
Emissivity	0.2 to 0.99
Operating	2 cm to 300

Figure 4.44 Everest 130.2L reading interface example and technical characteristics.

The portable Everest IR thermometer was used to measure the temperatures during the ASTER night passage on Iliano de Ucanca (Point O) test site. The measurements were taken pointing the gun normally to the surface and at a distance of about one meter or less; this means a spot on the surface of less than 7 cm of diameter. We report in the following figure 4.45 the geolocation of the measured points and in the table 4. the mean value and standard deviation for each points. The analysis of the data and comparison with ASTER temperature will be discuss in section 6.4.

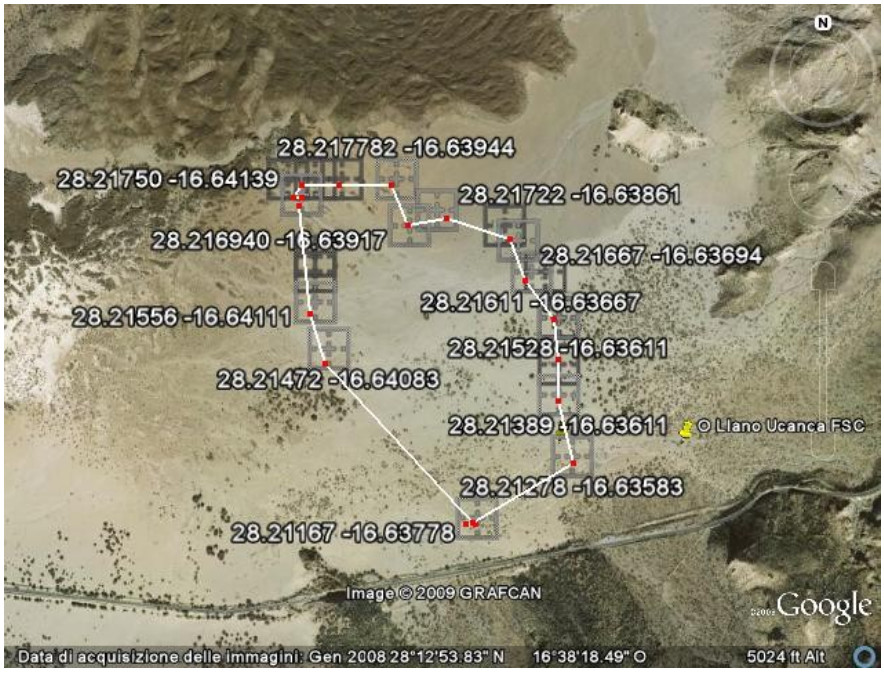

Figure 4.45 geo-location of the measured points; the polygon covers a surface of surface of 350m x 100m in order to comprehend different ASTER pixels.

Time GMT [h m]	LAT	LON	T in situ mean [°C]	T in situ stdev[°C]
21:23	28°12'46"	16°38'09"	7.71	0.10
21:29	28°12'48"	16°38'09"	6.36	0.05
21:33	28°12'50"	16°38'10"	5.11	0.03
21:36	28°12'52"	16°38'10"	5.79	0.03
21:39	28°12'55"	16°38'10"	5.26	0.41
21:43	28°12'58"	16°38'11"	4.27	0.49
21:49	28°13'00"	16°38'12"	4.97	0.42
21:54	28°13'00"	16°38'13"	8.9	0.58

22:00	28°13'01"	16°38'14"	4.64	0.57
22:05	28°13'02"	16°38'16"	3.4	0.28
22:08	28°13'02"	16°38'19"	2.72	0.36
22:12	28°13'04"	16°38'22"	2.25	0.48
22:16	28°13'04"	16°38'26"	1.93	0.29
22:20	28°13'04"	16°38'28"	1.75	0.39
22:34	28°13'04"	16°38'30"	2.42	0.32
22:32	28°13'03"	16°38'29"	2.18	0.82
22:36	28°13'01"	16°38'21"	2.34	0.28
22:48	28°12'59"	16°38'28"	1.78	0.37
22:52	28°12'58"	16°38'28"	1.05	0.51
23:00	28°12'56"	16°38'28"	1.02	0.33
23:11	28°12'53"	16°38'27"	1.30	0.16
23:15	28°12'42"	16°38'16"	2.66	0.27

Table 4.13 time, location and temperatures measurements on Ilano de Ucanca test site.

5. Laboratory Spectroscopy

Laboratory spectroscopy plays an important role in the intrinsic analysis of sample properties. They are used as support and guide for remote sensed data interpretation (Siegal B.R.and A.S. Gillespie, 1980).

Three samples of volcano Teide has been characterized by chemical analysis and by laboratory spectral measurement. Laboratory measurements were carried to complete the characterization of the surfaces on different scales.

5.1 Samples treatment

In order to realize spectral laboratory measurement, the samples were hand processed and analyzed for composition). The collected samples were processed at granulometry minor than 60µm.

The samples were prepared through a process of crushing and sieving. Crushing was done both by hand using a rock hammer and through a steel jaw crusher. Samples were then dry-sieved using a Ro-tap mechanical sieve shaker, and a minor 250 µm size fraction was separated by the sieve (Figure 5.1). The 250µm samples were powdered by using an agate-mill (Figure 4.2) and sieved at minor of 60µm granulometry.

Figure 5.1 Laboratory instruments used to crush and sieve samples (laboratory of Science Earth, University of Parma).

These very thin powder samples were used for total rock composition analysis.

Figure 5.2 Agate-mill used to reduce the samples granulometry minor 60 micron.

5.2 Chemical analysis

Chemical composition for all the Teide was measured by X fluorescence with an XRF ARL Advantix spectrometer at the lst laboratory of Science Earth, University of Ferrara.

The analytical program of Ferrara for XRF analysis allow a recalculation at 100 for main elements. The values of LOI (Loss Of Inition) were negative, probably due to an FeO oxidation major then volatiles component lost. So the LOI values were assumed to be equal to zero.

The results obtained on Mt. Teide samples are reported in the following table (tables 5.1).

Teide	M	F	P
classific	tra	ba	tr
SiO2%	59	46	6
TiO2%	0.	3.	0.
Al2O3%	19	16	1
Fe2O3%	3.	12	4.
MnO%	0.	0.	0.
MgO%	0.	3.	0.
CaO%	1.	9.	1.
Na2O%	7.	4.	8.
K2O%	4.	1.	4.
P2O5%	0.	1.	0.
LOI%	1.	0.	0.
TOTALE	10	10	1

Table 5.1 chemical analysis of three Teide rocks samples collected on 2007 .

5.3 laboratory reflectance measurement of samples

The set-up for spectral laboratory measurement at PLab INAF (Figure5.3) consists of a FieldSpec spectrometer of same class of that one used for in field measurements. The instrument fiber optics is connected to a goniometry, a second fiber optic is connected to a source Lamp and lights the sample lodged in a aluminum cylinder. The distance between sample and fiber may be micrometry controlled. Every samples was acquired 10 times and a mean value was calculated. A 30° source and 30° (standard used in laboratory measurements) instrument configuration was assumed.

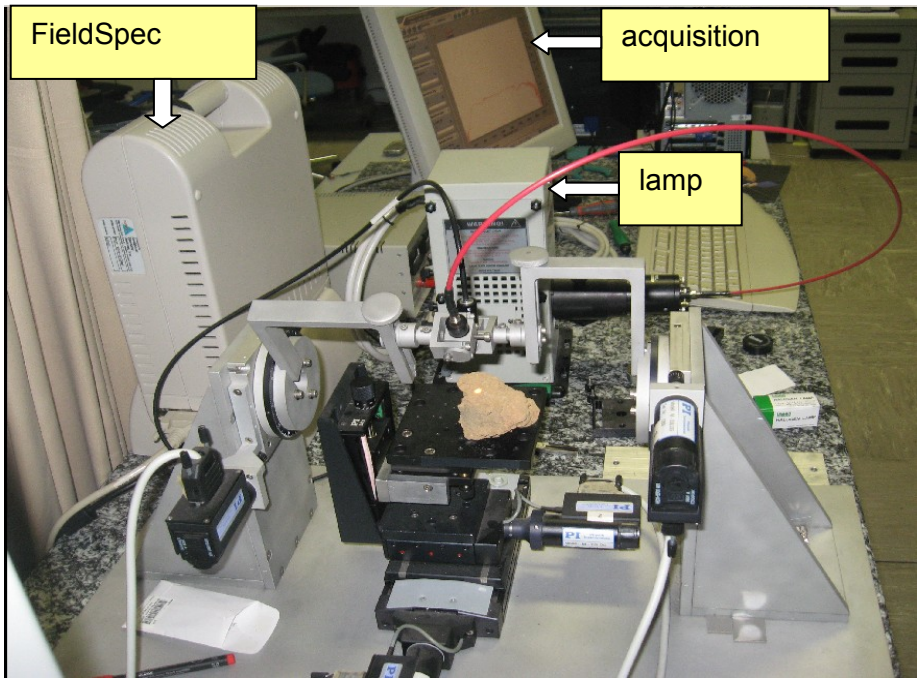

Figure 5.3 spectroscopy set-up: FieldSpec and goniometry; courtesy PLab INAF.

The reflectance spectra of the three samples acquired on test sites point M, F and P, were acquired on bulk rock for sample F and on powdered for samples M and F.

Test site id	Sample raw	60 micron
Teide (point F)	x	x
Teide (Point M)		x
Teide (Point P)		x

Table 5.4 list of Teide samples measured in Plab laboratory INAF for which also chemical analysis were implemented.

The sample F has been used in its original commission , no sample cutting, polishing was realized. The reflectance spectra acquired for the three samples are plotted in the following figures.

M.na Majua: Point F

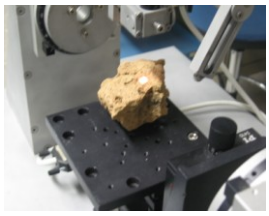

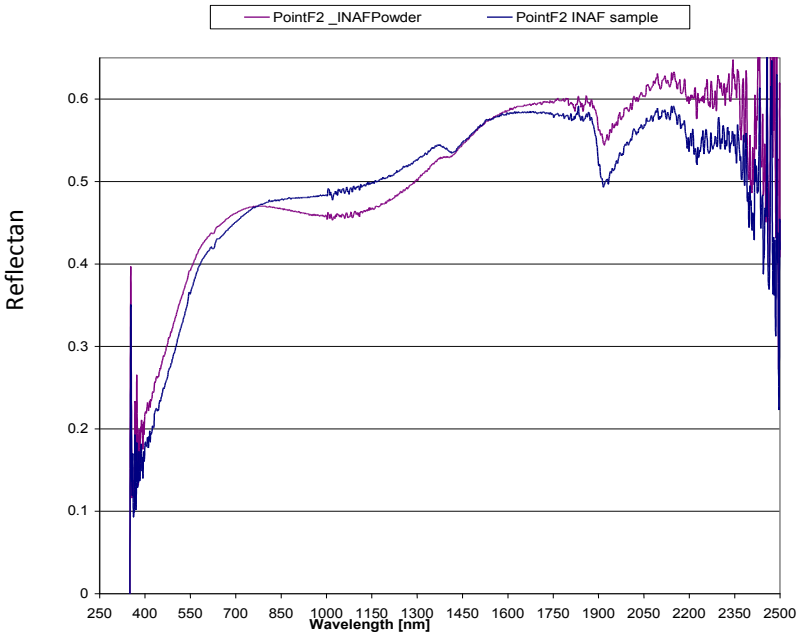

Figure 5.4 Teide point F, raw sample and <60 micron measured at Plab INAF, in Rome.

We can note that in the powdered spectrum the feldspar Fe absorption band intensity is higher than in the rock sample due to scattering effects.

El Piton: Point P

Tephra and oxidiane N 28° 15’ 19’’.9 E 16° 37 19’’.7 the data is quite noisy at the last part of spectrum between 2050-2500 nm.

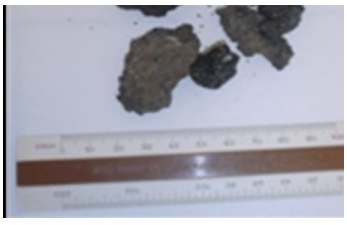

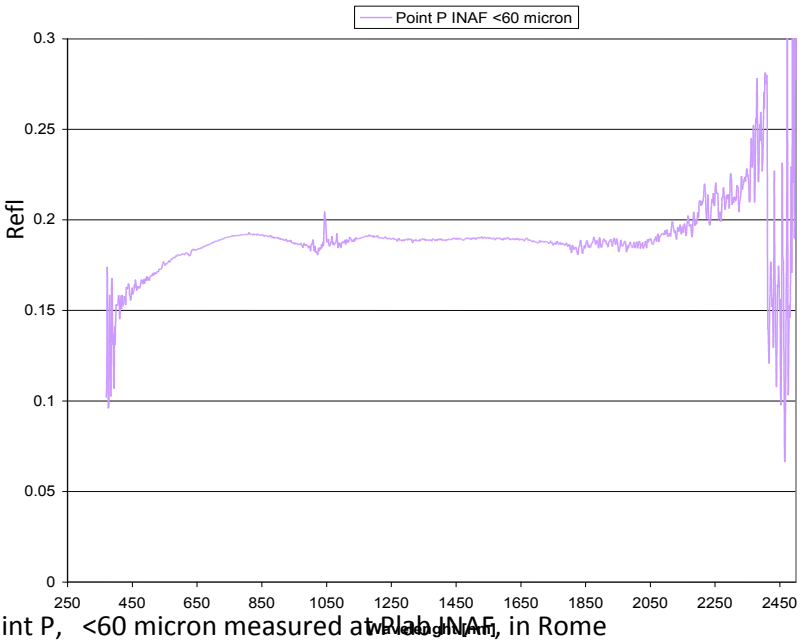

Figure 5.5 Teide point P, <60 micron measured at Plab INAF, in Rome

Teide Mna Majua Point M

The reflectance of sample from M.n Mjua test site powederd at 60µm is showed

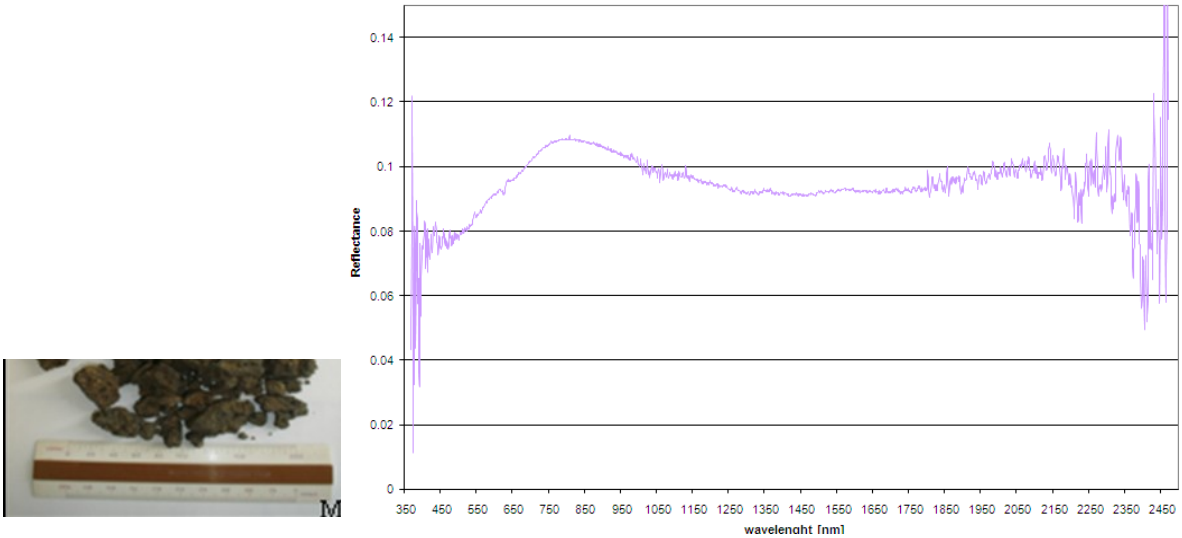

Figure 5.6 Teide point M, raw sample and <60 µm measured at Plab INAF, in Rome.

The standard deviation values at the beginning until 550 and in the last part the most noisy it spans from 0.04 to 0.0055 in the range 350nm to 500nm and 0.004 to 0.1 from 1700nm to 2450. The good signal exhibits a standard deviation ranging from 0.004-0.0005 in the central part of the spectrum.

6 Results and discussion

The most important aim of the campaign on Volcano Teide consisted in identifying a test site for calibration and validation of remote sensed data. The volcano Teide, being characterised by fumaroles activities (only in the summit crater) and not recent eruptions, seems to be a good candidate to find an area quite huge, flat, and homogenous, that maintains the same features in time and can be used as reference test site.

A second aim regarded the calibration of satellite remote sensed data and the validation of the models applied to retrieve reflectance and emissivity. The satellite reflectance satellite data has been retrieved by using the CIRILLO code (Teggi S. 2005, Musacchio et al.2007). This code has been used to calibrate the data and local atmospheric profiles has been apply for atmospheric correction. The use of local important factor because volcano Teide is placed in a subtropical area the use of middle summer atmospheric (standard) profile may be not adequate to describe the local atmospheric conditions. In order to validate the models, in field measurements have been compared with the corresponding satellite retrieved data.

The satellite emissivity data by ASTER sensor has been retrieved by using CIRILLO and TES code (ASI-SRV) and local atmospheric correction was applied. The results have been compared with ASTER emissivity standard product and in situ measurements.

A significant dataset of reflectance and emissivity in field measurements has been realized. It represents a unique spectral library for volcano Teide. No other in field measurements of this kind has been still realized. Different lithology sites have been spectrally characterised (reflectance and emissivity) on lava flows of different ages and represent different classes (end-members) for volcano Teide spectral library.

In this section the results obtained for the calibration test site are showed. Based on this results the inter-comparison between in field and satellite data are further showed and discussed in order to validate the calibration process.

Differences and/or agreement of the results are discussed for the different test sites taking into account the percentage error evaluated as follow:

$$Percentage_{error} = [(Measure - Reference)/Reference] * 100$$

Where *Measure*, is the Hyperion reflectance or ASTER emissivity and *Reference* is the corresponding in situ ground truth measurement: FieldSpec and FTIR respectively.

6.1 Satellite data validation

6.2.1 Liano de Ucanca (Point O): a validation test site

The **Liano the Ucanca** (N 28° 12’ 46.9’’, E 16° 38’10.0’’, **Point O**) is a flat area located in the southeast part of the Las Canadas Caldera (LCC) (Figure 6.1) of 1.8 km length and 0.75 km width. Llano de Ucanca is constituted by colluvium deposit recent in age (Ablay, Martì 2002). The site is smooth, flat and spectrally homogenous with little to no vegetation. The area presents some brushes spread not regularly on the surface so in situ spectra were acquired on surface and brushes respectively.

Figure 6.1 LIano De Ucanca test site as seen by Hyperion and Google Earth.

Hyperion data acquired on November 13rd 2003 with 30m/px and ASTER (August 4 2007 11:53GMT) with15m/px and 30m/p on VIS and SWIR bands respectively were analysed. The satellite data reflectance was retrieved by using CIRILLO procedure and local atmospheric profile (for ASTER data). The comparison between in situ measurement and Hyperion is showed in the following figure.

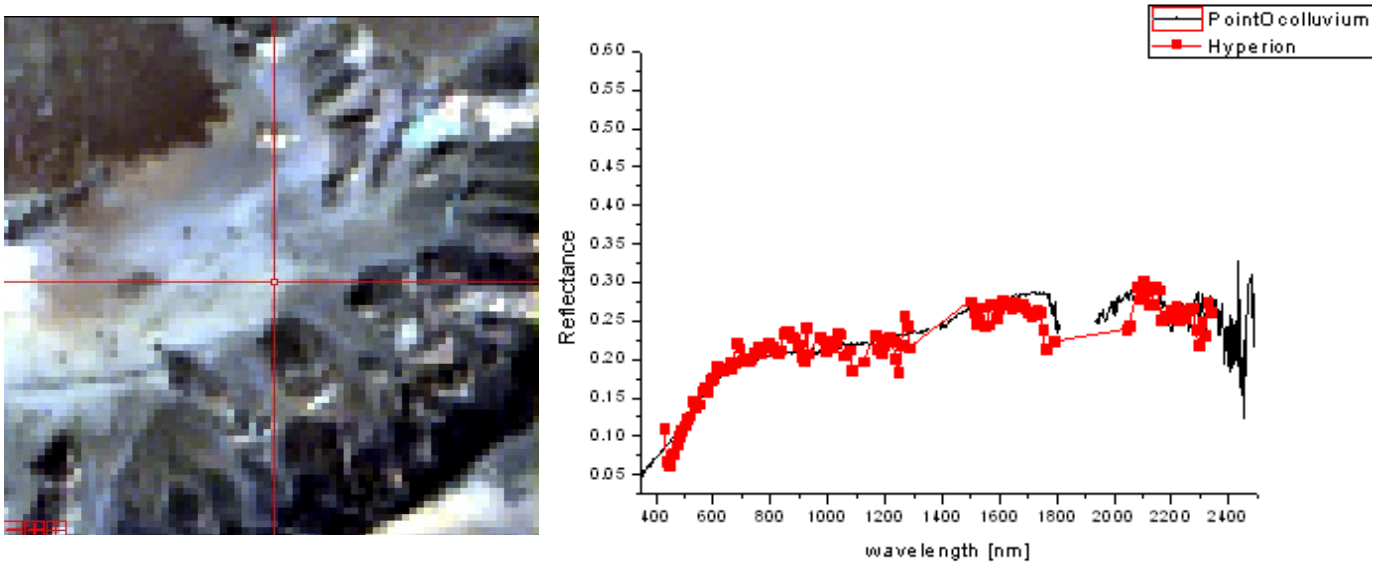

Figure 6.1 Liano de Ucanca by Hyperion (Point O N 28°12' 46.9'' 16° 38' 0.9''): reflectance comparison between Hyperion and in situ truth.

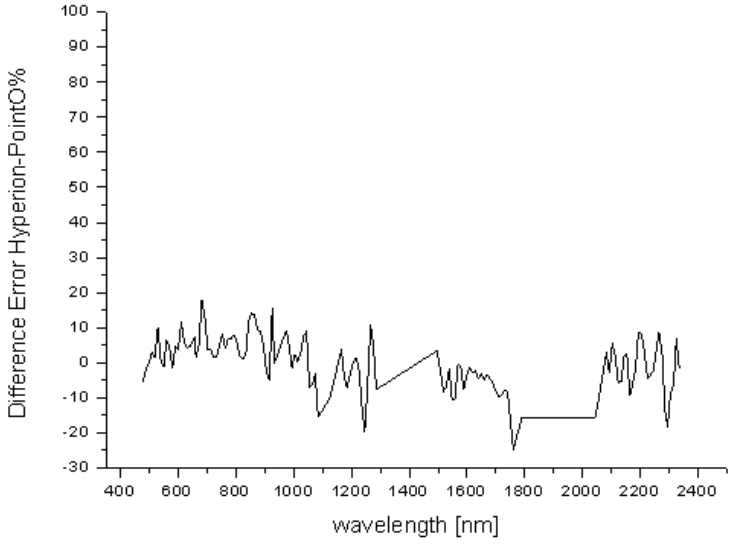

Figure 6.2 percentage error between Hyperion and in situ truth.

The comparison between Hyperion and in situ truth shows a good agreement. The maximum differences between the two spectra are 20% in few bands this means an 80% agreement in the worst case. In the range between 400-900nm the mean variation is about 5-8%.

The comparison between in situ measurement and ASTER is showed in the following figure.

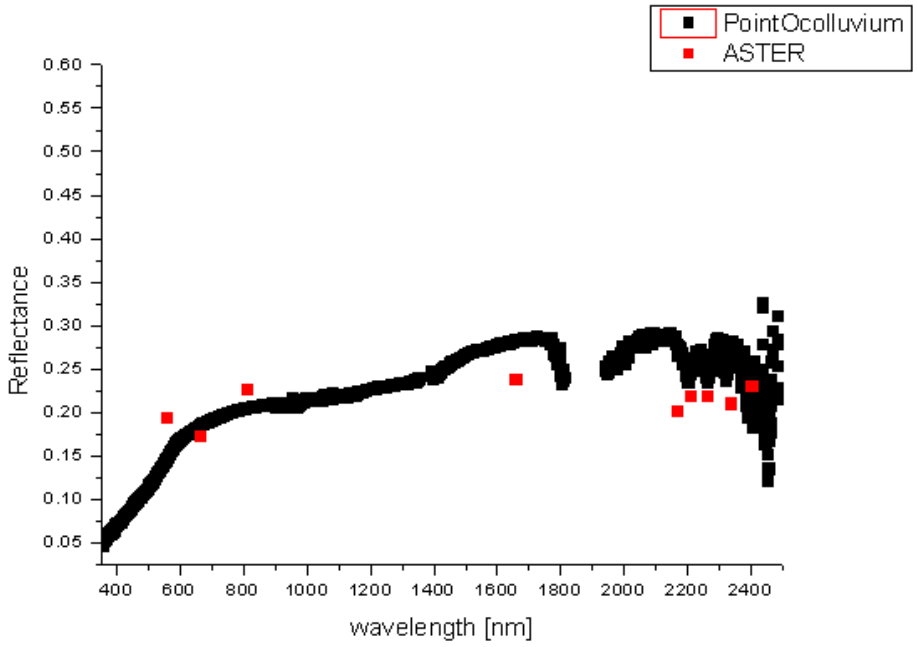

Figure 6.3 Reflectance comparison between ASTER and in situ truth in llaiano de Ucanca.

ASTER bands [mn]	ASTER Error%
556	30.5
661	-6.27
807	10.3
1656	-12.45
2167	-24.25
2209	-11.34
2262	-8.0
2336	-23.8
2400	19.0

Table 6.1 difference percentage error between ground truth and ASTER (VIS_NIR.)

As regards ASTER results the comparison shows differences between ground truth and ASTER data ranging from a minimum of 6% and a maximum of 24%. This means that in the worst case (at 2167nm) the agreement is 76%.

Because it is under evaluation the "goodness" of LIano de Ucanca as validation test site also the comparison with emissivity ground truth is done. The whole analysis of thermal range is done in section 6.3.1 ASTER night data (September 17 2007 23:16) has been corrected by using local atmospheric profile. Since the ASTER pixel resolution in IR spectral range is equal to 90m, we can have pixel mixing. To take into account of this effect, in situ emissivities were acquired on colluviums surface and brushes. ASTER emissivities from AST05 (standard product) and from that one retrieved by TES plus local atmospheric profile were compared with in situ data. A linear combination of 60% surface and 40% brushes agrees with ASTER emissivities in the corresponding geolocated area (see figure 6.4).

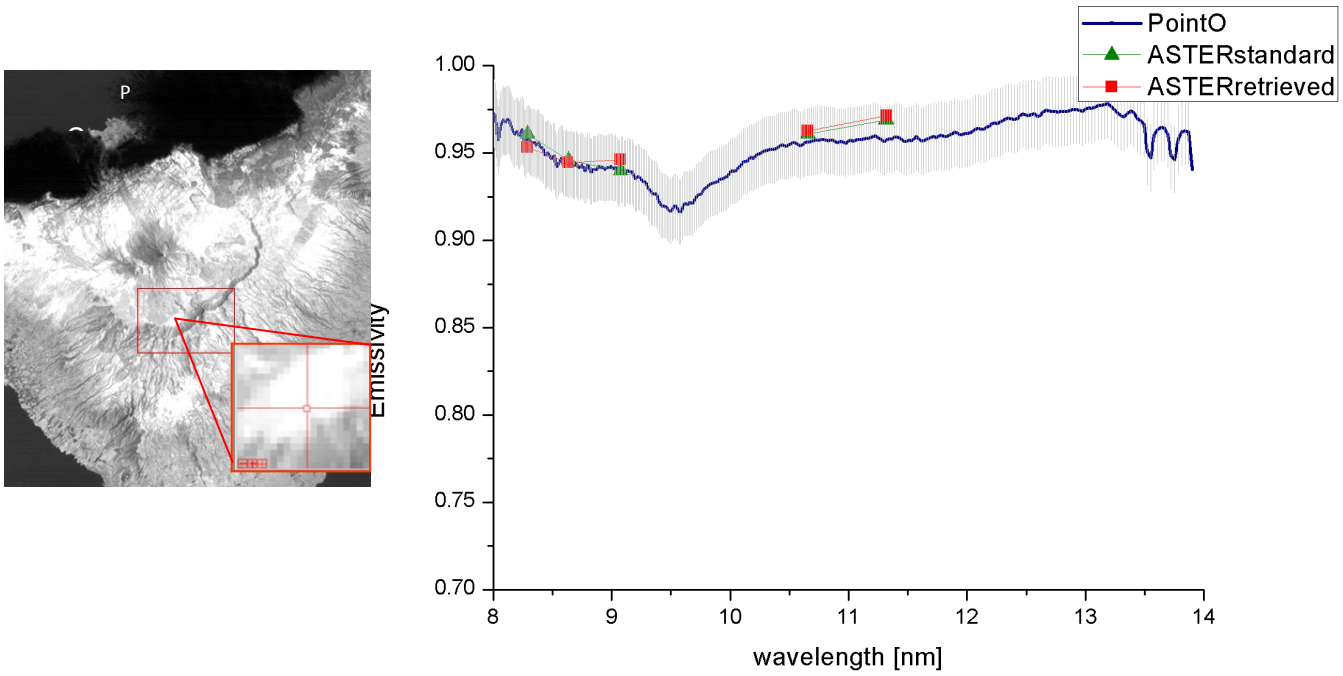

Figure 6.4 Point O N 28°12' 46.9''E 16° 38' 0.9''. The plots show the comparison between ASTER (AST05 and retrieved emissivity) and in situ emissivity linear combination (60%surface and 40%brush).

It is possible to verify a very good agreement between standard and atmospheric corrected data and the validation in situ measurement; in this case no topographic effect are present and the percentage difference between standard and retrieved data exhibits a maximum value of 1% and 2% respectively in correspondence of band 11.13micron.

ASTER bands [micron]	ASTER- AST05 Error %	ASTER- TESError%
8.29	0.3	0.5
8.63	0.2	0.15
9.08	0.1	0.7
10.65	0.5	0.6
11.13	1	2

Table 6.2 difference percentage error between ground truth and ASTER (AST05 and ASTER retrieved) emissivity.

The obtained results validate the models used to calibrate both Hyperion and ASTER data and Liano de Ucanca test site may be considered a good validation test site.

6.2 . VNIR range data discussion

In the following sections the validation of reflectance data and the comparison between in situ and ASTER Hyperion data are analysed. For each data test sites classification done by Ablay.Martì 2002 and Carracedo 2006 is considered.

6.2.1 Comparison of in situ reflectance with Hyperion and ASTER

As showed on figure 6.4 the Hyperion swath cover the central part of Volcano Teide. As described previously, the left and right side of the volcano surface were acquired but the data were clouds covered. Only the central part of the volcano has been studied. The comparison between in situ and satellite data is possible for a subset of ground truth sites (within the red dotted line in figure 6.5) and will discussed separately.

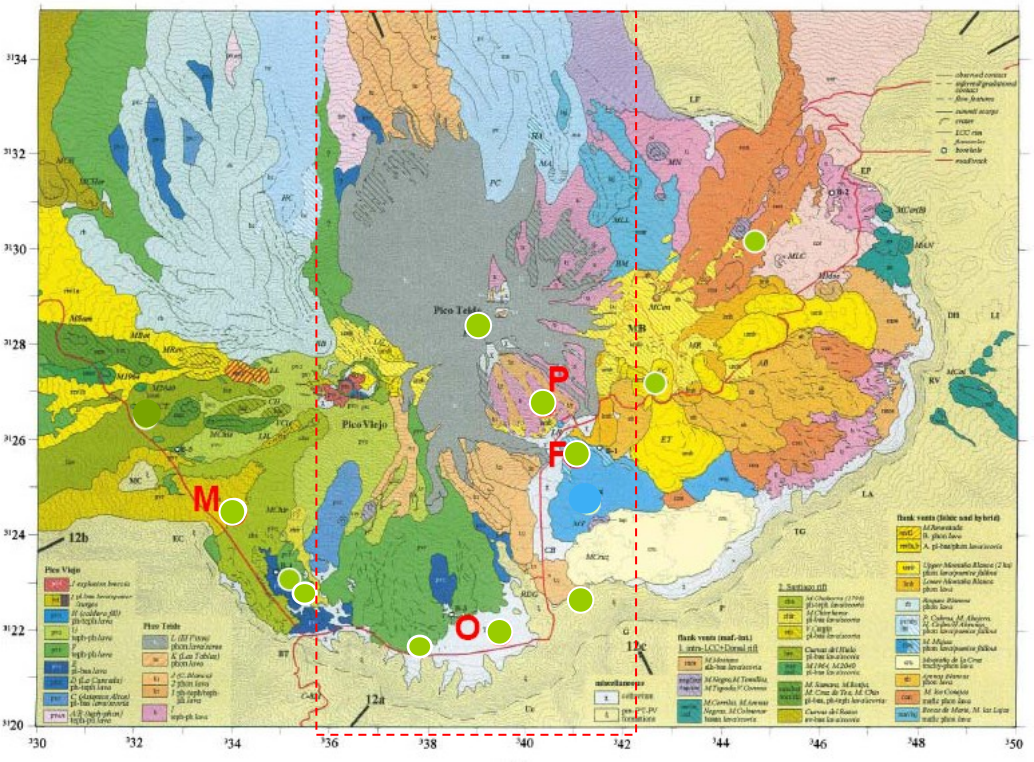

Figure 6.5 Location of the measured ground truth are located on the geological classification map (Ablay and Martì; the red dotted line represents the Hyperion swath.

6.2.2 Volcano Teide summit crater Point Z

The Pico Teide summit crater (about 95m diameter) is characterised by three different geologic units (surge and splatter deposits of dissected scoriae and thepra phonolite lava member according Ablay and Martì classification.

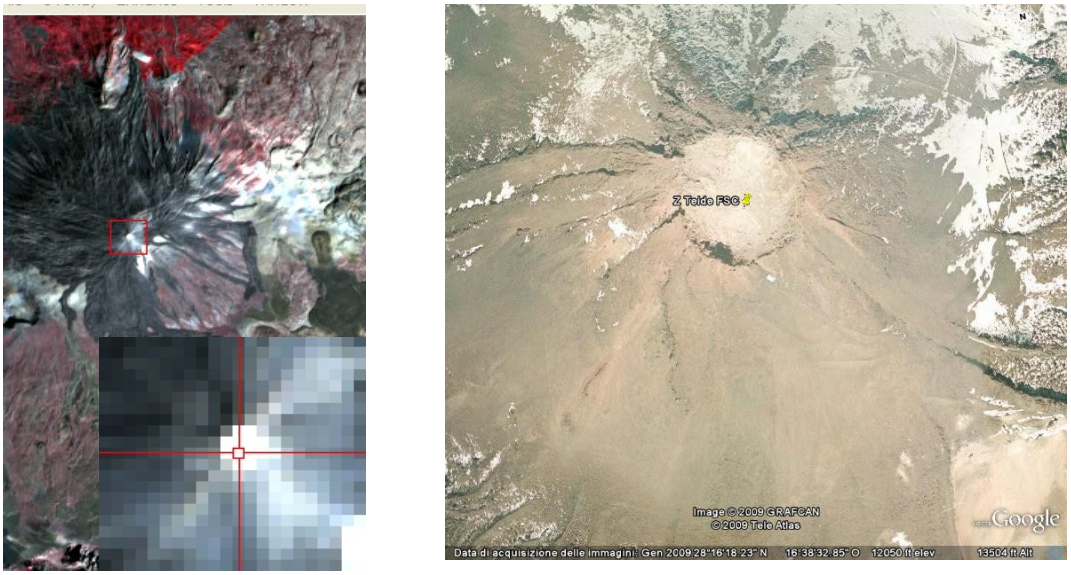

Figure 6.6 ASTER and Google view of Volcano Teide summit crater

A linear combination of the three classes in field measured classes (89%Z0 fumaroles, 10% of Z1 alterated rock argil type, Z2 1%amorphic sulphate) is compared with the Hyperion and ASTER spectrum. Since the Hyperion SNR is very low an average over 4 pixels has been realized and the standard deviation has been calculated. We can note a good agreement between ground truth and both Hyperion and ASTER reflectance.

The result points out the importance of ground truth spectral library especially in the case of non homogeneous surfaces within the spatial resolution of a satellite sensor. In case of spectral mixing the spectra of different components allow to use convolution routine to find the best fit with the spectra acquired by satellite and to interpret the composition.

The Teide summit crater as seen by Hyperion and ASTER pixel is an example of spectral mixing. By using in situ measurements a good agreement between the spectra is achieved.

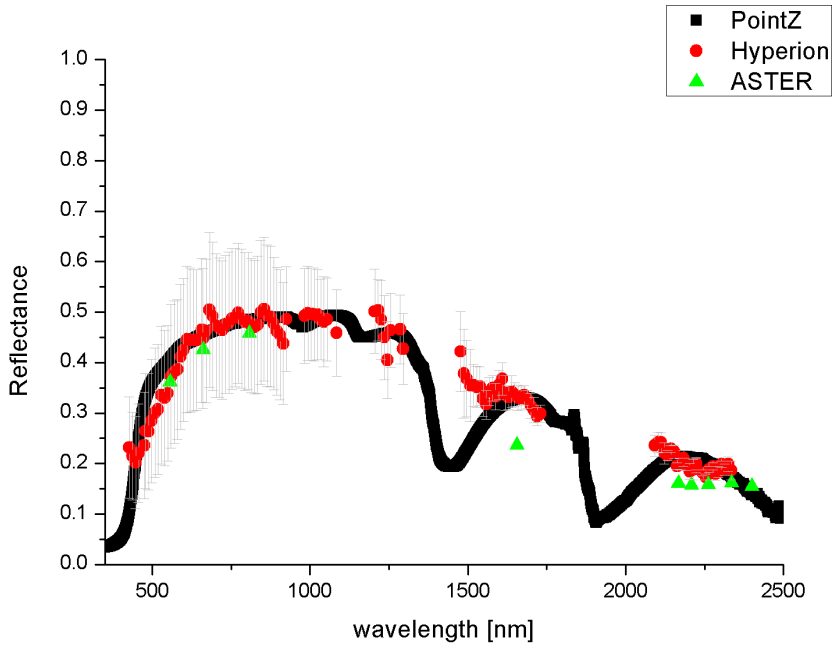

Figure 6.7 Volcano Teide summit crater reflectance (linear combination of Z0,Z1 and Z2) compared with Hyperion and ASTER reflectance.

6.2.3 Mna Majua test site Point F

Mna Majua is a test site being part of the Nord East rift about 4000-4200 years. the measurement have been done in the north homogenous area (about 300mx438m) of Mna Majua (figure 6.8)

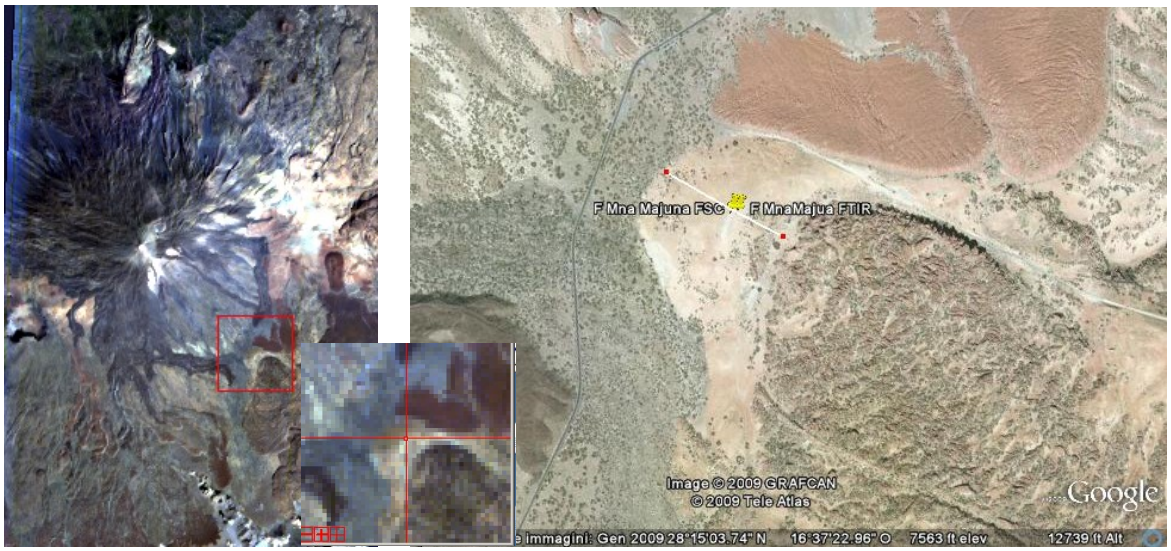

Figure 6.8 Hyperion image and Google view of the Mna Majua (in situ ground truth location).

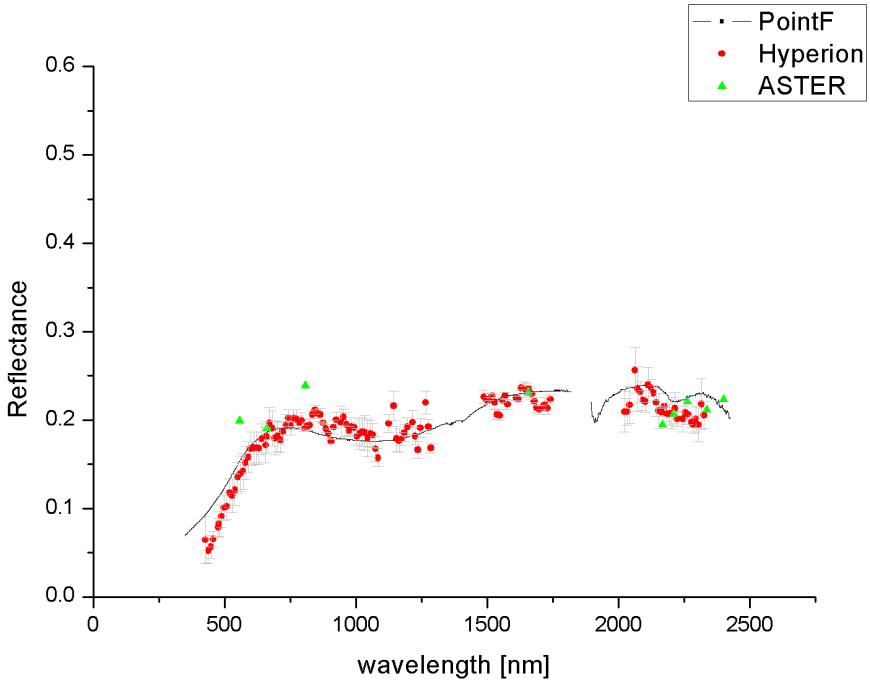

Figure 6.9 Point F, Mt Majua in situ reflectance compared with ASTER and Hyperion values.

A good agreement between the in situ truth and satellite (ASTER and EO1- Hyperion) spectra has been verified. In particular the Hyperion and "in situ truth" spectra fit very well on whole spectral range; differences of some Hyperion bands are probably due to high noise of the instrument in some channels.

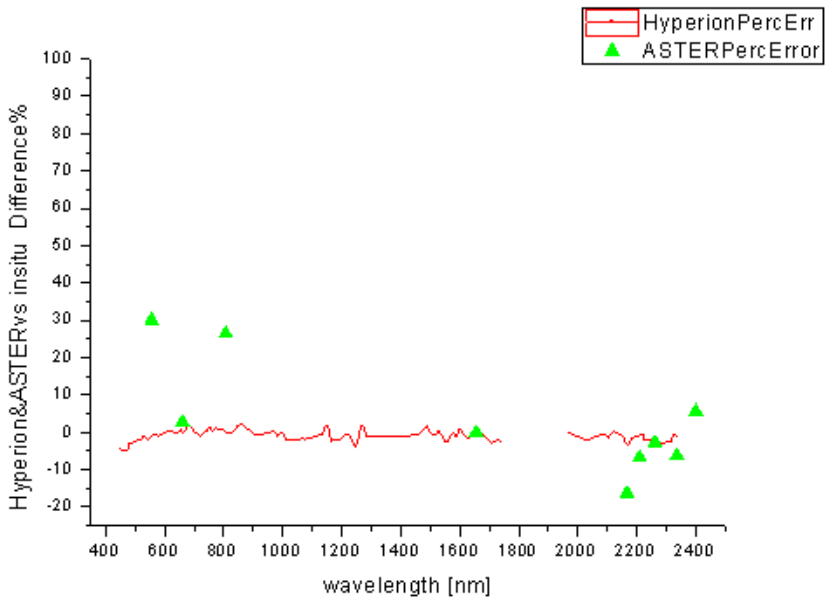

Figure 6.10 Mt Majua percentage difference between satellite (ASTER and Hyperion) and ground truth (reference).

The difference percentage error of Hyperion data with In situ measurement ranges between 0.01/% to a maximum of 3%.

As regards ASTER data, a multispectral sensor, we can note that bands exhibit an error about 2.5% (bands 2, band 4, band 5), band 6 and band 8 have percentage differences with ground truth of 6% a maximum of 30%. behaves better that other. The high differences values are for band 1 band3 and band 5 with a percentage difference of 30%, 26% and 16% respectively.

6.2.4 El Piton test site Point P

El Piton tested area is part of the Teide in the border of Mna Blanca 2000years, close to the eruption 1150years.

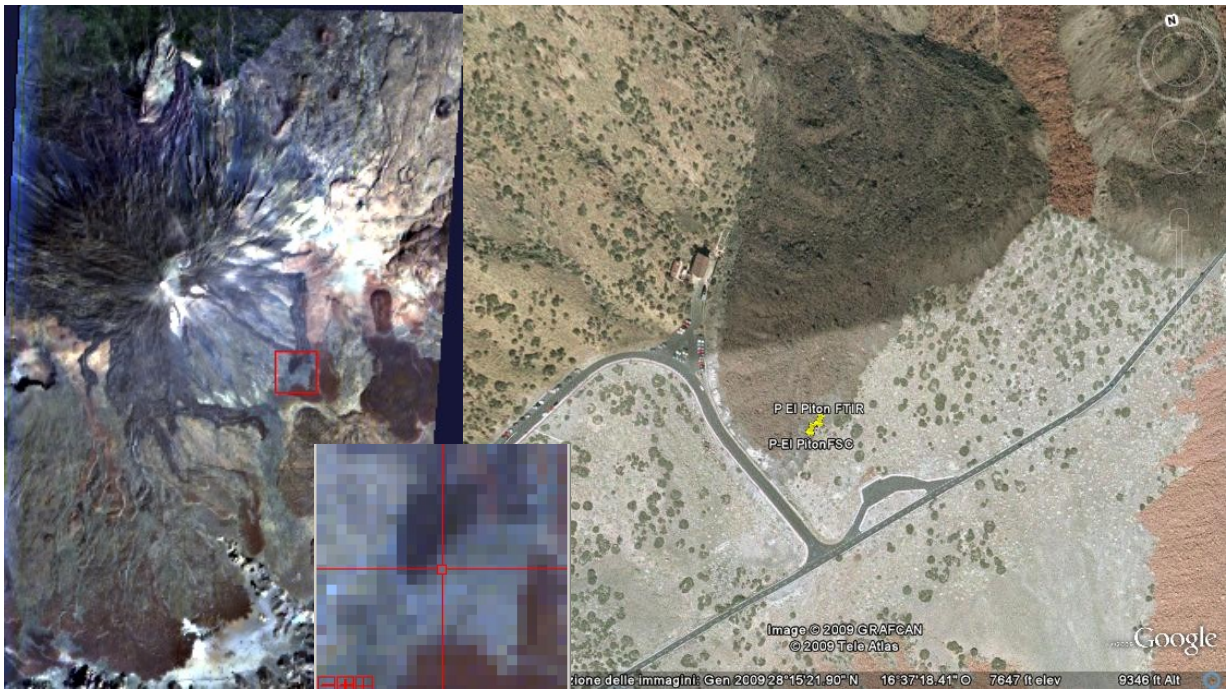

Figure 6.11 Hyperion and Google pixel in correspondence of the El Piton on ground truth.

The comparison between the ins situ reflectance acquired on El Piton area and the corresponding Hyperion and ASTER reflectance is showed in figure 6.12.

The FIELDSPEC measurement (reference) is compared with Hyperion and ASTER spectra.

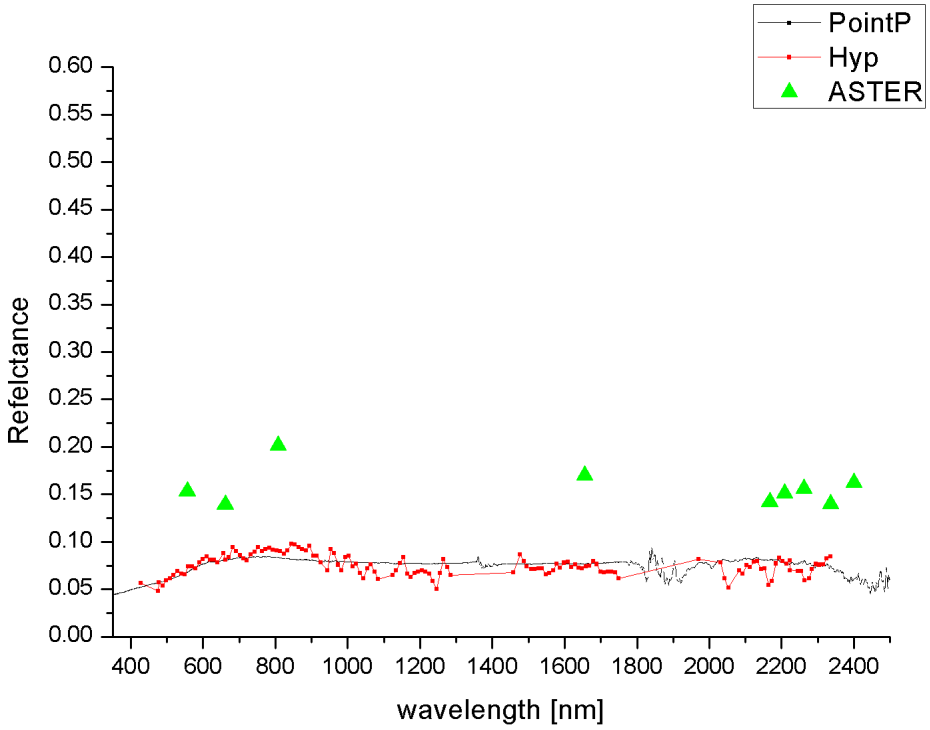

Figure 6.12 Point P, El Piton in situ reflectance compared with ASTER and Hyperion values.

The spectral shape by Hyperion is in good agreement with the ground truth respect ASTER. A reason for this may be effect of adiacency pixel.

The different percetage error for Hyperion is plotted in the following figure (Figure 6.13).

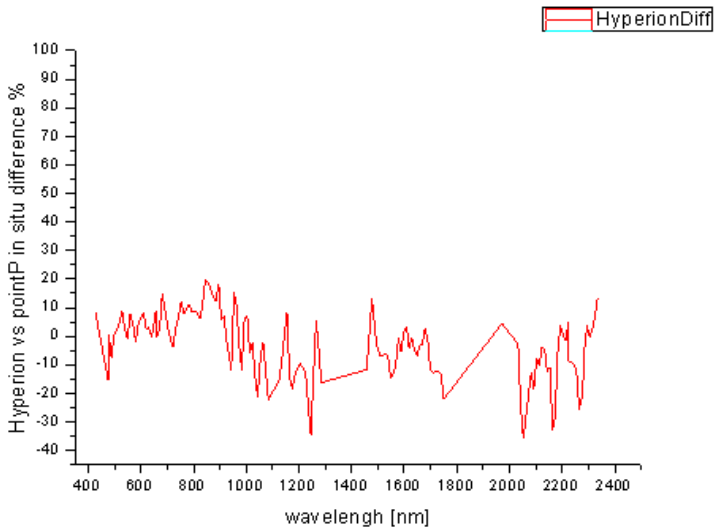

Figure 6.13 El Piton test site Hyperion minimum difference percentage ranges from 0.4% to 10% in the first part of the spectrum (between 350-950 nm). Some bands shows differences of 12-15% probably due to high noise values for that bands.

The overall comparison between in situ and remote sensed reflectance spectra has showed a good agreement. In particular, Hyperion sensor, which exhibiting in VIS-NIR range more bands than ASTER, shows a good capacity to reproduce the shape of the spectra and the spectroscopic features.

We can conclude that both Hyperion and ASTER provide data useful for scientific and operational applications.

6.3 IR range data discussion

6.3.1 Comparison of in-field emissivity with ASTER

Emissivity was extracted from thermal radiance ASTER data using the TES algorithm. A map of emissivity at ASTER in R= band 13, G=band 12 B=band 11 of the Teide and Pico Veio area is showed. The decorrelation stretching has been applied in order to distinguish different surface behaviour.

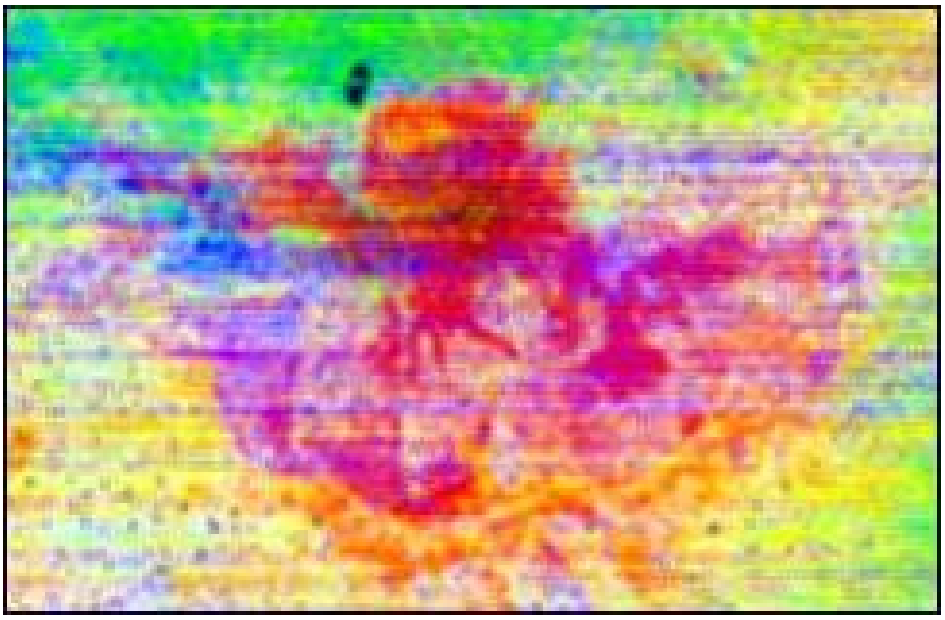

Figure 6.14 emissivity map of ASTER band after decorrelation stretching.

The emissivity profiles obtained by retrieving emissivity in the five ASTER TIR bands are compared with in field measurements (reference) and the results are discussed for each test sites.

6.3.2 Mna Majua:point F

We can note that ASTER retrieved and standard emissivity are in good agreement in the 10- 14µm spectral range. The retrieved emissivity shows a better agreement with in situ data between 8 -9 µm and follows the spectral shape.

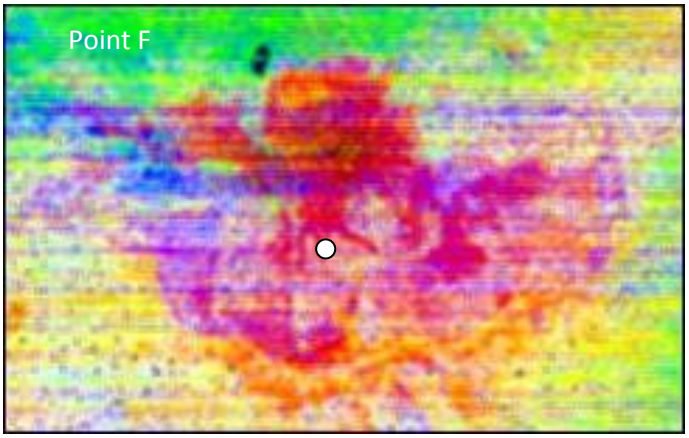

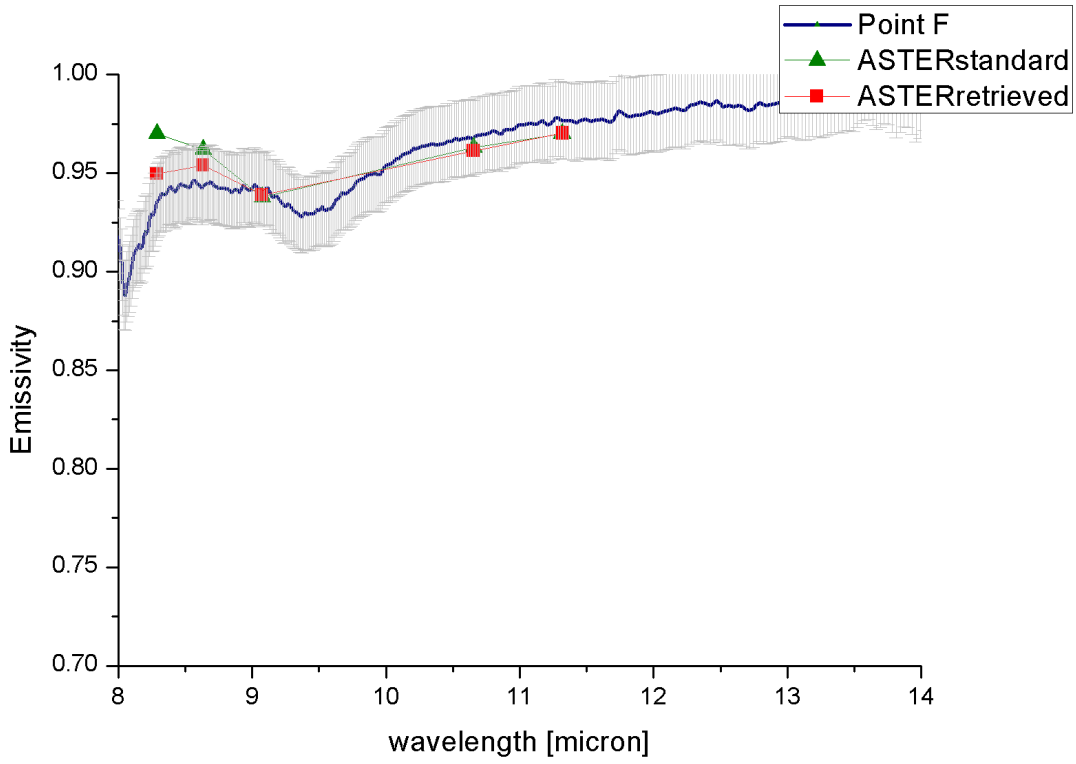

Figure 6.15 in situ emissivity Point F comparisons with ASTER standard and retrieved.

The percentage differences between the ASTER standard and ASTER TES is summarised in the following table. It is possible to note the good agreement of both data. A small percentage error is in the first two bands of TES retrieved emissivity.

ASTER bands [micron]	ASTER standard Error %	ASTER TES Error %
8.29	5.0	3.0
8.63	2.0	1.0
9.08	-0.4	0.3
10.65	-0.4	0.6
11.13	-0.7	0.7

Table 6.2 Percentage error between ASTER and in situ emissivity on M.na Majua test site.

6.3.3 Lava negra 1798: Point L

The comparison in this case confirms a good agreement in spectral shape of both ASTER standard and ASTER TES in the range 10- 14µm. A better fit of retrieved data between 8 -9 µm is also confirmed by the percentage error.

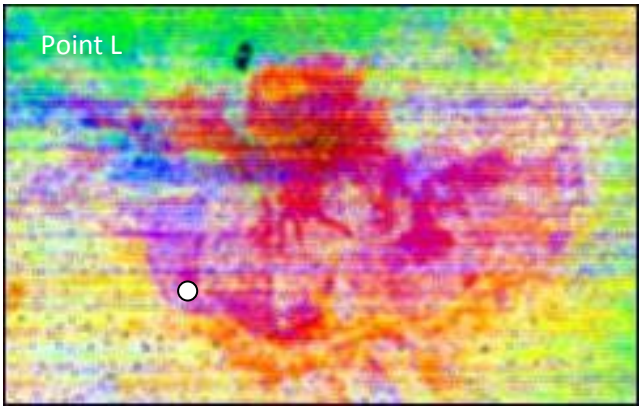

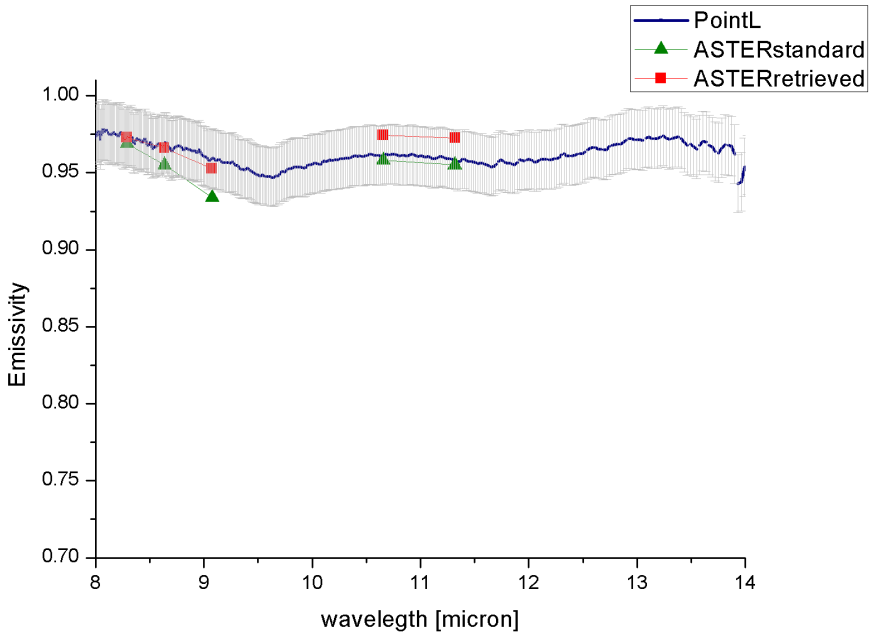

Figure 6.16 In situ emissivity Lava Negra test site is compared with ASTER standard and retrieved.

ASTER bands [micron]	ASTER standard Error%	ASTER TES Error%
8.29	-0.3	0.02
8.62	-1.0	-0.2
9.08	-7.0	-0.6
10.65	-0.3	1.0
11.13	-0.3	1.0

Table 6.3 Percentage error between ASTER (standard and TES) and in situ emissivity on Lava Negra test site.

Also in this case, a better shape agreement of ASTER TES vs in situ data is noticed in the spectral range 8-9µm.

6.3.4 Montana Mostaza: Point U

In this test site, the two ASTER data are in agreement in the 10-14 µm; a difference in the shape of spectrum a is showed in 8 -9 µm .

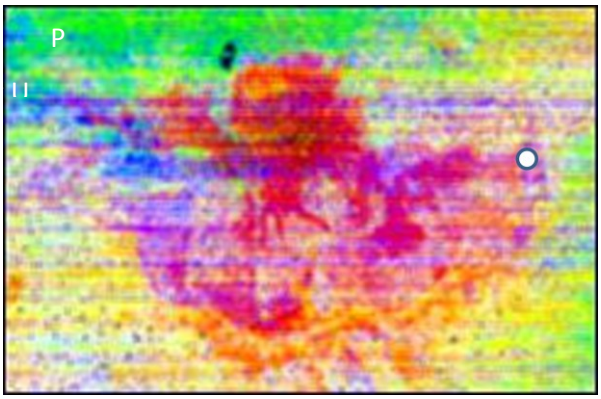

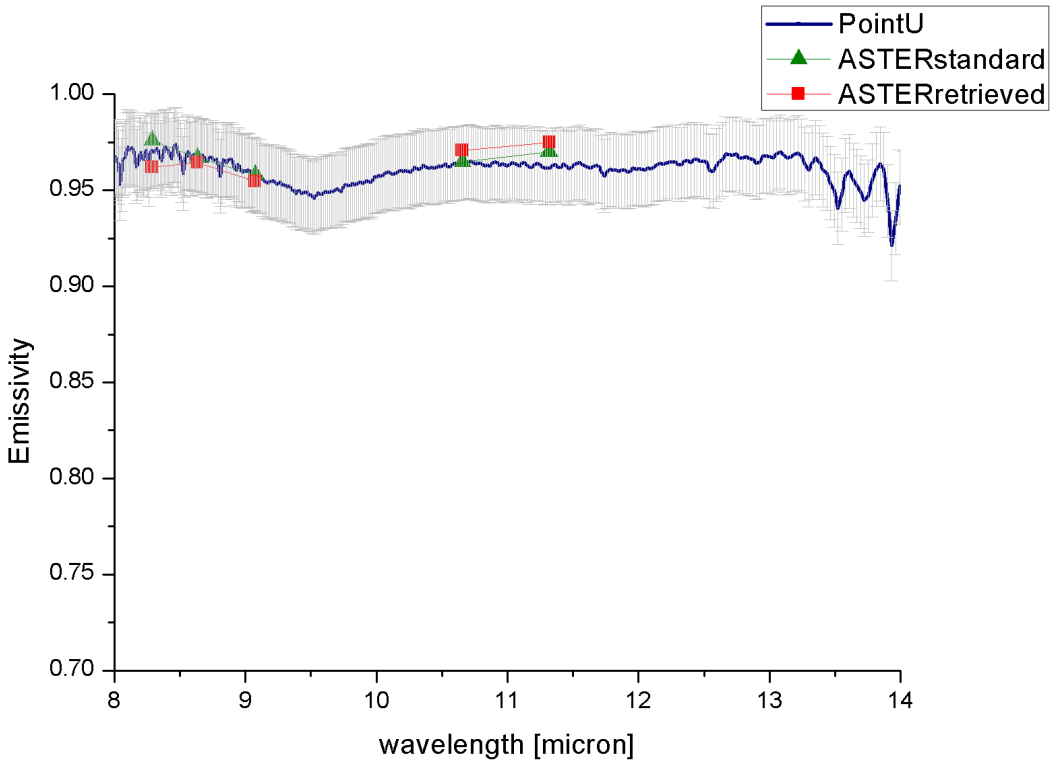

Figure 6.17 ASTER TIR band 11=8.6 um; in situ emissivity Point U comparison with ASTER standard and retrieved.

ASTER bands [micron]	ASTERstandard Error %	ASTER TES Error %
8.291	-0.8	-0.6
8.634	-0.1	-0.003
9.075	.-0.05	-0.3
10.657	-0.6	1.0
11.318	0.8	1.0

Table 6.4 Percentage differences among ASTER (standard and TES) and in situ emissivity on M.na Mostaza.

6.3.5 El Piton: Point P

In this point the two ASTER data are in agreement in the 10-14 µm; a difference in the shape of spectrum a is showed in 8 -9 µm.

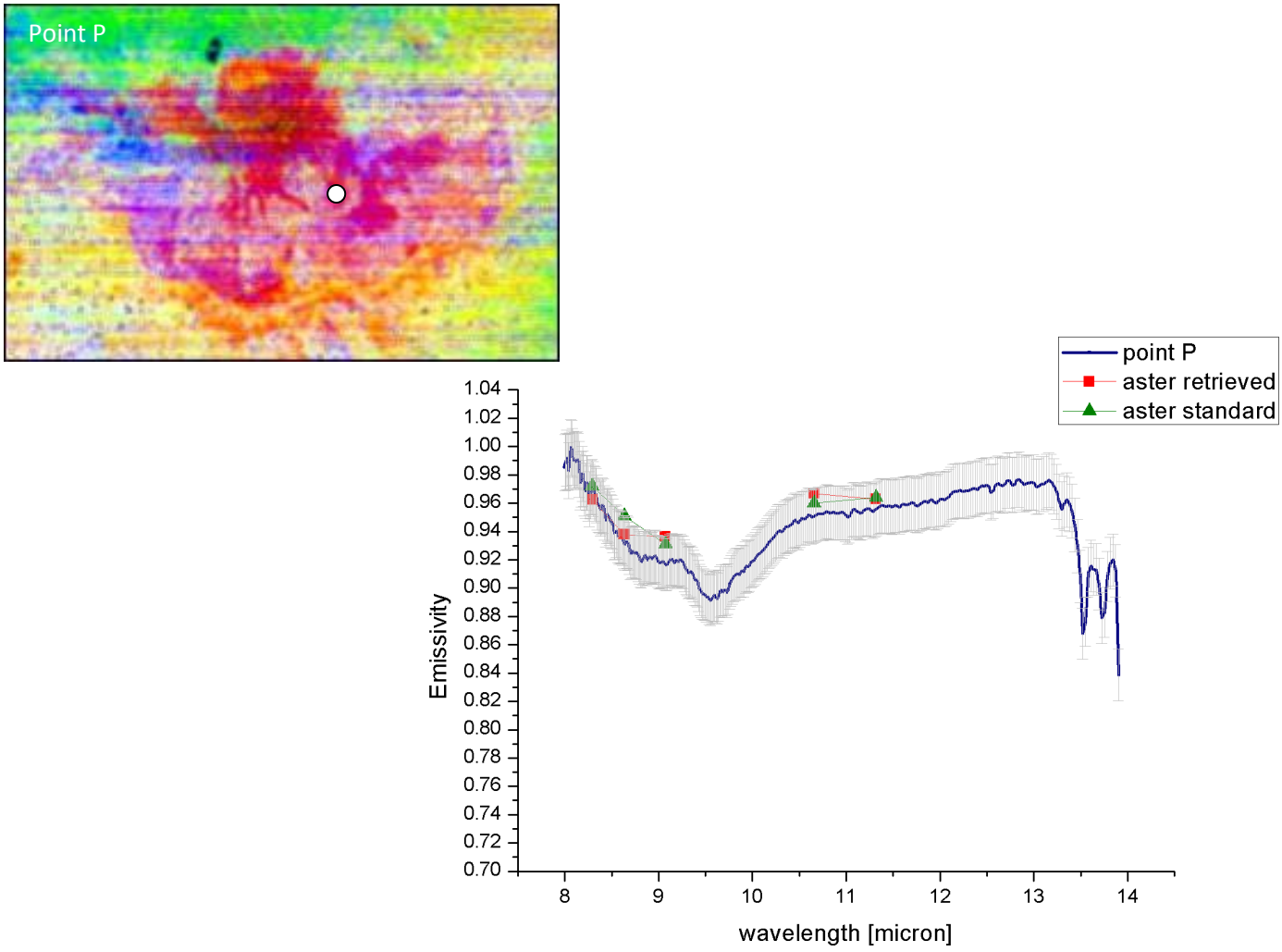

Figure 6.18 ASTER TIR band 11=8.6 um; in situ emissivity Point P comparison with ASTER standard and retrieved .

ASTER bands [micron]	ASTER Standard Error%	ASTER TES Error %
8.291	0.06	-0.9
8.634	2.0	0.6
9.075	1.5	2.0
10.657	1.0	2.0
11.318	0.8	0.7

Table 6.5 percentage differences among ASTER (standard and TES) and in situ emissivity on El Piton.

6.3.6 M. Chaorra: Point M

In this point there is a good agreement of retrieved and standard data which differ from the in situ in the 8-9 8 -9 µm. A possible explanation is that the in situ data was measured near a different type. The ASTER pixel may be a mixing of two different rock type. By magnifying the image, the pixel seems confirm this hypothesis..

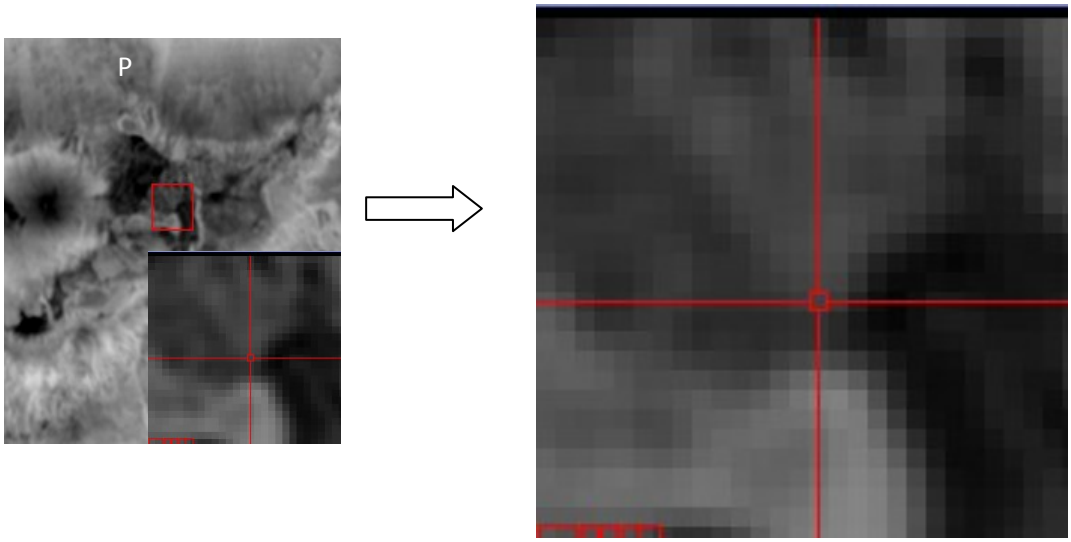

Figure 6.19 ASTER night 90mresolution image centered in the M Chaorra area shows the interested pixel between two difference surfaces type.

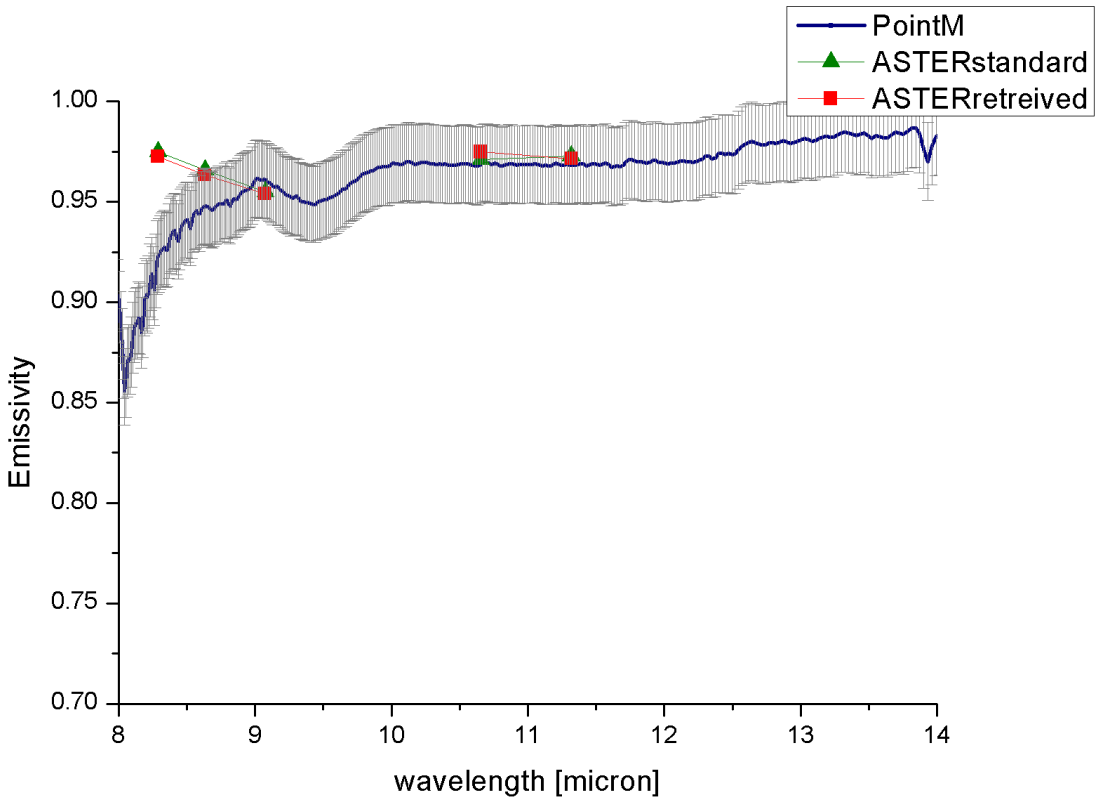

Figure 6.20 ASTER TIR band 11=8.6 um; in situ emissivity Point M comparison with ASTER standard and retrieved

The emissivity comparison between in situ and remote sensed retrieved data have showed as the Atmospheric compensation made with local profile affects the spectral shape of the emissivity in the range 8-9µm.

The discrepancy in the shape of emissivity values in the first three band may be interpreted as pixel mixture of two different surface components. It is quite clear also magnifying the ASTER image as shown in figure 6.19

ASTER bands [micron]	ASTER Standard Error%	ASTER TES Error%
8.291	6.0	5.0
8.634	2.0	2.0
9.075	-0.6	-0.7
10.657	0.3	0.7
11.318	0.5	0.3

Table 6.6 Percentage differences among ASTER (standard and TES) and in situ emissivity(reference) on M. Chaorra.

6.3.7 Point N

The emissivities measured in point N show quite good agreement

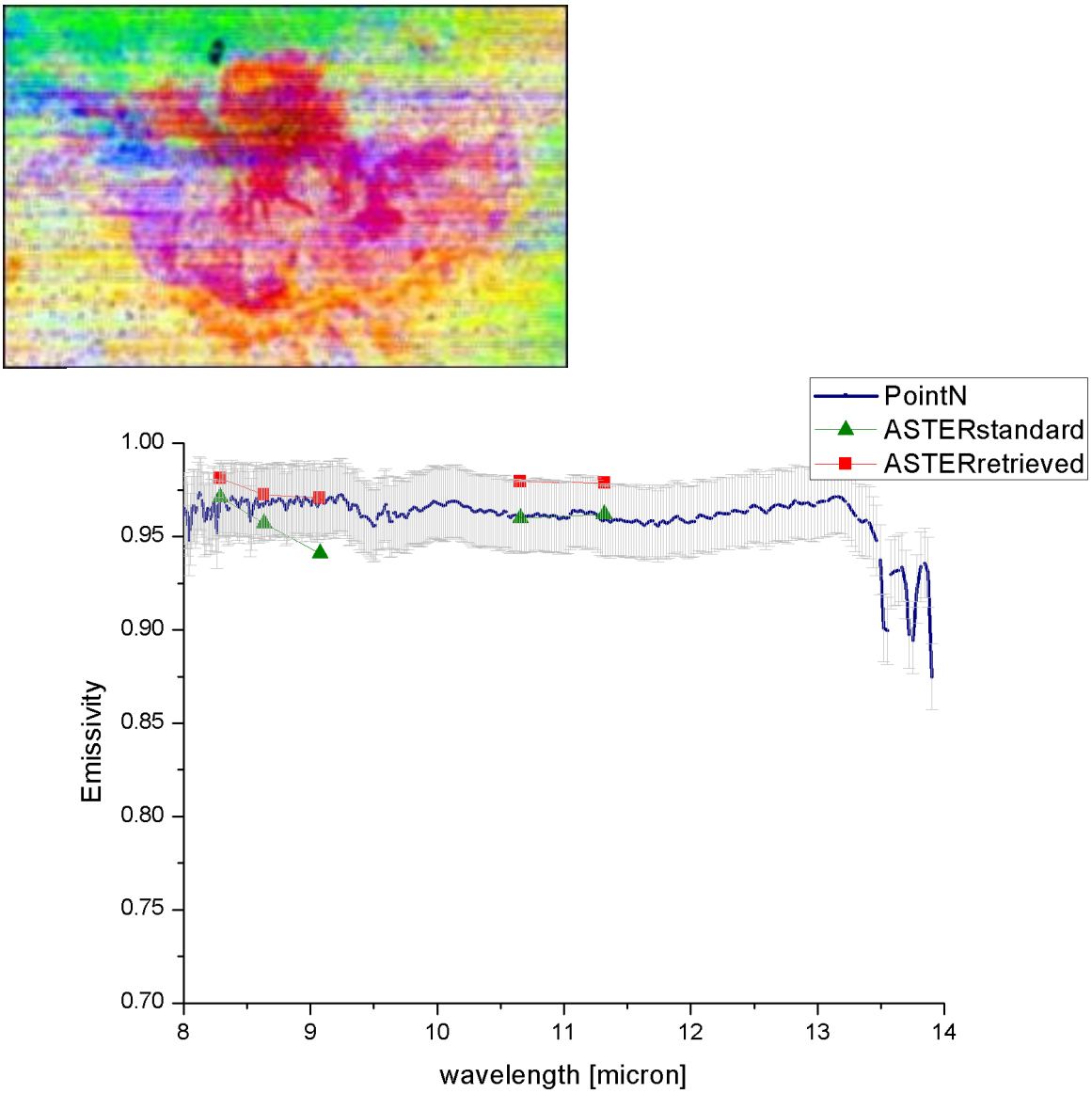

Figure 6.21 ASTER TIR band 11=8.6 um; in situ emissivity Point N

ASTER bands [micron]	ASTER standard Error%	ASTER TES Error %
8.291	-0.08	1.0
8.634	-1.0	0.6
9.075	-3.0	0.3
10.657	-0.04	2.0
11.318	0.4	2.0

Table 6.7 Percentage differences among satellite and in situ emissivity

6.3.8 Boca Tauce : Point S

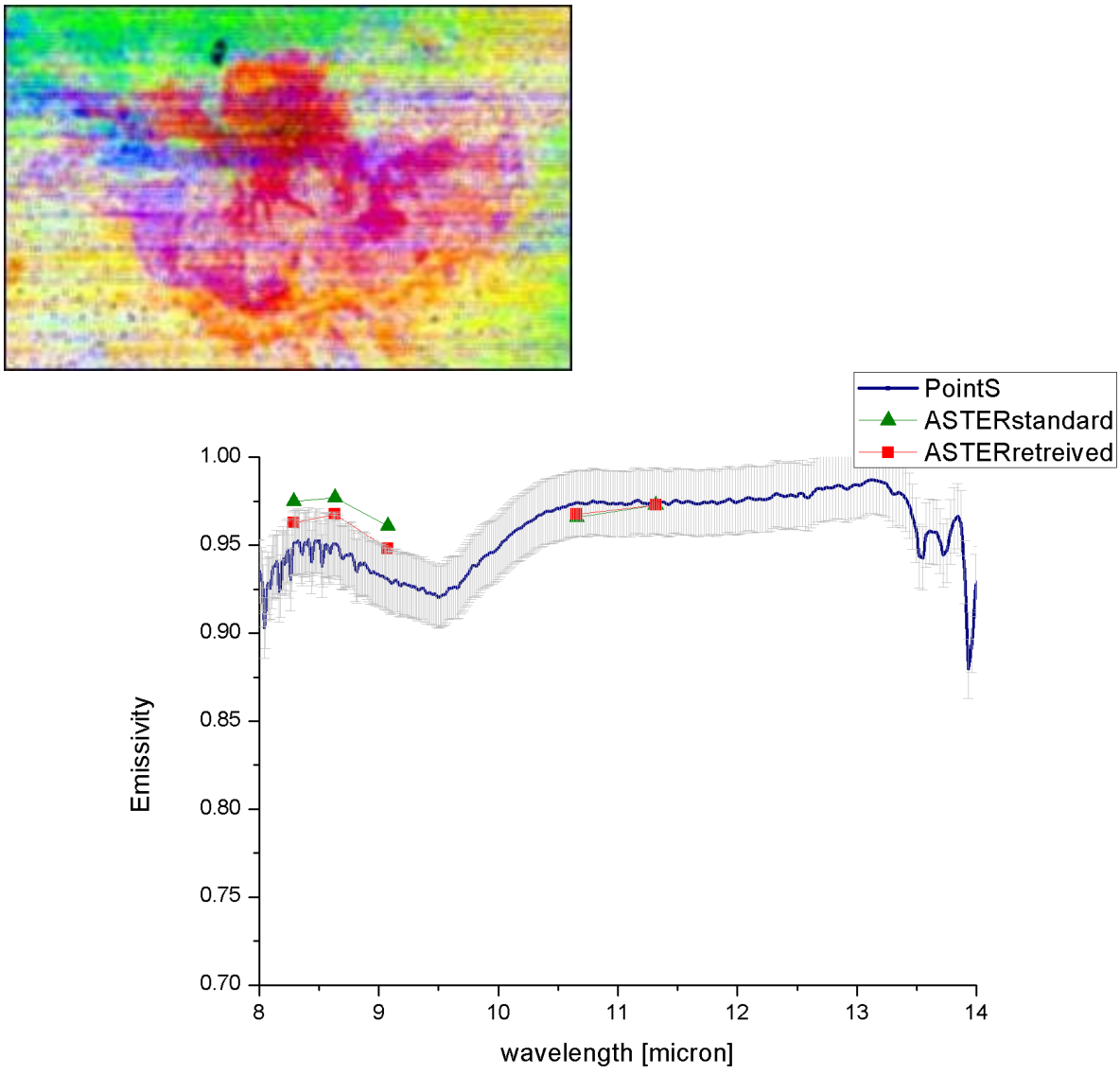

Figure 6.22 ASTER TIR band 11=8.6 um; in situ emissivity Point S.

ASTER bands [micron]	ASTER standard Error%	ASTER TES Error %
8.291	3.0	1.0
8.634	2.0	1.0
9.075	3.0	2.0
10.657	-0.8	-0.8
11.318	-0.2	-0.2

Table 6.8 Percentage differences among ASTER (standard and TES) and in situ emissivity on Boca Tauce.

The emissivity spectra were generally consistent both for AST05 and TES+local profile with the ground data. An improvement in shape was noticed in TES+local profile corrected spectra in the range 8-9µm respect to AST05. This is probably due to the highest absorption values of water vapour at 8.6µm. A standard seasonal atmospheric profile as used in AST05 is surely good for the spectral range (10-14 µm) where the effects of water vapour absorption are minor (in fact AST05 and ASTER+TES+local profile are both consistent in shape) but may affect the shape of spectra in 8-9µm range. This is relevant for scientists who study SO_2 from volcanic plume: an improvement of 1% in emissivity estimation affects the estimation of SO_2 of 5%.

Further, because these data are dominated by silicate minerals, the greatest amount of variance in emissivity spectra for the study area is contained within the range 8-.10 micron. A better spectral shape reproduction in this range is relevant because may give more accurate information to geologists who want analyze pixel composition. Moreover, Sprague A. (personal communication) emphasizes the importance to refer at maximum instead of minimum features, as regards emissivity; a more accurate spectral shape may be diagnostic also for this kind of analysis.

The emission spectra of different units of the latest volcano Teide Tenerife have been plotted to point out different features.

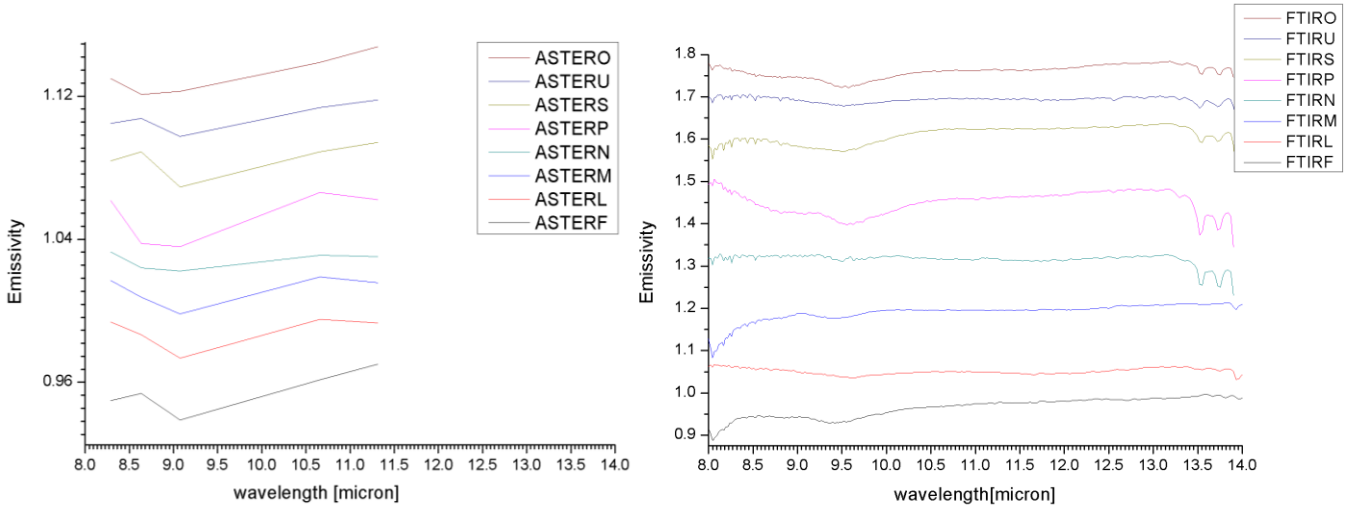

Figure 6.23 Emissivity spectra of different units of volcano Teide –Tenerife island.. Spectra are vertically offset for clarity. The figure shows the variability of the position and shapes of emission features in satellite and in situ measurements.

6.4 Temperature validation

For ASTER over flight during field campaign, radiant temperatures were measured in field (Liano de Ucanca test site using EVEREST radiometer (see section 4.5.2). The temperature acquisitions were made of two transects almost rectangular shape, within the validation site. The temperature of ASTER pixels in correspondence of in situ measured points are resumed on the following table.

Time GMT [h m]	LAT	LON	T in situ mean [°C]	T in situ stdev [°C]	ASTER TES [°C]
21:23	28°12'46"	16°38'09"	7.70	0.10	8.3
21:29	28°12'48"	-16°38'09"	6.36	0.05	7.9
21:33	28°12'50"	-16°38'10"	5.11	0.03	6.7
21:36	28°12'52"	-16°38'10"	5.79	0.03	6
21:39	28°12'55"	-16°38'10"	5.26	0.41	8.3
21:43	28°12'58"	-16°38'11"	4.27	0.49	8.4
21:49	28°13'00"	-16°38'12"	4.97	0.42	5.93
21:54	28°13'00"	-16°38'13"	8.9	0.59	7.5
22:00	28°13'01"	-16°38'14"	4.64	0.57	4.6
22:05	28°13'02"	-16°38'16"	3.4	0.28	4.73
22:08	28°13'02"	-16°38'19"	2.72	0.36	4.65
22:12	28°13'04"	-16°38'22"	2.25	0.49	5.34
22:16	28°13'04"	-16°38'26"	1.94	0.29	4.1
22:20	28°13'04"	-16°38'28"	1.75	0.39	3.1
22:34	28°13'04"	-16°38'30"	2.42	0.32	2
22:32	28°13'03"	-16°38'29"	2.18	0.82	3.1
22:36	28°13'01"	-16°38'21"	2.34	0.28	4.5
22:48	28°12'59	-16°38'28"	1.78	0.37	2.8
22:52	28°12'58"	-16°38'28"	1.05	0.52	2.8
23:00	28°12'56"	16°38'28"	1.02	0.33	2.8
23:11	28°12'53"	-16°38'27"	1.30	0.16	1.6
23:15	28°12'42"	-16°38'16"	2.66	0.28	2.64

Table 6.9 in situ temperatures measured before and during ASTER passage (17/09/2007).

The validation is possible by comparing the situ measurement with the corresponding ASTER data at same time. The mean temperature values (acquired in time progressing) are plotted versus gelocation (lat. and lon.) acquisition point. The corresponding ASTER values (at 11:15pm GMT)are plotted too.

We can note that temperatures form ASTER at 23:15 differs from that one acquired in the corresponding pixels before the satellite passage. There is a good correspondence for the

measurement acquired at the same time(Figure 6.24). The percentage difference is equal to the 0.7%.

This validates the models used to calibrate ASTER data.

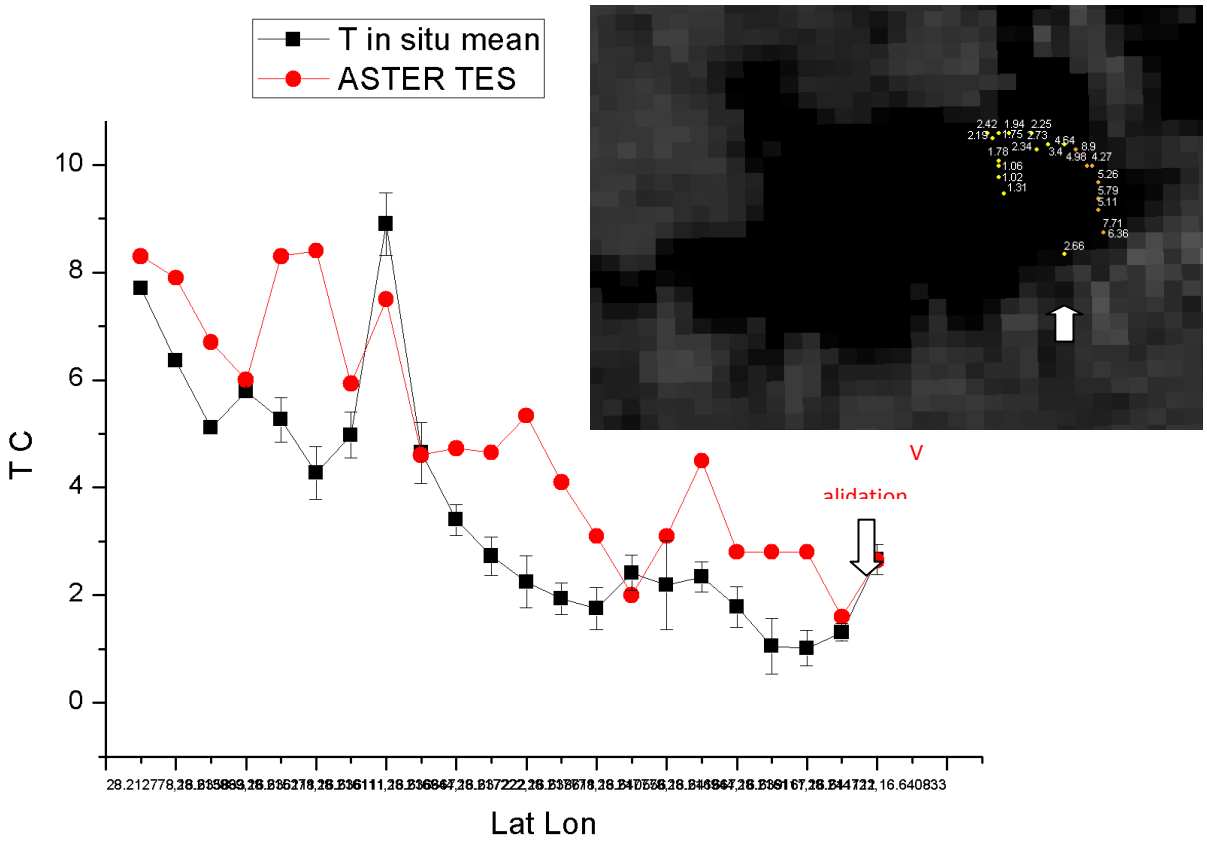

Figure 6.24 Temperature validation: black points represent the mean temperature acquired in situ by EVEREST in each location point, in progressive times, approaching the ASTER passage. The red points are retrieved ASTER temperatures values in correspondence of in situ measurements.

6.5 Map of temperature

By using emissivity map, obtained applying the TES algorithm (Figure 4.17) , the temperature map for the ASTER data acquired on September 17 2007 night passage has been retrieved (Figure 6.25).

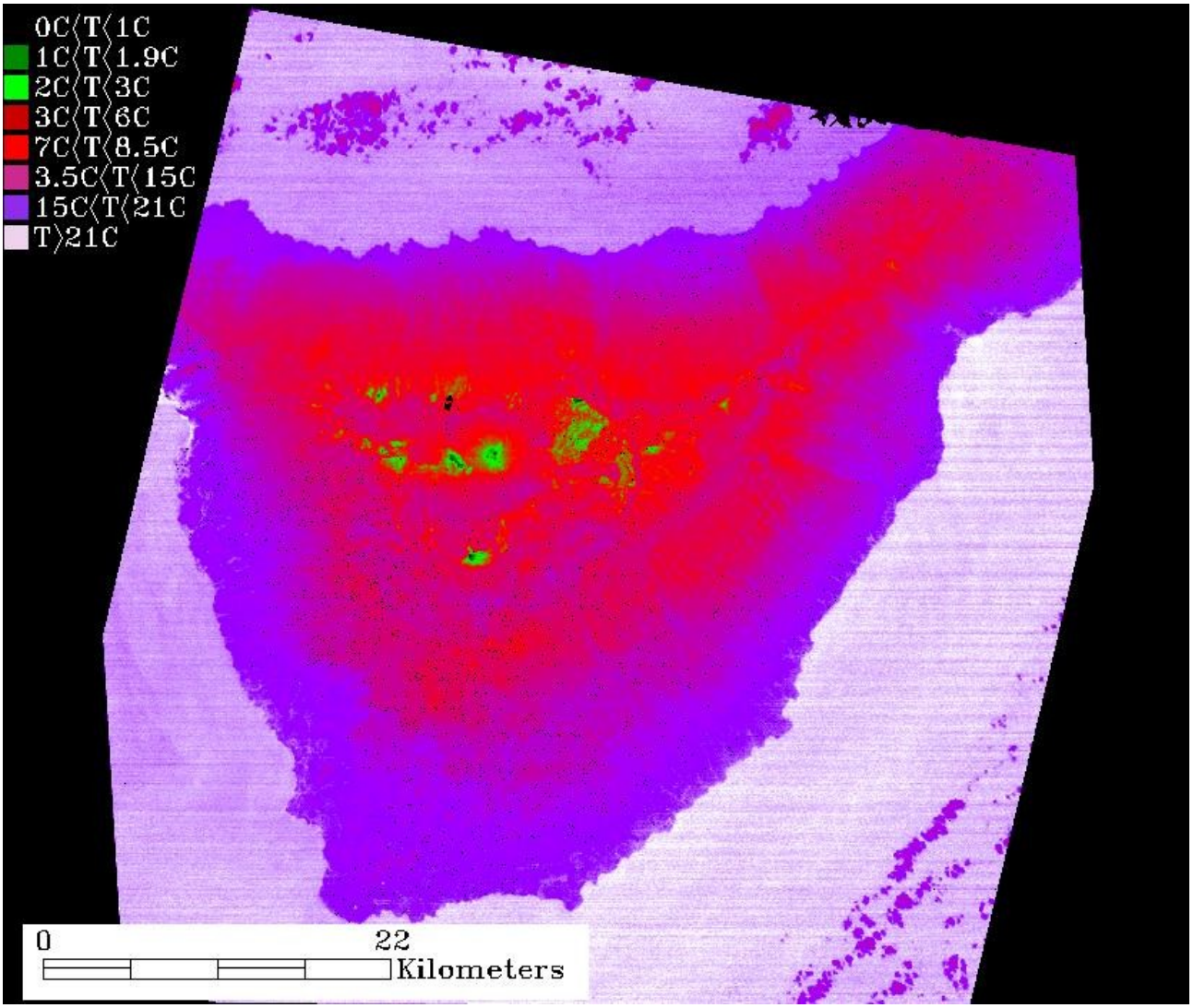

Figure 6.25 map of temperatures retrieved by ASTER night data acquired on 17/09/2007 23:16GMT.

Black and green colours indicate roughly the lower temperature values. If we magnify the top of crater we can note a pick in temperature due to the fumaroles activity (figure 6.26a, 6.26b).

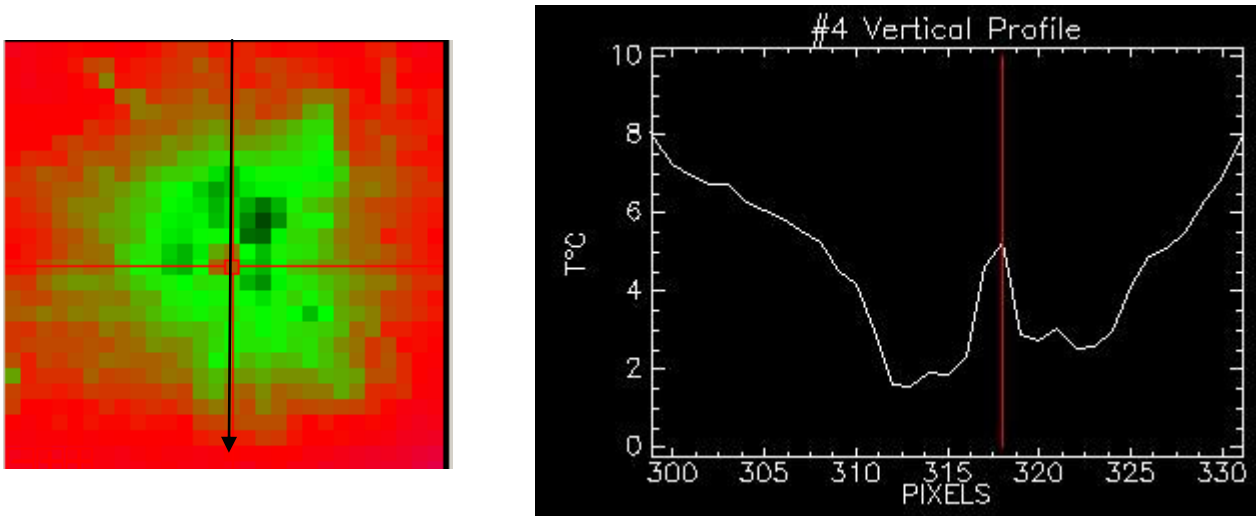

Figure 6.26a the vertical profile of the top volcano area is showed. It is along a distance of 2700 m. Each pixel is 90m. a value of 5C is detected for the warmer crater pixel.

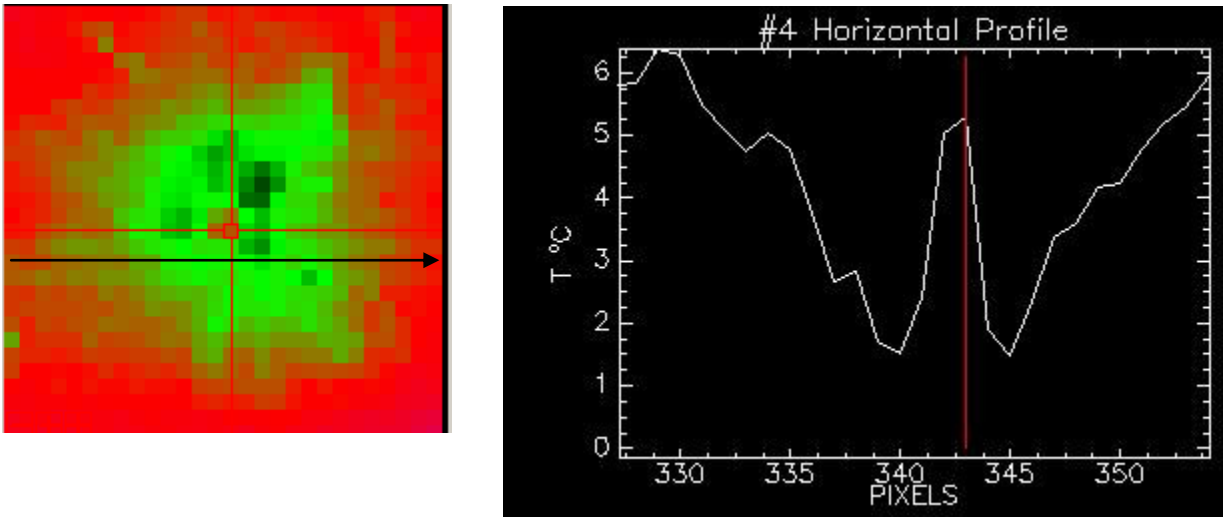

Figure6.26b The horizontal profile of the top of volcano is showed. It is along a distance of ....m . Each pixel is 90m. a value of 5C is detected for the warmer pixel.

6.6 Applications

In geologic and volcanology field of research, the remote sensed data may be used to identify the surfaces according to their lithology, soil coverage, texture and structure (classification).

The reflectance of a pixel (after calibration) is nearest to the reflectance of the geologic target (lithology) as much higher is the geometric resolution of sensor. Surfaces of 30x30m area (e.g. Hyperion or ASTER SWIR) do not reflect homogenously because of alterations and fractures that induce a texture variation. To overpass this question, spectral classification is often made by comparing the pixel reflectance with reference reflectance of minerals, rock and soils. Reference spectra are collected in spectral library and are used to optimize multispectral and hyperspectral data (e.g. ASTER spectral library, ...) analysis. Traditionally, spectra of selected samples (minerals and rocks, Clarks, 1999) are acquired in laboratory. Analysis of laboratory spectra provides a preliminary basis for determining the wavelength regions that show diagnostic spectral features and for determining separability of various materials. by means laboratory measurements is possible to analyze the micro–complexy features of rocks (related to intrinsic features as crystal structures, a grain sizes, different textural patterns) that affect bulk-rock spectral properties . A direct comparison between laboratory spectra and remote sensed spectra is difficult (Laurel E. et al. 2001); spectral library of “in situ truth” measurement (more representative of representative of remote sensed data) are under developing.

6.6.1 Volcano Teide classification

Image classification regards the aspect of image processing in which quantitative decisions are made on the basis of the data present in the image, grouping pixels or regions of the image into classes representing different ground –cover types. The output of the classification stage may be regarded as a thematic map rather than an image. Its accuracy is normally assessed using an error matrix.

Classification techniques can be broadly divided into two types: supervised classification and unsupervised classification. In supervised classification, information about the distribution of ground-cover types in part or parts of the image is used to initiate the process. Pixels or groups of pixels corresponding to known cover types are called training data or training areas and are used to ‘train’ the classification process to recognise other, similar pixels. In unsupervised classification, the entire image is first analysed by clustering to find distinguishable classes of pixels present

within it. After this stage has been completed, the classes present within the image are associated with the classes present on the ground by comparison with training data. In the frame of this work a supervised classification method named Support Vector Machine (SVM) has been used and the results are discussed. As a supervised classifier, the Support Vector Machine (SVM) has been chosen since it provides good results from complex and noisy data. Since it is not in the aim of this work to discuss the theory of the SVM method, only a brief description of the method is given for sake of clarity. The SVM classifier derived from statistical learning theory. It separates the classes with a decision surface that maximizes the margin between the classes. The surface is often called the optimal hyperplane, and the points closest to the hyperplane are called support vectors (Chih-Wei Hsu et al., 2009) The data used in this thesis have been processed by using SVM as implemented on ENVI software. Being a supervised method, a set of 18 classes based on "ground truth" and /or end members has been selected, and part of them have been used in the training phase.

The 18 classes are representative of different geologic units of different age. The attribution of age has been done considering Carracedo (2006) who divides the Teide in three main zones: NOROESTE rift, Pico Vejo and Teide and NORESTE rift. Starting from the 18 classes the corresponding Region Of Interest (ROI) have been chosen. The ROI are region containing pixels belonging the same class. In order to select the training data set, a stratified random sampling (SRS) method has been adopted (Biging.G.S et al, 1998). The classifier performs training at a lower resolution level (by choosing 10% of the pixels in each class) because this produce high accuracy. The evaluation of the goodness of classification has been evaluated by using the confusion matrix that compares the classification results with the ground truth. From the confusion matrix is possible to extract information about the commission (percentage of extra pixel in a class) and omission (percentage of pixel left out of the class) errors for each classes, and they are take in to account for calculate overall accuracy and the K coefficient. The overall accuracy is calculated by summing the number of pixels classified correctly and dividing by the total number of pixels. It represents the measure of omission. The Kappa coefficient is another way to measure the accuracy and it represents the proportion of agreement obtained after removing the proportion of agreement that could be expected to occur by chance. The kappa coefficients are based on a posteriori probabilities of category membership. The SVM has been applied to Hyperion and ASTER data.

6.6.2 Hyperion classification map

The outcome of classification process is a classification map (Figure 6.28). In order to compare the classification map with the geological map (Carracedo J. 2006), the geological map has been projected on Google Earth Teide image (Figure 6.27) and then the classification has been overlapped (Figure 6.28). The comparison between classification map obtained by SVM method on Hyperion data and geological map shows a good correspondence among the classes and the geological units. An overall accuracy of 88.45% and K coefficient of 0.8694 have been achieved (Table 10).

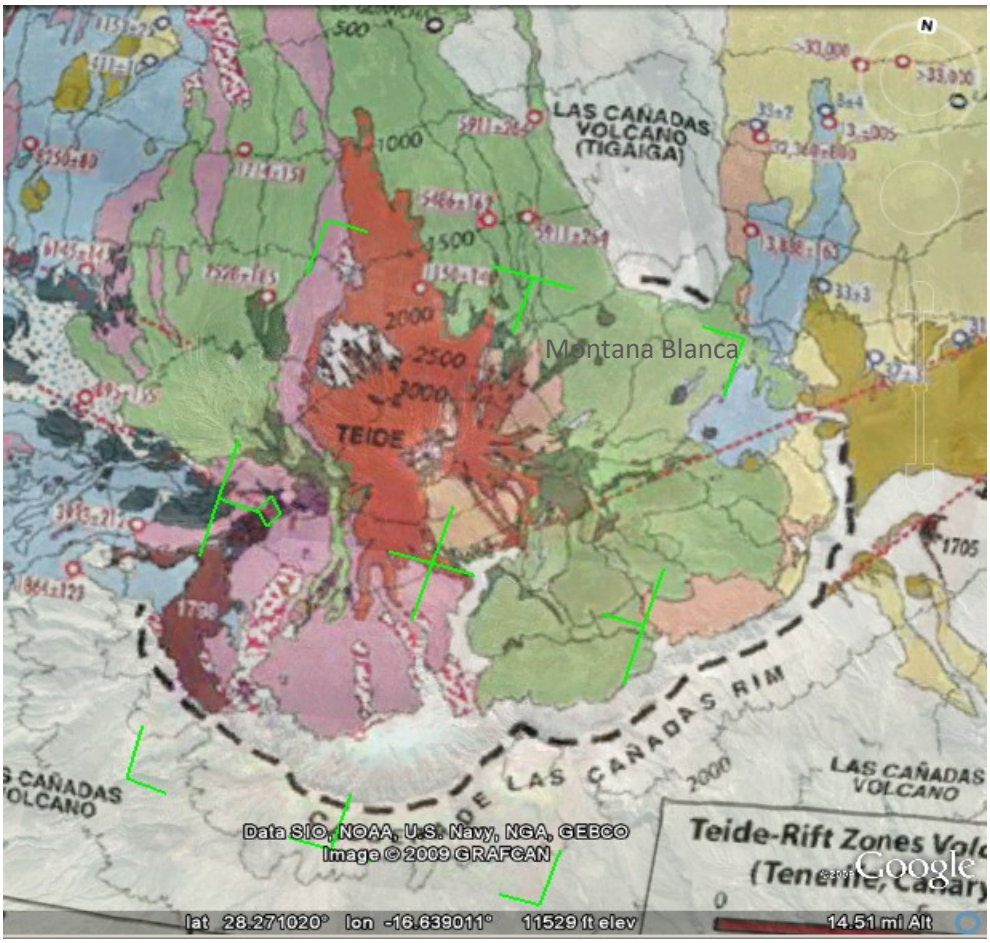

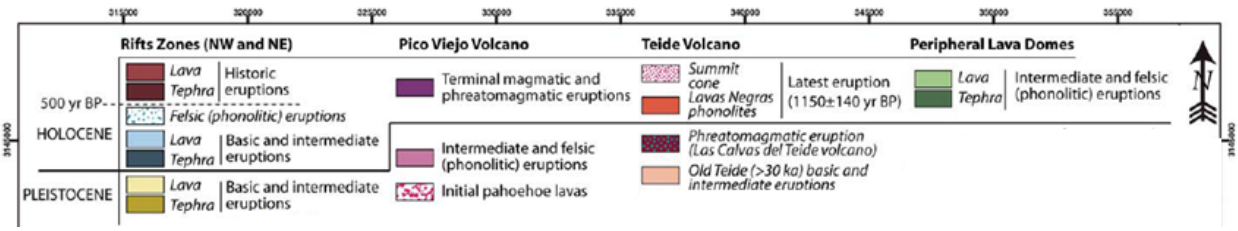

Figure 6.27 Geological map of volcano Teide (Carracedo J., 2006) overlapped on Google Earth.

In particular homogenous no vegetated units as Lava del Chaorra 1798 (pink), Teide Phase final (light green), Lava Negras sud (purple) are rightly classified (Figure 6.28).

As regards Mna Blanca area which on geological map appears quite homogeneous (lava-tephra) some differences are evident in the SVM classification. The Carracedo map doesn't describe the area located in the south of Las Canadas Rim but a characterization is given by Hyperion map.

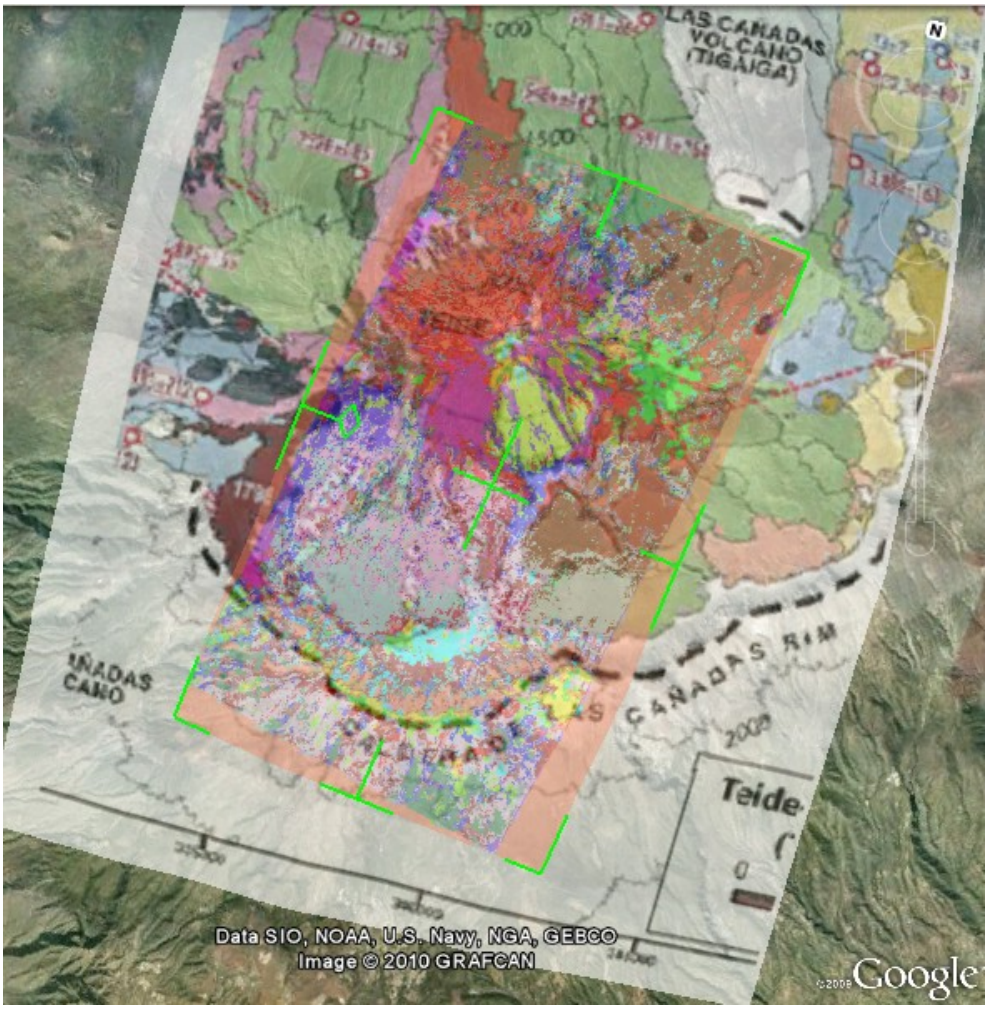

Figure 6.28 Hyperion classification map overlapped on Carracedo geological map (transparency 50%). The first view shows a good correspondence among main geological units.

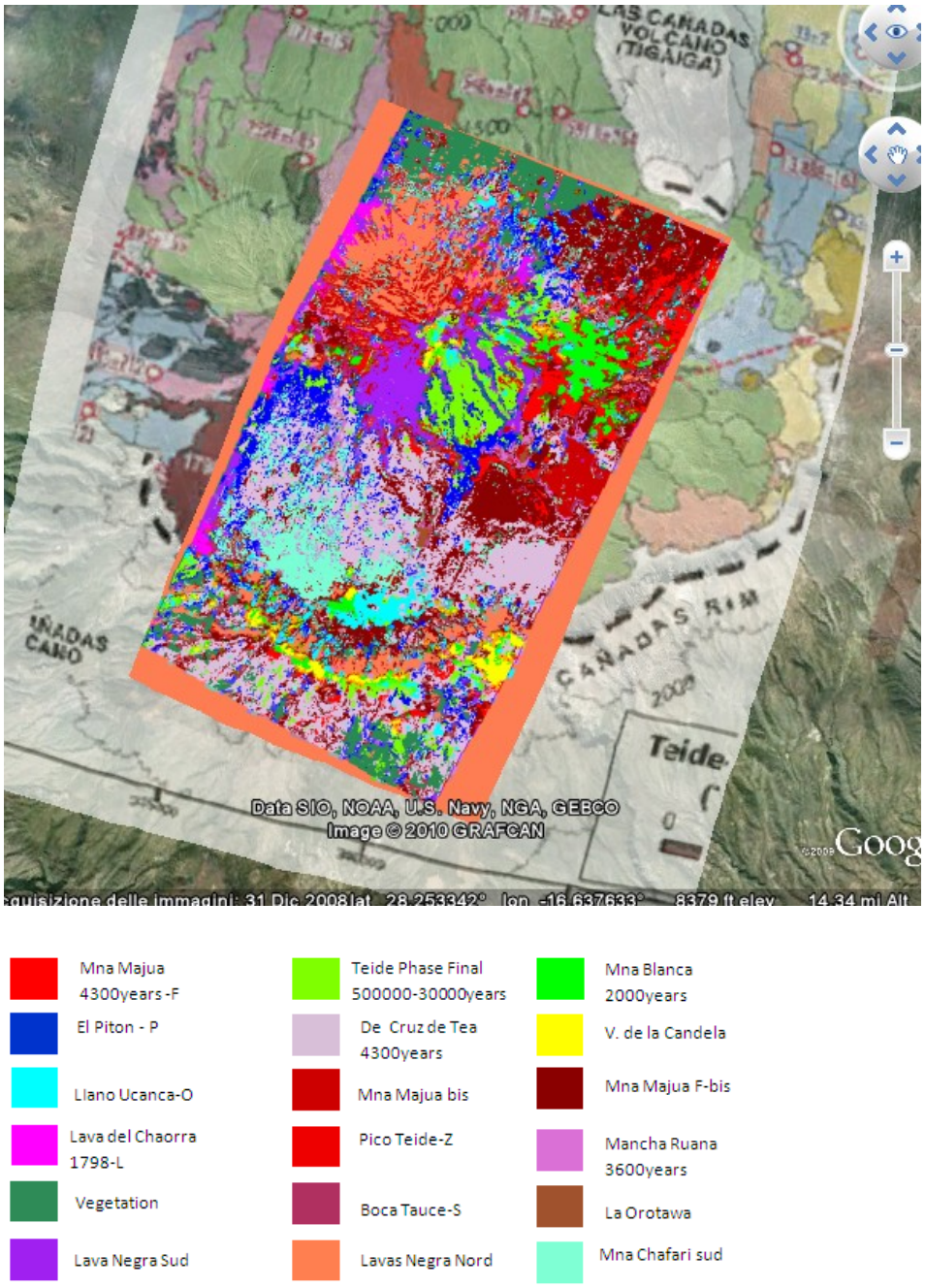

Figure 6.29 Hyperion classification map overlapped on Carracedo geological map on Google Earth.

	True class																			
Classified as	**Mna Maju**	**El Pito**	**Llano Ucan**	**Lavas del Chao**	**Boca Tau**	**Vegetatio**	**Lavas Negras s**	**Lavas Neg**	**Chafari S**	**La Orotat**	**Teide Phase Fi**	**De La C**	**Mna Majua B**	**El Pico Teic**	**Mna Blanc**	**V. Della Cande**	**Mna Majua -**	**Mancha Ruat**	**TOT**
Mna Majua	149	0	9	0	0	0	2	0	0	0	0	6	0	0	2	0	18	0	186
El Piton	0	124	0	0	1	0	4	0	0	0	5	0	0	0	0	0	0	3	137
Llano Ucanca	3	0	608	0	0	0	3	0	0	0	6	4	0	0	2	2	0	0	628
Lavas del Chaorra	0	0	0	110	1	0	0	17	0	0	0	0	17	0	0	0	0	1	146
Boca Tauce	0	0	0	0	27	0	1	13	0	0	0	0	0	0	0	0	0	0	41
Vegetation	0	0	0	0	0	357	0	0	1	0	0	0	0	0	0	0	5	0	363
Lavas Negras sud	0	13	0	0	1	0	261	6	8	0	6	3	4	0	0	0	0	6	308
Lavas Negras nord	0	0	0	1	1	1	3	273	0	0	0	0	0	0	0	0	0	2	281
Chafari Sud	0	0	0	0	24	2	0	3	1048	6	0	0	11	0	0	0	6	14	1114
La Orotava	0	0	0	0	1	2	0	0	5	119	0	0	11	0	0	0	1	15	154
Teide Phase Final	0	9	2	0	0	0	14	0	0	0	504	0	0	0	1	0	0	2	532
De La Cruz	2	1	2	0	3	0	0	0	5	3	0	1870	0	0	0	0	122	92	2100
Mna Majua Bis	0	0	0	5	8	6	54	2	13	14	0	0	1007	0	0	0	0	6	1115
Pico Teide	0	0	0	0	0	0	0	0	0	0	0	0	0	0	0	0	0	0	0
Mna Blanca	0	0	0	0	0	0	0	0	0	0	0	0	0	0	383	9	0	0	392
V. Della Candela	0	0	0	0	0	0	0	0	0	0	0	0	0	2	5	182	0	0	189
Mna Majua - F	49	3	6	0	5	6	1	0	8	16	1	209	0	0	0	0	905	22	1231
Mancha Ruana	0	3	0	0	9	0	3	0	6	8	0	21	1	0	0	0	7	96	154
Total	203	153	627	116	81	374	346	314	1094	166	522	2113	1051	2	393	193	1064	259	9071
Acc	88.45%																		
kappa coefficient	0.8694																		

Table 10 confusion matrix output of Hyperion SVM classification.

6.6.3 ASTER classification map

The comparison between classification map obtained by SVM method on ASTER data and geological map shows a good correspondence among the classes and the geological units. An overall accuracy of 96.83% and K coefficient of 0.9574 have been achieved (Table 11).

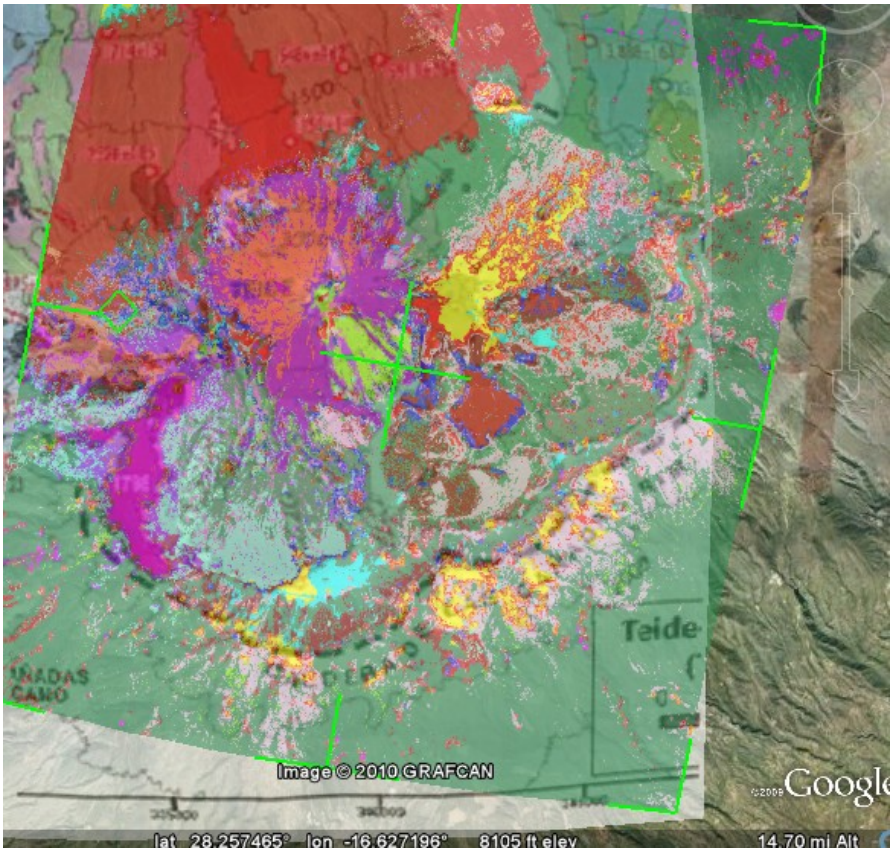

Figure 6.30 ASTER classification map overlapped on Carracedo geological map (transparency 50%). The first view shows a good correspondence among main geological units.

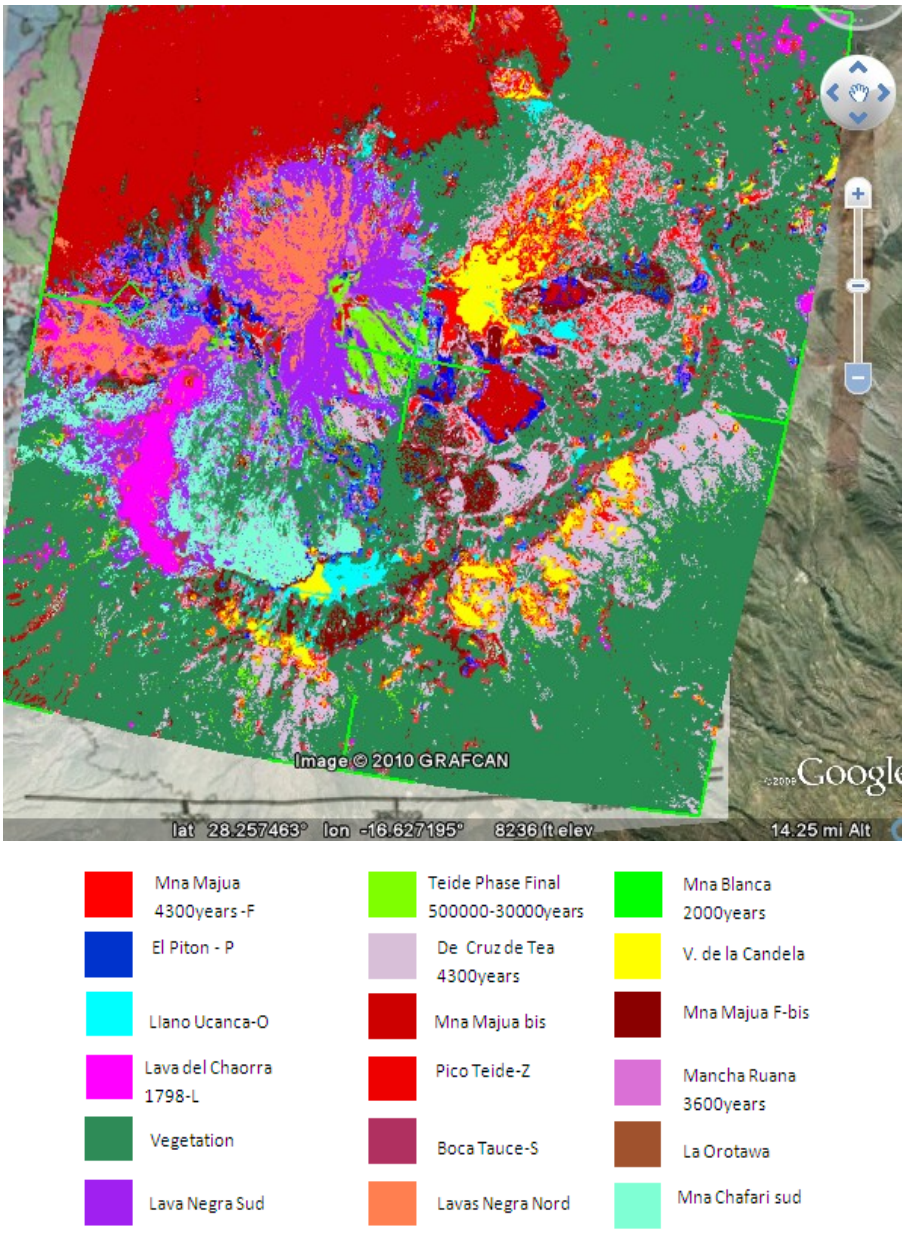

Figure 6.31 ASTER classification map of central part of Teide overlapped on Carracedo geological map on Google Earth

	True Class																		
	Mna Majua -	Ina Majua - F	bEl Piton - P	F. de la Candela	no de Ucanca -	va del Chaorra	oca Tauce -	vas negras su	vas negras no	veg	Ina Chafari s	tlancha Ruan	Orotaveide Phase	Finico Teide -	4auja bi	e Cruz de Te	Mna Blanca	Tot	
Mna Majua - F	37	0	0	2	0	0	0	0	0	0	0	0	0	0	0	0	2	41	
Mna Majua - F bi	0	73	10	0	0	0	0	4	0	32	6	0	0	2	0	0	0	127	
El Piton - P	0	0	2	0	0	0	0	0	0	4	0	4	0	0	0	0	0	10	
v. de la Candela	0	0	0	88	0	0	0	0	0	0	0	0	0	0	0	0	27	115	
Llano de Ucanca	2	1	0	0	692	0	0	0	0	8	0	0	0	0	0	0	0	703	
Lava del Chaorra	0	0	0	0	0	3820	0	0	138	0	0	0	0	0	0	0	0	3958	
Boca Tauce - S	0	0	0	0	0	2	61	8	1	0	0	0	0	0	0	0	0	72	
Lavas negras suc	0	0	0	0	0	2	34	3815	5	0	39	0	0	0	0	1	0	3896	
Lavas negras nor	0	0	0	0	0	150	0	1	2556	0	0	0	0	0	0	0	0	2707	
veg	0	78	64	0	7	0	0	0	0	13834	0	2	0	19	0	0	27	0	14031
Mna Chafari sud	0	0	0	0	0	0	37	112	0	0	1592	8	8	0	0	11	0	0	1768
Mancha Ruana	0	0	1	0	0	0	0	0	0	7	0	251	0	0	0	0	0	0	259
la Orotava	0	0	0	0	0	0	0	4	0	0	0	0	22	0	0	1	0	0	27
Teide Phase Fina	0	0	0	0	0	0	0	0	0	6	0	0	0	546	0	0	0	0	552
Pico Teide - Z	0	0	0	0	0	0	0	0	0	0	0	0	0	0	5	0	0	0	5
Mauja bis	0	0	0	0	0	0	1	19	0	0	24	3	25	0	0	1396	0	0	1468
De Cruz de Tea	1	0	0	1	8	0	0	0	0	14	0	0	0	1	0	0	946	0	971
Mna Blanca	0	0	0	0	0	0	0	0	0	0	0	0	0	0	0	0	0	0	0
Total	40	152	77	91	707	3974	133	3963	2700	13905	1661	268	55	568	5	1409	973	29	30710
Accuracy	96.83%																		
kappa coefficient	0.9574																		

Table 11 Confusion matrix output of ASTER SVM classification.

Conclusions

Remote sensing measurements made in situ and from airborne and spaceborne platforms give valuable information for research study. Sensors like ASTER and Hyperion provide such measurements and have been widely used in geological studies and other (Ducart et al 2006).

One of the purposes of this study is to validate the calibration models by comparing independent measurements coming from calibration sites to the products (reflectance and emissivity) derived from ASTER and EO1-Hyperion.

A field campaign has been realised on volcano Teide (FP7- Preview project) to collect a representative a data set of ground truth.

The test sites have been chosen as they are representative of different geological units and have been characterised both in reflectance and emissivity during the campaign. A FieldSpec Pro spectrometer and a μFTIR have been used for reflectance and emissivity measurements; an accurate protocol of measurement has been optimized for both instruments to guarantee the repetitivity of measurements.

For the sake of clarity VNIR and TIR results will be discussed separately.

VNIR spectral range:

The atmospheric correction model (CIRILLO) has been applied to calibrate both ASTER and EO1-Hyperion data and to retrieve the reflectance.

The analysis of Signal to Noise Ratio for ASTER and Hyperion data has been realised by a statistical method. The results pointed out differences with the nominal SNR of the sensors given before launch. This discrepancy is reasonable as different components, in particular the coating of CCD detectors, may degrade and change they performances in time. Furthermore , the analysis of Hyperion SNR pointed out very noisy bands with a good (more strong signal) SNR mainly in the first part of spectrum (500-800nm). This result can affect the possibility to distinguish some absorption feature.

To validate the retrieved satellite data a test site has been selected on volcano Teide. LIano de Ucanca responds to validation test site requirements: it is flat, homogenous, covered by a vegetation which is sufficiently tall, easy to reach, not subject to modification in time and covering a reasonable number of pixels (>10). The comparison between Hyperion retrieved reflectance with “in situ truth” has showed a good agreement. The maximum differences between the two spectra are 20% in few bands, this means an 80% agreement in the worst case. In the range between 400-900nm the mean variation is about

5-8%. For the ASTER results the comparison shows differences between ground truth and data ranging from a minimum of 6% to a maximum of 24%. This means that in the worst case (at 2167nm) the agreement is 76%. These results confirm that LlAno de Ucanca is good validation test site and validate the correction model.

The comparison of in situ reflectance measurements (ten test sites) and the corresponding Hyperion reflectance, has confirmed a good agreement (see section 6.2.1), demonstrating that the signal acquired by the sensor has been properly corrected (model validation) and that the resulting spectra are representative of the measured surface. The evaluation of the percentage differences between in situ and remote sensed spectra shows that the difference between Hyperion data and In situ measurement ranges between 0.01/% to 10% for noisy bands.

The obtained results confirm that both ASTER and EO-1 Hyperion sensors may be still considered as valid for scientific and operative applications (after 10 years from launch).

As example of proper data calibration and validation a supervised classification has been realised.

It is the first time that volcano Teide has been spectrally analysed and classified. The central part of Teide has been classified by using a supervised method (named single vector machine) with ENVI software. The comparison between the classification image obtained by SVM method on Hyperion data and the Teide geological map shows a good correspondence between the classes and the geological units. An overall accuracy of 88.45% and K coefficient of 0.8694 have been achieved. . While for ASTER we find an overall accuracy of 96.83% and K coefficient of 0.9574. Also in this case a good correspondence among the classes and the geological units is evident.

By comparing the two classification maps we have noticed how the good quality of image (derived by a good calibration) reflects on the results. The ASTER classification map shows a wide presence of vegetation with respect to Hyperion. This difference may be due to: a seasonal effect (Hyperion data is acquired on November 2003 , ASTER in August 2007). A three year time difference in which there was vegetation growth. The fact that ASTER is a multispectral sensor, and commission (?) may have occurred.

The classification results obtained from Hyperion and ASTER data are promising and represent the first classification realised on Teide.

TIR spectral range:

On demand ASTER night data (?) (September 17 2007) and simultaneous in-field

temperature measurements have been performed during the campaign. Llano de Ucanca test site answered requirements of test site also for ASTER TIR We should keep in mind that ASTER is the only commercial satellite sensor operating in the thermal spectral range with the spatial resolution of 90m (others sensors start from a 1Km resolution); the whole scientific community has a great interest in this sensor which will continue its operation only for two more years. Validation of ASTER data in the TIR range is very important as unique data product, and represents a relevant scientific contribution. The importance of in situ emissivity measurements and data validation comes from the relation of emissivity to the surface, allowing the retrieval of many kinds of information (e.g spectral features, temperature etc.). Furthermore, emissivity maps and in situ emissivity measurements represent good inputs for the next generation of orbiting thermal sensor.

ASTER night data (September 17 2007 23:16) has been corrected by using a local atmospheric profile. Since the ASTER pixel resolution in IR spectral range is equal to 90m, we can have pixel mixing. To take into account this effect, in situ emissivities were acquired on colluviums surface and brushes. ASTER emissivities from AST05 (standard product) and from TES plus local atmospheric profile, were compared with in situ data. A linear combination of 60% surface and 40% brushes agrees with ASTER emissivities in the corresponding geolocated area. A good agreement between standard and atmospheric corrected data and the validation in situ measurement has been verified; the percentage difference between standard and retrieved data exhibits a maximum value of 1% and 2% respectively in correspondence of band 11.13micron.

The obtained result confirms Llano de Ucanca as good validation test site also for thermal ASTER data.

In situ emissivity measurements of reflectance realised in the same test sites, and they have been compared with both ASTER retrieved emissivity and AST05 standard product. The emissivity spectra are generally consistent with the ground data for both AST05 and TES+local profile.

A better agreement in shape has been noticed in TES+local profile corrected spectra in the range 8-9μm with respect to AST05. This is probably due to the highest absorption values of water vapour at 8.6μm. A standard seasonal atmospheric profile as the one used in AST05 is surely good for the spectral range (10-14 μm) where the effects of water vapour absorption are minor (in fact AST05 and ASTER+TES+local profile are both consistent in shape) but may affect the shape of spectra in 8-9μm range. This is relevant for scientists who study SO2 from volcanic plume: an improvement of 1% in emissivity

estimation affects the estimation of SO2 by 5%.

The temperature validation is possible by comparing the situ measurement with the corresponding ASTER data at same time. The radiant temperatures were measured in field (Liano de Ucanca test site using EVEREST radiometer) starting two hours before the ASTER passage. The percentage difference between the measured on ground temperature and the corresponding at same time of ASTER passage is 0.7% . This validates the models used to calibrate ASTER data.

References

Ablay G.J., Martì J., Stratigraphy, structure, and volcanoic evolution of the Pico Teide±Pico Viejo formation, Tenerife, Canary Islands, Journal of Volcanoology and Geothermal Research 103 (2000) 175-208.

Abrams, M 2000 the advanced spaceborne Thermal Emission and Reflectance Radiometer (ASTER) Datta products for the high spatial resolution imager on NASA 's Terra platform. Int. J. Rem, Sens, 21 , 847-859.

Allard P, Behncke B, D'Amico S, Neri M, Gambino S (2006) Mount Etna 1993-2005: Anatomy of an Evolving Eruptive Cycle. Earth Sci Rev 78:85-114. DOI 10.1016/j.earscirev.2006.04.002

Amici S., Corradini S., Merucci L., Pugnaghi S.(2006). On ground Italian volcanoic area spectral characterization for validation of remote sensing data , SPIE Europe Remote Sensing and Optics /Photonics in security & Defence, S. Amici Stockholm International Fairs Sweden 11-14 September 2006 Proc. of SPIE Vol 6361 6361113-1.

Amici S.,.Buongiorno M. F., Corradini S., Pugnaghi S. and Sgavetti M. (2007). Airborne FTIR Measurements over the Mt. Etna Volcanoo: preliminary results from the 2003 FASA Campaign. IJRS 28(17) 3871-3893

Andronico D. , Branca S., Calvari S., Burton M.,· Caltabiano T., Corsaro R. A.,· Del Carlo P. , Garf G.,Lodato L.,· Miraglia L .,· Murè F., Neri M. · Pecora E., ·Pompilio M., Salerno G., Spampinato L. A multi-disciplinary study of the 2002–03 Etna eruption:insights into a complex plumbing system, Bull Volcanool (2005) 67:314–330 DOI 10.1007/s00445-004-0372-8.

ASI-SRV, Contratto ASI n° I/091/06/0 Sistema Rischio Vulcanico

Bailey G.B:, (2007). ASTER data and products:generation, characteristics, and access. Rivista Italiana di Telerilevamento-2007-39-19-31

Barducci, A., De Cosmo, V., Marcoionni, P., and Pippi, I., 2004, ALISEO: A new stationery imaging interferometer, in Shen, S.S., and Lewis, P.E., eds., Proceedings,

Imaging Spectrometry X: Denver, Colorado, The International Society for Optical Engineering (SPIE), v. 5546, p. 262–270.

Bryan Brailley G. , ASTER data products:generation,characteristics and access, AIT -2007,39,19-31.

Barry PS, Jarecke P, Pearlman J, Jupp DLB, Lovell J, Campbell S (2002) Radiometric calibration validation of the Hyperion instrument using “in situ truth” at a site in Lake Frome. Proc SPIE 4480:242-246

Becherer G.1979, Radiometry, vol.1 Academic press 1979.

Bailey G.B:, (2007). ASTER data and products:generation, characteristics, and access. Rivista Italiana di Telerilevamento-2007-39-19-31.

Berk A., Bernstein L.S., Robertson D.C. (1989) - MODTRAN: a moderate resolution model forLowtran7. GL-TR-89-0122, AFG Lab., Hanscom Air Force Base, MA 01731-5000, USA.

Byrnes JM, Ramsey MS, King PL, Lee RJ (2007) Thermal infrared reflectance and emission spectroscopy of quartzofeldspathic glasses. Geophys Res Lett 34, L01306. DOI 10.1029/2006GL027893.

Biging.G.S , Colby D.R, and Colgalton R.G.,(1998):Sampling system for change detection accuracy assessment, Remote Sensing Change detection, In: Lunetta, R.S. and Elvidge, C.D., Editors, 1998. Remote Sensing Change Detection: Environmental Monitoring Methods and Applications, Ann Arbor Press, Ann Arbor, MI, pp. 281–308.

Buongiorno et al. 2008, Etna 2003 Field Campaign: Calibration and Validation of Spaceborne and Airborne Instruments for Volcanoic Applications - ASI Projects: I/R/157/02, I/R/203/02, Quaderni di geofisica, http://www.ingv.it/produzione-scientifica/quaderni-di-geofisica/archivio/quaderni-di-geofisica-2008/.

Carracedo J.C., Rodriguez Badiola E., Guillon H., Paterne M., Scaillet A., Perez Torrado.FJ., Paris R., Fra-Paleo U., Hansen A; Eruptive and structural history of Teide Volcanoo and rift zones of Tenerife, Canary IsLANDS; gsa Bullettin 2007- v.119, no 9/10;p.1027-1051 doi: 10.1130/B26087..

Carracedo Joan Carlos, EL VOLCANO TEIDE VOLCANOOLOGIA INTERPRETACION DE PAISAJES E ITINERARIOS COMENTADOS, 2007 CajaCanarias.

Carracedo, J. C., Outstanding geological values: the basis of Mt Teide’s World Heritage nomination, Geology Today, Vol. 24, No. 3, May–June 2008.

Chih-Wei Hsu, Chih-Chung Chang, and Chih-Jen A Practical Guide to Support Vector Classfication 2009, Lin, http://ntu.csie.org/~cjlin/papers/guide/guide.pdf.

Christensen PR, Bandfield JL, Smith MD, Hamilton VE, Clark RN (2000) Identification of a basaltic component on the Martian surface from Thermal Emission Spectrometer data. J Geophys Res 105:9609–962.

Clark R.N., (1983) Spectral properties of mixture of Montmorillonite and dark carbon grains: implication for remotes sensing minerals containing chemically and physically adsorbed water, J.Geophys. Res., 88,10635-10644,1983.

Clark R.N., Roush TL. (1984) Reflectance spectroscopy: Quantitative analysis techniques for remote sensing applications. J Geophys Res 89:6329- 6340.

Clark R.N., (1995) Reflectane spectra, Rock Physics and Phase Relations A Handbook of Physical Constants, AGU reference Shelf3, American Geophysical Union.

Clark R.N. (1999) Spectroscopy of Rocks and Minerals, and Principles of Spectroscopy. In Rencz A (ed) Manual of Remote Sensing. John Wiley & Sons, New York pp 3- 58

Connolly, Thomas, and Caroln Begg. Database Systems. New York: Harlow, 2002.

Date, C. J. An Introduction to Database Systems, Eighth Edition, Addison Wesley, 2003.

Ducart D. F., Crosta, A.P., Souza, C.R., and Conciclio, J., Alteration mineralogy at the Cerro La Mina epithermal prospect, Patagonia, Argentina,.Field mapping, shortwave infrared spectroscopy and ASTER images, Economic Geology, 101,981-996.

Duggin M.J. 1974,On the natural limitations of target differentiation by means of spectral discrimination techniques, Proceedings of the 9th international Symposium on Remote Sensing of environment (Ann Arbor, Michigan: environmental Research Institute of Michigan) pp.499-514.

Favalli M and Pareschi MT (2004) Digital elevation model construction from structured topographic data: the DEST algorithm. J Geophys Res 109 DOI 10.1029/2004JF00015

Gillespie, A., Rokugava, S., Matsunaga, T., Cothern, J.S., Hook, S., Kahle, A.,1998. A temperature and emissivity separation algorithm for advanced spaceborne thermal emission and reflection

radiometer (ASTER) images. IEEE Trans Geosci Remote Sensing, 36(4), 1113-1126. Goetz AFH (1992) Imaging Spectrometry for Earth Observations. Episodes 15:7-14

Hapke, B., 2001, Space weathering from Mercury to the asteroid belt: Journal of Geophysical Research, v. 106, p. 10,039–10,073, doi: 10.1029/2000JE001338

Hapke B (1993) Introduction to the theory of reflectance and emittance spectroscopy. Cambridge University Press, New York.

Hatchell D. C., ASD Technical G uide 3rd Ed Managing Editor: Copyright©1999 Analytical Spectral Devices Inc (2002) FieldSpec Pro user's guide

Holst G. C. 2000, Common sense approach to thermal imaging, SPIE Volume PM-86, ISBN:0-8194-3722-0.

Hunt G.R. and Salisbury,, Spectral signatures of particulates minerals, in visible and nerar infrared, Ghophysics, 42, 501-513, 1977.

Justice, C. O., and Townshend, J. R. G., 1994, Data sets for global remote sensing: lessons learnt. International Journal of Remote Sensing, 15, 3621–3639.

Justice, C. O., Starr, D., Wickland, D., Privette, J., and Suttles, T., 1998a, EOS land validation coordination: an update. Earth Observer, 10, 55–60. NASA/GSFC.

Krumbein WC (1938) Size frequency distribution of sediments and the normal phi curve. J Sediment Petrol 8:84-90

Kimes D.S.,Kirchner J.A., Necomb W.W., 1982,Spectral radiance errors in remote sensing ground studies due to nearby objects, Applied Optics, 22, 6-258.

Kneizys, F.X., Shettle, E.P., Gallery, W.O., Chetwynd Jr., J.H., Abreu, L.W., Selby, J.E.A., Clugh, S.A., Fenn, R.W., 1983. Atmospheric trasmittance/radiance: Computer code LOWTRAN 6, Environ. Res. Pap., 846, Air Force Geophys. Lab., Hanscom AFB, Mass.

Korb, A.R., P. Dybwad, W. Wadsworth, and J.W. Salisbury, 1996, Portable Fourier Transform Infrared Spectrometer for Field Measurements of Radiance and Emissivity, Applied Optics, v.35, p.1679-1692.

Lentini F (1982) The geology of the Mt. Etna basement. In: Romano R (ed) Mount Etna Volcanoo, a Review of Recent Earth Sciences Studies. Mem Soc Geol Ital 23:7-25

Lichti DD, Harvey BR (2002) The effects of reflecting surface material properties on time-of-flight laser scanner measurements. Symposium on Geospatial Theory, Proceedings and Applications, Ottawa

Mazzarini F, Pareschi MT, Sbrana A, Favalli M, Fulignati P (2001) Surface hydrothermal alteration mapping at Vulcano island Using MIVIS data. Int J Remote Sens 22:2045-2070

Meigs, A.D., Otten, L.J., III, Cherezova, T.Y., Rafert, B., and Sellar, R.G., 1997, LWIR and MWIR ultraspectral- Fourier transform imager, in Fujisada, H., ed., Proceedings, Sensors, systems, and next generation satellite:London, The International Society for Optical Engineering (SPIE), v. 3221, p. 421–428.

Milton E.J., "Principles of field Spectroscopy", Int. J. remote Sensing, 8, 12, 1807-1827, 1987.

Milton E.J.,1987, Principle of field spectroscopy, nt. J. Remote sensing, 1987, vol8, no 12,1807-1827

Monteith J.L., 1973, Principle of environmental Physics (London :Edward Arnold) p.29

Musacchio M., Amici S., Teggi S.Pompilio. L, Sgavetti M. e BuongiornoM.F., (2007), Una nuova procedura per le correzioni atmosferiche: applicazione sulla solfatara di Pozzuoli. F., Rivista Italiana di Telerilevamento, numero 39-anno 2007.

Pieri, D.C. and Abrams, M.J., (2004). ASTER watches the world's volcanooes: a new paradigm for volcanoological observations from orbit. J. Volcanool. Geotherm. Res. 135, pp. 13–28

Rahaman H., Dedieu G. (1994) - SMAC: a simplified method for the atmospheric correctionof satellite measurements in the solar spectrum. Int. J. Remote Sens., 15: 123-143

Ramsey M. S. and Cristensen, P. R. Mineral abundance determination: Quantitative deconvolution of thermal emission spectra, Journal of Geophysical Research, vol 103, No, B1, pages 577-596, January 10, 1998.

Ramsey MS (2002) Ejecta distribution patterns at Meteor Crater, Arizona: On the applicability of lithologic end-member deconvolution for spaceborne thermal infrared data of Earth and Mars. J Geophys Res 107. DOI 10.1029/2001JE001827

Realmuto, V.J., 1990. Separating the effects of temperature and emissivity: emissivity spectrum normalization. 2nd thermal infrared multispectral scanner (TIMS) workshop. In: Abbot EA (ed) Proceedings of the Second TIMS Workshop. JPL Publication 90-55, Pasadena, 310-316

Realmuto V.J, (1990). Separating the effects of temperature and emissivity: emissivity spectrum normalization, in Proc. 2nd TIMS Workshop. Pasadena, CA: Jet Propul.Lab., JPL Publication 90-55.

Richter R. (1997) - Correction of atmospheric and topographic effects for high spatial

resolution satellite imagery. Int. J. Remote Sens., 18: 1099-1111

Robinson, T. P., 1996, Spatial and temporal accuracy of course-resolutionproducts ofNOAAAVHRR

NDVI data. International Journal of Remote Sensing, 17, 2303–2321.

Salvaggio C., Miller C. J. Methodologies and protocols for the collection of midwave and longwave infrared emissivity spectra using a portable field spectrometer, Spectral Information Technology Applications Center, Copyright 2001 Society of Photo-Optical Instrumentation Engineers

Sgavetti M., Pompilio L., Meli S., Reflectance spectroscopy (0.3-2.5micron) at various scales for bulk-rock identification, Geosphere, May,2006; v2;no 3;p.142-160.

Siegal B.S and Gillespie A.R., Remote sensing in geology,1980, John Wiley and Sons, Inc.

Slater, P.N., 1980 Remote sensing optics and optical systems (Maccachusetts: Addison-Wesley ABP) 315-575.

Teggi S. Calcolo della Riflettanza e della radianza al suolo da immagini tele rilevate VIS-SWIR: la procedura CIRILLO, per ENVI,2005.

Teggi S., M. Musacchio, M.F. Buongiorno, “CIRILLO: a new software for topographic and atmospheric corrections of spaceborne remote sensing data”, Journal of Applied Remote Sensing, submitted (2007).

Teggi, S., M.P., Bogliolo, M.F., Buongiorno, S., Pugnaghi and Sterni, A. (1999). Evaluation of SO2 emission from Mt. Etna using diurnal and nocturnal MIVIS TIR remotesensing images and radiative transfer models. Jurnal of Geophysical Research Vol 104, NO B9, pp 20,069-20,079, September 10.

Vermote E., Tanre´ D., Deuze´ J.L., Herman M., Morcrette J.J. (1997a) - Second simulationof the satellite signal in the solar spectrum, 6S: an overview. IEEE Trans. Geosci.Remote Sens. 35: 675-686.

Vermote E., Tanre´ D., Deuze´ J.L., Herman M., Morcrette J.J. (1997b) - 6S User GuideVersion I. ftp://kratmos.gsfc.nasa.gov/pub/6S/.

Wilcox, B.B., Lucey, P.G., and Gillis, J.J., 2005, Mapping ion in the lunar mare: An improved approach: Journal of Geophysical Research, v. 110, p. E11001, doi:10.1029/2005JE002512.

Yamaguchi, Y. Kahake, AB, Tsu, H., Kawakami T. And Pniel M., 1998 Overview of the Advanced Spaceborne Thermal Emission and Reflectance Radiometer (ASTER) IEE trans. Geosci REm. Sens. 36, 1062-1071.

Appendix 1: FieldSpec and micro FTIR in situ measurement details

In situ FieldSpec and micro FTIR measurement summary :

Site feature	Geology type	Fieldspec Lat Lon WGS 84	FTIR Lat Lon WGS 84	sample
Point P	Tephra and oxidiane Alt 2307 asl	28° 15' 19.7'' 16°37' 20.0''	N 28° 15' 19''.9	x
Point L	Alt 2085 asl	N28°13'2.3'' E16°40'53.8''	N 28° 13' 01.5''	
Point M	Alt 2112 asl Ph. Tephra-lava scoriae	N 28°14'7.2'' E 16°41' 45.8''	N 28° 14' 18.2''	x
Point F	Ph. lava/ pumice follow	N 28° 15' 1.3" E 16 °37' 25.2	N 28° 15' 1.2'' E 16° 37' 25.3''	x
Point N	Alt2280 asl Lava tephra intermediate felsic /phonolite pumice follow	N 28°15' 52.7'' E 16° 35' 19.6''	N28° 15' 57.6'' E 16° 35' 21.9''	
Point S	Pl.bas. lava	N28°12'52.1'' E16°40'42.1''	N 28° 12' 51. 9''	
Point O	Alt 2017asl colluvium	N 28°12' 46.9'' E 16° 38' 0.9''	N 28° 12' 46.9''	
Point U	Alt 2142asl Maphic phon lava	N 28 16' 54.2'' E 16° 34' 19.1''	N 28° 16° 57.4''	
Point I	Alt 2063 asl Pl.bas. lava		N28° 12' 39.9''	
Point V	Pl.bas. lava		N 28° 12' 40.5''	
Point Z (0,1,2)	Alt. 3718m	N 28°16'20.17" E 16°38'32.81"		

FIELDSPEC in situ measurements sheets

Date	Type	Lat Lon	Altitude	Filename.txt	photo
18-09-2007 1 Point N	Pumice lava	N 28°15' 52.7'' E 16° 35' 19.6''	2280asl	Teide18(0to29) Teide18(30to55)	Njpg
2Point O	Ucanca Etero vegetation	N 28°12' 46.9'' E 16° 38' 0.9''	2017asl	Teide18_2(00to29) Teide18_2(30to48)	O. Jpg
3 PointP	El Piton Lava vetrosa funivia	28° 15' 19.7'' 16°37' 20.0''	2307asl	Teide18_3(0to29)	P. Jpg
19-09-2007 3	Cespuglio Scoria Ossidiana			Tde19_3_0to44	3.jpg
4				Tde19_4_0to15	
5				Tde19_5_0to15	
6 Point M				Tde19_6_0to15	
7 Point L				Tde19_7_0to15	
8				Tde19_8_0to15	
Point F montagnola				montag_0to15	

20-09-2007					
	Hydro		3800 m asl	Hydro1.(0to15) Hydro2.(0to15)	Hydro.jpg
	Site w	N28°18'10.5'' E16°33'57.50''	2068m asl	Tde1W(0to15) Tde2W(0to15)	W.jpg

Top Crater	Pico teide Lava cone Alteration fumaroles		3800m asl	Pteide1(0 to15) Pteide2(0 to15) Pteide3(0 to15)	Pteide1.jpg Pteide2.jpg Pteide3.jpg

21-09-2007					
Point S	Lave blu	N 28° 12' 52,1" E 16° 40' 42.7"	2057 m a.s.l.	Laveblu(0 to29)	Blu.jpg
	Scoria pomice	N 28° 15' 58,2" E 16° 43' 31.9"	1904 asl	Pepito(0to 59)	Pom.Jpg
Point U Montana mostaza		N 28° 16' 54,2" E16° 34' 19.1"	2280 a.s.l.	monmos(0to29)	U.Jpg

FTIR in situ measurements sheets

Date	Site	Coordinate	Photo Site	Filename Meas.	Temp. Amb. (T_a)°C	Temp. gold plate (T_{gold})°C	Surf. Temp. (calibration) (T_s)°C	Surf. Temp. (emissivity) (T_s)°C	Comments
17.09.07	N	N28 15 57.6 E 16 35 21.9	N_01	n01_1740.cbb n01_1742.wbb n01_1746.dwr n01_1749.sam/.emx n01_1752.sam/emx	18.5	Tc=22.2	Tc=20.8 T_t=20.8	Tc=20.4 T_t=20.5	
17.09.07	N			n02_1800.dwr n02_1802.sam n02_1804.sam n02_1807.sam n02_1809.sam/emx		Tc=20.9 Tt=21.8 Tm=21.5		T=22 T=20.8	rocks
17.09.07	O	N 28 12 46.8 E16 38 10.2		o01_1855.cbb o01_1857.wbb o01_1900.dwr o01_1902.sam/emx o01_1909.sam.emx	Tt=18.2	Tc=18.2 Tt=18.0 Tm=18.1	Tc=18.5 Tt=18.7	Tc=20.5 Tt=18.09.2007	

								Tm=19	
Date	**Site**	**Coordinate**	**Photo Site**	**Filename Meas.**	**Temp. Amb. (T_a)°C**	**Temp. gold plate (T_{gold})°C**	**Surf. Temp. (calibration) (T_s)°C**	**Surf. Temp. (emissivity) (T_s)°C**	**Comments**
17/09/07	O			o02_1917.cbb o02_1920.wbb o02_1923.dwr o02_1925.sam/emx	T=16.0	 Tc=15.8 Tt=15.5 Tm=15.7	Tc=15.7 Tt=16.1		Green T=18 e 21x 1 BB
	O	N 28 12 46.9 E 16 38 10.0		o03_2147.cbb o03_2149.wbb o03_2153.dwr o03_2156.sam/emx o03_2159.sam/emx o03_2209.dwr o03_2213.sam/emx o04_2216.sam/emx	Tc=12.2	 Tt=10.3	Tt=9.1	T=9.1 T=9.5	Night
	O	N 28 12 47.0 16 08 10.1			T=5.8		Tt=6.7 Tc=5.8	Tc=8.5	FTIR out of range!!!!x aster

Date	Site	Coordinate	Photo Site	Filename Meas.	Temp. Amb. (T_a)°C	Temp. gold plate (T_{gold})°C	Surf. Temp. (calibration) (T_r)°C	Surf. Temp. (emissivity) (T_r)°C	Comments
19/09/07	P	N 28 15 19.1 E16 37 20.2		P01_0803.cbb p01_813.wbb p01_819.dwr	Tc=14.9 Tw=20 Tamb=10	 T=19.2			Obsidian and rock (P01) Altitude=232lm
19/09/07	P	N 28 15 19.1 E16 37 20.2		P01_0830.sam /emix			T=21.3		
19/09/07	P	N 28 15 19.1 E16 37 20.2		P01_0833sam/ emix			T=19.08		
19/09/07	P	N 28 15 19.9 E 16 37 19.7		P02_0855.sam /emix			T=19.5		previous calib. e dwr obsidian
19/09/07	P	N 28 15 19.9 E 16 37 19.7		p02_0858.dwr		T=22.5			new dwl old calib.
19/09/07	P	N 28 15 19.9 E 16 37 19.7		p02_0900.sam /emix				T=20.5	
19/09/07	P	N 28 15 19.9 E 16 37 19.7		p02_0902.sam /emix			T=22.5		
		N 28 15 19.9 E 16 37 19.7							

Date	Site	Coordinate	Photo Site	Filename Meas.	Temp. Amb. (T_a)°C	Temp. gold plate (T_{gold})°C	Surf. Temp. (calibration) (T_s)°C	Surf. Temp. (emissivity) (T_s)°C	Comments
19/09/07	F	N28 15 01.2 E16 37 25.3		F01_1013.cbb F01_1016.wbb	Tt=22 C Tcbb=17 (usata 16.7)		Tc=31 Twbb=36		New calib, no cloudy, windy. Altitude= 2318m
19/09/07	F	N28 15 01.2 E16 37 25.3		f01_1019.dwr		T=29.2		34.5	
19/09/07	F	N28 15 01.2 E16 37 25.3		f01_1024.sam/ emx			T=35.0		
19/09/07	F	N28 15 01.2 E16 37 25.3		f01_1026.sam/ emx			T=35.5		
19/09/07	F	N28 15 01.2 E16 37 25.3		f01_1030.sam f01_1032.sam f01_1034.sam					SKY measurement.
19/09/07	F	N 28 15 00.4 E 16 37 25.9		f02_1042.dwr		Tc=28			New gold
19/09/07	F	N 28 15 00.4 E 16 37 25.9		f02_1044.sam/ emix			T=33	T=33	
19/09/07	F	N 28 15 00.4 E 16 37 25.9		F02_1102.sam /emx			T=36		
19/09/07	M	N 28 14 18.2 E 16 41 52.6		M01_1601.cbb	Tc=25C Tcbb=19.8		T=45 Twbb=50.1		New calib. Less wind Altitude=2104
19/09/07	M	N 28 14 18.2 E 16 41 52.6		M01_1604.wbb					

Date	Site	Coordinate	Photo Site	Filename Meas.	Temp. Amb. (T_a)°C	Temp. gold plate (T_{gold})°C	Surf. Temp. (calibration) (T_r)°C	Surf. Temp. (emissivity) (T_s)°C	Comments
19/09/07	M	N 28 14 18.2 E 16 41 52.6		M01_1608.dwr		Tc=30C			
19/09/07	M	N 28 14 18.2 E 16 41 52.6		M01_1608.emx				Tc=43.5	
19/09/07	M	N 28 14 18.2 E 16 41 52.6		M01_1612				Tc=44.0	
19/09/07	M	N 28 14 18.2 E 16 41 52.6		M01_1614				Tc=45	
19/09/07	M	N 28 14 18.7 E 16 41 52.7		M02_1619.dwr		T=30.6			Nuova downwelling
19/09/07	M			M02_1621.sam/emx				Tc=42	
19/09/07	M			M02_1623.sam/emx				Tc=42.5	
19/09/07	M			M02_1625.sam/emx				Tc=42.3	

Date	Site	Coordinate	Photo Site	Filename Meas.	Temp. Amb. (T_a)°C	Temp. gold plate (T_{gold})°C	Surf. Temp. (calibration) (T_s)°C	Surf. Temp. (emissivity) (T_s)°C	Comments
19/09/07	M	N 28 14 18.7 E 16 41 52.7		M02_1619.dwr		T=30.6			Nuova downwelling
19/09/07	M			M02_1621.sam/emx				Tc=42	
19/09/07	M			M02_1623.sam/emx				Tc=42.5	
19/09/07	M			M02_1625.sam/emx				Tc=42.3	
19/09/07	L	N 28 13 01.5 E 16 40 55.7		L01_1700.cbb L01_1702.wbb	T=21- Tcbb= 15.8		Tc=29 Twbb=34.1		
19/09/07	L	N 28 13 01.5 E 16 40 55.7		L01_1709.dwr		Tc=29.0			
	L	N 28 13 01.5 E 16 40 55.7		L01_710.sam/emx				Tc= 29	
19/09/07	L	N 28 13 01.5 E 16 40 55.7		L01_1712.sam/emx				Tc=29	
19/09/07	L	N 28 13 01.5 E 16 40 55.7		L01_1714.sam/emx				Tc=29	
19/09/07	S	N 28 12 51. 9 E 16 40 41.1		S01_1752.cbb S01_1755.wbb	T=22 Tbb=16.8		Tc=35 Twbb=40.2		
19/09/07	S	N 28 12 51. 9 E 16 40 41.1		S01_1759.dwr		T=16			
19/09/07	S	N 28 12 51. 9 E 16 40 41.1		S01_1800.sam				Tc=31	

Date	Site	Coordinate	Photo Site	Filename Meas.	Temp. Amb. (T_a)°C	Temp. gold plate (T_{gold})°C	Surf. Temp. (calibration) (T_s)°C	Surf. Temp. (emissivity) (T_s)°C	Comments
19/09/07	S	N 28 12 51. 9 E 16 40 41.1		S01_1803.sam				Tc=32.5	
19/09/07	S	N 28 12 51. 9 E 16 40 41.1		S01_1805.sam				Tc=32	
19/09/07				S02_1809.dwr		T23			new dwr
19/09/07	S	N 28 12 51. 9 E 16 40 41.1		S01_1811.sam/emx S01_1813.sam/emx				T=32 T=32	
19/09/07	I	N28 12 39.9 E16 39 23.1		I01_1845.cbb I01_1847.wbb	T=19.5 Tcbb=24.5		T=17.5 Twbb=12.3		Alt= 2064m
19/09/07	I	N28 12 39.9 E16 39 23.1		I01_1849.dwr		Tc=17			
19/09/07	I	N28 12 39.9 E16 39 23.1		I01_1851.sam/				T=16.6	
19/09/07	I	N28 12 39.9 E16 39 23.1		I01_1853				T=17.0	

Date	Site	Coordinate	Photo Site	Filename Meas.	Temp. Amb. (T_a)°C	Temp. gold plate (T_{gold})°C	Surf. Temp. (calibration) (T_s)°C	Surf. Temp. (emissivity) (T_s)°C	Comments
19/09/07	V	N 28 12 40.5 E 16 39 23.4		V01_1900.dwr		Tc=17.5			Stessa calib, nuova dwr fronte della lava roccia
19/09/07	V	N 28 12 40.5 E 16 39 23.4		V01_1904.sam/emx				T=21.5	
19/09/07	V	N 28 12 40.5 E 16 39 23.4		V01_19006.sam/emx				T=21.4	roccette
19/09/07	V	N 28 12 40.5 E 16 39 23.4		V02_19015.dwr			T=18		Superficie omogenea, sassone nuova dwr
19/09/07	V	N 28 12 40.5 E 16 39 23.4		V02_19017.sam/emx				T=18	
19/09/07	V	N 28 12 40.5 E 16 39 23.4		V02_19020s/m/emx				T=20	

Date	Site	Coordinate	Photo Site	Filename Meas.	Temp. Amb. (T_a)°C	Temp. gold plate (T_{gold})°C	Surf. Temp. (calibration) (T_s)°C	Surf. Temp. (emissivity) (T_s)°C	Comments
21/09/07	U	N 28 16 57.4 E 16.34 17.2		U01_0743.cbb U01_745.wbb	T=10 Tcbb=5		T=11.5 Twbb=16.5		Montagna Mostaza al 215lm
21/09/07	U	N 28 16 57.4 E 16.34 17.2		U01_0748.dwr		T=15.0			
21/09/07	U	N 28 16 57.4 E 16.34 17.2		U01_0753.sam/emx				T=16	
21/09/07	U	N 28 16 57.4 E 16.34 17.2		U01_0755.sam/emx				T=17.5	
21/09/07	U	N 28 16 57.4 E 16.34 17.2		U01_0800.sam/emx				T=18.0	
21/09/07	U	N 28 16 57.4 E 16.34 17.2		U01_0802.sam/emx				T=19	
21/09/07	U	N 28 16 57.4 E 16.34 17.2		U02_0820.dwr		T=20.8			Montagna Mostaza , new dwr
21/09/07	U	N 28 16 57.4 E 16.34 17.2		U02_0822.sam/emx				T=22	
21/09/07	U	N 28 16 57.4 E 16.34 17.2		U02_0827.sam/emx				T=24	Wrong calib

Date	Site	Coordinate	Photo Site	Filename Meas.	Temp. Amb. (T_a)°C	Temp. gold plate (T_{gold})°C	Surf. Temp. (calibration) (T_s)°C	Surf. Temp. (emissivity) (T_s)°C	Comments
21/09/07	U	N 28 16 57.4 E 16.34 17.2		U02_0830.dwr		T=24.5			
21/09/07	U	N 28 16 57.4 E 16.34 17.2		U02_0832.sam/emx				T=24	
21/09/07	U	N 28 16 57.4 E 16.34 17.2		U02_0835.sam/emx				T=25.5	
21/09/07	U	N 28 16 57.4 E 16.34 17.2		U02_0846.cbb U02_0848.wbb	T=16.5 Tcbb=11.4		T=27 Twbb=32.1		Nuova calibrazione Stesso punto U02
21/09/07	U	N 28 16 57.4 E 16.34 17.2		U02_0851.dwr		T=30.4			
21/09/07	U	N 28 16 57.4 E 16.34 17.2		U02_0854.sam/emx				T=28.3	Perfetta!!!!"!
21/09/07	U	N 28 16 57.4 E 16.34 17.2		U02_0858.sam/emx				T=30	
21/09/07	F	N 28 15 04.8 E 16 37 30.3		f03_0944.cbb f03_0946.wbb	T= 20C Tcbb=14.8		T=24C Twbb=29C		Collinetta alla base, più rossiccia per vedere alterazioni Altezza 2273
21/09/07	F	N 28 15 04.8 E 16 37 30.3		f03_0949.dwr		T=28.8			
21/09/07	F	N 28 15 04.8 E 16 37 30.3		F03_0951.sam/emx				T=28.8	

Date	Site	Coordinate	Photo Site	Filename Meas.	Temp. Amb. (T_a)°C	Temp. gold plate (T_{gold})°C	Surf. Temp. (calibration) (T_s)°C	Surf. Temp. (emissivity) (T_s)°C	Comments
21/09/07	F	N 28 15 04.8 E 16 37 30.3		F03_0953.sam/emx				T=30.5	ok
21/09/07	F	N 28 15 04.8 E 16 37 30.3		F03_0955.sam/emx				T=31.5	un pò alta
21/09/07	F	N 28 15 04.8 E 16 37 30.3		F03_0957.sam/emx				T=32	
21/09/07	F	N 28 15 04.8 E 16 37 30.3		F04_1010.sam/emx					Autofit con 10 -14
21/09/07				F05_1012.sam/emx				T=36.2	

Appendix 2: Error evaluation for in situ reflectance and emissivity measurements

Standard deviation values for In situ Field Spec measurements

Point P :El Piton

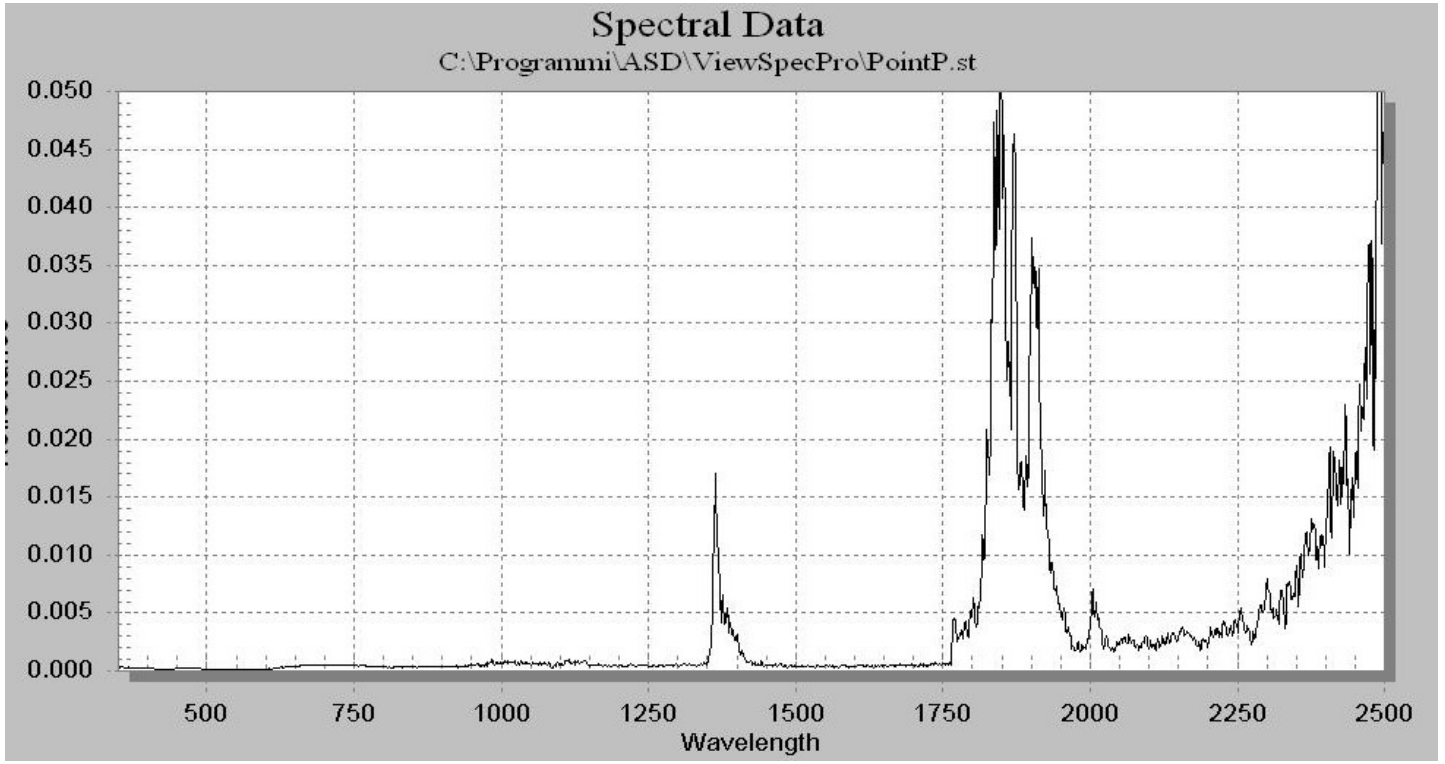

Point L:Lava negra 1798

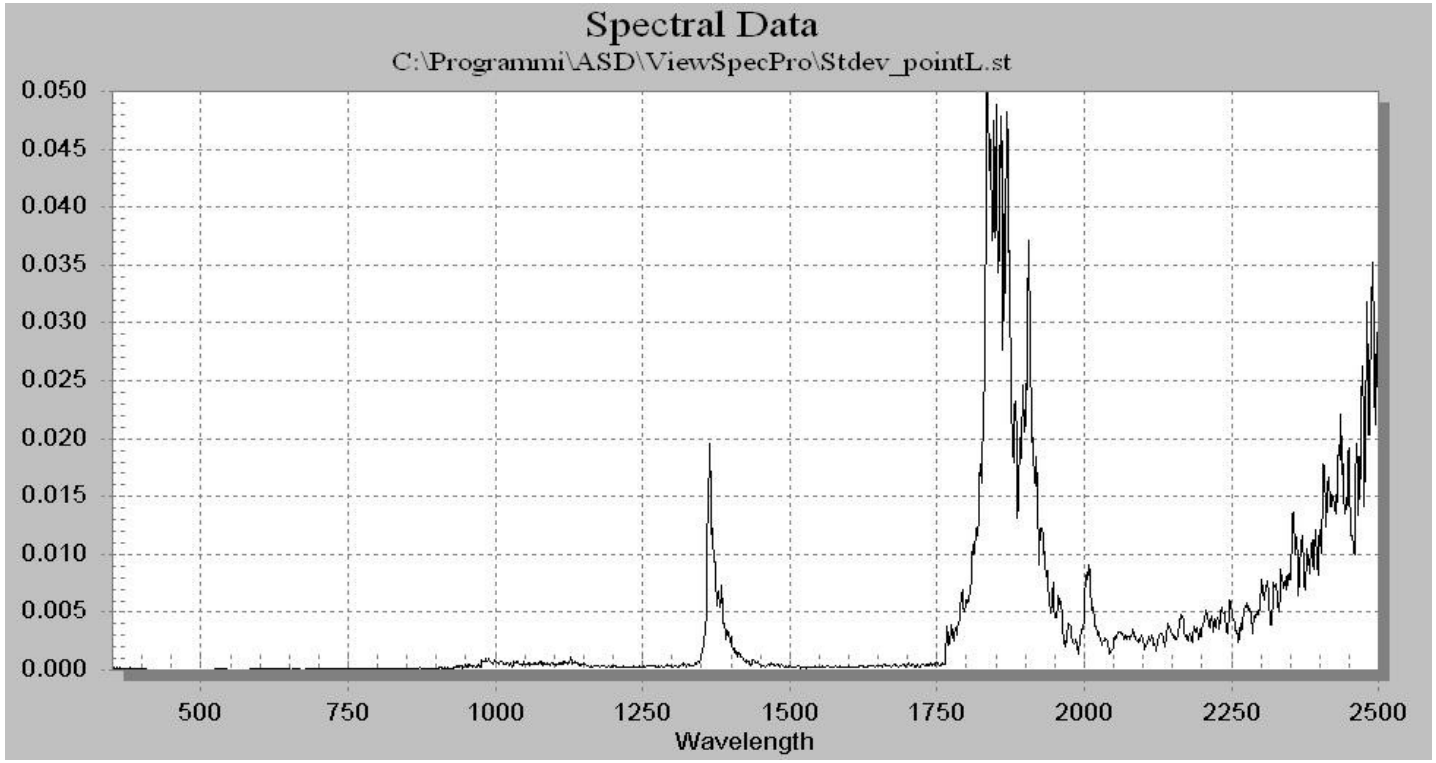

Point M: M.Chaorra

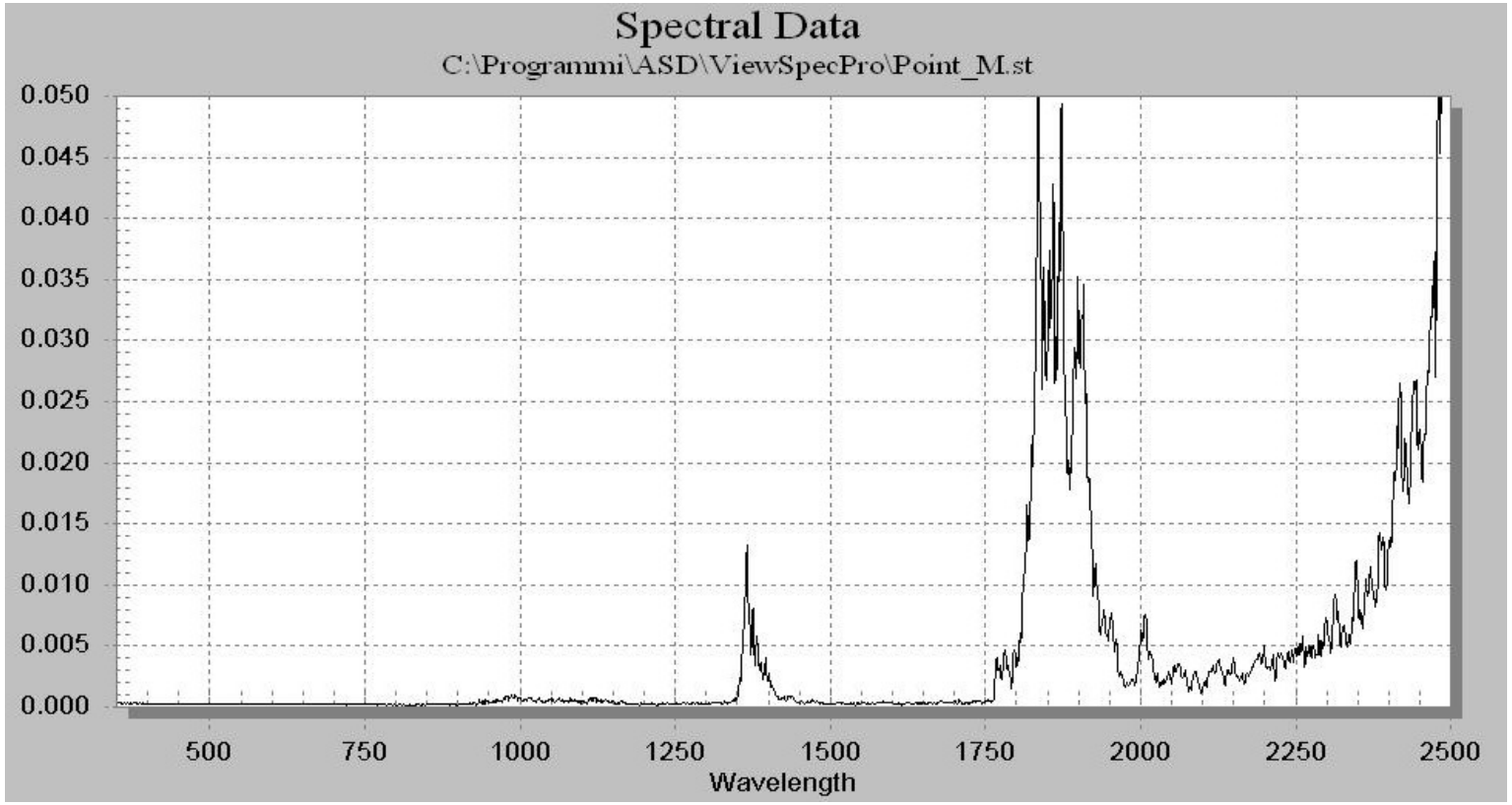

Point F Mna. Majua

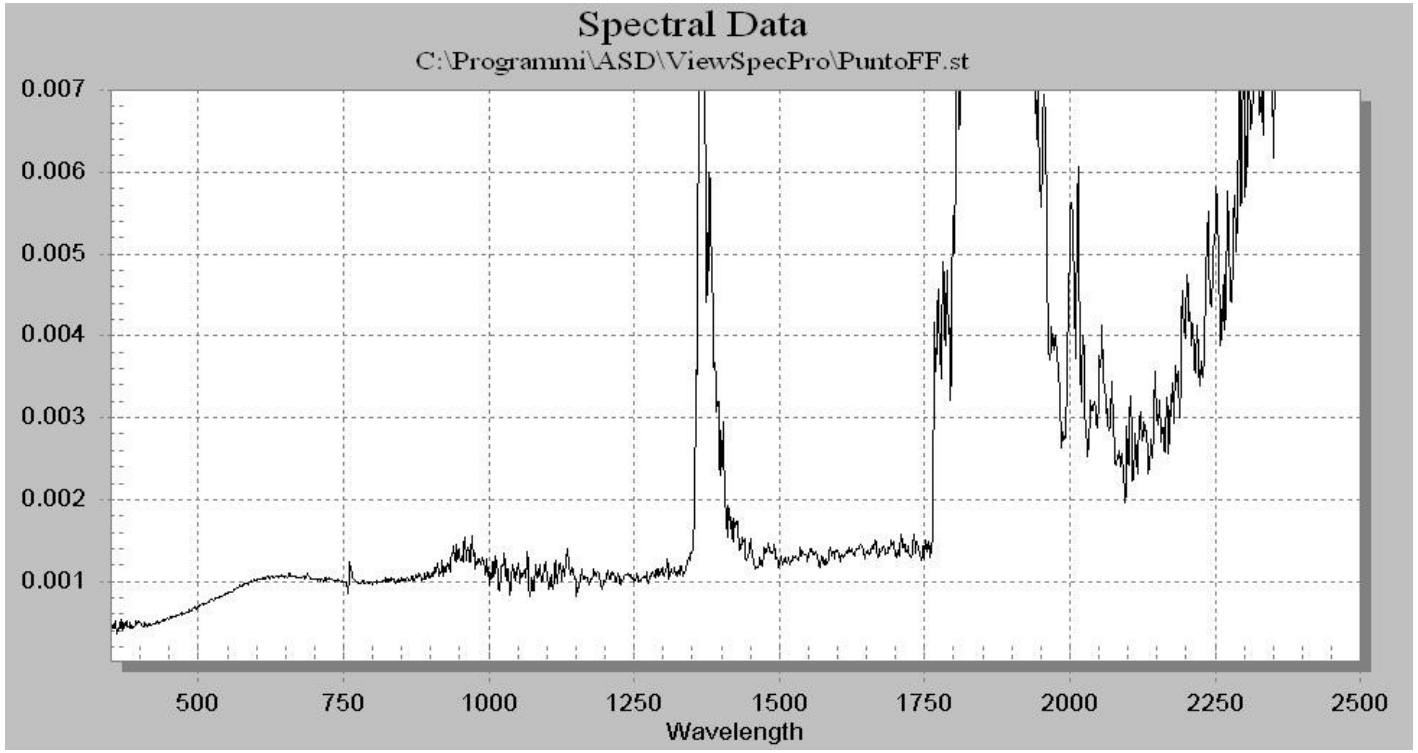

Point N

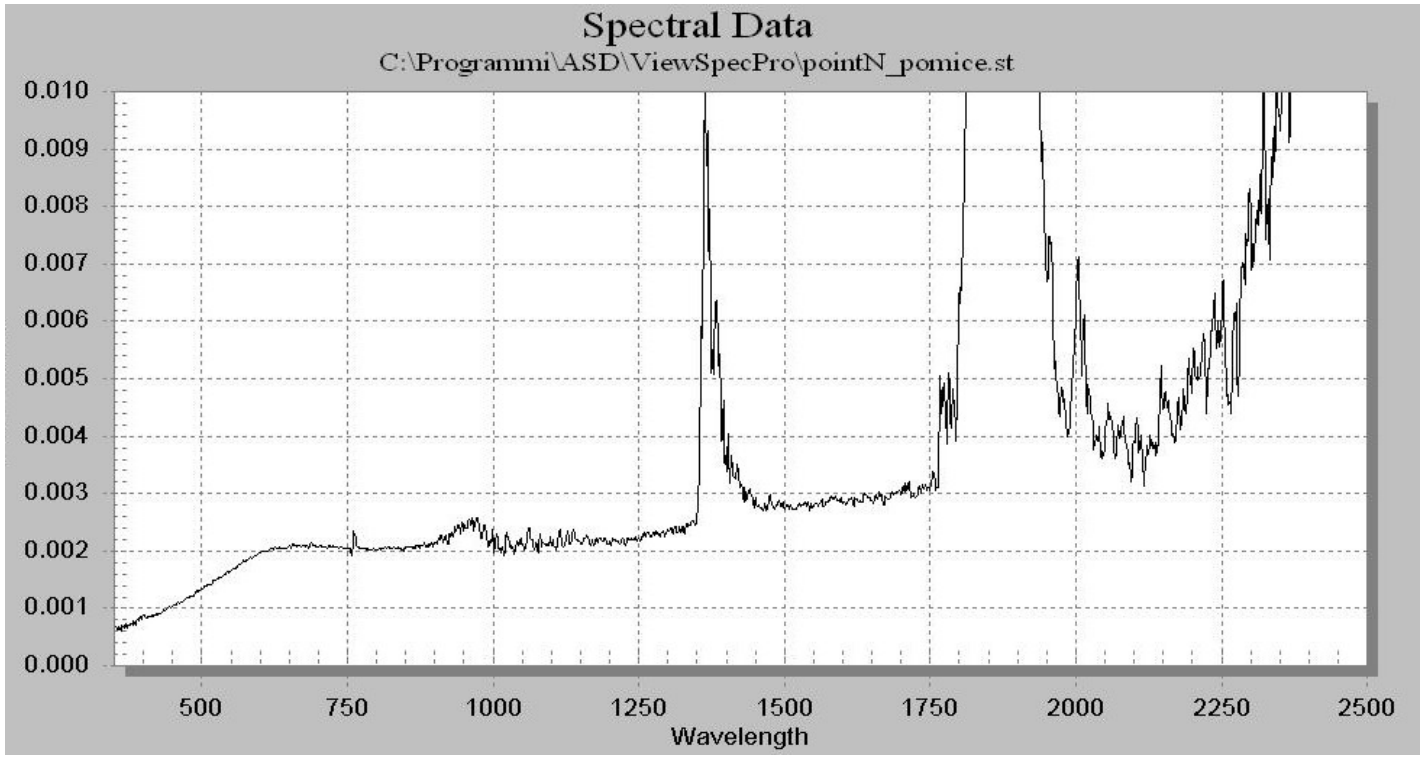
Spectral Data
C:\Programmi\ASD\ViewSpecPro\pointN_pomice.st
0.010
0.009
0.008
0.007
0.006
0.005
0.004
0.003
0.002
0.001
0.000
500
750
1000
1250
1500
1750
2000
2250
2500
Wavelength

Point N

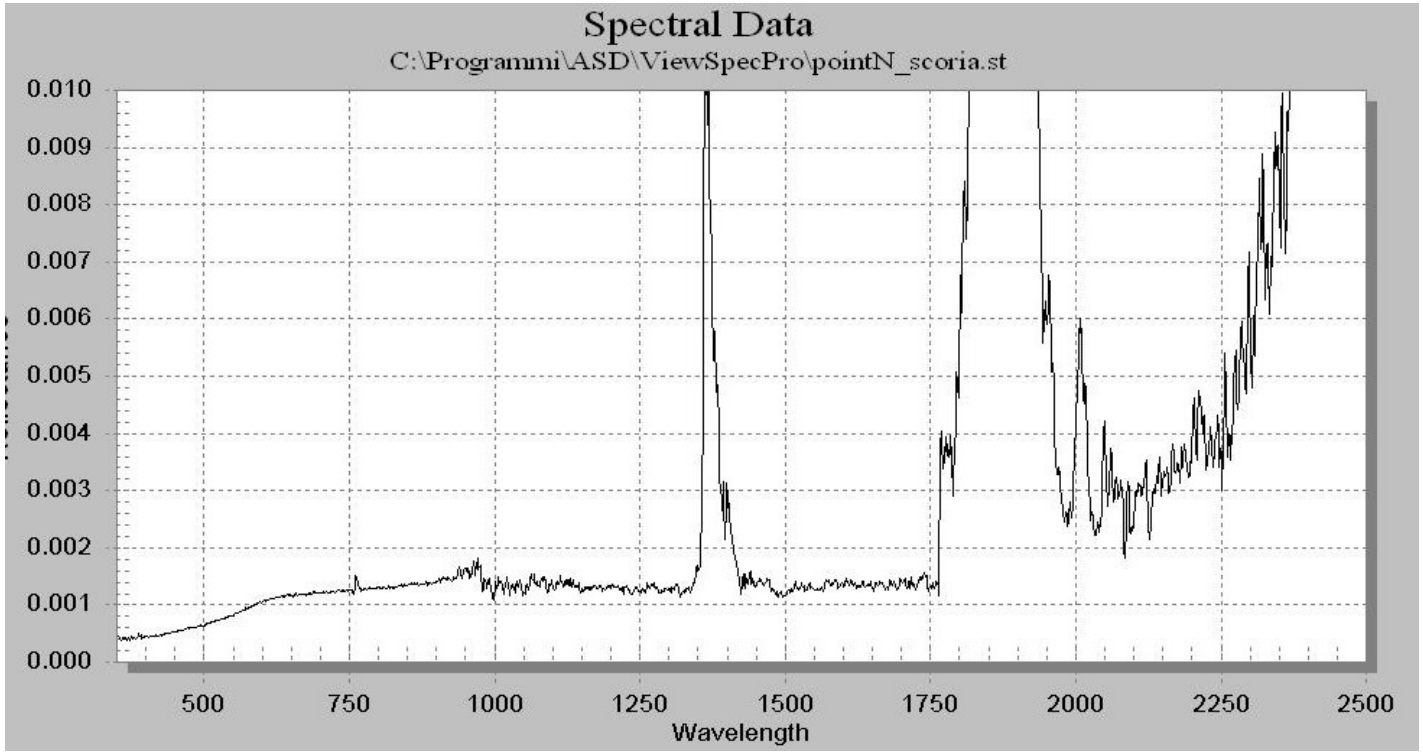
Spectral Data
C:\Programmi\ASD\ViewSpecPro\pointN_scoria.st
0.010
0.009
0.008
0.007
0.006
0.005
0.004
0.003
0.002
0.001
0.000
500
750
1000
1250
1500
1750
2000
2250
2500
Wavelength

Point O: Llano Ucanca scoria

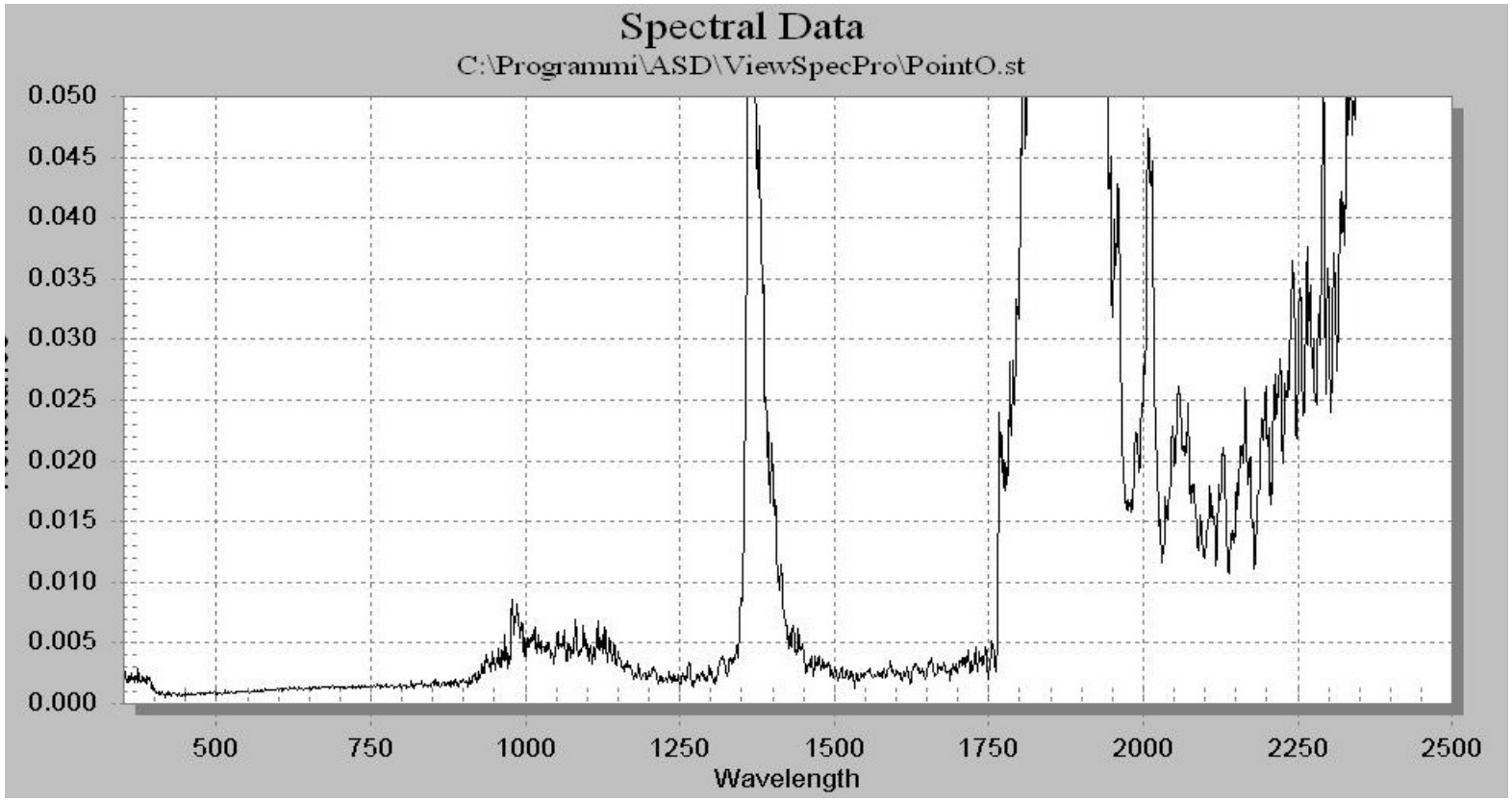

Point O: Llano Ucanca vegetation

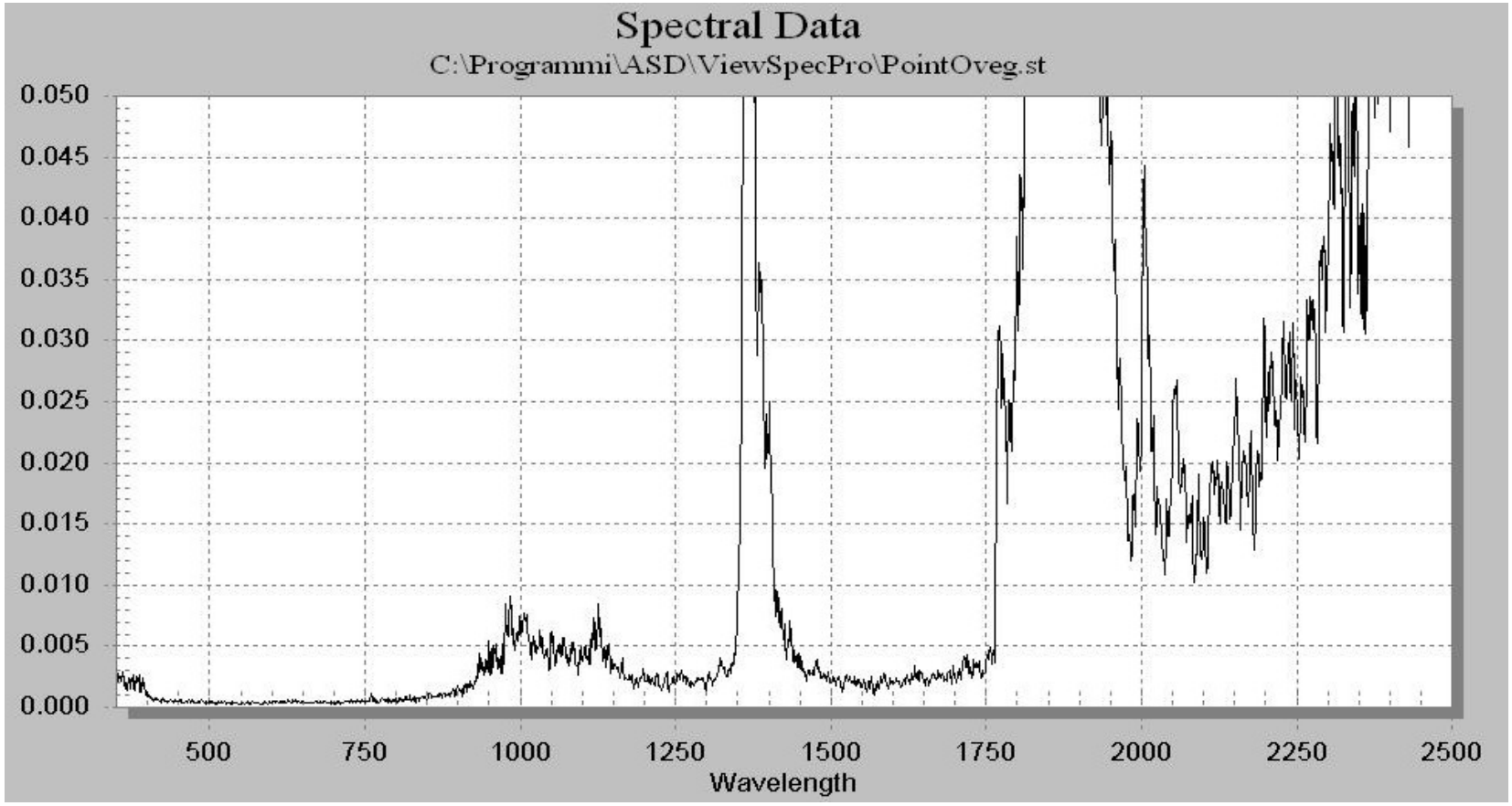

Point U: Mna Mostaza

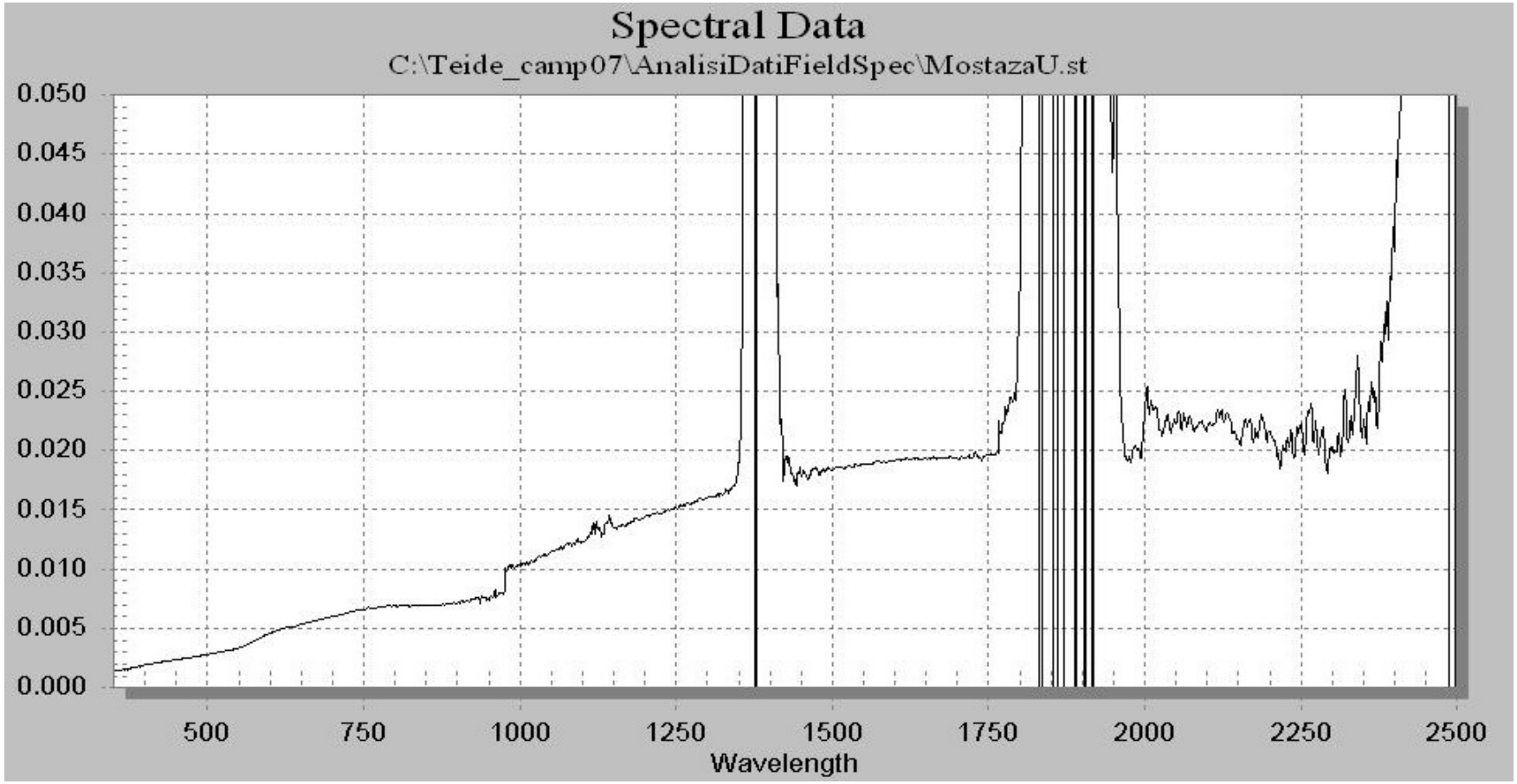

Point I

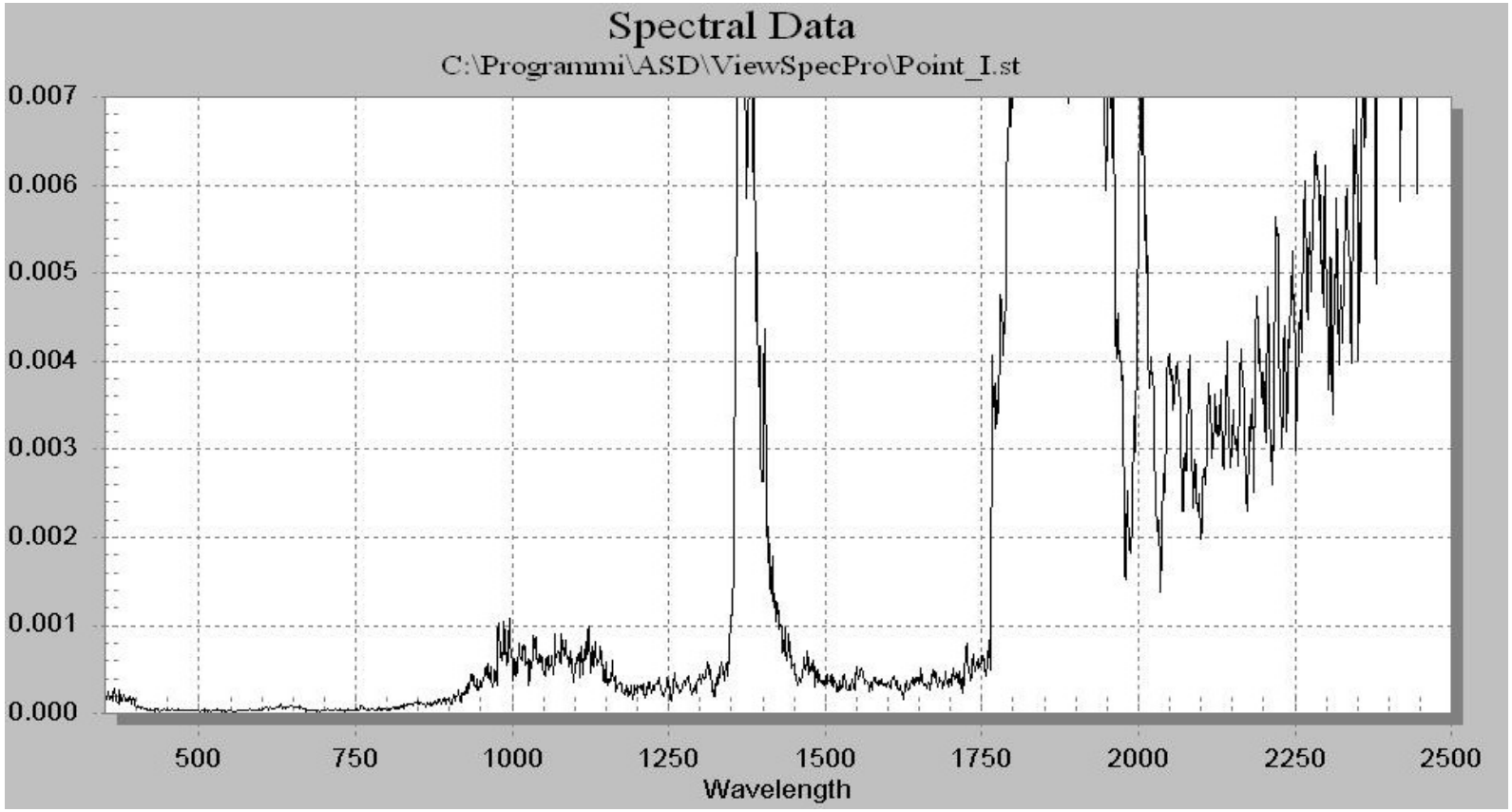
Spectral Data
C:\Programmi\ASD\ViewSpecPro\Point_I.st
0.007
0.006
0.005
0.004
0.003
0.002
0.001
0.000
500
750
1000
1250
1500
1750
2000
2250
2500
Wavelength

Point Z (0) Teide crater

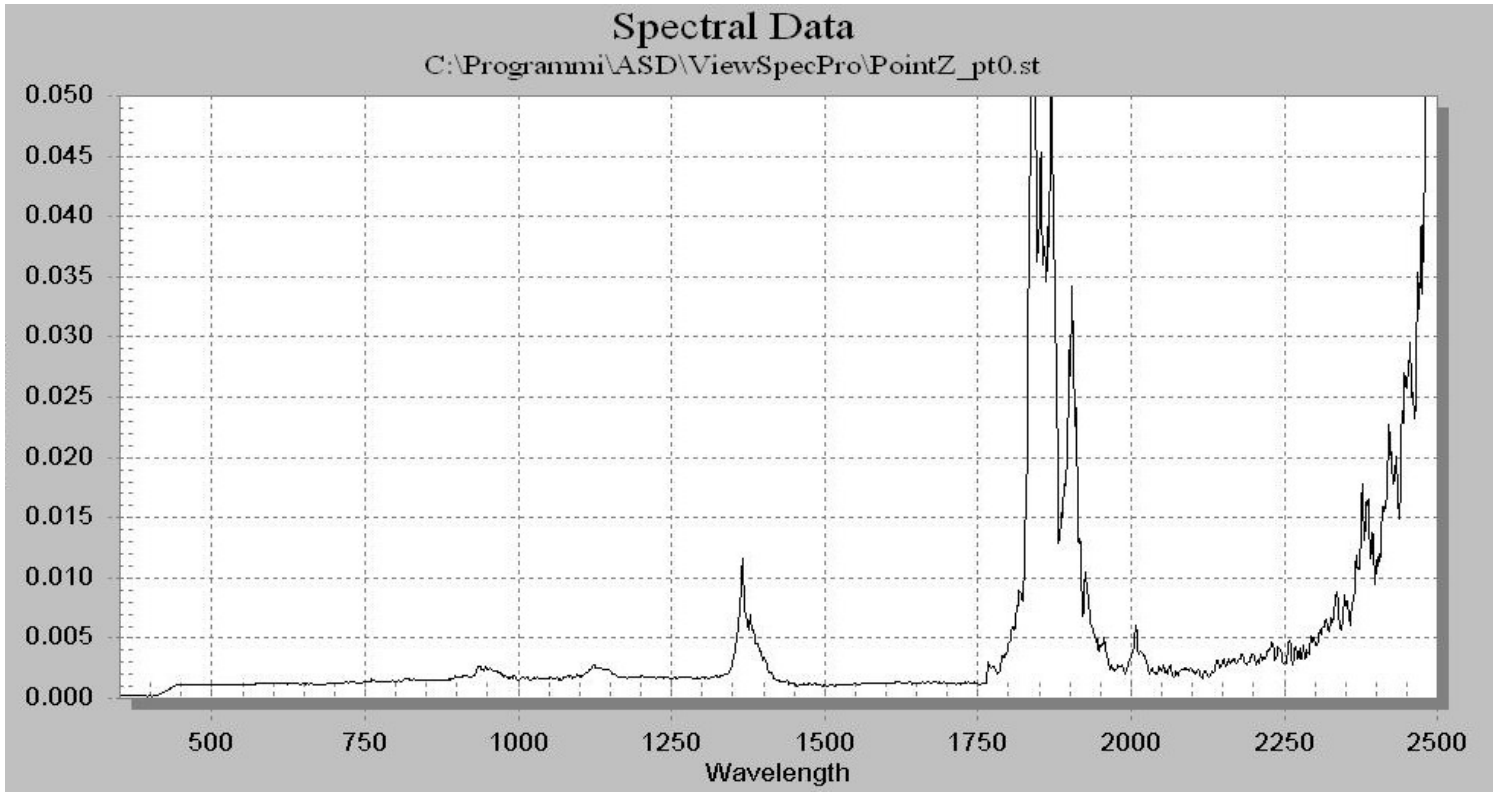

Point Z (1) Teide crater

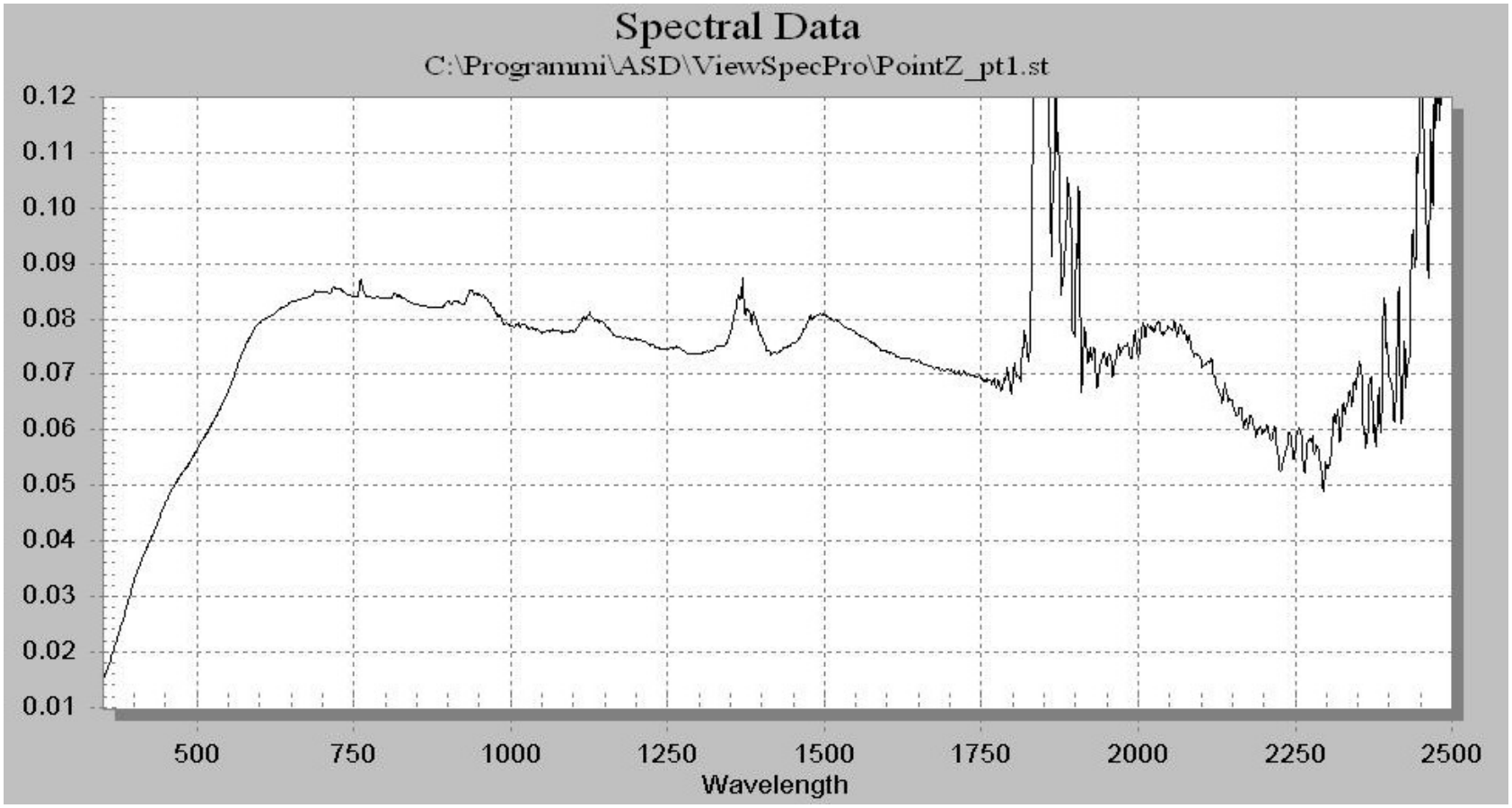

Point Z (2) Teide crater

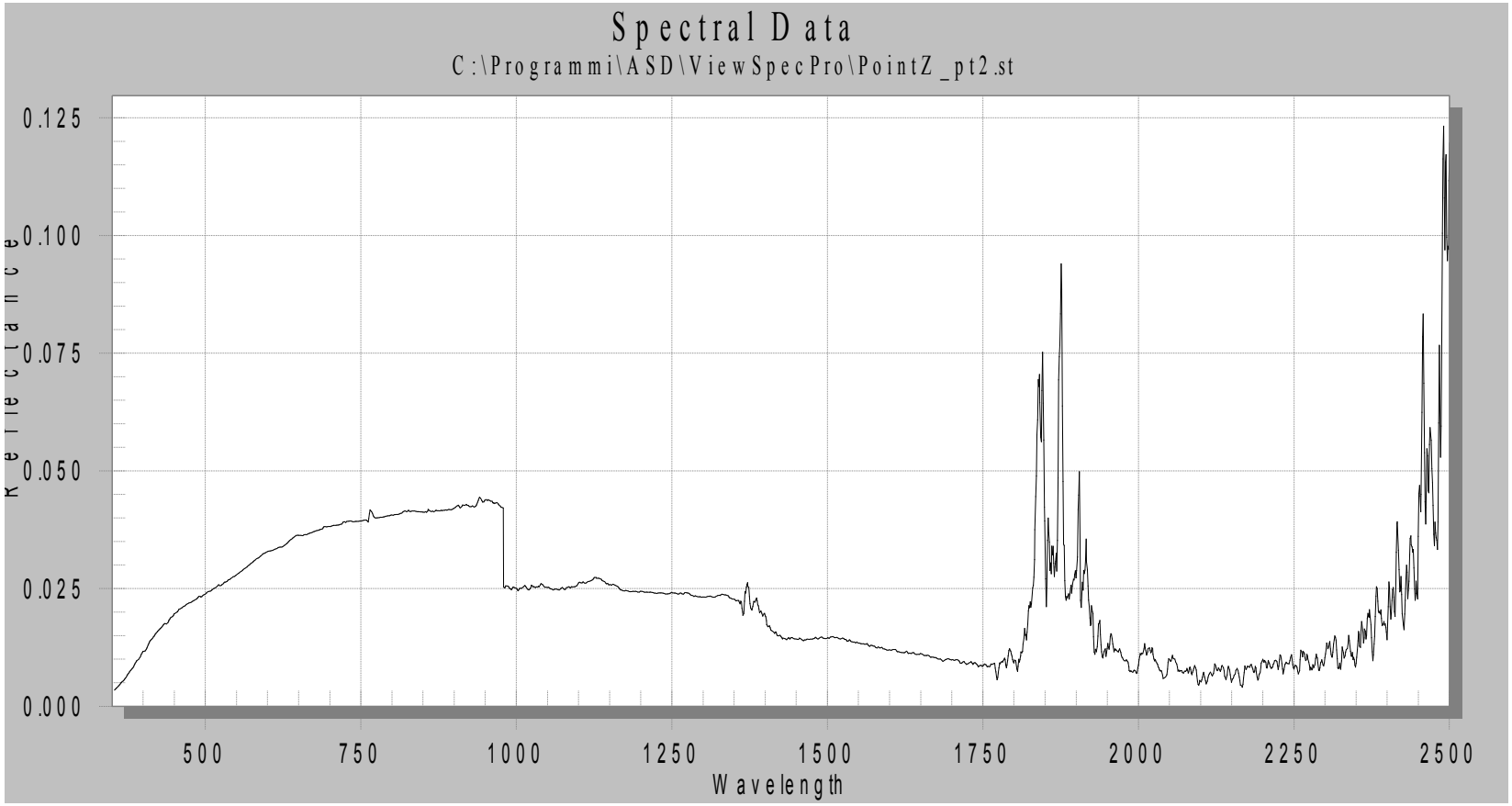

Point S: Boca Tauce

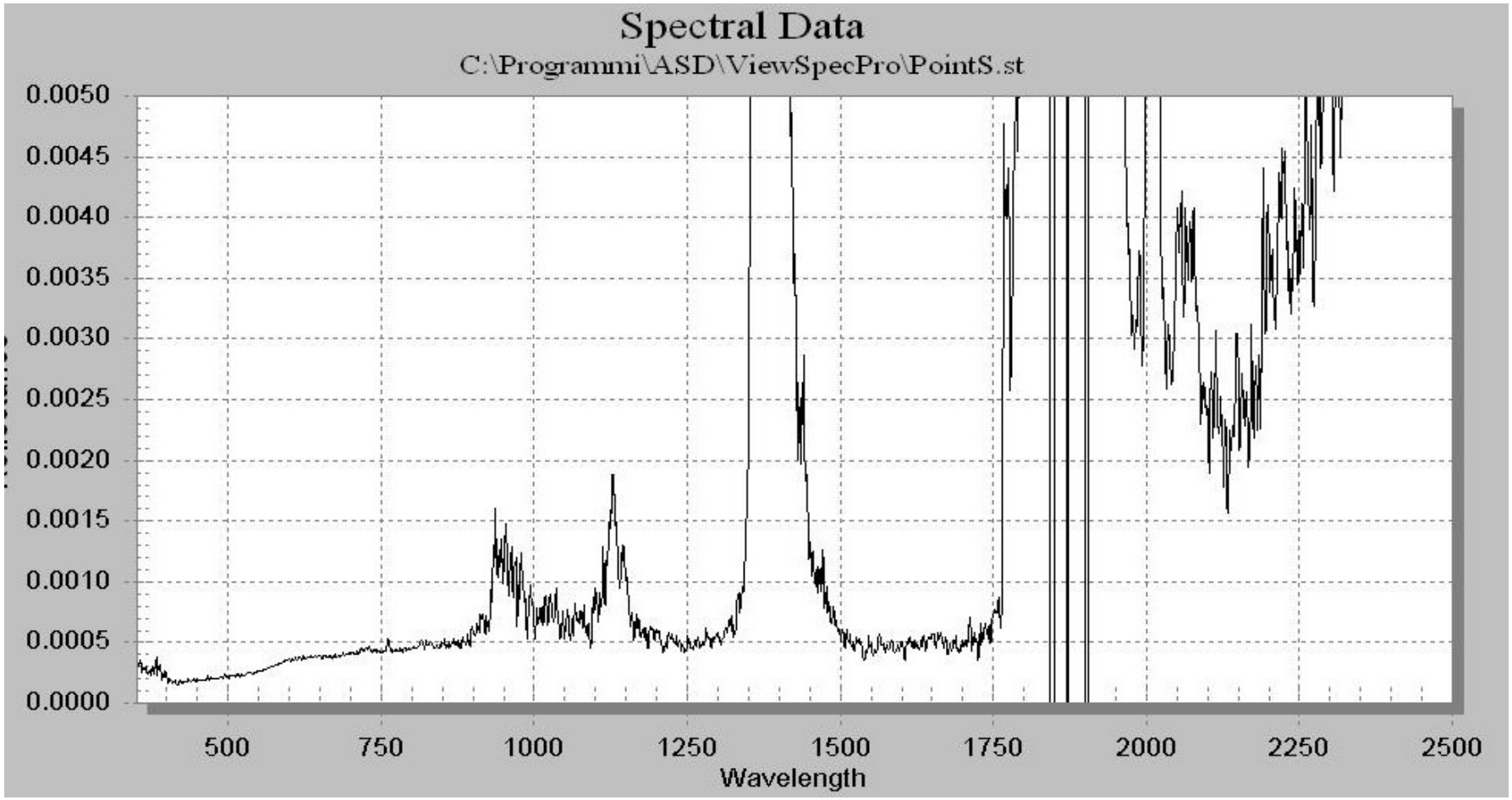

Appendix 3 Standard deviation values for In situ emissivity measurements as error bars

Point P :El Piton

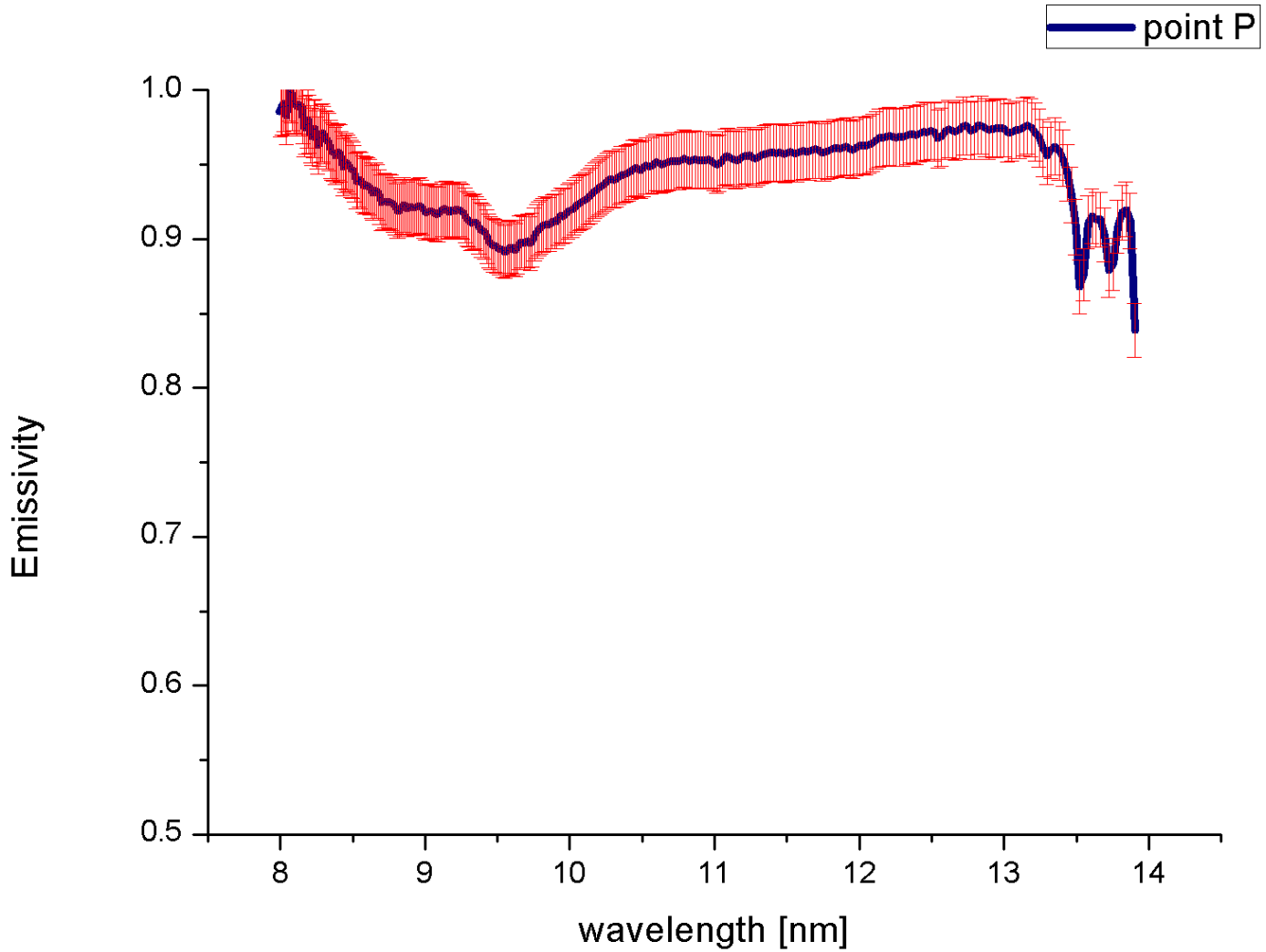

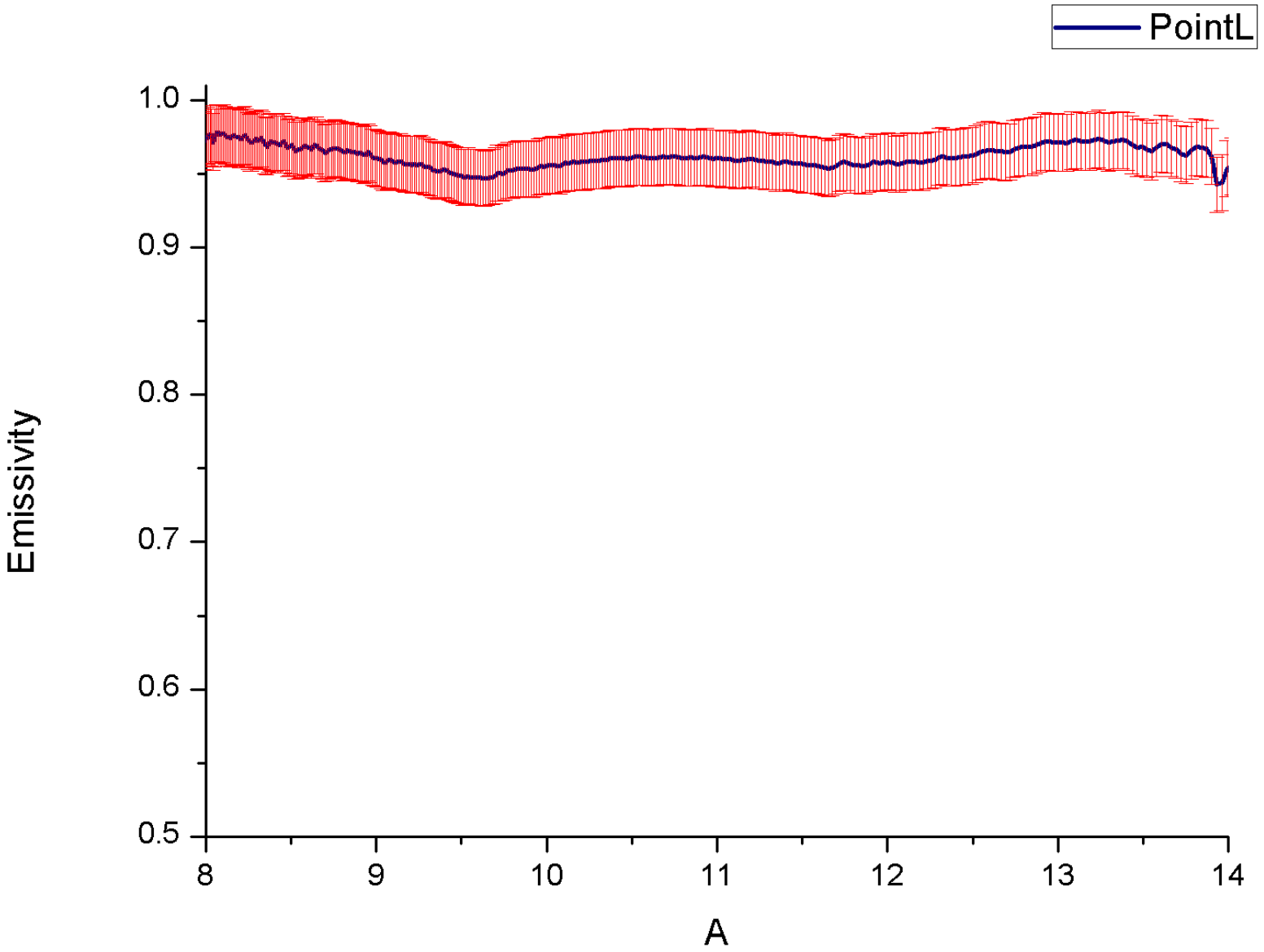
PointL
1.0
0.9
0.8
0.7
0.6
0.5
Emissivity
8
9
10
11
12
13
14
A

Point M: M.Chaorra

Point N

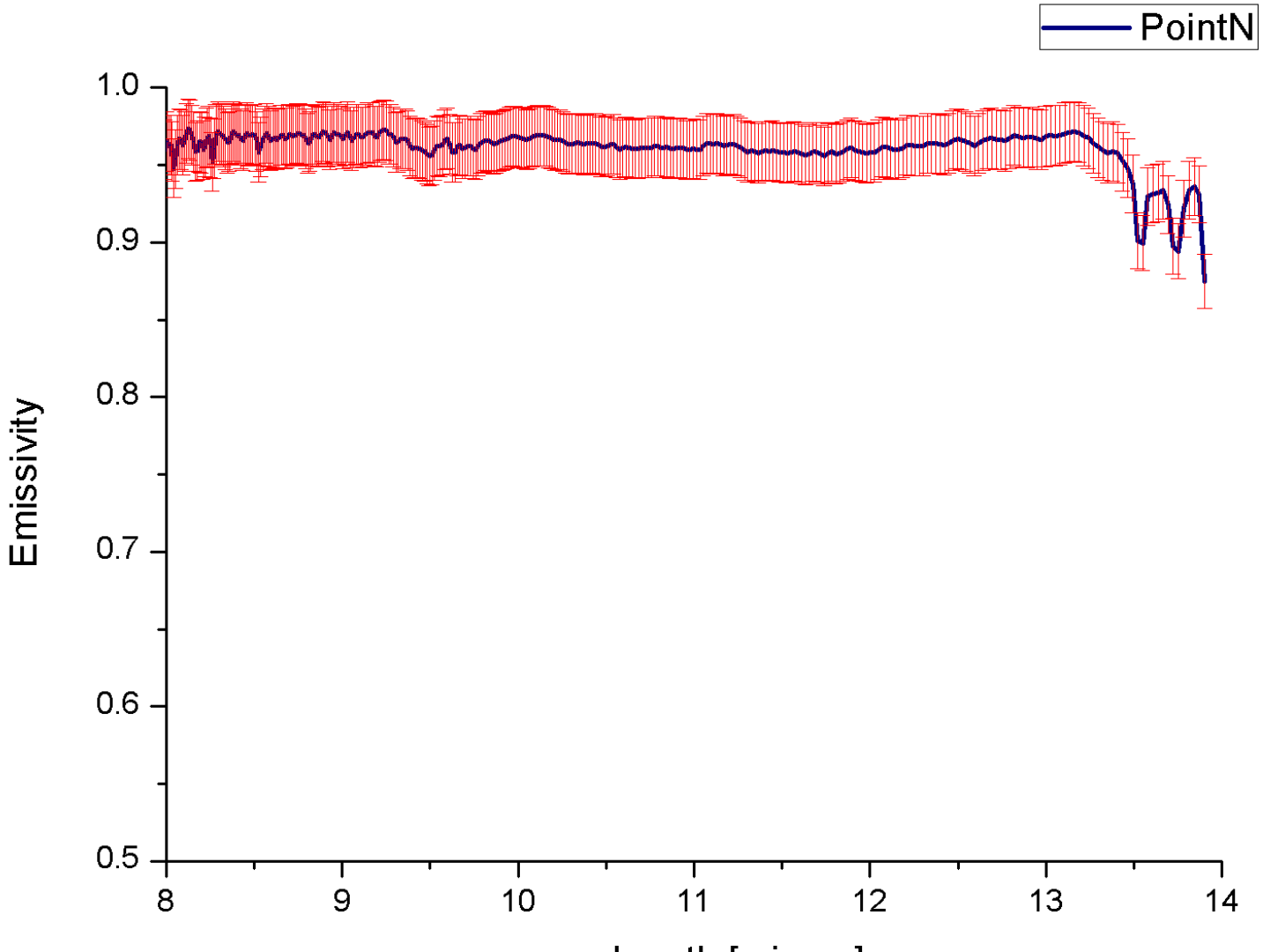

Point O: Llano Ucanca

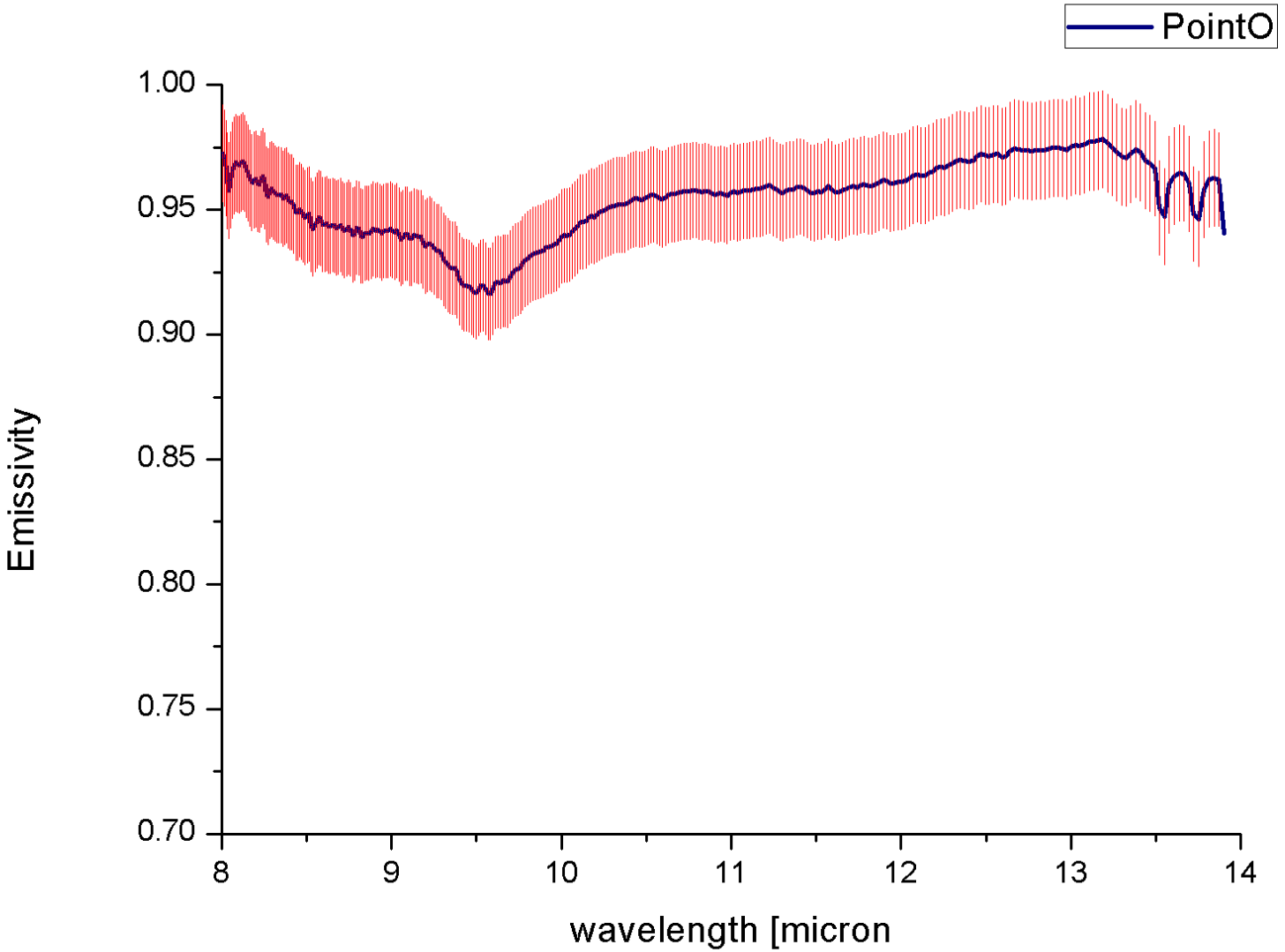

Point U: Mna Mostaza

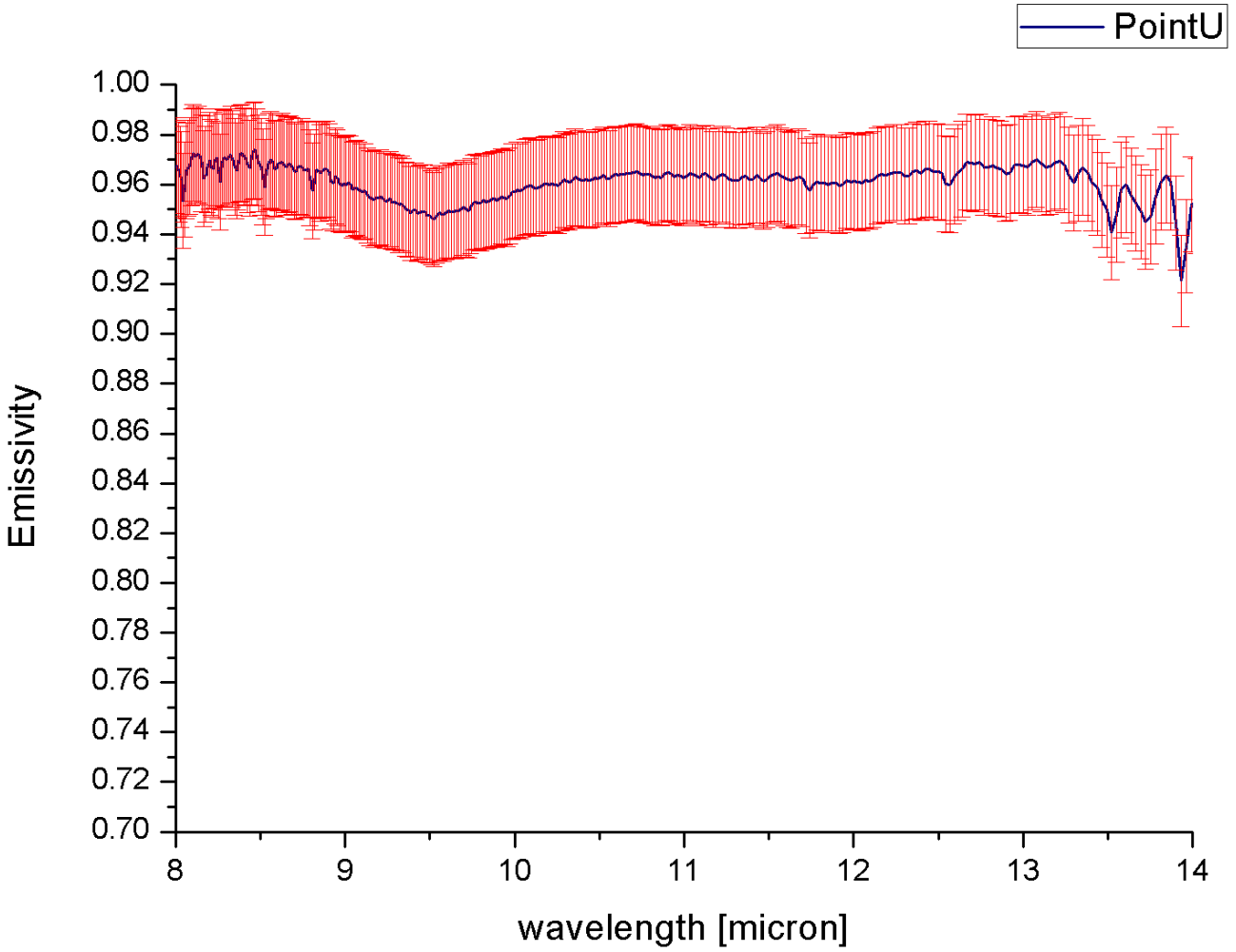

PointV

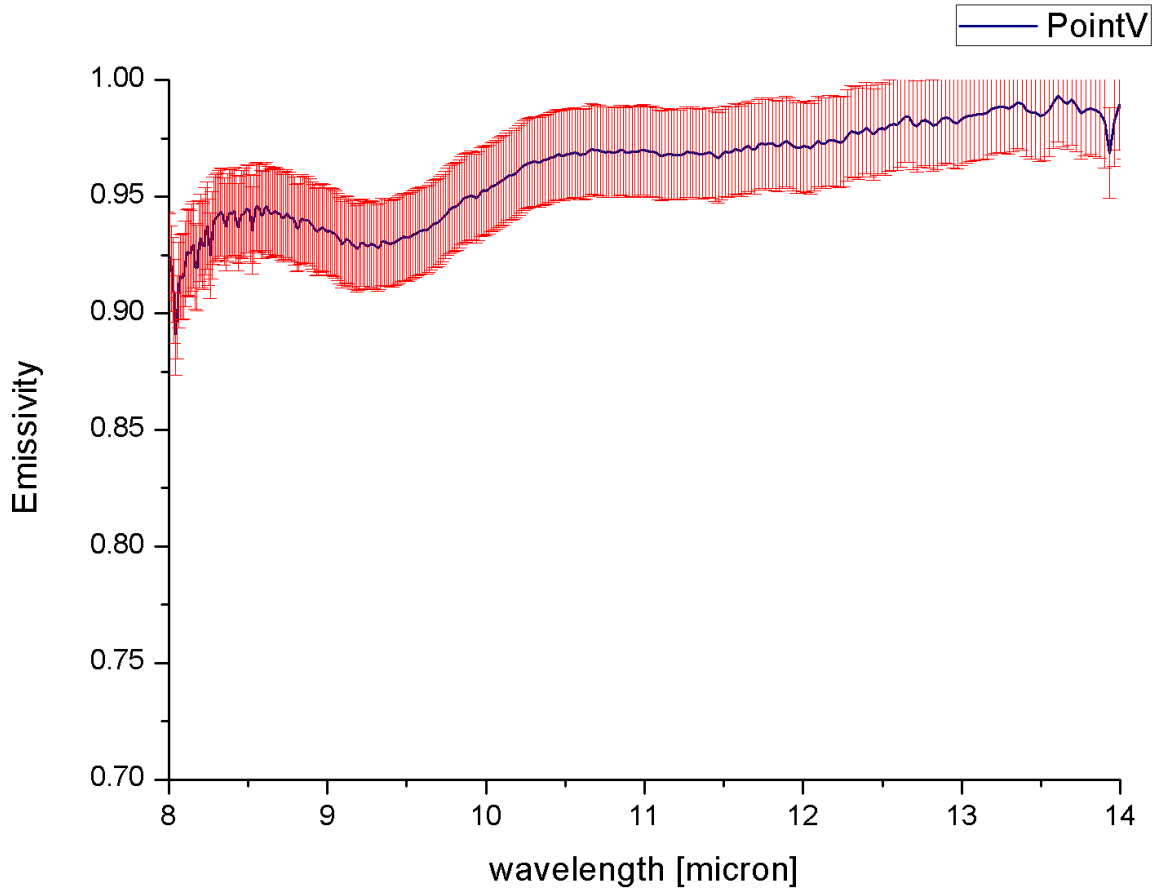
PointV
1.00
0.95
0.90
0.85
0.80
0.75
0.70
Emissivity
8
9
10
11
12
13
14
wavelength [micron]

Point I

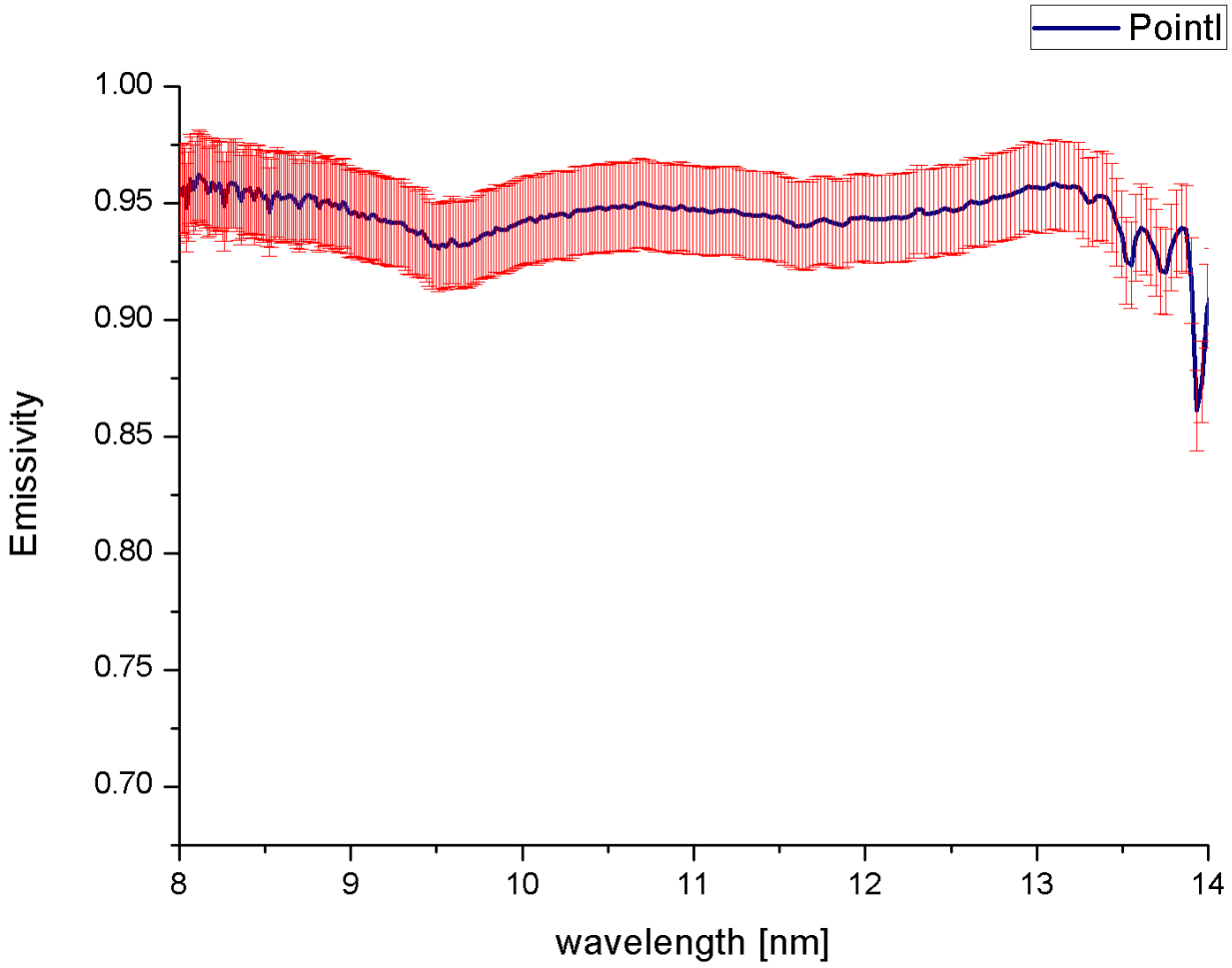
PointI
1.00
0.95
0.90
0.85
0.80
0.75
0.70
Emissivity
8
9
10
11
12
13
14
wavelength [nm]

Point S Boca Tauce

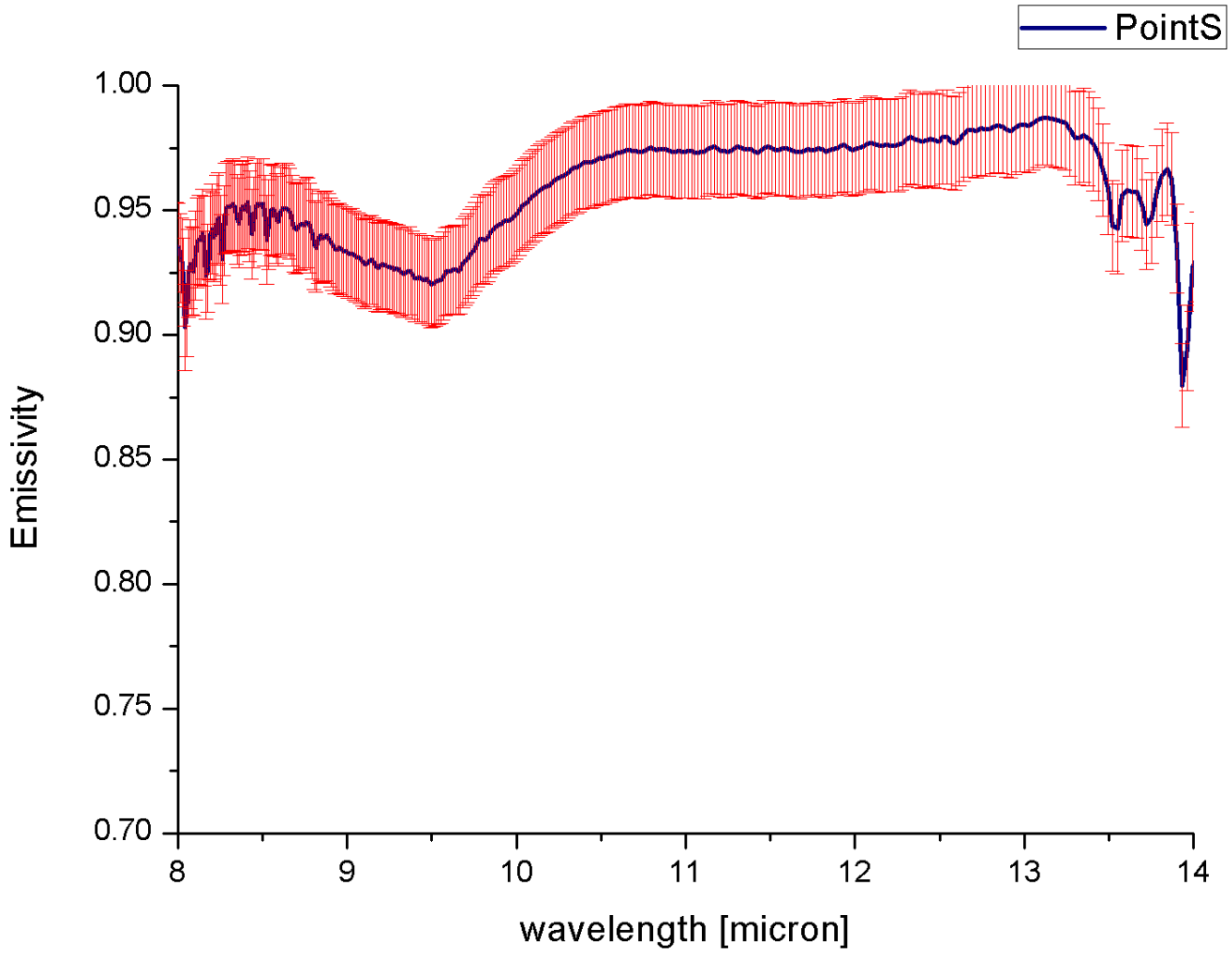

Appendix 4 EVEREST 130,2L OPERATING INSTRUCTIONS

Operating the instrument is quite easy:

Pressing the middle “E” on the back readout panel turns the instrument on.

The abbreviations “IR” stand for current infrared surface temperature reading of the target that the instrument is focused on. While “A” stands for the Average Temperature Reading of the last five or ten readings taken, depending on the Average Mode being utilized.

The EVEREST 130,2L is equipped with a great number of functions. To access and change a variety of functions we use the keypads INDEX and ENTER (

The INDEX key is used to change display modes. The ENTER key is used to finalize functions or exit a mode. Repeatedly pressing the INDEX key will provide access to a variety of standard functions of the infrared thermometer Table .4 :

Function name	Function action
CHANGE F/C	Used to change from C to F
CHANGE AVE MODE:	Used to change from FAST to SLOW Averaging Mode. SLOW Mode takes the average of the last five seconds (or the last ten readings) while the FAST Mode takes the average of the last 2.5 seconds (or the last five readings)
CHANGE RS-232:	Used to change from ECHO to POLL Mode or vice versa. “ECHO” refers to when the computer is simply outputting all the information being processed by the instrument through the RS-232 port. “POLL” means that the instrument is switched to a duplex mode of operation whereby the computer requests the data it wants.
RESET PEAK	Used to reset the PEAK temperature value to current IR Temperature in Real Time Mode The PEAK Temperature is the highest temperature of a target that the instrument has had in

Function name	Function action
	its field of view since initial turn-on or after resetting the Peak Temperature value through the Reset Peak function.
RESET VALLEY:	Used to rest the VALLEY Temperature to the current IR Temperature in Real Time Mode. The VALLEY Temperature is the lowest temperature of a target that the infrared thermometer has had in its field of view since stabilizing after initial turn-on or after resetting the VALLEY Temperature value through the Reset Valley Function.

Table EVEREST functions.

Appendix 5 Data dissemination strategy: FRIENDSpecLib

There are a lot of spectral library of minerals and rocks but they comprehend mainly laboratory data.

The new idea presented here consists in qualifying rock samples, according to the information remotely acquired from space and ground-based platforms obtained following the previously described protocols (in a wide spectral range VIS-MIR) and to disseminate them.

A well characterized spectral library requires set of rocks samples accurately described and complete of ancillary data, able to fully describe chemistry, mineral assemblage and fabric of the rock samples. Furher a great relevance was given to the methodology of in situ spectra acquisition that was realized following precise protocols of measurement.

The strucure of the spectral library that will contain the dataset collected in the frame of this work is showed in the follow paragraph.

A 5.1 Spectral library architecture

In order to develop a spectral library it is necessary to organize the data into a database. A database is a structured collection of records or data that is stored in a computer system. The structure is achieved by organizing the data according to a database model, The relational model is currently the most used and we will refer to RDBMS (Relational Data Base Management System). The fundamental assumption of the relational model is that all data is represented as mathematical n-array relations. The relational model of data permits the database designer to create a consistent, logical representation of information.

To reach this goal are important some steps: collecting the requirements, developing an architecture, planning and development of logical data model and at database implementation (Connolly, T., and Begg C.2002).

Collecting the requirements and developing an architecture is the most onerous part of the job.

An important role is plaid by description of the requirements. It should be most detailed as possible. In fact from requirements will depend the possible queries to question the data base.

In the following is reported a reletional model.

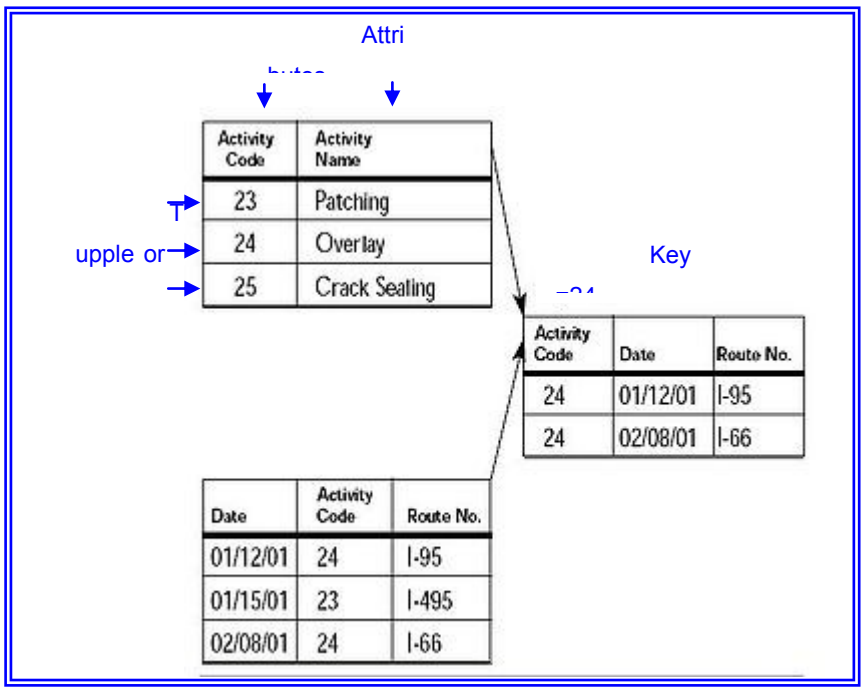

Figure A5.1 :example of relational model (http://en.wikipedia.org/wiki/Relational_model)

To reach this goal are important four step: collecting the requirements, developing an architecture, planning and development of logical data model and at database implementation.

A diagram describing the database philosophy for the FRIENDSpecLib is in Figure

The requirements consist on all information that must be available to the users in form of query.

So an accurate description of the information contained in the data base must be implemented in order to develop the structure of the data base.

The FRIENDSpecLib will be based on the following scheme (Date, C. J., 2003).

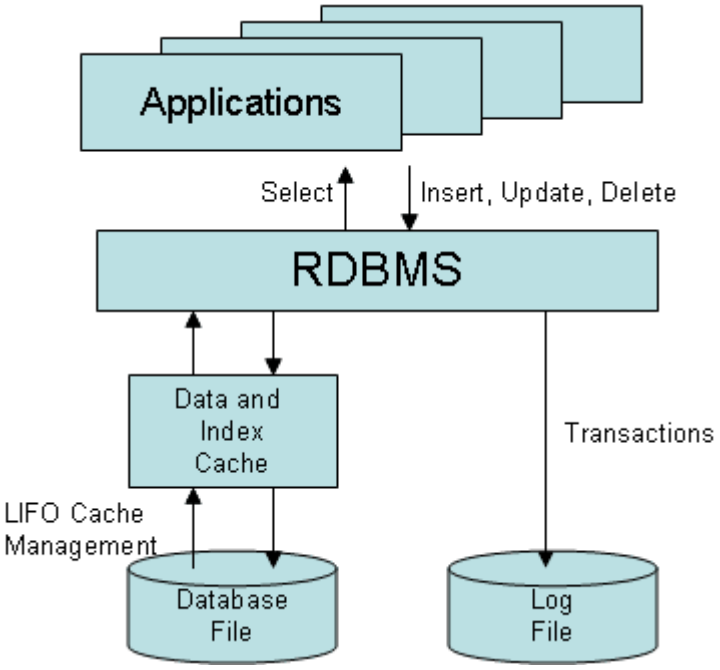

A5.2 Flow diagram of RDBMS

The idea of the spectral Library is that to distribute the data to the scientific community and at the same time to collect data from scientific institutions.

To perform this goal a web interface has been thought according the following scheme:

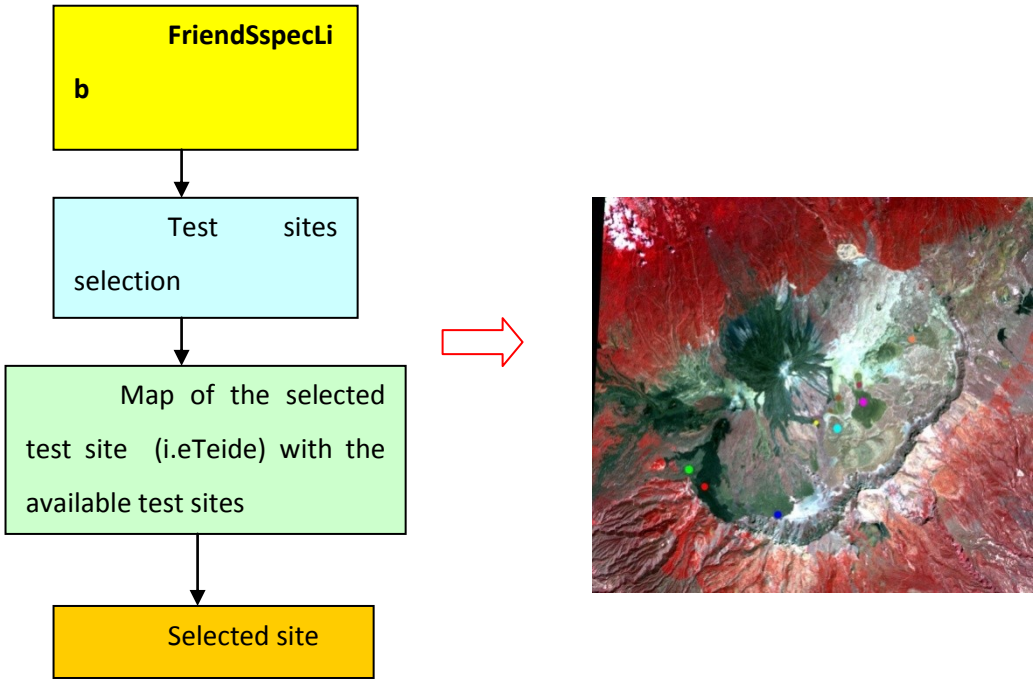

Figure A5.3structure of the FriendSpecLib

For each selected test site a table with available data is provided.

Site ID	
Chemical measurements	Ancillary data file (*.txt)
Laboratory measurements	Ancillary data file(*.txt)
In Situ	Ancillaty data file(*.txt)
Satellite	Ancillary data file(*.txt)

Table 7.1 type of data selection interface.

By the hyperlink is possible to selctthe kind of measurements

For instance by click on In Situ,

On the other side they give information for the requirements of the spectral library.

In the following is showed an example as should appear the the FRIENDSpecLib interface.

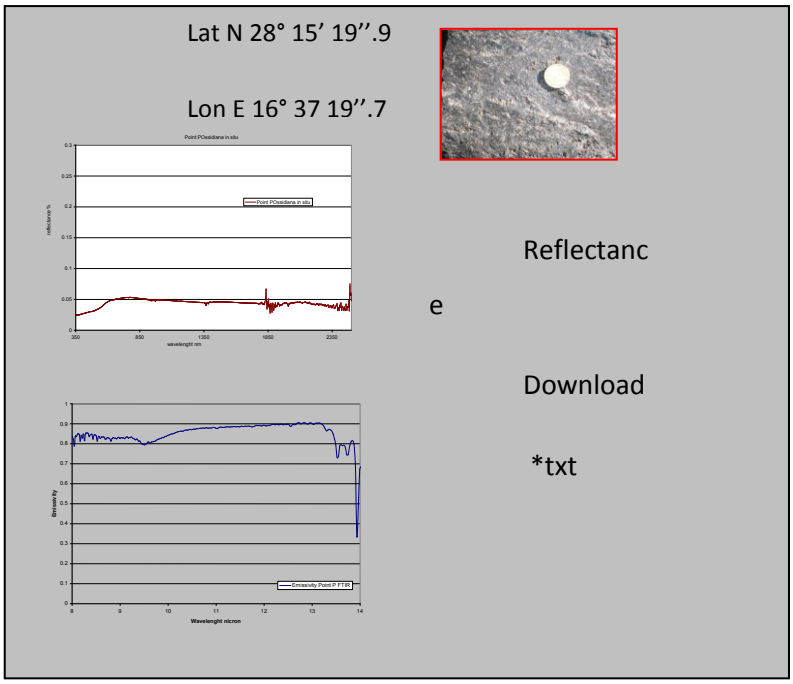

Figure A5.4 interface for the data download